A Study on Laser Forming Processes with Finite Element Analysis

Hyung-Chul JUNG

A thesis submitted in partial fulfillment
of the requirements for the degree of
Doctor of Philosophy
in
Mechanical Engineering
at the
University of Canterbury
Christchurch, New Zealand

April 2006

Abstract

Laser forming is an innovative technique that uses a defocused laser beam to form sheet metal by thermal stresses rather than external forces. Promising potential applications of laser forming include rapid prototyping, straightening, aligning and adjusting of macro/micro-metallic components. Research to-date on laser forming has been largely focused, theoretically and experimentally, on the problem of characterization of process parameters on the forming results, and computational simulations of laser forming remain limited only providing the insight into the process. This study investigates the laser forming processes using the finite element analysis with respect to material responses during the processes, including complex processes, process optimization, process reliability and the effects of thermal and mechanical material properties.

The first part of this thesis describes a nonlinear transient three-dimensional heat transfer finite element model and a rate dependent three-dimensional deformation model, which are developed for the laser forming simulations. Simulations are performed using an indirect coupled thermal-structural method for the processes of a straight-line heating, a circle-line heating, and a laser micro-adjustment. The thermo-mechanical behaviours during the straight-line heating process are presented in terms of temperature, stress and strain, and displacement distributions. The emphasis in the circle-line heating simulations is placed on the characterization of the quality of the deformed geometry by obtaining the radial and circumferential waviness. The micron size movements induced by laser point heating are focused the simulations of the micro-adjustment process. Simulation results are validated by comparison with published data or correlation to engineering point of view.

The second part of this thesis presents the development of an effective method to determine optimum process parameters in laser forming. For the process optimization, design optimisation techniques are introduced into the finite element analysis of the laser forming process. The optimum parameter values to produce a predefined bend angle of 3° in the straight-line heating process are sought by two optimization procedures – one is the procedure involving the non-gradient method and the other is the gradient-based method. Optimum values of laser power, feed rate, beam diameter and number of passes are determined to produce a predefined bend angle in a multiple straight-line heating process using the two optimization procedures. A more suitable optimisation method for laser forming is chosen, which is used for a new optimisation problem to generate a maximum bend angle in a single pass of laser forming.

In the third part of this thesis, a strategy to assess the reliability of the laser forming process is established by employing a well-known reliability analysis method, the Monte Carlo simulation. Robustness of the straight-line heating process of producing 3° with the optimum parameters determined by process optimization is evaluated with regard to the uncertain input variables of laser power, feed rate, plate thickness and coefficient of thermal expansion via the Monte Carlo simulations based on the finite element simulations of the process.

The final part of this thesis identifies the effects of material properties on the bend angle resulting from laser forming. Process sensitivity to the properties of coefficient of thermal expansion, thermal conductivity, specific heat capacity and elastic modulus is investigated by measuring the Pearson product-moment correlation coefficient between the properties and the bend angle, which are based on the Monte Carlo simulations of laser forming.

The conclusion is that the developed finite element models contribute to a better understanding of the laser forming process, and the optimization procedure is able to be used for straightening, aligning and adjusting of components.

Acknowledgements

It is a pleasure for me to record my appreciation to individuals who have helped me either directly or indirectly, in initiating and completing this thesis. First and foremost I am deeply grateful to Dr Susan Krumdieck for supervising this study. Her enthusiasm, guidance and support have been much appreciated. I would also like to thank Dr Paul Tu (now at Calgary University in Canada), who initiated the research described in this thesis and suggested access to laser facilities at Calgary University for experiments. I am very afraid that the experimental work couldn't be progressed to make it into the final version of this thesis. The kind advice and help of Dr Mark Staiger with regard to microstructure change of material after laser forming has been invaluable during my research work. I am only sorry that this interesting work wasn't developed into this thesis. I record my appreciation to Professor Seong-Cheol Lee (at Chonbuk National University in South Korea) who recommended me to the Department of Mechanical Engineering when I applied to the course of this degree, and provided constant encouragement during my study.

I would like to acknowledge the financial support provided by the University of Canterbury in the form of a doctoral scholarship.

I would like to thank Adam Latham and Paul Southward for their technical support.

Thanks are also due to all those friends and family who gave moral support during the time I worked on this thesis and a calming influence during many stressful Ph.D. moments.

Finally, and most importantly, I would like to acknowledge the support and encouragement of my dear wife Suk-Yun Hong and pretty daughter Da-Bin Jung, without whom this thesis would never have been completed.

Contents

List of Figures

List of Tables

Chapter 1
Introduction

1.1 Introduction

Laser forming is a newly developed technique for the shaping of metallic components. The process is achieved by introducing thermal stresses into a sheet of metal by controlled irradiation with a defocused laser beam [1]. In laser forming, the shape and position of a bend are determined by the intensity, scanning speed, beam size and positioning of the laser which are process variables that can be changed or adjusted through electronic control [2]. In conventional forming techniques such as bending, drawing, pressing and stamping special heavy tools (i.e., die and punch) and application of external forces are required to bend flat sheet metal into a component, where the process is changed through re-tooling or re-building the forming machines [3, 4]. Thus, the greatest advantage of the laser forming technique over the conventional methods for small batch production can be placed on process flexibility and reduction of manufacturing cost and time [5, 6, 7, 8].

Promising potential applications of laser forming to macro-scale forming arise in rapid prototyping and shape correction in the automotive, aerospace, and shipbuilding sectors [2, 9, 10, 11, 12]. Micro-scale laser forming for precision adjustment of components in the microelectronics industries is another application, and several laser micro-adjustment techniques are currently under development [13, 14, 15, 16, 17, 18]. Figure 1.1 shows an

Figure 1.1 Near complete folding of a part from a flat steel sheet using multiple linear irradiations. Reproduced from [19].

example of a laser formed part, demonstrating near complete folding from a flat steel sheet using multiple passes [19].

The aim of this research includes: developing the finite element models of the laser forming processes; establishing and implementing process optimization; providing an assessment strategy of the process reliability; and identifying the effects of thermal and mechanical properties on the laser forming process.

The next section of this chapter provides a brief overview of laser forming, including three different processes for which numerical models are developed in this work. The sections thereafter set out the motivation for choosing the research subjects and conducting with the finite element analysis, and the objectives and scope of this study. The final section outlines the organization of the rest of this dissertation.

1.2 Laser Forming

This section describes an overview of laser forming. It begins with a brief description of the laser forming process, followed by the principle of thermal deformation using a straight-line irradiation strategy which is the most widely used to generate a bend angle from a flat metal sheet. Then the laser forming processes to produce complex shaped-parts are discussed. Next, laser micro-adjustment process is briefly introduced. Lastly, advantages and limitations of laser forming are described.

1.2.1 Process description

Figure 1.2 illustrates the schematic diagram of a straight-line irradiation process which produces a bend angle from a flat sheet metal piece. The sheet metal is clamped at one side on a CNC (Computer Numerical Control) machine. The heating on the material surface by a laser beam occurs on one side along a selected line while the CNC table is moving. The surface melting of the material is avoided by adjusting the laser parameters such as laser power, feed rate and beam diameter. The sheet metal expands in the heated zone and thermal stresses are produced by the restriction of the surrounding material. The thermal stresses lead to a bend angle in the sheet metal. The principle of the thermal deformation is described in detail in the following section.

Irradiation intensity is $10^3 \sim 10^4$ W/cm^2. Industrial lasers are used as a beam source, including excimer, carbon dioxide (CO_2) and neodymium:yttrium-aluminum garnet (Nd:YAG). The choice of the laser depends on the task. The excimer laser can be used for the production of parts with length and width dimensions in the range of 10 μm due to its extremely short pulse duration [20, 21]. An overview of some typical lasers is given in Appendix A.

Although laser forming uses active energy from a laser beam instead of external forces, small gravitational forces are induced in the region of the

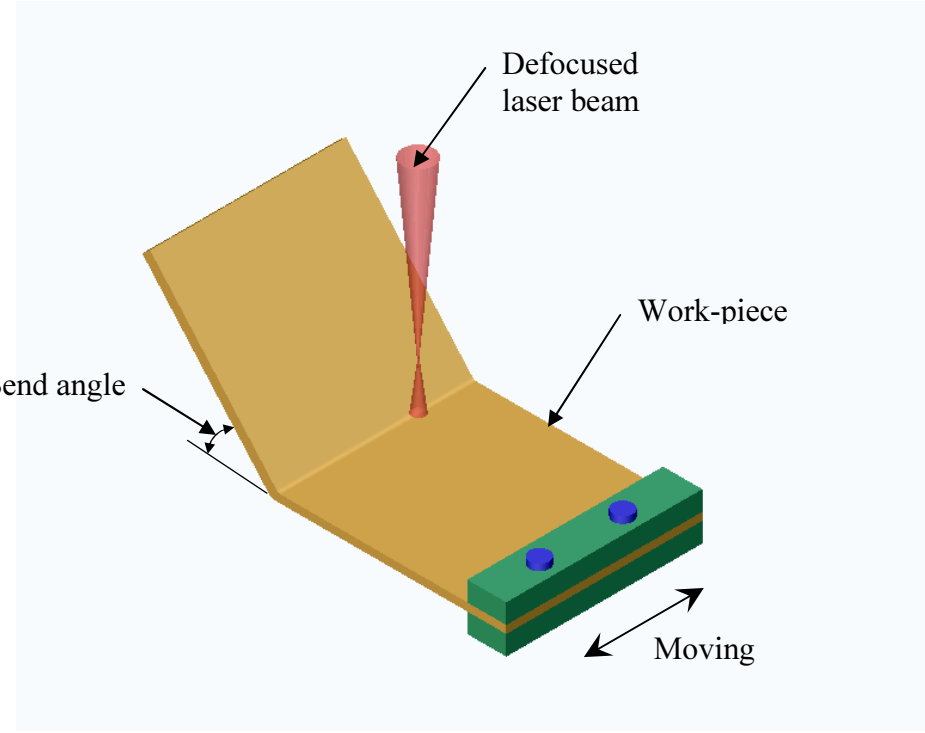

Figure 1.2 Schematic view of a straight-line irradiation by a defocused laser beam to produce a bend angle from a flat sheet metal.

bend edge by part of plate weight. The influence of the gravitational forces can be neglected unless the operation is associated with precision bending involving a large part [10].

Generally, coatings (for example, graphite or phosphate) are used in order to improve the absorption of the laser beam energy into the surface. Without any coating, the absorption rate can be enhanced by using polarized light or using Nd:YAG laser [22].

In general, one or two degrees of bend angle are achieved per irradiation. The bend angles may increase up to 180° with repetition of irradiations [1].

The path of the laser is dependent on the desired shape. In the simplest case, the path may be a point [23], in other cases the path may be a straight line

across the whole part [1, 2, 9, 24] and, for spatially formed parts and extrusions the path would be very sophisticated radial and tangential lines [25, 26, 27, 28].

1.2.2 Principle of thermal deformation

In the traditional metal forming processes such as bending, drawing, stamping and pressing, a sheet of metal is plastically deformed when it is subjected to stress that is greater than the yield point. In the laser forming process, the plastic deformation occurs by the thermal stresses introduced into the surface of a metal sheet during the laser heating and subsequent cooling. The principle of thermal deformation is qualitatively described in this section using a laser forming mechanism (i.e., temperature gradient mechanism), which is based on the work of Namba and Vollertsen [1, 29]. Quantitative explanation of the forming principle is presented in Chapter 4 with the finite element analysis.

Figure 1.3 shows the temperature gradient mechanism involved in the laser forming process. When a laser beam of high power density is rapidly guided across the surface of a metal sheet, the material absorbs a part of the laser energy on the surface and the thermal energy is conducted into the material in lower rate than that of the absorption on the surface, resulting in a steep temperature gradient through the thickness direction as shown in Figure 1.3(a). As a result, a differential thermal expansion occurs through the thickness direction. Initially, the material expands in the heated zone so that the whole shape of the material bends away from the beam as shown in Figure 1.3(b). This is called ‘counter-bending’. This thermal expansion is converted into elastic tensile strain and compressive stress because free expansion of the heated material is restricted by surrounding material. Once the stress reaches the temperature-gradient flow stress, any additional thermal expansion is converted into a plastic strain. To achieve higher efficiency in the process, the thermal expansion has to be converted into more plastic than elastic strain. The amount of elastic strain may be minimized by using high temperatures.

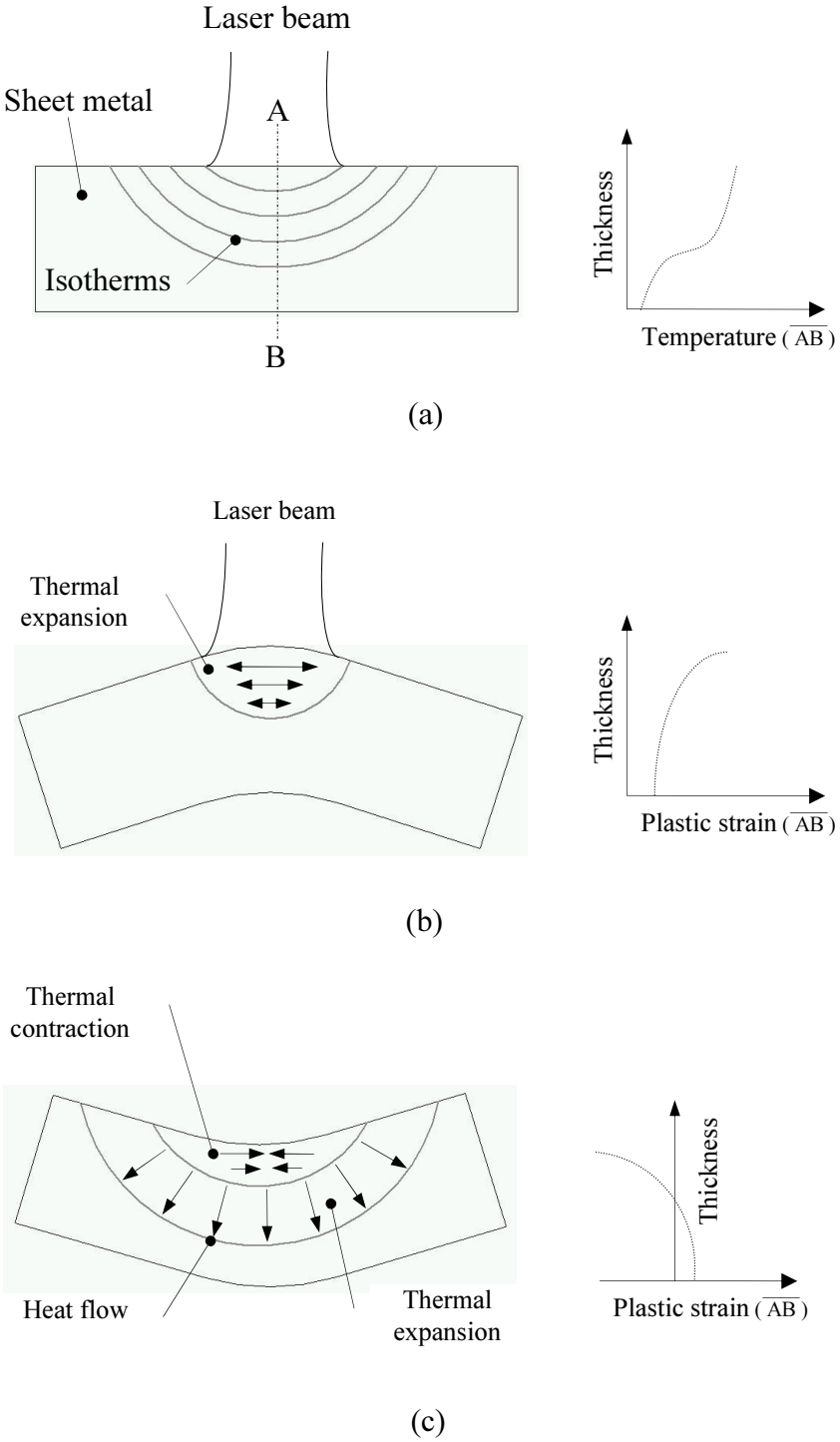

Figure 1.3 Temperature gradient mechanism involved in the laser forming process: (a) temperature gradient; (b) during heating; and (c) during cooling. Redrawn from [68].

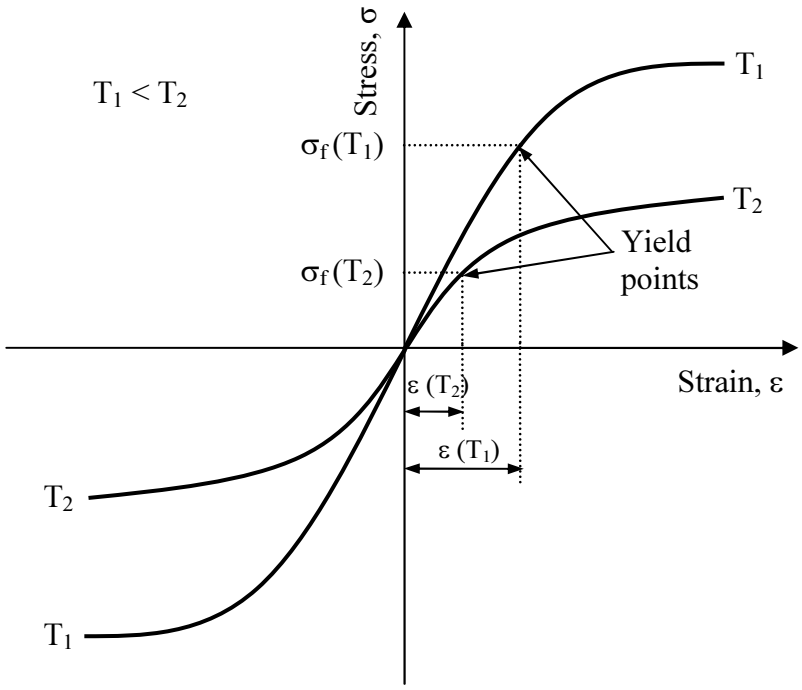

Figure 1.4 Stress-Strain relationships of material as a function of temperature.

As shown in Figure 1.4, the elastic strain as a function of temperature, $\varepsilon(T)$, is determined by the elastic modulus E and the flow stress $\sigma_f(T)$, $\varepsilon(T) = \sigma_f(T)/E$. During cooling mainly by the heat conduction into the material, the material contracts in the upper layer of the sheet so that the higher tensile stress occurs in the upper region. Therefore, the sheet metal is plastically bent toward the cooling laser path to relax the higher tensile stress as shown in Figure 1.3(c). A flow chart of this forming process is shown in Figure 1.5.

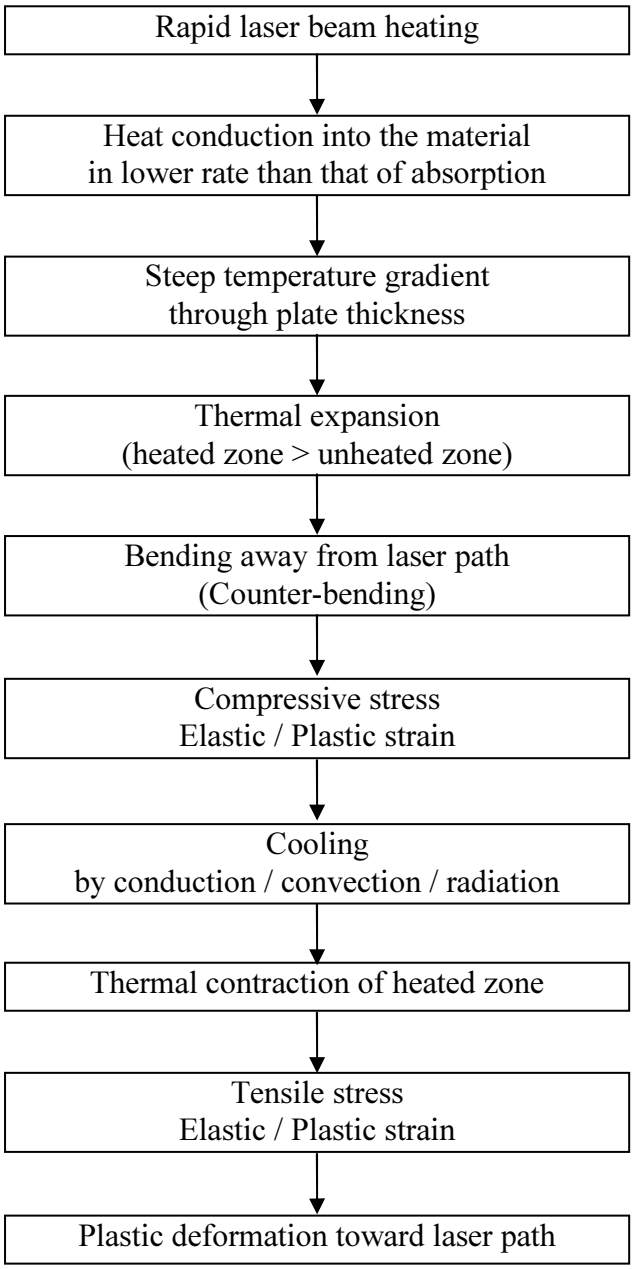

Figure 1.5 A flow chart of laser forming process.

1.2.3 Review of laser forming of complex shaped-parts

Although most research on laser forming is focused on the straight-line irradiation producing a bend angle from a flat plate, laser forming can be used to form a metal sheet into complex structures (for example, dish-shape, saddle, pillow and cone).

Scully [2] proposed that sine, dish, saddle, cone, and screw shapes could be produced by applying different heating patterns.

Hennige [26] presented the capability of laser forming of spherical structures with experiments using curved irradiation lines onto the parts of ring segment and circle sector. He suggested that future work should concentrate on the optimization of the irradiation patterns, and finite element simulation for the process of producing spatially curved parts could be a promising approach to identify the quality of the formed part.

Magee and Watkins [27] reported the generation of a dish-shaped part from a flat circular sheet by the laser forming. He investigated radial, circular scan patterns and a combination of the two patterns to form the dish-shape. The circle-line irradiation pattern with square root radius increase was found to be the best scan strategy. However, they could not measure the radial waviness of the formed part.

Edwardson [25] investigated irradiation strategies to achieve the symmetrical forming of a flat sheet into shapes with double curvatures (i.e., saddle). He found the concentric ‘racetrack’ irradiation strategy gives the better uniformity and least distortion.

Figure 1.6 shows the schematic diagram of the circle-line laser forming process with a circular plate to produce a dish-shaped part. This process is one of the processes to be investigated through the numerical simulations in this study.

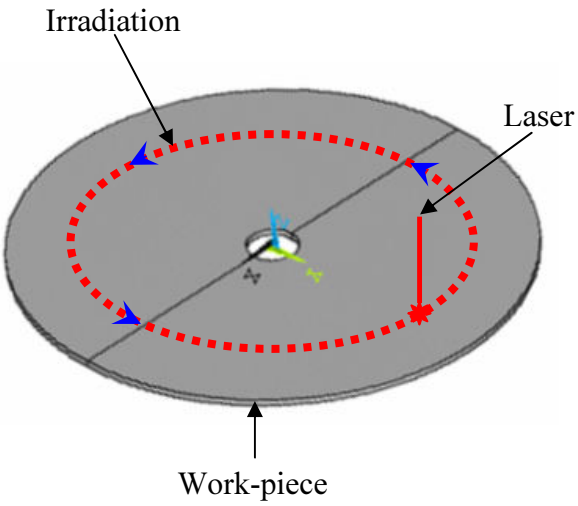

Figure 1.6 Schematic diagram of the circle-line irradiation to produce a dish-shaped part from a flat circular plate.

1.2.4 Review of laser micro-adjustment

The increasing demands in Microsystems led to requirements in production technology for these devices. Especially the packaging and assembly of optical devices like high power diode lasers required high accuracy in positioning. Also adjustment of parts after joining was needed additional expensive mechanical devices that need to be accessible after joining. After the assembly is completed, precise adjustment of components is possible, without mechanical tools, by creating bend angle or changing the length of the parts into a micro size scale by laser micro-adjustment [15]. It is often required to introduce particular geometries (or actuators), on which irradiations are carried out, to effectively adjust objects using the laser adjustment.

Muller [13] used the laser adjustment to adjust a lens in a fiber-coupling module where the lens is positioned between the emitting diode and the fiber. The lens was fixed on an actuator built of three legs (Figure 1.7) and then the actuator was irradiated to obtain a sub-micron displacement.

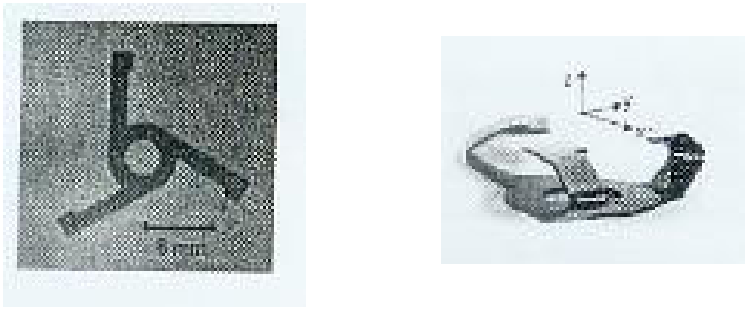

Figure 1.7 Schematic diagram of an actuator for a fiber-coupling module. Reproduced from [13].

Hoving [17] investigated micron level adjustments of a lens by the laser forming of actuator frames during the final assembly of a CD player. An actuator design resembling a 'basket ball basket' was found to give the greatest flexibility of movement and reduced number of steps to achieve a desired lens alignment. Freedom of movement in a number of axes is achieved by applying laser energy in small strokes over several areas of the actuator frame, thereby inducing either in-plane or out-of-plane deformations on the micron scale, as required by the alignment task.

The Laser adjustment has been used for bending 50 μm thick beams in wet-etched silicon micro-scale structures [18].

Currently micro cylindrical lenses for beam collimating of diode lasers are adjusted using extensive manipulation equipment to generate the movements of the lenses. This procedure is expensive and time consuming because the lenses have to be positioned with high accuracy. Olowinsky [15] investigated the adjustment of the lens using a tube-like actuator with its three double bridges (Figure 1.8) that was inserted between the lens and the diode bar. The adjustment in the micron range was realized by irradiating the actuating

structure from one direction (for example, position ‘a’). However, analysis of the behaviours of the actuator was limited due to the difficulty of the experiment. This laser adjustment process is numerically studied in this thesis to improve its fundamental understanding.

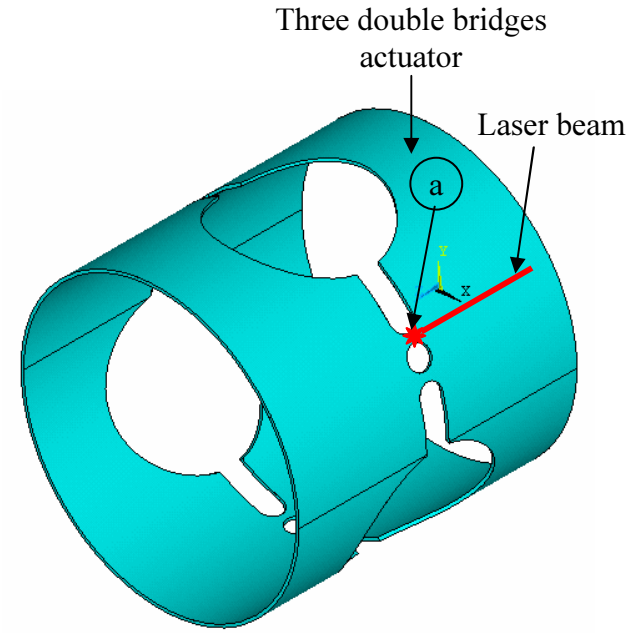

Figure 1.8 Schematic diagram of the point irradiation for the laser micro-adjustment. Redrawn from [15].

1.2.5 Advantages and disadvantages

Due to the fact that the laser forming process involves thermal stresses introduced into a metal sheet by irradiation rather than external forces, which is employed in the conventional forming methods, the laser forming technique has the following advantages compared to the conventional forming operations [1, 2, 5, 9, 10, 12, 24, 25, 26, 27, 30, 31, 32]:

- Flexible forming processes and the elimination of lead time associated with producing component for specific tooling can be realized because special hard tools are not required in this process.
- Precise deformation can be achieved because spring-back behavior is not involved which is related to the quality of product.
- Forming is available in inaccessible areas because this process is a non-contact forming process.
- Brittle, hard and thick material can be processed.
- A wide variety of complex shaped parts can be obtained through the development of new irradiation patterns.

Despite its potential advantages, the laser forming technique is not entirely free of drawbacks which may not yet be eliminated at the present development stage. Some limitations are addressed as follows [5, 7]:

- The forming process is somewhat slow. For some types of forming it is slower by a factor of 5, for others it may be a factor of 20 when compared to traditional methods of stamp and die.
- The process is energy consuming because of the low energy conversion factor of laser sources.

- The process requires safety protection equipment for the personnel because of multidirectional reflection of the laser beam from the metal.

1.3 Motivation

This section outlines the motivation for the numerical investigation of the laser forming processes, process optimization, process reliability, and process sensitivity to the material properties in this study.

Firstly, research to-date on the laser forming has been largely experimental with a straight-line heating process. However, this experimental work is time consuming and expensive, and has limitations for expanding results into the general case. In addition, the forming mechanism was not yet fully understood by empirical work because the laser induced forming process involves very complex, three-dimensional thermal deformations influenced by process parameters such as laser power, scanning speed, beam diameter, scan pattern, material properties and plate dimension. In order to describe the laser forming behavior during the process and characterize the quality of formed parts (especially complex parts), the numerical approach has great advantages.

Secondly, in order to exploit the advantages of the laser forming technique for manufacturing, it is necessary to develop a method for determining the optimum condition of the process required to satisfy forming requirements. The process optimization is possible with the numerical simulations, without trial and error, by introducing a design optimization technique into the numerical model of the laser forming process.

Thirdly, under real life conditions, a bend angle generated with an optimum condition in a straight-line heating process is subjected to uncertainties of input variables. For example, the laser power and feed rate could be fluctuating during the forming process, and the material properties and geometric dimensions of the sheet metal used are not perfect, but within some range of

tolerance. Therefore, it is required to evaluate how much the resulting angular changes are affected by the uncertain input variables in terms of process robustness. It is a strategy of the reliability assessment to incorporate the numerical simulations with a statistical analysis.

Lastly, detailed information about the effects of mechanical and thermal properties on the laser forming process cannot be expected with empirical work and analytical formulae because the deformation pattern in the laser forming is too complex to be investigated using experimental or analytical models. A numerical and statistical approach can be used to overcome the shortcomings of the models.

1.4 Objectives and Scope

The objectives and scope of this research are as follows:

1. *Numerical Model:*

   Develop three dimensional finite element models consisting of thermal, elastic and plastic fields of the laser forming processes – the straight-line irradiation for a simple bend, the circle-line heating for a dish-shaped part, and the laser micro adjustment of an actuator.

2. *Characterization of Laser Forming Process:*

   Identify quantitatively the laser forming behavior through the finite element analysis of the straight-line irradiation process, and characterize the quality of the dish-shaped part and the change in displacements in the actuator with the finite element analysis of each process.

3. *Optimization:*

   Develop an optimization algorithm of process parameters that incorporates with the finite element analysis and a design optimization

technique, as well as determining optimum values of these variables (e.g., laser power, feed rate, beam diameter and number of irradiations) to produce a predefined bend angle in the straight-line laser forming process.

4. *Reliability:*

   Establish an assessment strategy of the reliability of the laser forming process, as well as evaluating the process robustness with regard to uncertainties of the input variables (e.g., laser power, feed rate, plate thickness and coefficient of thermal expansion). It is assumed that the variations of the input variables follow the Gaussian distribution.

5. *Property Sensitivity:*

   Identify which material properties significantly affect the angular change in the straight-line process. The material properties to be investigated are confined to coefficient of thermal expansion, thermal conductivity, specific heat and modulus elasticity.

6. *Future Work:*

   Propose an experiment protocol for future work.

1.5 Outline of the Thesis

This section provides an outline of the organization and contents of the remainder of the thesis.

The organization of the work in this thesis is presented in Figure 1.9. Work began with the finite element analysis of the laser forming processes, followed by process optimization, process reliability, process sensitivity to the material properties, and experiment protocol. Each chapter, starting with the background chapter (not included in Figure 1.9), is outlined as follows:

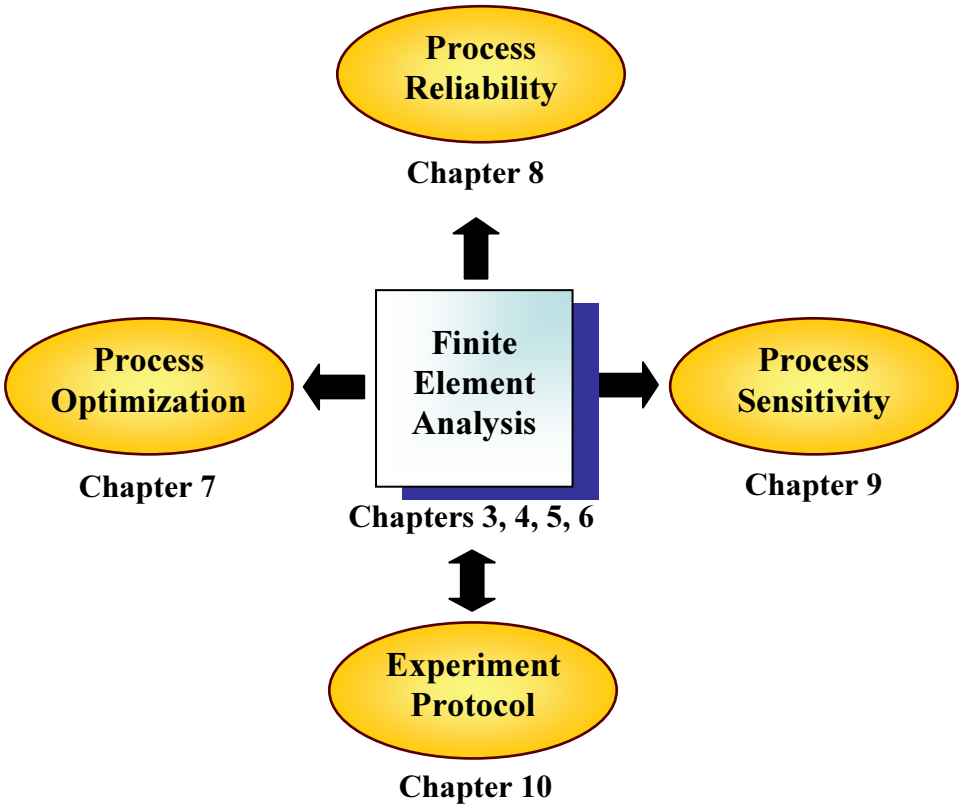

Figure 1.9 Organization of the work in this thesis.

Chapter 2 gives a review of relevant literature for the laser forming technique.

Chapter 3 summarizes the finite element formulations for both the heat transfer and the structural problems which are involved in the laser forming.

Chapter 4 deals with the finite element modeling for the thermal and the elasto-plastic deformation and provides simulation results for the straight-line irradiation process producing a simple bend.

Chapter 5 describes simulation condition on the circle-line heating process for the generation of a dish-shaped part and presents simulation results of the process.

Chapter 6 demonstrates simulation of the laser micro-adjustment using a tubular type of actuator with three double bridges.

Chapter 7 extends the finite element analysis of the straight-line process introduced in Chapter 5 to the process optimization to meet a forming requirement. Two design optimization techniques are discussed and adopted for simulations.

Chapter 8 uses the finite element analysis and statistical approach to establish an evaluation method of the reliability of the laser forming process.

Chapter 9 investigates the material properties significantly affecting the angular change in the laser forming process using the concept of the sensitivity analysis.

Chapter 10 gives the experiment protocol for future work.

Finally, Chapter 11 summarizes the results, and discusses the possibilities for future work.

Chapter 2

Literature Review

2.1 Introduction

This chapter provides background information relating to laser forming, which has been under investigation for about two decades. The research methodologies for the laser forming can be classified into three categories – analytical modelling, experimental work and numerical simulation – as shown in Figure 2.1. Analytical models have contributed to characterizing laser forming mechanisms. The empirical work has concentrated on investigating the effects of process parameters on the angular change, as well as material types amenable to laser forming and metallurgical variations after forming. Finite element simulations have been carried out to improve the fundamental knowledge of laser forming. This literature review begins with a description of the laser forming mechanisms derived from analytical models. Factors important in the laser forming are mainly discussed by review of experimental work. Next, the work done by the numerical simulations are described. At the end of this chapter, conclusion remarks are made concerning the recent development of laser forming techniques and the remaining issues.

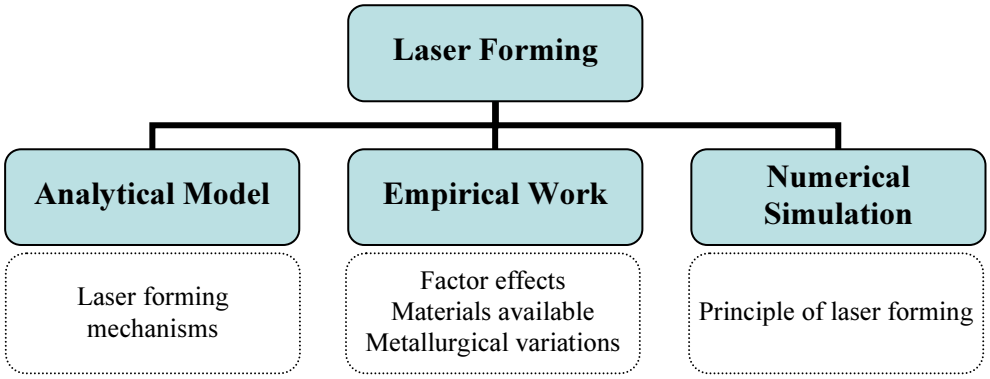

Figure 2.1 Research methodologies and disciplines of laser forming.

2.2 Analytical Models of Laser Forming Mechanisms

Research to-date on the laser forming has been largely experimental. The experimental work, however, is time consuming and expensive, and has limitations for expanding results into the general case. Hence, efforts have been made to develop analytical models to overcome the experimental restrictions. The analytical models were used to identify relationships between the bend angle and the process parameters (i.e., forming mechanisms).

At present, it is not clear how many mechanisms exist in the laser forming. In general, three mechanisms are suggested by many researchers: temperature gradient mechanism (TGM); buckling mechanism (BM); and upsetting mechanism (UM) [30].

2.2.1 Temperature Gradient Mechanism (TGM)

The TGM, which is the most widely known mechanism, explains the principle of thermal deformation (See Section 1.2.2). Characteristics of this mechanism are [29, 30, 33, 34]

- A high temperature gradient through the thickness direction is induced by a rapid feed rate and a small beam diameter (for example, in the order of 1 to the sheet thickness).
- The bending develops to the opposite side of the laser beam during the heating.
- The bending direction is towards the laser beam upon cooling.

The TGM may be used to bend thick plates towards the laser beam source.

An analytical model for the TGM proposed by Vollertsen [30] is described in this section. For his model, he used a pure energy approach, made for flame bending, which is based on the assumption that the power transferred to the sheet metal is converted into a bending action similar to that which would be produced by mechanical bending using the same power. However, the bend angle from the energy approach yielded very high angle which lies some orders of magnitude above the measured one.

The pure energy model was enhanced by introducing a geometrical calculation for the bend angle as shown in Figure 2.2. In the model, it is assumed that the thermal expansion is fully restricted, thus it is fully converted into plastic compression. The temperature increase of the heated layer is calculated as follows:

$$\Delta T = \frac{2Ap_l}{v_l c_p l_h t \rho} \tag{2.1}$$

where:

A = laser power absorption coefficient

p_l = laser beam power

v_l = feed rate

c_p = heat capacity

l_h = length heated

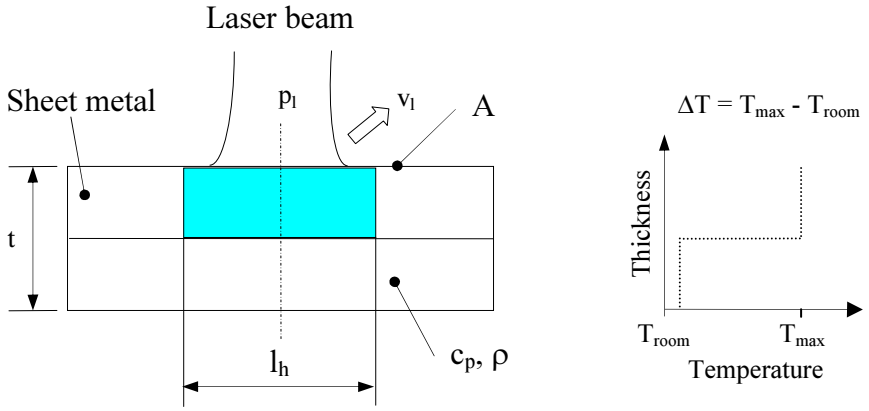

(a)

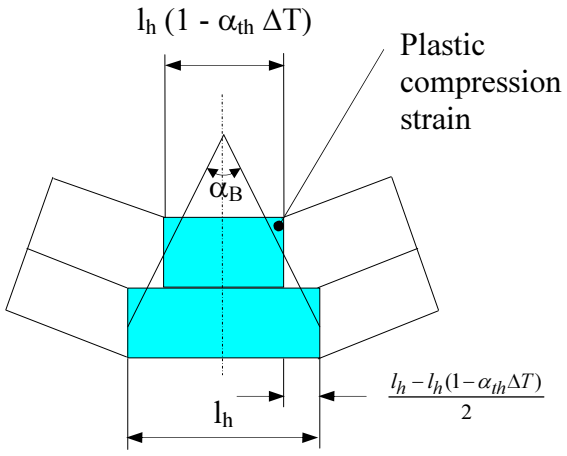

(b)

Figure 2.2 A simple geometrical model for the analytical analysis using an energy approach: (a) during heating; and (b) during cooling. Redrawn from [30].

t = plate thickness

ρ = material density

α_{th} = coefficient of thermal expansion

α_B = bend angle

He assumed that the thermal expansion of the upper layer is fully converted into plastic compressive strain. The plastic strain is given from the coefficient of thermal expansion and the temperature increase of Eq. (2.1). The bend angle after cooling is obtained from the geometrical conditions defined in Figure 2.2(b).

$$\alpha_B = \frac{4Ap_l\alpha_{th}}{v_l c_p \rho t^2} \tag{2.2}$$

In order to account for the restraining forces due to the moment of inertia during cooling, Eq. (2.2) was further developed into a somewhat more sophisticated model [34].

$$\alpha_B = \frac{3Ap_l\alpha_{th}}{v_l c_p \rho t^2} \tag{2.3}$$

Calculations from the two-layer analytical model have been compared to the experimental results of commonly used aerospace alloys (i.e., Ti6Al4V and AA 2024 T3) [8]. There were considerable differences in the analytical model predicted values compared with the empirical data. These differences were attributed to no account being taken of the strength of the material, the elastic counter bending, or the details of the temperature field.

Vollertsen's model also does not include the effect of beam diameter on bend angle. All remaining terms in this equation, that is, α_{th}, ρ, c_p, and A, are essentially constant for materials. Consequently, Eq. (2.3) is not considered to be a good predictor of bend angle behavior [7].

2.2.2 Buckling Mechanism (BM) [30, 35]

Compared to the TGM, the BM can be generated by reducing the feed rate and increasing the beam diameter in order to avoid the steep temperature gradient involved in the TGM. For example, the ratio of the diameter of the heated area to the sheet thickness is on the order of 10 in the BM. Unlike the TGM, the bending direction is not changing during the heating and cooling process. An important feature of the BM is that the direction of the geometry change is not defined by the process itself. It depends on the boundary conditions, mainly to the precurvature of the sheet, internal stresses and external or gravitational forces. However, it is possible to bend a sheet of metal in a defined way using the BM, which allows the mechanism to be used as a flexible forming process. Therefore, it is suggested that the BM may be employed for bending thin sheets along a straight line towards or away from the laser beam [38, 44, 57]. It is also proposed that it may be used for a tube bend [36, 37].

Figure 2.3 shows the developing stages of a bend angle from a sheet of metal under the BM. Figure 2.3 (a) illustrates the compressive thermal stresses generated by a laser beam. It can be seen from the figure that there is no steep temperature gradient in the sheet metal. Figure 2.3 (b) shows buckling starting to develop in the sheet metal which is originated from instability due to thermal stresses. As discussed above, the buckle can be towards or away from the laser beam, depending on the pre-stressing condition of the material. Figure 2.3 (c) presents the development of both the plastic deformation and the elastic deformations in the sheet metal. The plastic buckling occurs preferentially at the top of the metal sheet because the flow stress is low in this region due to the temperature rise (See Figure 1.4), and the elastic deformation is involved at the neighboring region of the plastic buckling due to the lower heating. Forces caused by the elastic deformation are counteracted by the constraints from surrounding material. The buckling increases along the scanning line. Figure 2.3 (d) shows the full development of a bend angle. The buckle is generated across the whole sheet when the laser beam leaves the sheet surface because no

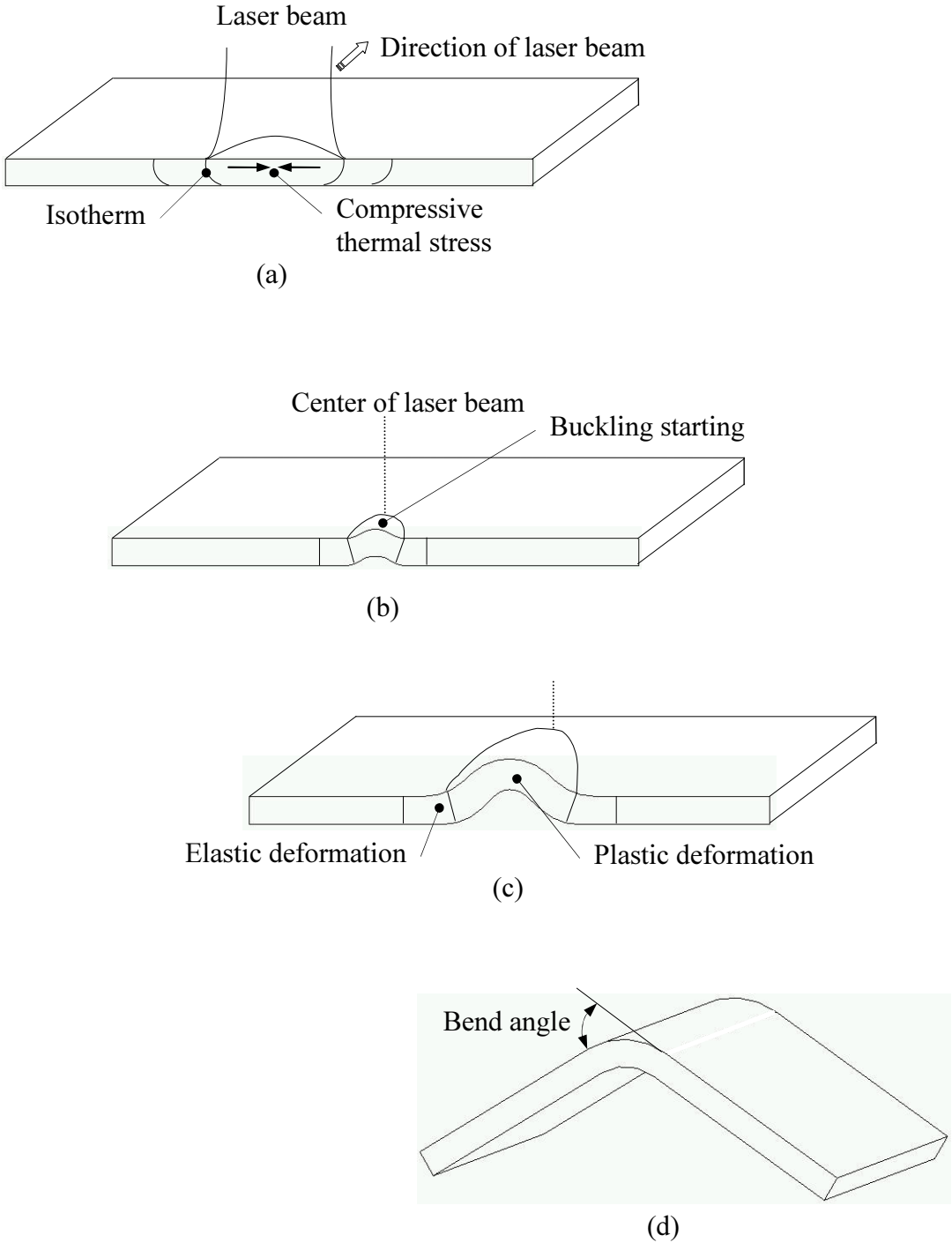

Figure 2.3 Laser forming stages by BM: (a) generation of thermal compressive stresses by a laser beam; (b) development of buckling by thermal stresses; (c) development of elastic and plastic deformations; and (d) development of a bend angle. Redrawn from [30].

restraining forces against the elastic strains are left, and the elastic strains relax becoming straight, whereas the plastic bend remains.

2.2.3 Upsetting Mechanism (UM) [30]

The UM is a shortening (or thickening) mechanism as shown in Figure 2.4. Compared to the parameters used in the BM, this mechanism is based on a sheet metal thicker and stiffer to avoid a buckling, and involves a smaller beam diameter. In the UM process, the sheet metal is almost constantly expanded through the thickness direction during heating, and it contracts in the width direction of the sheet metal during cooling. Thus, the thickness of the plate increases. This heating process is repeated across the whole width of the material to change the thickness in the plate. This mechanism can be used to form a plane sheet into a spacially formed part with a proper heating strategy. Aligning, adjustment and rapid prototyping are also possible.

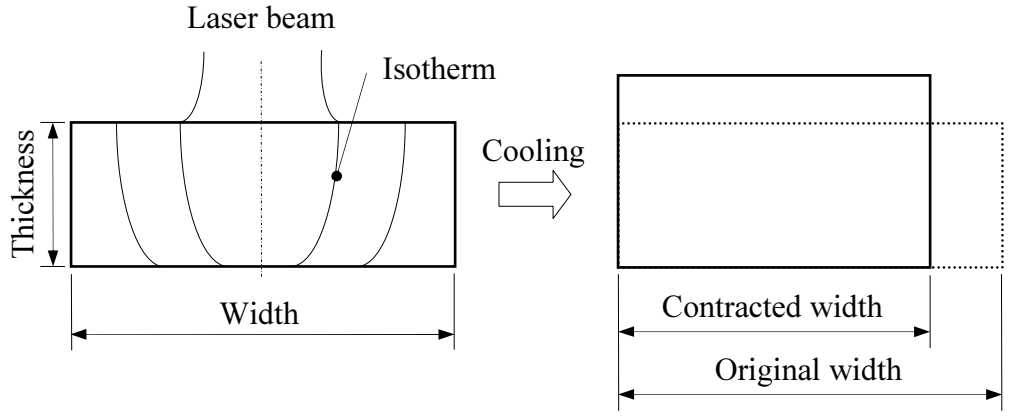

Figure 2.4 Laser forming by the UM. Redrawn from [30].

As stated above, in the laser forming process, a forming mechanism is mainly determined by the temperature distributions produced inside the material. Thus, a desired mechanism can be generated by controlling laser parameters (i.e., laser power, feed rate and beam diameter) and plate dimensions. The laser forming mechanisms are summarized in Figure 2.5.

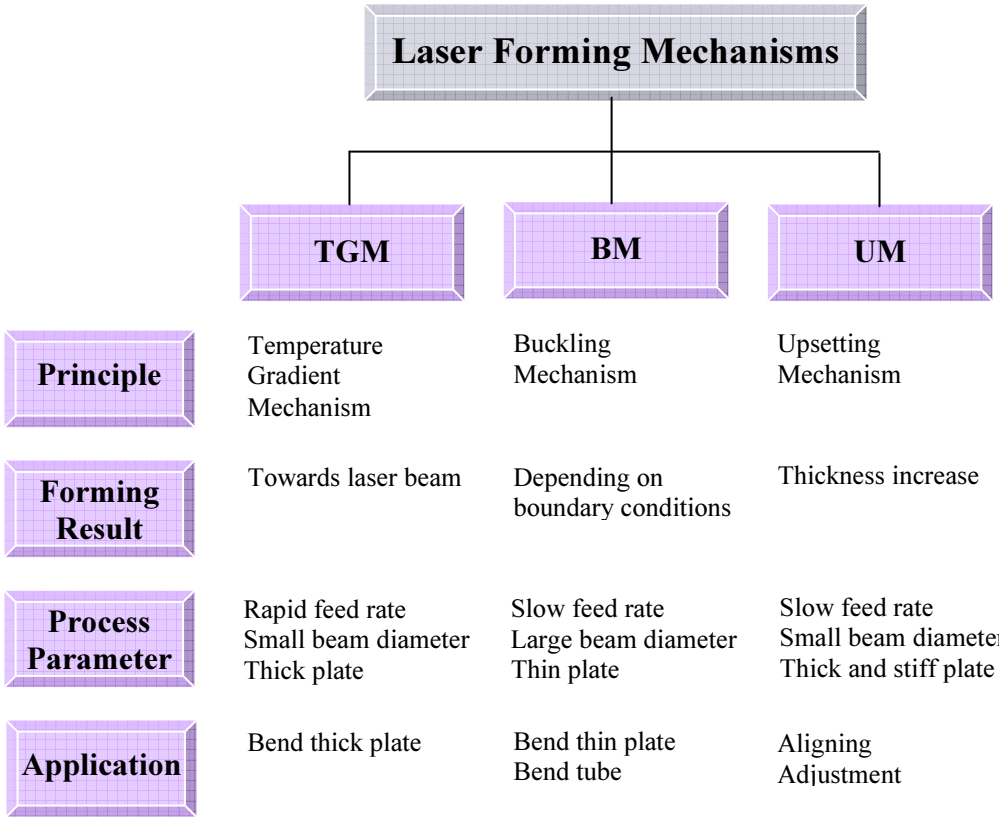

Figure 2.5 Summary of laser forming mechanisms.

2.3 Empirical Studies of Factors in Laser Forming

Great efforts have been made experimentally in order to identify the effects of factors on the geometry change in laser forming. The factors important in laser forming can be divided into three groups – energy parameters, material properties and plate geometry - as shown in Figure 2.6.

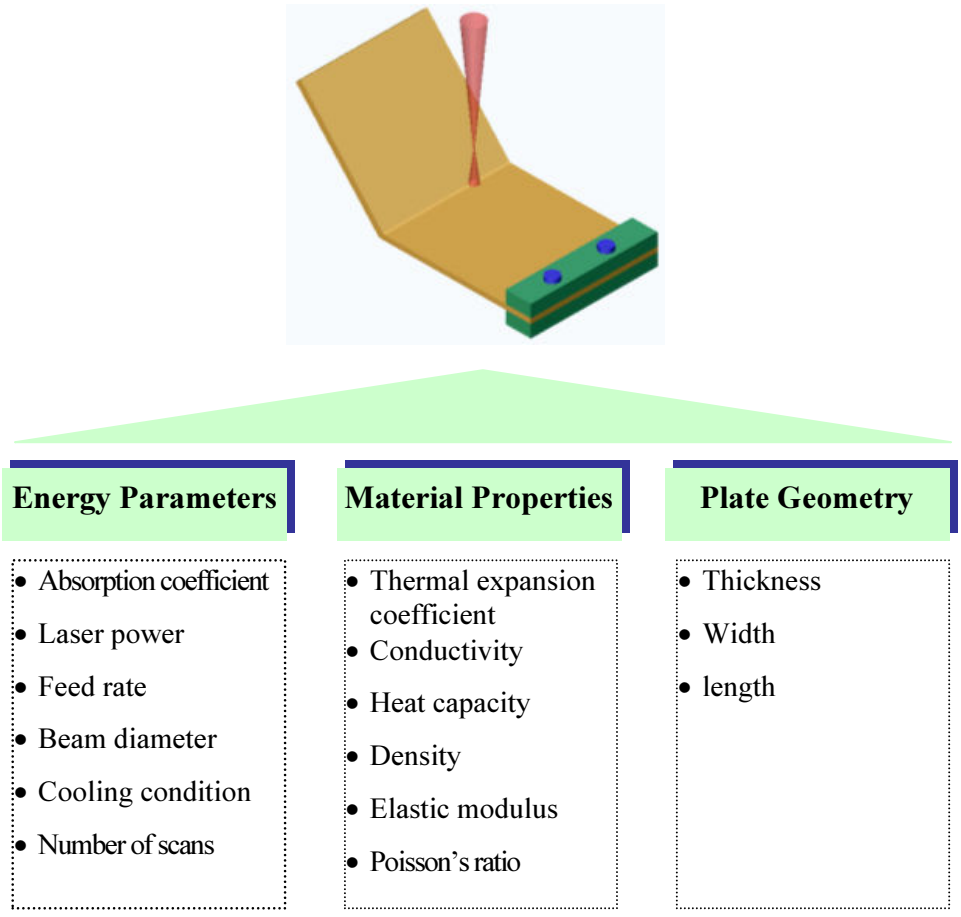

Figure 2.6 Factors important in laser forming.

2.3.1 Energy parameters

Laser forming is associated with the energy absorption into the metal sheet because the process is based on the surface heating by a laser beam. The heat flux on to the surface of the sheet metal by a laser beam obeys a normal distribution, and is expressed as a function of beam radius as follows [38]:

$$q(r) = \frac{2\eta P}{\pi R^2} \exp\left(-\frac{2r^2}{R^2} \right) \tag{2.4}$$

where:

q = the heat flux density

η = the absorptivity on the sheet metal surface

P = the laser beam power

R = the laser beam radius

r = the distance from the center of the laser beam.

It has been shown that the primary factors involved in the energy absorption are surface property of the material, laser power and scanning speed [20]. Beam diameter and cooling effect are considered to be less important than the primary factors in the laser forming [2]. The relationship between the critical parameters is investigated using a concept of line energy [2, 10, 28, 39, 40].

2.3.1.1 Surface absorption of the material

There are complex interactions between the absorption behavior and the processing parameters. It has been demonstrated that the laser intensity has a strong influence on the absorption behavior. For example, the absorption of CO_2 laser light is very low (i.e., on the order of 0.1) for uncoated materials. The absorptivity, which depends on the kind of material, increases when a laser beam with a shorter wavelength (e.g., YAG laser) is used [20].

The absorptivity is also strongly dependent on the surface condition of the metal sheet. Surface coating can be used to increase the absorption. The use of graphite coating is preferred for the laser forming because it has a very high absorption coefficient in the range of 60 ~ 80% and the coating method is simple. Some disadvantages of the graphite coating are that it is somewhat difficult to automate the coating procedure and, in addition, with the coating thickness changing during multiple irradiations, the absorption behavior is not constant for multiple irradiations, which makes some control of the absorption behavior very complicated [41].

2.3.1.2 Laser power

In general, there is a linear relationship between the laser power and the bend angle, and in modern laser machines, the laser power is controlled in a wide range of the nominal power (for example, 1 ~ 100 % in steps of 1% of the nominal power). Therefore, one of the easy approaches to obtain a desired bend angle is to control the laser power [20].

As the power increases, the bend angle increases, goes through a maximum, then decreases. It indicates that there is an optimal laser power that yields a maximum bend angle [11, 42].

The bend angle from an aluminum alloy was significantly smaller than expected from the linear relationship for the high range of the laser power. This may be explained by an increased dissipation of energy in the material and a loss of efficiency at the high energy input levels. It is found that there is no bending below a certain laser power due to reversible elastic effects or the threshold energy [34].

2.3.1.3 Scanning speed

The scanning speed (actually, the feed rate of the CNC machine on which the plate is placed) is the easiest way to control the energy absorption in laser forming [20]. Thus, many experiments have been done with a variation of the

feed rate. It has been reported that the general effect of increasing the feed rate on bend angle is that the angle decreases in a linear pattern [7]. The reason for this effect is that a lesser amount of heat energy per unit time is transferred in the sheet metal, thereby causing less angular development.

However, the linear decrease of bend angle against the scanning speed could not be found in an experiment [43]. In spite of the fact that the input energy by laser heating is constant, the bend angle increases as the path feed rate increases. The reason for this behavior is that different scanning speeds change the temperature profile. In the case of a low scanning speed the temperature field is more homogeneous due to the fact that there is more time for heat conduction into the lower layer of the sheet. Therefore, the difference in plastic strain of the irradiated layer and the layer not irradiated is smaller. For high path feed rates a very steep temperature gradient occurs in the plate and the steep gradient generates high gradients of the plastic compression.

The report by Watkins [8] proposed that the bend angle increases with the scanning speed up to a certain level of scanning speed, indicating that an optimum of the temperature gradient to maximize the bend angle is reached at the certain scanning speed.

2.3.1.4 Beam diameter

The effect of the beam diameter on the forming results is much smaller than that of the laser power or the feed rate [20]. However, the beam diameter is related to the laser forming mechanisms because it is associated with the energy density (See Section 2.2) [8, 42, 44].

The general effect of increasing beam diameter on bend angle is similar to that of increasing feed rate, that is, the angle decreases [7]. Increasing the beam diameter lowers the energy density of the laser spot, which may account for the reduced bend angle.

2.3.1.5 Cooling effect

In the TGM (See Section 1.2.2), the angular change is generated by temperature differences between the irradiated top surface and the cool bottom surface. Scully [2] investigated the cooling effects to improve the process efficiency by increasing the temperature differential. It was shown that the cooling has no effect on the angular change in the laser forming as shown in Table 2.1.

Table 2.1 Effects of cooling on angular change [2]

Cooling method	Bend angle (°)
Water bath, natural convection, with steel support	1.16
Water bath, natural convection, no steel support	1.08
Dry ice, entire plate rested on a block of dry ice	1.11
Forced air convection, plate suspended by clamp on one edge	1.13
Natural air convection, plate rested on an aluminum table	1.28

2.3.1.6 Number of irradiations

In straight-line laser bending, a single scanning pass can only generate a deformation of a few degrees. Thus, in order to produce the required bend angle multi-passes must be applied over the same scanning path [1, 2, 43, 45, 46].

The angular distortions obtained were 1.1 ° per pass for low-carbon steel and 0.8 ° per pass for the HY-80 steel with a laser power of 12.7kW and a travel speed of 0.005 m/s [2]. A bend angle of 132 ° in AISI 304 stainless steel was achieved with the repetition of laser scans of 54 [1].

A linear relationship between bend angle and the number of scans is commonly found [2, 7, 40, 42, 45, 47]. However, the rate at which the bend

angle grows decreases with the number of scans [26, 31, 46]. The cause of this reduction has been reported as being due to the strain hardening of the material [46] and a change in absorption as the number of scans increases [20]. The effect of sheet thickness increase in the irradiated area per scan is reported as a greater significance than strain hardening [8, 40, 42]. The reduction of bend angle is attributed to an increase in the section modulus of metal sheet due to the thickening of the material along the bending edge [11]. The thickening rate reduces with the number of scans, as does the bending rate [42].

2.3.1.7 Line energy

As mentioned in previous sections, the energy absorption into the material is mainly determined by the laser power, the scanning speed and the absorptivity of the material. In general, the bend angle increases with the increase of the laser power and the absorptivity due to higher absorbed energy. However, there is no simple relation between these parameters.

A concept of line energy was used to investigate the relationship, which is defined as the ratio of the laser output power (W) times the absorptivity (%) to the scanning speed (m/sec) [10, 40]. The results of the bend angle fall into three ranges, as shown in Figure 2.7. Region I is the region ranged from zero input line energy to threshold line energy where the bend angle is zero. In region II above the threshold energy, a linear increase of bend angle is found. Region III involves the higher line energy where the linear increase of bend angle ends and starts less increase. Even though the change of the scanning speed has an influence on the bend angle by adjusting the line energy input like the change of the laser power, applying low scanning speed to increase the energy absorptivity leads to lower bend angles than by the use of high laser power. Therefore, it would be easier to adjust the laser output power than the scanning speed for the adjustment of the line energy for a bending operation.

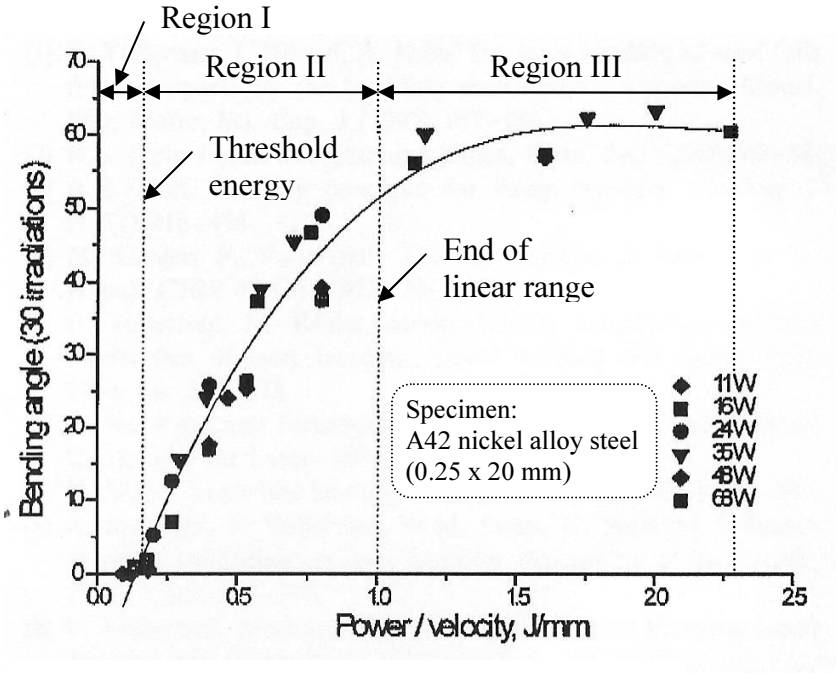

Figure 2.7 Variation of bend angle with line energy. Reproduced from [73].

The threshold line energy is a critical energy input below which no plastic straining occurs [48]. This is due to the elastic behavior of the material, which causes a reversible elastic bend in every case. This means that the heating of the sheet metal is stopped at a temperature which is below the boundary temperature. This temperature can be calculated from the coefficient of thermal expansion, the elastic modulus and the flow stress [20]. Plastic straining will set in when the thermal expansion exceeds the elastic strain at the flow stress (See Figure 1.4). Therefore, the boundary temperature, T_B, is given by the equilibrium of the thermal strain, $\varepsilon_{th} = \alpha_{th}(T)T_G$, and the elastic strain at the flow stress, $\varepsilon_e = \sigma_f(T)/E(T)$.

$$T_B \text{ where } \alpha_{th}(T)T_G \approx \alpha_{th}(T)T_G \tag{2.5}$$

The bend angle can possibly be controlled accurately by adjusting the laser power and the feed rate within the range where the bend angle increases linearly with line energy [40].

The parameter of $P/(t\sqrt{v})$, where P is laser power, v scanning speed and t plate thickness, may be used effectively for estimating the amount of bend angle of a plate [2, 10]. For example, given a required bend angle and knowing the plate thickness, one may vary the laser power and scanning speed to obtain the necessary bend angle.

Experimental studies of laser forming have shown that it can be done to obtain a necessary bend angle from a flat metal sheet. The important process parameters associated with energy are surface absorption of the material, laser power, scanning speed, beam diameter and number of irradiations. Each process for each material for each shape must be developed though an extensive experimental program. Thus, a means to model and reduce experiments would be valuable.

2.3.2 Material properties

The material properties of a metal sheet play an important role in laser forming because the process is based on thermal expansion caused by laser beam heating. The important thermal properties are thermal conductivity, heat capacity, density and the coefficient of thermal expansion.

A linear relationship is found between the bend angle and the ratio of the coefficient of thermal expansion to the volumetric heat capacity (expressed by the product of the specific heat and the density) [9]. The magnitude of the thermal expansion is determined by the temperature increase and the coefficient of thermal expansion for all laser forming mechanisms.

The thermal conductivity is an important parameter affecting the temperature profile in the sheet metal during the laser beam heating. It determines the magnitude of the temperature gradient along the sheet thickness

direction and the diameter of the temperature field. Thus, this parameter especially contributes to the process in which the temperature gradient mechanism is involved. The effect of the thermal conductivity is smaller in the BM and UM, compared to the role in the TGM, because the temperature gradient is small in those mechanisms [8].

The effects of the mechanical properties can be described by low strength and high strength material. Low strength material (e.g., low alloyed steel) has a low ratio of the flow stress to the elastic modulus. The ratio of the flow stress to the elastic modulus equals the elastic strain at the yield strength. Low strength material has a small elastic strain at the yield point. Thus, the irreversible elastic strain is small. This results in a very effective conversion of the thermal expansion into a plastic strain. On the contrary, the high strength material (e.g., titanium alloy) shows a high ratio of the flow stress to the elastic modulus. The elastic strain at the yield point is a factor of more than two larger than for the low strength material. Thus, very great reversible elastic strains occur in the high strength material which results in low bend angles compared to that in the low strength material [20]. In an experiment, the bigger bend angle in low-carbon steel (AISI 1018) was obtained than in the HY-80 steel plates [2].

Investigating the effects of material properties in laser forming by empirical work is expensive and time-consuming. It is suggested that effects of the parameters can be identified by numerical analysis.

2.3.3 Plate geometry

The geometry parameters of sheet thickness, length and width influence on the angular change in the laser bending.

The most important parameter among the geometry parameters is the sheet thickness [20, 45]. There is a linear relationship between the bend angle and the inverse of the square of the sheet thickness, at least for the TGM (See Section 1.2.2) [10].

Increasing the length of the bend edge increases the bend angle by a factor of three [2]. Even though this is an effect significantly smaller than the influence of the sheet thickness, it must be considered especially if small parts have to be bent. When the path of the laser beam is positioned near the edge of the sheet, there is a decreased bend angle. The maximum bend angle is produced in the middle of the sheet. This effect may be attributed to two reasons. One is that when the heating line is very close to an edge, the heat flow pattern is altered by the presence of the edge. Areas near the edge are heated to temperatures higher than those in areas away from the edge, resulting in a smaller temperature differential, hence causing less bend angle near the edge. The other is that when the heating line is close to an edge, the restraint or the bending rigidity of the plate becomes nonsymmetric, resulting in less bend angle.

2.4 Material Types, Metallurgical Variations and Edge Effects

In addition to the factors in laser forming, described in the previous section, the empirical studies have investigated material types, metallurgical variations after forming and edge effects.

A variety of material types have been tested to find the applicability of laser forming. Namba [1] bent Ti, Ta, Al, AISI 304 stainless steel and AISI 1045 carbon steel into V-shapes using a CO_2 laser. Glass, alumina and zirconia sheets were all broken by the laser scans because of lack of plasticity. Masubuch [28] investigated plates of 6 to 25 mm thick low-carbon steel and three types of low-alloy high-strength steels of HY-80 steel, K-TEN80CF steel and ASTM A710 steel called HSLA-80 using a CO_2 laser. The results showed that various experimental parameters such as laser power, feed rate and plate thickness affect angular distortion. CuCoBe-alloys were not suitable for laser beam bending due to the considerable reduction of the material properties of

strength and hardness [49]. Plates of an α-β titanium [50, 51] and a high strength AlCuMg aluminium alloy [24] and a thin steel alloy strip (A42 nickel alloy) used for integrated circuit leadframes [40] were successfully tested to create angular changes in the specimen.

A series of tests was carried out using a 9 kW CO_2 laser to determine the effect of laser heating on material properties for HY-80 [2]. The toughness test results showed that as the heat input increases, the ductile-to-brittle transition temperature decreases. Also, an increasing hardening effect was observed as the heat input was increased. The fracture toughness of the HAZ was as good as that of the base metal for multi-pass heating. Single pass heating with high heat input (54 kJ/in.) caused some degradation in fracture toughness of HY-80 steel. Multi-pass heating with low heat input per pass (18 kJ/in.) and single pass with intermediate heat input (33 kJ/in.) showed a beneficial effect of hardening while the fracture toughness was maintained. Temper embrittlement due to laser line heating was not observed.

In a straight-line laser bending of a metal sheet, a slight curvature has been observed along the bending edge as shown Figure 2.8. This results in a small variation in bending angle along the irradiation path. This behavior is termed ‘edge effect’ [52]. This effect is attributed to the changing mechanical restraint which hinders the free thermal expansion with distance from the edge of the metal sheet [53]. This phenomenon is a drawback of laser forming because the dimensional accuracy of the metallic parts must be ensured to allow practical application. The bending variation is dependent on the laser processing parameters [52, 54]. For example, small change in the feed rate can lead to large change in the bend angle along the bending edge.

Experimental investigation to relationship between edge effect and process parameters has limitations in terms of cost and time. Numerical analysis could be an alternative to experimental study.

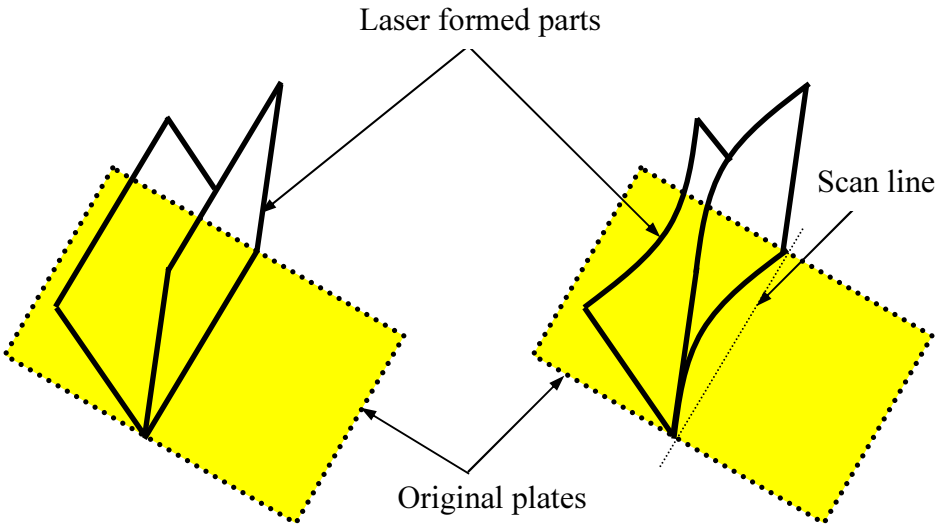

Figure 2.8 Changing bend angle along the length of the bending edge: (a) ideal case of uniform bend angle; and (b) exaggerated view of edge effects.

2.5 Numerical Simulations

As described in the previous section, the results from the analytical model were not reliable due to many assumptions to simplify the model. In another expression, the laser forming process was too complex to characterize the forming pattern from a simplified model. Therefore, numerical simulations have been performed in order to improve the fundamental knowledge of the principles of the forming operations.

The numerical simulation was first carried out by Vollertsen and Geiger using the finite difference method (FDM) and the finite element method (FEM) [55]. They obtained temperature and bend angle distributions from the simulations. It was reported that the temperature was strongly affected by the discretization but the bend angle was not. The absorption coefficient was regarded as a critical parameter because it was related to the laser energy

delivery onto the plate surface, but absorptivity is difficult to measure accurately. The difficulty of the simulation was addressed with unknown material properties at high temperature from experiment. The FEM model generated more accurate results than the FDM model because the FDM model had limitations concerning correct calculation of the effect of sheet thickness due to the assumptions and simplifications which were made for this calculation.

The FE-simulation of the BM (See Section 2.2) was performed using a FEM code, ABAQUS [38]. The intensity of the laser beam onto the plate surface prescribed in Eq. (2.1) was used in the simulation. Profiles of temperature, plastic and elastic strain, and displacement were achieved. The simulation demonstrated that laser forming is a process producing plastic deformation.

In a paper by researchers at MIT and The Boeing Company [39], a finite element model for Inconel 625 specimens was built. Transient angular distortions were obtained from the FE-simulation. The possibility of modeling a laser tube bending and a dome shape forming was proposed. The need to develop a technology to form a plate into a pre-determined shape using both heating patterns and heating conditions was also suggested.

Li and Yao used the finite element analysis to investigate strain rate effects in laser forming introducing a concept of “constant peak temperature” at the upper surface of the plate [56]. They extended the numerical study to laser tube bending, investigating wall thickness variation, cross-section ovalization and bending radius [37, 57].

The transient processes and patterns of edge effects (See Section 2.4) were examined by numerical simulations where strain rate dependency of flow stress was considered to improve prediction accuracy [54].

Cheng and Yao [58] proposed a microstructure integrated finite element model in order to increase model accuracy in predicting bend angle and

mechanical properties in laser forming operations, which involved an adequate constitutive model to better describe the hot flow behavior.

Although many FE-simulations [43, 44, 59, 60, 61, 62, 63, 64, 65], including the works above, offered satisfactory results in terms of temperature, stress and strain and displacement distributions, they were confined to traditional analysis – an analysis based on a given set of specific values of process parameters. Numerical simulation for the purpose of process design to generate a particular complex part has not been reported in the literature. As shown in Figure 2.9, advanced analysis is required for laser forming to be a viable process for rapid prototyping, shape correction and micro-adjustment.

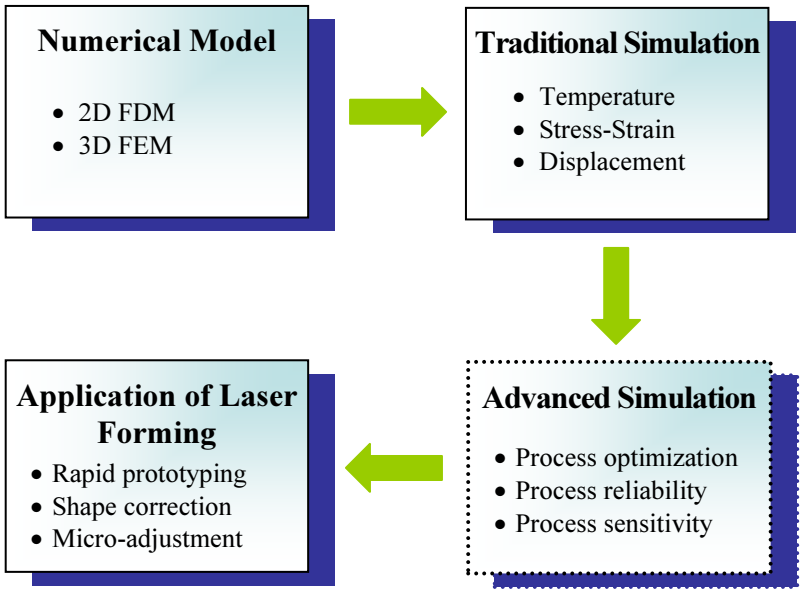

Figure 2.9 Availability of numerical simulation in laser forming.

2.6 Summary

This chapter has provided coverage of background material relating to laser forming. The key points and some concluding comments can be made with respect to the laser forming research to date:

- In general, there are three mechanisms involved in laser forming – temperature gradient mechanism (TGM), buckling mechanism (BM), and upsetting mechanism (UM). A forming mechanism is mainly determined by the temperature distributions produced inside the material. Thus, a desired mechanism can be generated by controlling laser parameters (i.e., laser power, feed rate and beam diameter) and plate dimensions.

- The factors in laser forming can be classified into three groups – energy parameters, material properties and plate geometry. Energy parameters include absorption coefficient, laser power, feed rate, beam diameter, cooling condition and number of scans. Material properties which primarily affect laser bending are the coefficient of thermal expansion and thermal conductivity. The most important geometry parameter is plate thickness.

- Great efforts have been made experimentally in order to identify the effects of factors on geometry change. The factors important in laser forming are: absorption coefficient, laser power, feed rate, number of scans, thermal expansion coefficient, conductivity, and plate thickness. However, the experimental work encountered some problems in that it was a time consuming work and the results from the experiments cannot be generally applied.

- Efforts have been made to create an analytical model. Relationships between the bend angle and the process parameters have been

investigated through the analytical models. However, the model does not accurately represent the complex process.

- The laser forming process was too complex to fully understand through experimental work and analytical modelling. A numerical approach has been employed to increase the insight to laser forming. Satisfactory results were achieved through the computational simulations providing temperature, displacement, stress and strain distributions. However, no information on the numerical simulation for the generation of complex parts is available. There is no published work on process optimization, a strategy evaluating the process reliability and sound characterization of the effects of the material properties in the laser forming.

Chapter 3

Finite Element Formulations

3.1 Introduction

The aim of this chapter is to review the theoretical background of the finite element method (FEM) employed in the analysis of the laser forming processes. The concepts of the FEM are briefly presented first in terms of continuum problems, the weighted residuals approach, and interpolation functions. Then how the partial nonlinear differential equations representing the thermal and structural fields can be formulated into finite element equations through the finite element discretization process is described in two consecutive sections. Finally, the concept of a nonlinear equation solver is demonstrated.

3.2 Finite Element Method (FEM)

FEM is a computer-based numerical method to solve engineering problems in bodies of user-defined geometry. The bodies are discretized into elements. Each element has nodes that are used to represent the value of the field variables (for example, temperature, stress and displacement) over the element by interpolation function (sometimes called approximating function). The matrix equations expressing the properties of the individual elements are determined using one of the three approaches – the direct approach, the variational approach, or the weighted residuals approach [66]. The individual matrix equations are assembled to find the overall system equations. Known

nodal values of the field variables are imposed on the system equations. The unknown nodal values of the problem are obtained solving the system equations. Engineering problems addressed by the FEM are: structural, thermal, fluid flow, electrical, magnetic, acoustic noise etc. Both the structural problem and thermal problems are involved in the laser forming process. In this section, the concepts of the FEM are briefly described in terms of continuum problems, the weighted residuals approach, and interpolation functions, based on Huebner [66] and Meinders [67].

3.2.1 Continuum Problems

Problems in engineering can be divided into two fundamentally different categories – discrete and continuum. In the discrete problem, all matter is taken into account discrete particles that retain their identity and nature as they move through space. In the continuum problem (the one that we will use), all bodies of interest are treated as continuous at all points in space to the extent that all field quantities describing the state of the body are sufficiently differentiable in the independent variables of the continuum, space and time. In this viewpoint, it is possible to focus on one point in space and time and observe the phenomena occurring there.

Continuum problems are concerned with the fields of temperature, stress, mass concentration, displacement, and potentials (e.g., electromagnetic and acoustic), etc. Continuum problems can be approximately represented by partial differential equations and their boundary conditions. These governing equations are often called boundary value problems because their solution is determined in some domain defined by a given boundary on which boundary conditions are specified, and can be formulated in general terms to be solved.

When Ω is a domain bounded by the surface Γ and ϕ is a scalar function defined in the interior of Ω, the behavior of ϕ at any point in Ω is expressed:

$$A(\phi) - f = 0 \tag{3.1}$$

where:

f = a known scalar function of the independent variables

A = some linear or nonlinear differential operator.

If $A(\phi)$ is a partial differential operator, the results of the integration of Eq. (3.1) will always contain arbitrary functions. These functions can be found only if the boundary conditions are specified. In principle, the finite element method can be employed to solve linear and nonlinear partial differential equations valid over domains of any geometrical shape when boundary conditions are given.

3.2.2 The weighted residuals approach

The method of weighted residuals (MWR) is a global technique for obtaining approximate functional representation of the governing linear and nonlinear partial differential equations in a way as to formulate the element equations. This section provides the basic concept of the MWR in such a way that we want to find an approximate functional representation for a field variable ϕ governed by the differential equation (3.1). It is assumed that boundary conditions are prescribed on Γ.

The dependent variable, ϕ is approximated by

$$\phi \approx \tilde{\phi} = N_0 + \sum_{i=1}^{m} N_i C_i \tag{3.2}$$

where:

N_0 and N_i = the assumed functions

C_i = either the unknown parameters or unknown functions of one of the independent variables

m = number of unknowns C_i

When ϕ is substituted into Eq. (3.1), it is likely that the equations will include some error (called a residual), that is,

$$A(\tilde{\phi}) - f = R \tag{3.3}$$

where:

R = the residual or error that results from approximating ϕ by $\tilde{\phi}$.

The m unknown C_i are determined in such a way that the residual R is vanished or small over the entire solution domain. To do this, m linearly independent weighting functions W_i are chosen and applied to meet the following equation:

$$\int_{\phi} \left[A(\tilde{\phi}) - f\right] W_i d\Omega = \int_{\Omega} R W_i d\Omega = 0, \quad i = 1,2,\ldots,m \tag{3.4}$$

In order to obtain an approximate representation of the unknown field variable ϕ by Eq. (3.2), Eq. (3.4) can be solved for the C_i using the Galerkin method, a weighted residual technique most often used to derive finite element equations. In the method, the weighting functions are selected to be the same as the approximating functions, N_i. Thus Eq. (3.4) is expressed in the following form:

$$\int_{\Omega} \left[A(\tilde{\phi}) - f\right] N_i d\Omega = 0, \quad i = 1,2,\ldots,m \tag{3.5}$$

The equations can be solved for the C_i by performing the integrations, and an approximation solution of ϕ is obtained via Eq. (3.2).

The functions N_i are recognized as the interpolation functions $N_i^{(e)}$ defined over the element, and the C_i are the undetermined parameters, which may be the nodal values of the field variable or its derivatives. The equations governing the behavior of an element therefore are written:

$$\int_{\Omega^{(e)}} \left[A(\phi^{(e)}) - f^{(e)} \right] N_i^{(e)} d\Omega = 0, \quad i = 1,2,\ldots,r \tag{3.6}$$

where:

e = one element

$\phi^{(e)} = \lfloor N^{(e)} \rfloor \{\phi\}^{(e)}$

$f^{(e)}$ = forcing function defined over element (e)

r = number of unknown parameters assigned to the element

A set of equations like Eq. (3.6) are derived for each element of the whole assemblage.

Integration by parts in one dimension, where the domain of interest is $a \le x \le b$, is

$$\int_a^b u dv = uv\Big|_a^b - \int_a^b v du \tag{3.7}$$

where:

u and dv = the weighting function W_i and derivatives of the differential operator A in Eq. (3.4), respectively.

Integration by parts in two dimensions and three dimensions are known as *Green's theorem* and *Gauss's theorem*, respectively, and is given by:

$$\int_\Omega u(\nabla \cdot \mathbf{v}) d\Omega = \int_\Gamma u(\mathbf{v} \cdot \hat{n}) d\Gamma - \int_\Omega \mathbf{v} \cdot \nabla u d\Omega \tag{3.8}$$

where:

u = the weighting function W_i

$\nabla \cdot \mathbf{v}$ = the derivatives in the differential operator A.

∇ = the gradient operator

$\hat{n}$ = a unit normal vector to the boundary.

The order of differentiation on $\tilde{\phi}$ is reduced by one in the resulting equation by the result of integration by parts, which means that the continuity restrictions on the approximating function $\tilde{\phi}$ have been reduced or weakened. The resulting integral equation is known as the weak form of the boundary value problem. The integration by parts is effectively used in obtaining element equations of thermal and structural problems in Sections 3.3 and 3.4, respectively.

3.2.3 Interpolation functions

In the finite element method, a domain Ω consists of sub-domains, Ω_e (i.e., elements) with a finite size and respective interpolation functions. Evaluation of integrals is performed over these elements. Later, the contribution of each element is assembled into a large system representing the whole domain, yielding an approximate solution for the whole domain.

An element is defined by means of shape and pre-defined points (i.e., the nodes). A particular element type is characterized with the number and type of nodal variables chosen for it. The nodal variables or the parameters assigned to an element are often called the *degrees of freedom* (*DOF*) of the element. For example, in the solid mechanics field, the nodal variables are usually displacements and sometimes derivatives of displacements (i.e., strains and stresses). In the thermal mechanics discipline, the nodal variable is temperature.

The functions used to express the behavior of a field variable within an element are called 'interpolation functions' that relate quantities at any point in the interior of the element to the nodal point values. The interpolation functions have to provide continuous functions for the interpolated field within an element. Polynomials are widely used as interpolation functions because they are relatively easy to integrate or differentiate. Thus, within an element, a field variable can be represented as a polynomial series whose coefficients are the generalized coordinates. The number of coefficients in the polynomial should equal the number of nodal variables available to evaluate these coefficients.

The interpolation functions are derived using a 'natural coordinate system'. That is a local coordinate system that relies on the element geometry for its definition and whose coordinates range between zero and unity within the element. The basic purpose of a natural coordinate system is to describe the location of a point inside an element in terms of coordinates associated with the nodes of the element. For example, one type of natural coordinate system can be established for a four-node quadrilateral element in two dimensions as shown in Figure 3.1 - a general quadrilateral element in the global Cartesian coordinate system (a) and a local natural coordinate system (b). In the natural coordinate system whose origin is at the centroid, the quadrilateral element is a square with sides extending to $\xi=\pm1$, $\eta=\pm1$. The global and local coordinates are related by the following equations:

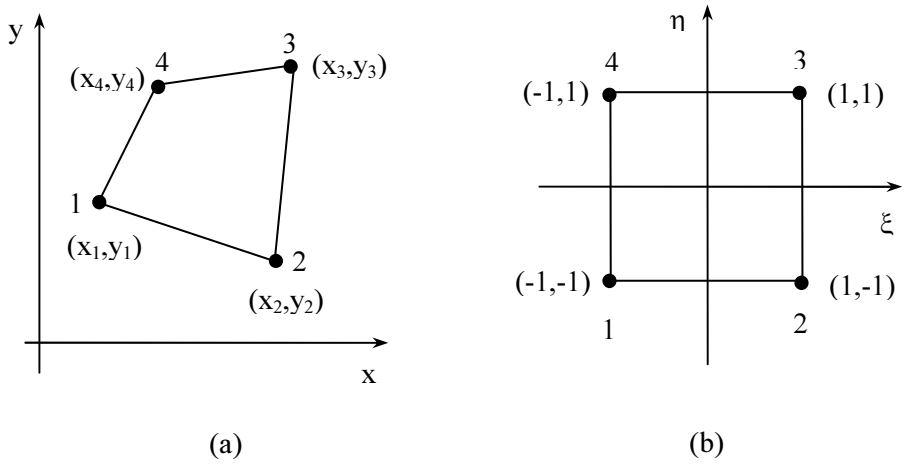

Figure 3.1 Coordinates for a general quadrilateral: (a) cartesian coordinates; (b) natural coordinates.

$$x = \frac{1}{4}[(1-\xi)(1-\eta)x_1 + (1+\xi)(1-\eta)x_2 + (1+\xi)(1+\eta)x_3 + (1-\xi)(1+\eta)x_4]$$

$$y = \frac{1}{4}[(1-\xi)(1-\eta)y_1 + (1+\xi)(1-\eta)y_2 + (1+\xi)(1+\eta)y_3 + (1-\xi)(1+\eta)y_4] \quad (3.9a)$$

Eq. (3.9a) can be rewritten in a compact form:

$$x = \sum_{i=1}^{4} L_i(\xi,\eta)x_i$$

$$y = \sum_{i=1}^{4} L_i(\xi,\eta)y_i \quad (3.9b)$$

where:

$$L_i = \frac{1}{4}(1+\xi_i\xi)(1+\eta_i\eta) \quad (3.9c)$$

The natural coordinates are denoted as L_i (i = 1,2,3 and 4), where i is the external nodes of the element. One coordinate is associated with node i and has unit value there. ξ_i, and η_i represent the coordinates of the nodes in the ξ, η natural coordinates. For example, for i = 1, ξ_1 = -1, η_1 = -1; for i = 2, ξ_2 = 1, η_2 = -1; and so on. Eqs. (3.9) represent interpolation functions for a general quadrilateral element.

3.3 Heat Transfer Problem

Heat transfer is involved in the laser forming process due to the heating by a laser beam on the surface of a plate. As shown in Figure 3.2, the heat transfer modes in the problem are characterized by conduction, convection, and radiation – part of the heat is transferred inside the plate by conduction, and part of the heat is transferred to the surroundings by convection and radiation effects. The temperature distributions in the plate can be calculated using the finite element method. In this section, the finite element formulations of the

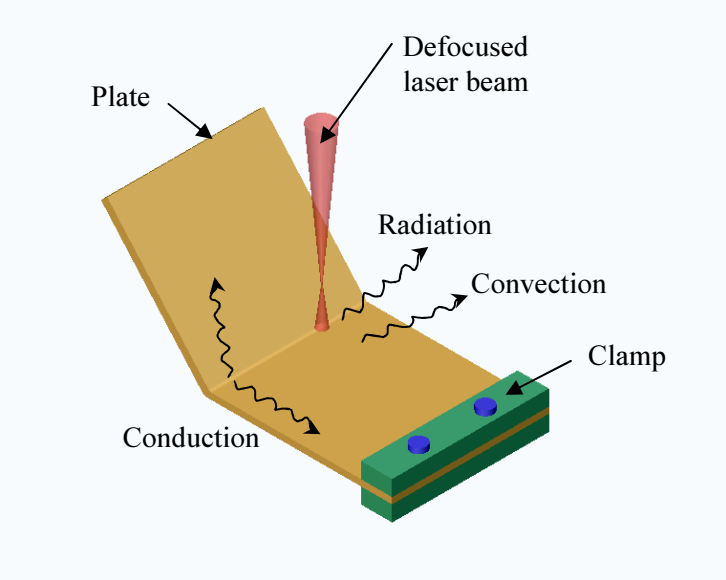

Figure 3.2 Heat transfer modes involved in the laser forming process.

heat transfer problem are derived from the law of conservation of thermal energy, which are applied at modes in the sheet metal material.

3.3.1 Heat diffusion equation [68]

Consider a homogeneous medium and the temperature distribution *T(x, y, z)* is expressed in Cartesian coordinates. The temperature distribution in an infinitesimally small (differential) control volume defined in the medium is governed by the law of conservation of thermal energy as follows:

$$\rho c_p \frac{\partial T}{\partial t} = \frac{\partial}{\partial x}\left(k\frac{\partial T}{\partial x}\right) + \frac{\partial}{\partial y}\left(k\frac{\partial T}{\partial y}\right) + \frac{\partial}{\partial z}\left(k\frac{\partial T}{\partial z}\right) + \dot{q} \tag{3.10}$$

where:

ρ = the density of the medium

c_p = the specific heat of the medium

k = the thermal conductivity of the medium

$\dot{q}$ = the rate at which heat is generated per unit volume of the medium

$\rho c_p \dfrac{\partial T}{\partial t}$ = the time rate of change of the thermal energy of the medium per unit volume

$k\dfrac{\partial T}{\partial x}, k\dfrac{\partial T}{\partial y}$ and $k\dfrac{\partial T}{\partial z}$ = the rate of heat transfer per unit area (heat flux) at the x, y, and z coordinate locations, respectively.

Eq. (3.10) is the general form of the *heat diffusion equation*. This equation provides the basic tool for heat conduction analysis. From its solution, the temperature distribution *T(x, y, z)* is obtained as a function of time.

For heat conduction from one surface of a solid to another, the heat flux equation is more generally stated (*Fourier's law*).

$$\{q''\} = -k\left(\frac{\partial T}{\partial x} + \frac{\partial T}{\partial y} + \frac{\partial T}{\partial z}\right) = -k\nabla T \tag{3.11}$$

The negative sign is necessary because heat is always transferred in the direction of decreasing temperature.

Thus, Eq. (3.10) is simply expressed:

$$\rho c_p \frac{\partial T}{\partial t} = -\nabla \cdot \{q''\} + \dot{q} \tag{3.12}$$

To determine the temperature distribution in the medium, it is necessary to solve the differential heat equation, Eq. (3.12), for prescribed boundary conditions. The boundary conditions at defined surfaces encountered in heat transfer are presented below.

For specified surface temperature, T_s,

$$T_{(x,y,z,t)} = T_s \tag{3.13a}$$

For specified surface heat flux, q'',

$$-k\nabla T = q'' \quad \text{for finite heat flux} \tag{3.13b}$$

$$\nabla T = 0 \quad \text{on adiabatic surface} \tag{3.13c}$$

For convection surface condition,

$$-k\nabla T = h\left[T_\infty - T_{(x,y,z,t)}\right] \tag{3.13d}$$

where:

h = a convective heat transfer coefficient

T_∞ = the surrounding temperature

For radiation heat exchange,

$$-k\nabla T = \alpha q_r'' - \sigma\varepsilon T^4_{(x,y,z,t)} \tag{3.13e}$$

where:

α = the surface absorptivity

q_r'' = the incident radiant heat flux

σ = the Stefan-Boltzmann constant

ε = the surface emissivity, which is a function of the surface temperature

The problem is inherently nonlinear due to temperature-dependent material properties and nonlinear boundary conditions. In the following section, the derivation of the finite element equations is presented, based on Huebner [66].

3.3.2 Finite element formulation

A general formulation of element equations for transient heat transfer in a medium can be derived from a three-dimensional solid Ω bounded by a surface Γ with various heat transfer modes as shown in Figure 3.3.

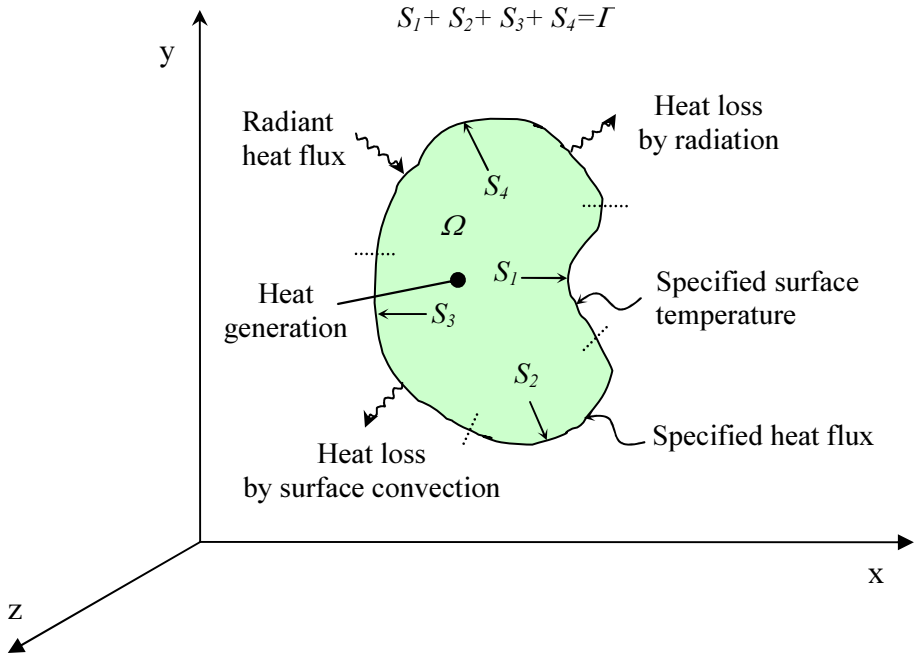

Figure 3.3 Various heat transfer modes in a three-dimensional solid Ω bounded by a surface Γ.

The solution domain Ω is divided into M elements, and each element has r nodes. Within each element, the temperature and temperature gradients is expressed by the usual procedure as:

$$T^{(e)}(x,y,z,t) = \sum_{i=1}^{r} N_i(x,y,z)T_i(t) \tag{3.14a}$$

$$\frac{\partial T^{(e)}}{\partial x}(x,y,z,t) = \sum_{i=1}^{r} \frac{\partial N_i}{\partial x}(x,y,z)T_i(t) \tag{3.14b}$$

$$\frac{\partial T^{(e)}}{\partial y}(x,y,z,t) = \sum_{i=1}^{r} \frac{\partial N_i}{\partial y}(x,y,z)T_i(t) \tag{3.14c}$$

$$\frac{\partial T^{(e)}}{\partial z}(x,y,z,t) = \sum_{i=1}^{r} \frac{\partial N_i}{\partial z}(x,y,z)T_i(t) \tag{3.14d}$$

where:

N_i = the temperature interpolation function

$T_i(t)$ = the value of the temperature at each node

Eqs. (3.14a – 3.14d) are simply expressed in matrix form:

$$T^{(e)}(x,y,z,t) = \lfloor N(x,y,z) \rfloor \{T(t)\} \tag{3.15a}$$

$$\nabla T_{(x,y,z,t)} = [B_{(x,y,z)}]\{T(t)\} \tag{3.15b}$$

where:

$\{T(t)\}$ = the vector of element nodal temperatures

$\lfloor N_{(x,y,z)} \rfloor = \lfloor N_1 \quad N_2 \quad \cdots \quad N_r \rfloor$ = the temperature interpolation matrix

$$\left[B_{(x,y,z)}\right]=\begin{bmatrix} \frac{\partial N_1}{\partial x} & \frac{\partial N_2}{\partial x} & \cdots & \frac{\partial N_r}{\partial x} \\ \frac{\partial N_1}{\partial y} & \frac{\partial N_2}{\partial y} & \cdots & \frac{\partial N_r}{\partial y} \\ \frac{\partial N_1}{\partial z} & \frac{\partial N_2}{\partial z} & \cdots & \frac{\partial N_r}{\partial z} \end{bmatrix} = \text{the temperature gradient interpolation}$$

matrix

For a single element, the method of weighted residuals (See Section 3.2.2) is used to derive the element equations starting with the energy equation, Eq. (3.12):

$$\int_{\Omega^{(e)}} \left(\nabla \cdot \{q''\} - \dot{q} + \rho c_p \frac{\partial T}{\partial t} \right) N_i d\Omega = 0 \tag{3.16}$$

where:

$\Omega^{(e)}$ = the domain for element (e)

By *Gauss's theorem* (Eq. 3.8) which introduces surface integrals of the heat flow across the element boundary $\Gamma^{(e)}$, the term of $\int_{\Omega^{(e)}} (\nabla \cdot \{q''\}) N_i d\Omega$ is integrated. Thus, the following re-arranged form is obtained from Eq. (3.16):

$$\int_{\Omega^{(e)}} \rho c_p \frac{\partial T}{\partial t} N_i d\Omega - \int_{\Omega^{(e)}} \nabla \cdot \lfloor N_i \rfloor \{q''\} d\Omega = \int_{\Omega^{(e)}} \dot{q} N_i d\Omega - \int_{\Gamma^{(e)}} (q'' \cdot \hat{n}) N_i d\Gamma \text{ , i=1,2,...,r} \tag{3.17}$$

Next when the surface integral is expressed as the sum of integrals over S_1, S_2, S_3, and S_4, and the boundary conditions, Eqs. (3.13) are introduced:

$$\int_{\Omega^{(e)}} \rho c_p \frac{\partial T}{\partial t} N_i d\Omega - \int_{\Omega^{(e)}} \nabla \cdot \lfloor N_i \rfloor \{q''\} d\Omega$$

$$= \int_{\Omega^{(e)}} \dot{q} N_i d\Omega - \int_{S_1} (q'' \cdot \hat{n}) N_i d\Gamma + \int_{S_2} q'' N_i d\Gamma - \int_{S_3} h(T_{(x,y,z,t)} - T_\infty) N_i d\Gamma$$

$$-\int_{S_4}(\sigma\varepsilon T^4_{(x,y,z,t)}-\alpha q''_r)N_i d\Gamma,\ i=1,2,\ldots,r \tag{3.18}$$

As the last step, the element temperatures for Eq. (3.15a) and Fourier's law (Eq. 3.11) are introduced. Fourier's law is expressed with Eq. (3.15b) as follows:

$$\{q''\}=-[k][B]\{T\} \tag{3.19}$$

After some manipulation, the resulting element equations become

$$[C_p]\left\{\frac{dT}{dt}\right\}+[[K_c]+[K_h]]\{T\}=\{R_{Ts}\}+\{R_q\}+\{R_{q''}\}+\{R_h\}+\{R_\sigma\}+\{R_{q''_r}\} \tag{3.20}$$

where:

$[C]$ = element capacitance matrix = $\int_{\Omega^{(e)}}\rho c_p\{N\}\lfloor N\rfloor d\Omega$ (3.21a)

$[K_c]$ = element conductance matrix related to conduction = $\int_{\Omega^{(e)}}[B]^T[k][B]d\Omega$ (3.21b)

$[K_h]$ = element conductance matrix related to convection = $\int_{S_3}h\{N\}\lfloor N\rfloor d\Gamma$ (3.21c)

$\lfloor R_{T_s}\rfloor$ = heat load vector arising from specified temperatures=

$$-\int_{S_1}(q''\cdot\hat{n})\{N\}d\Gamma \tag{3.22a}$$

$\lfloor R_q\rfloor$ = heat load vector arising from internal heat generation = $\int_\Omega \dot{q}\{N\}d\Omega$ (3.22b)

$\lfloor R_{q''}\rfloor$ = heat load vector arising from specified surface heating = $\int_{S_2}q''\{N\}d\Gamma$ (3.22c)

$[R_h]$ = heat load vector arising from surface convection = $\int_{S_3}hT_\infty\{N\}d\Gamma$ (3.22d)

$[R_\sigma]$ = heat loss vector arising from surface radiation = $-\int_{S_4}\sigma\varepsilon T^4_{(x,y,z,t)}\{N\}d\Gamma$

(3.22e)

$\left\lfloor R_{q_r''} \right\rfloor$ = heat load vector arising from surface radiation = $\int_{S_4} \alpha q_r'' \{N\} d\Gamma$ (3.22f)

Eq. (3.20) represents a general nonlinear formulation of element equations for transient heat conduction in a medium. In order to obtain the system equations, the element equations are assembled by the standard procedure.

In the general nonlinear transient case (for example, the laser forming case), the formulations are written as follows:

$$\begin{aligned} &[C_p(T)]\{\dot{T}\} + [[K_c(T)] + [K_h(T,t)]]\{T(t)\} \\ &= \{R_q(T,t)\} + \{R_{q''}(T,t)\} + \{R_h(T,t)\} + \{R_\sigma(T,t)\} + \{R_{q_r''}(T,t)\} \end{aligned} \tag{3.23}$$

It can be shown from Eq. (3.23) that element matrices and heat load vectors are both temperature and time dependent, and for the solution, a time-marching scheme is required.

3.3.3 Radiation matrix

The heat flow by radiation from cooling surfaces is considered to increase the precision of the results. In this section, the radiation matrix is described, which is highly nonlinear because the radiant heat flow varies with the fourth power of the surface absolute temperature.

Extending the Stefan-Boltzmann Law for a system of N enclosures, the energy balance for each surface in the enclosure for a gray diffuse body is given by [69], which relates the energy losses to the surface temperatures:

$$\sum_{i=1}^{N} \left(\frac{\delta_{ji}}{\varepsilon_i} - F_{ji} \frac{1-\varepsilon_i}{\varepsilon_i} \right) \frac{1}{A_i} q_i = \sum_{i=1}^{N} \left(\delta_{ji} - F_{ji} \right) \sigma T_i^4 \tag{3.24}$$

where:

N = number of radiating surfaces

δ_{ij} = Kronecker delta

ε_i = effective emissivity of surface i

F_{ij} = radiation view factors

A_i = area of surface i

q_i = energy loss of surface i

σ = Stefan-Boltzmann constant

T_i = absolute temperature of surface i

The view factor F_{ij} is defined as the fraction of the radiation leaving surface i that arrives directly on surface j, as shown in Figure 3.4. The general expression of F_{ij} is as follows [70]:

$$F_{ij} = \frac{1}{A_i} \int_{A_i} \int_{A_j} \frac{\cos\theta_i \cos\theta_j}{\pi R^2} dA_j A_i \tag{3.25}$$

where:

A_i, A_j = area of arbitrarily oriented surface i and surface j

R = distance between differential surfaces dA_i and dA_j

θ_i = angle between the surface normal n_i and the radius line to surface dA_j

θ_j = angle between the surface normal n_j and the radius line to surface dA_i.

N_i,N_j = surface normal of dA_i and dA_j

In the radiation matrix method, Eq. (3.24) can be used to construct a single row in the following matrix equation:

$$[C]\{Q\} = [D]\{T^4\} \tag{3.26}$$

such that:

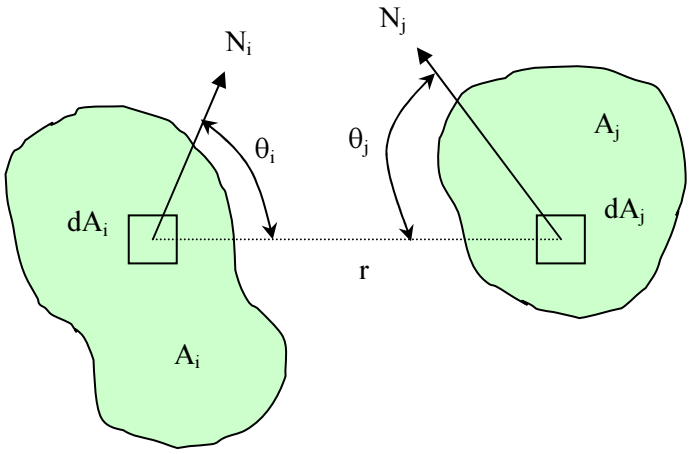

Figure 3.4 View factor calculation terms.

$$\text{each row } j \text{ in } [C] = \left(\frac{\delta_{ji}}{\varepsilon_i} - F_{ji} \frac{1-\varepsilon_i}{\varepsilon_i} \right) \frac{1}{A_i}, i = 1,2,...,N \tag{3.27}$$

$$\text{each row in } [D] = (\delta_{ji} - F_{ji})\sigma, i = 1,2,...,N \tag{3.28}$$

By solving for $\{Q\}$:

$$\{Q\} = [C]^{-1}[D]\{T^4\} \tag{3.29}$$

Eq. (3.29) is analogous to Eq. (3.24) and can be linearized for standard matrix equation solution:

$$\{Q\} = [h_r]\{T\} \tag{3.30}$$

$[h_r]$ now includes T^3 terms and cannot be calculated directly since it is a function of the unknown T_i. The temperatures from previous iterations are used to calculate $[h_r]$ and the solution is computed iteratively.

3.4 Structural Problem

The thermal expansion caused by heating by a laser beam in the laser forming process is enough to produce large plastic strains in the plate via a mechanical process. Thus, in order to incorporate the finite element method in the mechanical problem of the laser forming, the elasto-plastic element formulation has to be addressed. In this section, the elasto-plastic finite element equation is derived from the principle of virtual work.

3.4.1 Stresses in a continuum [71, 75]

Consider a three-dimensional body in equilibrium under the action of a set of the external forces (F_1, F_2, F_3 and F_4) as shown in Figure 3.5(a). The application of the external forces will result in the development of stresses within the medium. The stress, $\boldsymbol{\sigma}$, acting on a small area, δa can be divided into the normal stress, σ_n and two shear-stress components, τ_x and τ_z. This indicates that stress on an area is fully defined if the three values are known. When a small cube is taken into account as shown in Figure 3.5(b), nine values of stress components are necessary for the stresses in the body to be fully calculated. The nine components of the stress are known as the *stress tensor*, $\boldsymbol{\sigma}$, which can be displayed as elements of the square matrix:

$$\boldsymbol{\sigma} = \begin{bmatrix} \sigma_{11} & \sigma_{12} & \sigma_{13} \\ \sigma_{21} & \sigma_{22} & \sigma_{23} \\ \sigma_{31} & \sigma_{32} & \sigma_{33} \end{bmatrix} = \begin{bmatrix} \sigma_{xx} & \tau_{xy} & \tau_{xz} \\ \tau_{yx} & \sigma_{xy} & \tau_{yz} \\ \tau_{zx} & \tau_{zy} & \sigma_{zz} \end{bmatrix} \tag{3.31}$$

In indicial notation, the stress matrix is given by

$$\boldsymbol{\sigma} = \sigma_{ij}, \qquad i = x, y, z; \qquad j = x, y, z \tag{3.32}$$

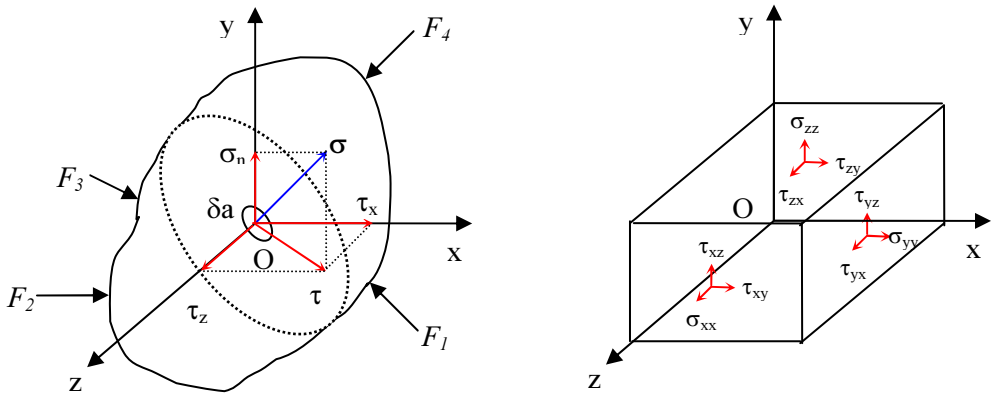

Figure 3.5 Stress at a point: (a) Normal and shear stresses; and (b) Components of stress tensor.

3.4.2 Equation of equilibrium [72, 75]

Consider a body occupying a finite volume V and bounded by a surface S, which is subjected to external tractions T_j ($j = x, y, z$) acting on a point P as shown in Figure 3.6. For the medium to be in equilibrium under the tractions distributed over S, and body forces (i.e., gravitational and centrifugal forces) distributed throughout V, the following condition has to be satisfied:

$$\int_S \sigma_{ij} n_i dS + \int_V \rho g_j dV = 0 \tag{3.33}$$

where:

σ_{ij} = the stress tensor

n_i = the outward unit normal to the tractions, T_j ($i = x, y, z$)

ρ = the density of the medium

g_j = the body force per unit mass ($j = x, y, z$)

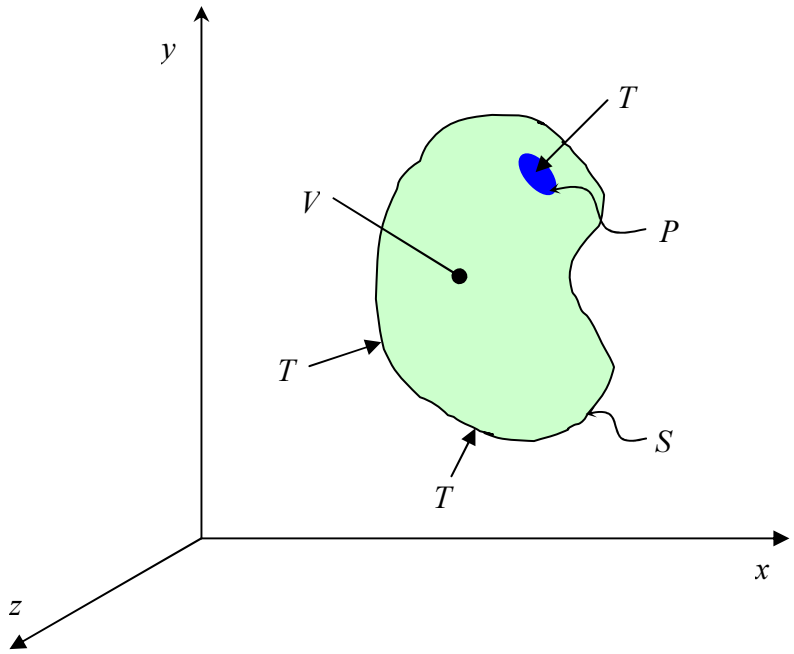

Figure 3.6 External tractions acting on a point *P*.

Using *Green's theorem*,

$$\int_V \left(\frac{\partial \sigma_{ij}}{\partial x_i} + \rho g_j\right) dV = 0 \tag{3.34}$$

Therefore, the equilibrium condition becomes

$$\frac{\partial \sigma_{ij}}{\partial x_i} + \rho g_j = 0 \tag{3.35}$$

Eq. (3.35) must be satisfied throughout the interior of the body.

At the boundary of the body, the force T_j must be equal to the stress vectors:

$$\begin{aligned} T_x &= n_x\sigma_{xx} + n_y\sigma_{yz} + n_z\sigma_{zx} \\ T_y &= n_x\sigma_{xy} + n_y\sigma_{yy} + n_z\sigma_{zy} \\ T_z &= n_x\sigma_{xz} + n_y\sigma_{yz} + n_z\sigma_{zz} \end{aligned} \tag{3.36}$$

In indicial notation, Eq. (3.36) can be written as:

$$T_j = n_i\sigma_{ij} \tag{3.37}$$

To determine the stress components uniquely, Eqs. (3.35) and (3.37) must be supplemented by boundary conditions of displacement.

Considering a continuous velocity field v_j, the rate of work done by the distribution of surface traction T_j (in the absence of body forces) is

$$\int_S T_j v_j dS = \int_S n_i\sigma_{ij} v_j dS = \int_V \frac{\partial}{\partial x_i}(\sigma_{ij} v_j) dV = \int_V \sigma_{ij} \frac{\partial v_j}{\partial x_i} dV \tag{3.38}$$

Applying *Green's theorem* to the vector $\sigma_{ij}v_j$, the *equation of equilibrium* is obtained in an integral form:

$$\int_S T_j v_j dS = \int_V \sigma_{ij} \dot{\varepsilon}_{ij} dV \tag{3.39}$$

where:

$\dot{\varepsilon}_{ij}$ = the displacement rate

Eq. (3.39) states that the rate of work done by the external forces through any virtual velocity field is equal to the rate of dissipation of internal energy.

3.4.3 Finite element formulation

The finite element equation in problems involving large plastic strain is derived, based on Chakrabarty [72] and Huang [73]. The variational principle for the equilibrium equation, Eq. (3.39), is expressed as follows:

$$\delta\left\{\int\left[\dot{\sigma}_{ij}\dot{\varepsilon}_{ij}-\sigma_{ij}\left(2\dot{\varepsilon}_{ik}\dot{\varepsilon}_{jk}-\frac{\partial v_k}{\partial x_i}\frac{\partial v_k}{\partial x_j}\right)\right]dV-2\int\dot{T}_j v_j dS\right\}=0 \tag{3.40}$$

In Eq. (3.40), the second term in the volume integral represents the change in geometry due to the large strain.

For a finite volume element, the nonzero components of the *Jaumann* stress rate are described by a column vector $\dot{\sigma}$:

$$\{\dot{\sigma}\}=[C]\{\dot{\varepsilon}\} \tag{3.41}$$

where:
[C] = the constitutive matrix

In an elasto-plastic element obeying the *Prandtl-Reuss flow rule*, [C] is expressed by a symmetric square matrix (See Chapter 2 of [72] for more details).

In the variational form expressed by Eq. (3.40), the second term in the volume integral can be omitted because the positional changes are negligible when the strains are small. Thus, the matrix form of this equation becomes

$$\delta\left(\int\{\dot{\varepsilon}\}^T[C]\{\dot{\varepsilon}\}dV-2\int\{v\}^T\{\dot{T}\}dS\right)=0 \tag{3.42}$$

In general, the velocity distribution in a typical element, and the associated strain rate, can be expressed in the form (irrespective of the choice of the element).

$$\{v\} = [N]\{d\} \tag{3.43a}$$

$$\{\dot{\varepsilon}\} = [B]\{d\} \tag{3.43b}$$

where:

$\{d\}$ = the displacement vector

$[N]$ and $[B]$ = the displacement and displacement rate interpolation matrix, respectively.

Substituting Eqs. (3.43a and b) into Eq. (3.42), the variational principle is reduced to

$$\{\delta d\}^T \left(\int [B]^T [C][B]\{d\} dV - \int [N]^T \{\dot{T}\} dS \right) = 0 \tag{3.44}$$

Since the variation of the nodal velocities is arbitrary, the above equation requires the expression in the parenthesis to vanish. Therefore, the rate equation of equilibrium for the element becomes

$$[k]\{d\} = \{\dot{r}\} \tag{3.45}$$

where:

$[k] = \int [B]^T [C][B] dV$ = the element stiffness matrix

$\{\dot{r}\} = \int [N]^T \{\dot{T}\} dS$ = the associated load rate vector

In problems involving large plastic strains, the variational form leads to an additional stiffness term in the finite element equation. To derive the second stiffness matrix,

$$v_i = [N_i]\{d\} \tag{3.46a}$$

$$\dot{\varepsilon}_{ij} = [B_{ij}]\{d\} \tag{3.46b}$$

where:

$[N_i]$ and $[B_{ij}]$ = the row vectors identical to the rows of $[N]$ and $[B]$, respectively.

Then the rate equation of equilibrium, Eq. (3.45), becomes

$$([k]+[k_s])\{d\} = \{\dot{r}\} \tag{3.47}$$

where:

$$[k_s] = \int([N_k]_{,i}^T \sigma_{ij} [N_k]_{,j} - 2[B_{ki}]^T \sigma_{ij} [B_{kj}])dV$$

Therefore, the global equilibrium equation for elastic-plastic problems is expressed

$$[K]\{U\} = \{\dot{R}\} \tag{3.48}$$

where:

$[K]$ = the global stiffness matrix

$\{U\}$ = the global displacement vector

$\{\dot{R}\}$ = the global load rate vector

In Eq. (3.48), nonlinearities arise due to the work hardening effect and large deformation. The calculation procedure for the finite element equation is based on the incremental method of calculation that uses a tangent stiffness matrix. Using the constitutive matrix appropriate for the elasto-plastic element, the tangent stiffness matrix is constructed to obtain the increments of nodal displacement corresponding to a specified load increment. In the subsequent section, a commonly-used method of solving the nonlinear equation is described.

3.5 Solution Methods for Nonlinear Equations

The nonlinear equations (3.23 and 3.48) produced through the finite element discretization process can be solved by a nonlinear equation solver that incorporates a multiple linear system in an iterative process to seek a solution. In this section, the popular *Newton-Raphson* (*N-R*) method is presented, which is characterized by its favorable convergence [70, 74].

3.5.1 Concept of Newton-Raphson iteration method

Eqs. (3.23) and (3.48) can be written in the general matrix form as:

$$[K]\{u\} = \{F^a\} \tag{3.49}$$

where:
$[K]$ = coefficient matrix
$\{u\}$ = vector of unknown DOF values
$\{F^a\}$ = vector of applied loads

In thermal equations, $[K]$ is the conductivity matrix and $\{u\}$ is the temperature vector, and in structural equations, $[K]$ is the tangent stiffness matrix and $\{u\}$ is the displacement vector. The coefficient matrix $[K]$ is a function of the unknown DOF values $\{u\}$ (or their derivatives), and $\{u\}$ cannot be solved directly because information needed to construct $[K]$ is not known in advance. $\{u\}$ and its related $[K]$ can be obtained by an iterative process for which Eq. (3.49) is expressed as:

$$[K_i]\{\Delta u_i\} = \{F^a\} - \{F_i^{nr}\} \tag{3.50}$$

$$\{u_{i+1}\} = \{u_i\} + \{\Delta u_i\} \tag{3.51}$$

where:

$[K_i]$ = updated coefficient matrix

i = subscript representing the current equilibrium iteration

$\{F_i^{nr}\}$ = vector of restoring loads corresponding to the element internal loads

$\{\Delta u_i\}$ = DOF increment vector

The iterative process to seek a solution known as the *N-R* method is shown in Figure 3.7. $\{u_i\}$ is assumed, and both $[K_i]$ and $\{F_i^{nr}\}$are calculated from configuration $\{u_i\}$. $\{\Delta u_i\}$ is computed from Eq. (3.50). The next approximation $\{u_{i+1}\}$ is obtained adding $\{\Delta u_i\}$ to $\{u_i\}$ in Eq. (3.51). This process is repeated until convergence is satisfied.

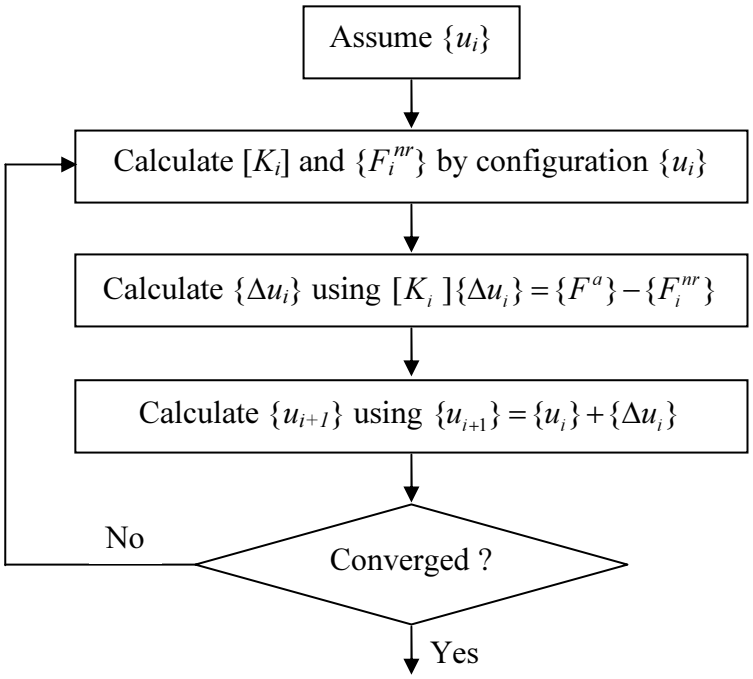

Figure 3.7 Newton-Raphson iteration procedure.

3.5.2 Incremental Newton-Raphson iteration method

In the analysis of plasticity that includes path-dependent nonlinearities, the solution process has to be carried out by a step-by-step incremental analysis in order to correctly follow the load path. Thus, the load vector $\{F^a\}$ is divided into many steps to be applied in increments, and the *N-R* iterations are performed at each step:

$$[K_{n,i}]\{\Delta u_i\} = \{F_n^a\} - \{F_{n,i}^{nr}\} \tag{3.52}$$

where:

$[K_{n,i}]$ = updated coefficient matrix for time step n, iteration i

$\{F_n^a\}$ = total applied force vector at time step n

$\{F_{n,i}^{nr}\}$ = restoring force vector for time step n, iteration i

This incremental *N-R* procedure is graphically illustrated in Figure 3.8. When the coefficient matrix [*K*] is updated every iteration, as depicted in Figure 3.8, the process is termed a full *N-R* solution procedure. Instead of updating [*K*] in every iteration, [*K*] can be used in many iterations in each step until convergence is obtained at each step. This solution method is the modified *N-R* method. Although more iterations are required in this method than the full *N-R* method, every iteration is accomplished more quickly avoiding repeated generation of [*K*], which leads to computational cost reduction.

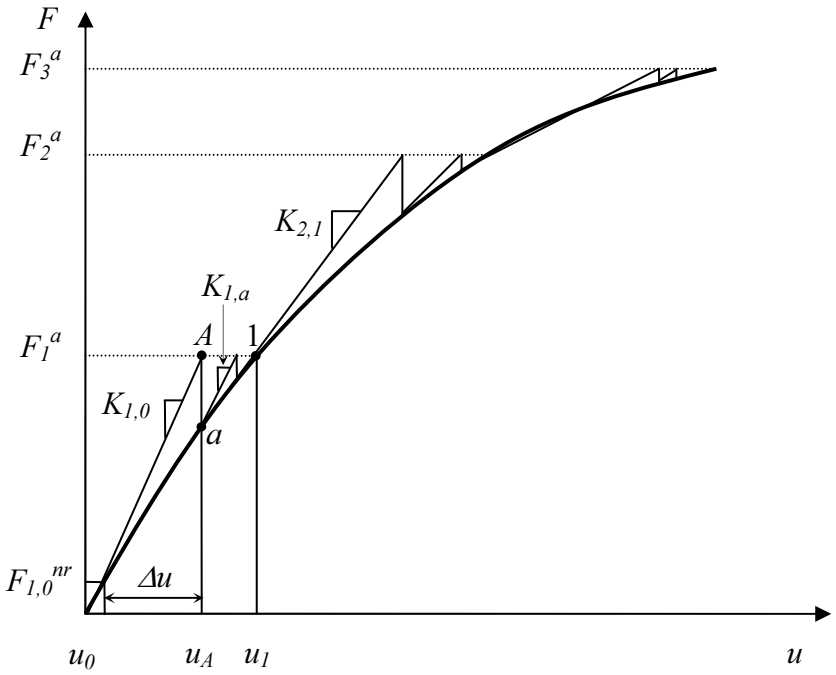

Figure 3.8 Incremental Newton-Raphson procedure.

3.5.3 Convergence

The iterative process at each step continues until the result meets one or more convergence criteria. Two common criteria are:

$$\left\|\{R\}\right\| < \varepsilon_R \left\|\{F^a\}\right\| \quad \text{(out-of-balance convergence)}$$

and/or

$$\left\|\{\Delta u\}\right\| < \varepsilon_U \left\|\{\Delta u_0\}\right\| \quad \text{(DOF increment convergence)}$$

where:

$\{R\}$ = the out-of-balance load (or residual) vector (= $\{F^a\}$-$\{F^{nr}\}$)

$\{\Delta u\}$ = the DOF increment vector of the load step n

$\{\Delta u_0\}$ = the initial DOF increment of the load step n

ε_R and ε_U = tolerances

$\| \ \|$ = a vector norm; that is, a scalar measure of the magnitude of the vector

There are three defined norms as follows:

a. Infinite norm $\|\{R\}\|_\infty = \max|R_i|$

b. *L1* norm $\|\{R\}\|_1 = \sum|R_i|$

c. *L2* norm $\|\{R\}\|_2 = (\sum R_i^2)^{1/2}$

The tolerances ε_R and ε_U may be in the range 0.001 to 0.01, but quite different values can be adopted which depend on the nature of the problem or the accuracy required.

3.5.4 Line search

Line search is a technique to improve a *N-R* solution when the use of the full $\{\Delta u_i\}$ leads to solution instabilities [70]. In the case, Eq. (3.51) is modified using the line search technique as follows:

$$\{u_{i+1}\} = \{u_i\} + s\{\Delta u_i\} \tag{3.53}$$

where:

s = line search parameter

s is automatically determined by minimizing the energy of the system, which reduces to finding the zero of the nonlinear equation:

$$g_s = \{\Delta u_i\}^T(\{F^a\} - \{F^{nr}(s\{\Delta u_i\})\}) \tag{3.54}$$

where:

g_s = gradient of the potential energy with respect to s

An iterative solution scheme is used to solve Eq. (3.54). The scaled solution $\{\Delta u_i\}$ is used to update the current DOF values $\{\Delta u_{i+1}\}$ in Eq. (3.51) and the next equilibrium iteration is performed.

3.6 Summary

This chapter has given a brief description of concept of the FEM and the derivation of the finite element equations from the partial nonlinear differential equations of the heat transfer and structural problems. It has also presented a nonlinear solution algorithm for the solution of the matrix equations. The key points of this chapter include:

- FEM is a computer-based numerical method used to solve a continuum problem. The body is discretized into elements with nodes which are used to represent the variation of the field variable over the element by interpolation function.

- The finite element equation expressing the heat transfer due to heating by a laser beam is derived from the *law of conservation of thermal energy* via the weighted residuals approach.

- The matrix equation involving the large plastic strain due to thermal expansion is formulated from the *equation of equilibrium*, which is characterized nonlinearities due to the work hardening effect and large deformation.

- The well-known *Newton-Raphson* iteration procedure used to solve the nonlinear equations produced through the finite element discretization process is presented with a line search technique for the improvement of its convergence.

Chapter 4

Finite Element Analysis of Straight-Line Laser Forming

4.1 Introduction

The finite element equation formulations and solution method for both thermal and structural problems were presented in Chapter 3.

This chapter investigates the thermal and mechanical responses of the material during laser forming via the finite element simulations. It develops a nonlinear, transient, three-dimensional heat transfer model and a nonlinear, rate dependent three-dimensional structural model for a straight-line laser heating process. The finite element models are parametrically built using a scripting language, APDL (ANSYS Parametric Design Language) provided by the commercial code ANSYS [77]. A series of three tests with different processing conditions are conducted by a thermal-stress coupled field method. A detailed analysis of the simulation results is presented. The models are also validated comparing the results with established experimental and numerical data.

This chapter begins with a brief description of the straight-line heating process. Then the heat transfer and deformation models are presented in two consecutive sections. Finally, simulation results are demonstrated and discussed.

4.2 Process Description

The configuration of the straight-line laser forming process used in this study is illustrated in Figure 4.1. A test plate is heated along its centerline by the incident irradiation from the laser source (See Sections 1.2.2, 2.2.2 and 2.2.3 for the forming mechanisms). The heating, which is actually realized by moving the plate (held by a clamp at one end side) against the fixed laser in experiments, can start on any point on the centerline, depending on the desired forming mechanism. In this simulation, the laser beam is moving from point 1 to point 2 in a single line process. In a multiple heating process, the path direction alternates for each pass. The losses of the heat transferred to the plate are largely governed by conduction into the surrounding material for the duration of the operation, and a small amount of the heat is lost by natural convection and radiation from plate surfaces. Parameters and their values used for the simulations are listed in Table 4.1 which are part of the data used in an experimental paper [63].

Table 4.1 Parameters and values used for simulations.

Plate dimension			Laser parameter		
Length (mm)	Width (mm)	Thickness (mm)	Power (Watts)	Feed rate (mm/s)	Beam diameter (mm)
150	300	4, 6	1500, 3000	5, 10	16

The plate material used in the analysis is the ship-building carbon-manganese steel DIN 1.0584 (D36), which chemical composition is presented in Table 4.2 [76].

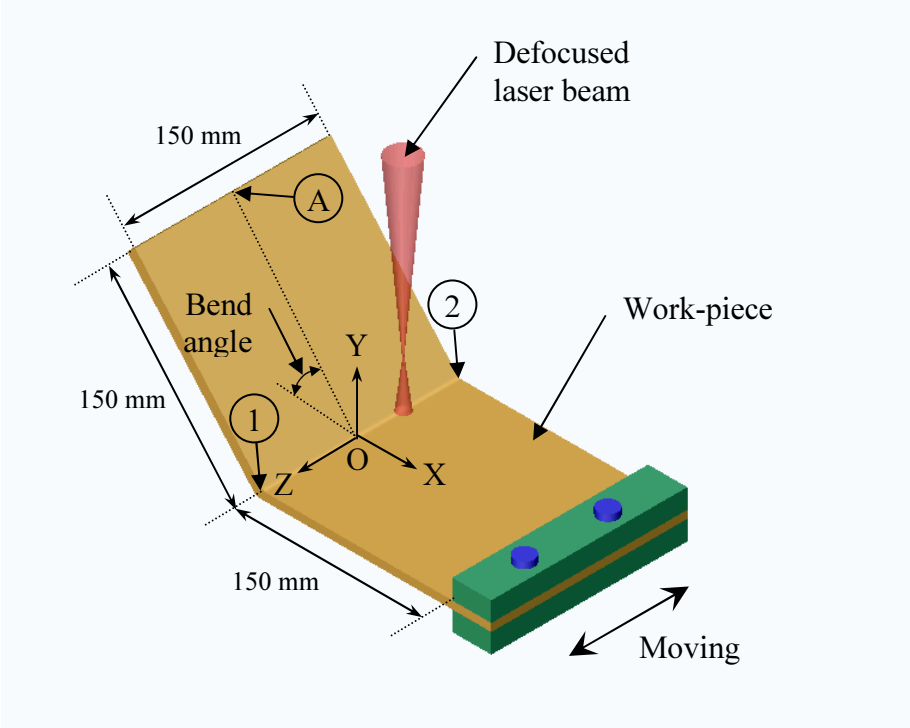

Figure 4.1 Graphical representation of the straight-line laser forming process.

Table 4.2 Chemical composition of carbon-manganese steel (DIN 1.0584).

Nearest SAE grade	DIN number	Composition, wt%					
		C	Si	Mn	P	S	Others
1513	1.0584, D36	0.18	0.10-0.50	0.90-1.60	0.04	0.04	0.15Al, 0.02-0.05Nb, 0.05-0.10V

4.3 Heat Transfer Model

Temperatures induced in the plate by irradiation can be calculated by the nonlinear transient thermal finite element equation (See Eq. 3.23). As can be seen in the equation, the temperature-dependent material properties of the plate have to be involved for the nonlinear problem, and the time-dependent heat loads are required for the transient problem. In addition to the material model and the heat load moving scheme, the heat transfer model developed for the thermal analysis is described in this section in terms of assumptions, the elements employed, mesh management, surface heat flux model, and boundary conditions.

4.3.1 Assumptions

A number of assumptions have been made in developing the finite element model, which include:

- Heating and thermal boundary conditions are symmetrical across the centerline (i.e., heating line) of the plate.
- No melting occurs for the period of the process.
- The plate material is isotropic and homogeneous.
- Heat transfer from the work-piece to the clamp is so small that it is negligible.

With these assumptions, the numerical model can be made with half the plate, employing symmetry to reduce simulation time. This idealization of the model is adequate to represent the problem to achieve study goals.

4.3.2 Elements employed

Three types of solid elements are commonly used for a three-dimensional model – brick, wedge, and tetrahedron. It is a primary condition to use the appropriate elements for finite element models to obtain the most accurate solution through the finite element analysis. In the present thermal analysis, the sheet metal is meshed using a brick element (called SOLID70) because the element is more accurate and more computationally efficient than a comparable tetrahedron one.

Figure 4.2 shows the geometry, node locations, and the coordinate system of SOLID70, which has eight nodes with a single degree of freedom, temperature, at each node. Heat fluxes and convections can be input as surface loads at the element faces as shown by the circled numbers on the element geometry. The surface loads are defined with the nodes or elements. An advantage of the use of the element is that this element can be replaced by an equivalent structural element for structural analysis.

For the consideration of the radiation effect on the plate surface, a three-dimensional thermal surface effect element (SURF152) is used overlaying it onto the faces of the base elements made by SOLID70. Figure 4.3 shows the geometry, node locations, and the coordinate system of the element, which is defined by four to nine nodes and the material properties (e.g., emissivity). An extra node has to be generated to reflect the radiation effect, which is positioned away from the base element. Interpolation functions of the two elements, SOLID70 and SURF152, are presented in Appendix B.

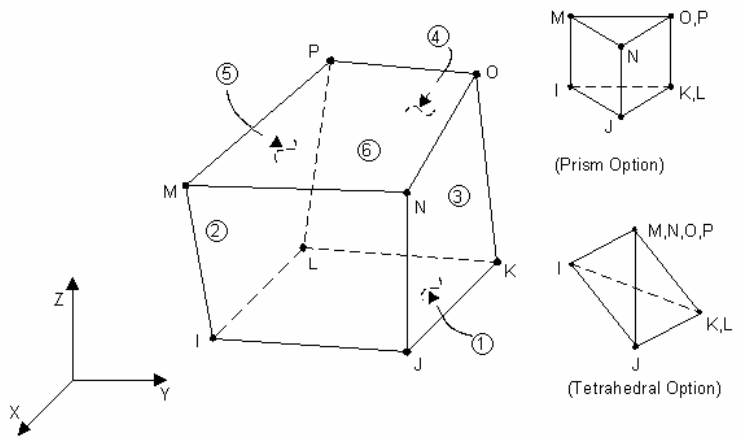

(a)

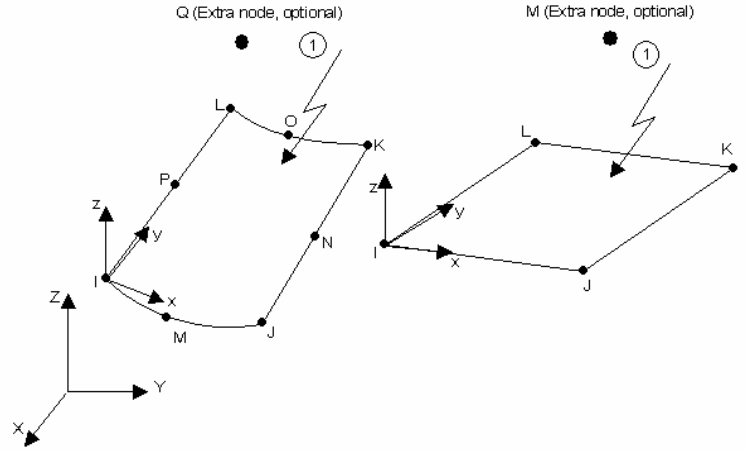

(b)

Figure 4.2 Geometries of: (a) the three-dimensional thermal solid element, SOLID70; and (b) the thermal surface effect element, SURF152. Reproduced from [70].

4.3.3 Material properties

As can be seen Eq. (3.19), temperature response in a material involved in high heat fluxes is determined by the thermal material properties of thermal conductivity, specific heat, and density, which are dependent on temperatures. The accurate calculation of temperatures is critical in laser forming because bending variables of stress and strain are dependent on temperatures. Therefore, temperature dependent thermal properties of carbon-manganese steel are used in the finite element model.

The thermal material properties at high temperatures are shown in Figure 4.3. Thermal conductivity and specific heat at the temperature ranges of 0 °C to 700 °C are obtained from [65], and the properties at higher temperatures (above 700 °C) are linearly extrapolated. The dotted lines indicate the extrapolated values. Density, which is not critical to the simulation, is not known from the source so that the value 7859 kg/m^3 of AISI 1024, having similar chemical composition, is used.

In order to define the temperature dependent property data in the model, temperatures are defined in tables using MPTEMP command first, then the data are associated with the input tables using MPDATA command.

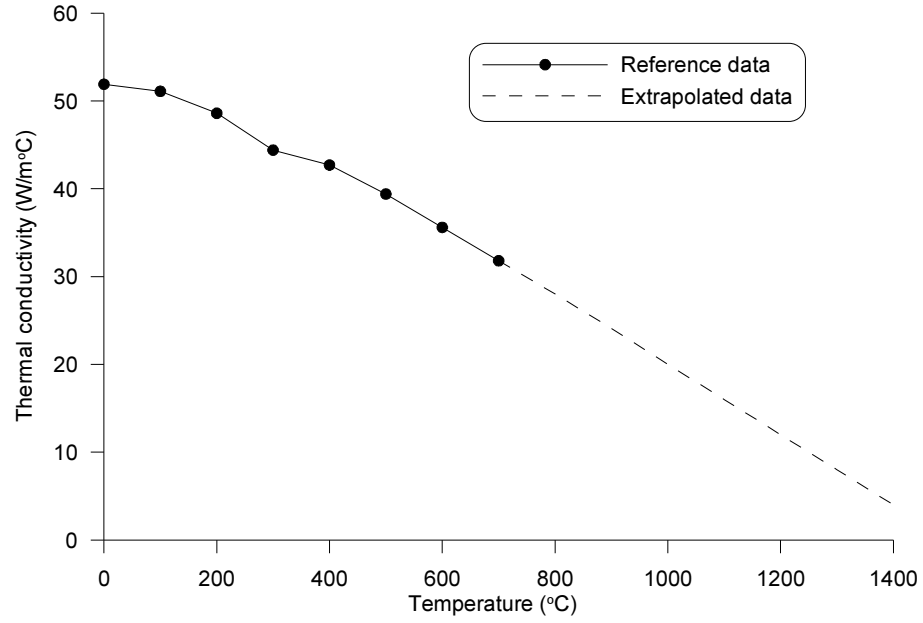

(a)

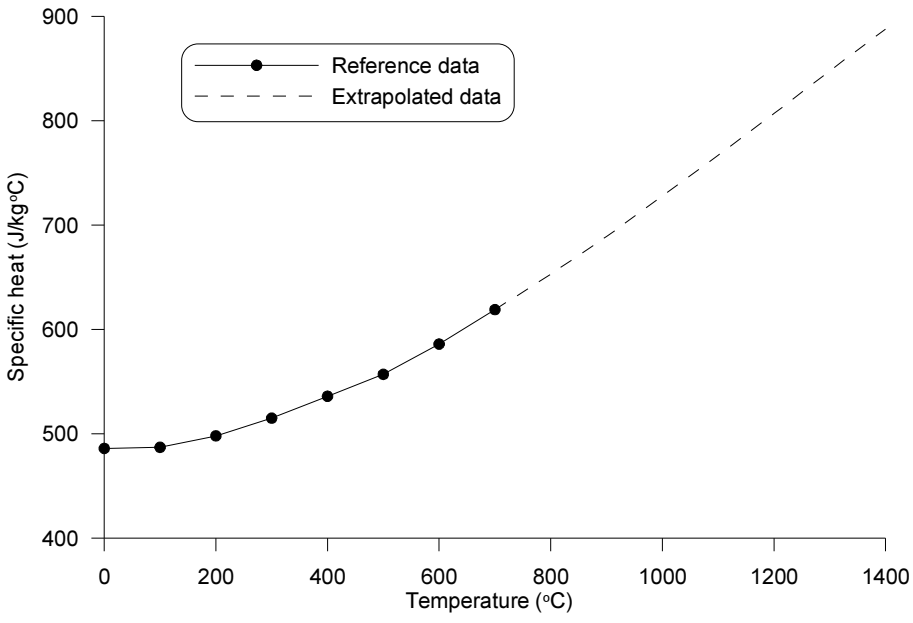

(b)

Figure 4.3 Thermal properties of carbon-manganese steel DIN 1.0584 (D36): (a) thermal conductivity; and (b) Specific heat.

4.3.4 Mesh managements

Half the plate (i.e., 150 mm x 150 mm) is used for generation of meshes as it was assumed that the heating and boundary conditions are symmetrical across the laser path. A non-uniform mesh pattern was devised: fine meshes are created in the region near the laser path due to the high heat flux involved in the portion; less fine meshes in the neighboring zone of the fine meshes; and coarse meshes in the outer portion of the plate. With this mesh pattern, both accurate results of simulation and reduction of simulation time can be achieved.

Figure 4.4 (b) shows the meshes generated for the present simulation. The meshes are composed of a total number of 2040 elements: 1520 elements for the fine meshes; 360 elements for the less fine meshes; and 160 elements for the coarse meshes.

Even though the ideal shape of the brick element (SOLID70) is an equilateral solid, it could not be maintained in mesh geometry because transitional meshes should be involved between regions with different mesh sizes.

The non-uniform mesh pattern and the tapered-element for the transitional meshes can not be directly produced from an ANSYS command so that, as shown in Figure 4.4 (a), the corresponding nodes (i.e., 2801 nodes, including one extra node for radiation effect) to the mesh pattern were generated first, then the elements were directly created using the nodes.

The quality of the mesh was confirmed by a series of tests increasing the mesh density until the temperatures calculated are consistent.

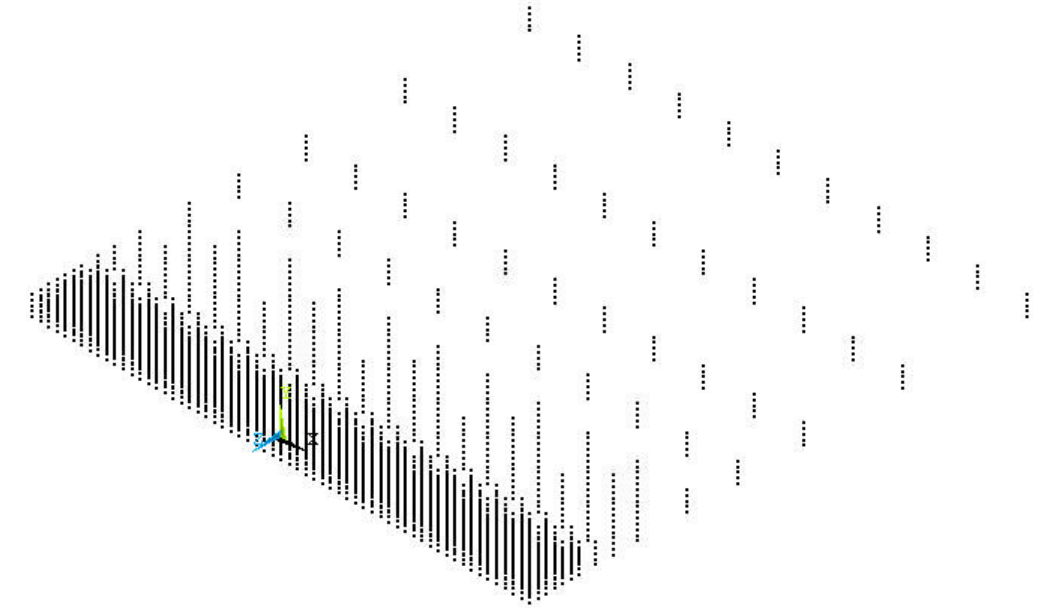

(a)

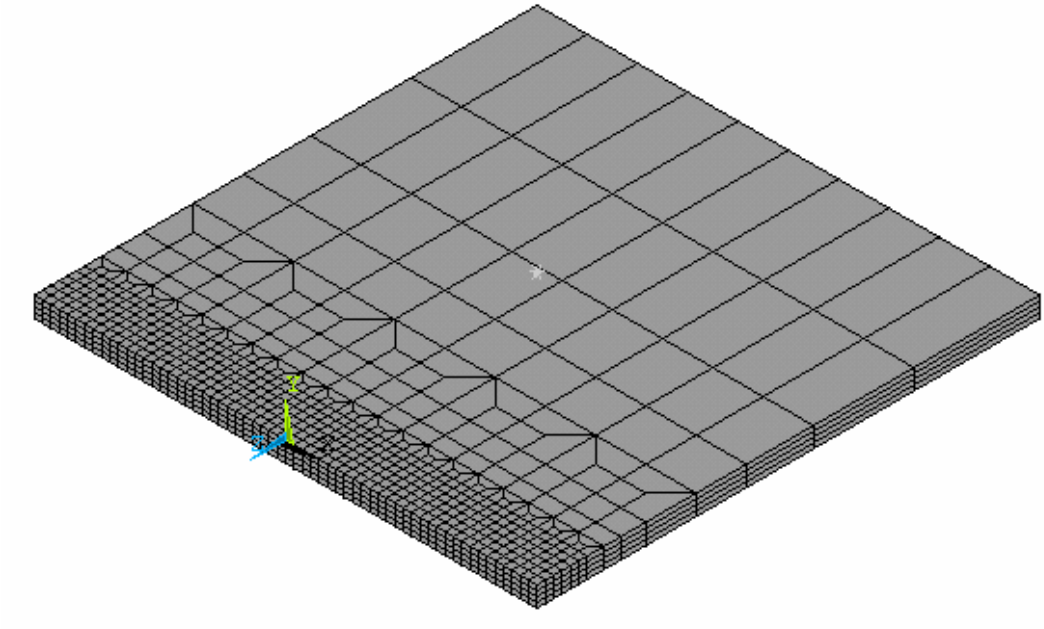

(b)

Figure 4.4 Nodes (a) and meshes (b) generated in half of the work-piece.

4.3.5 Heat flux input

The heat intensity on the plate surface by laser beam is modelled as an idealized Gaussian distribution, and the heat flux is described as follows [38]:

$$q_{(r)} = \frac{2\eta \cdot P}{\pi \cdot R^2} \exp\left(-\frac{2r^2}{R^2}\right) \tag{4.1}$$

where:

$q_{(r)}$ = the intensity of the incident heat flux at the material surface

η = heat transfer efficiency

P = beam power

R = beam diameter

r = distance from the center of the laser beam

The mean thermal flux density, $\overline{q}_{(r)}$, within the area of the laser beam is calculated from Eq. (4.1) as follows [43]:

$$\overline{q}_{(r)} = \frac{1}{\pi R^2} \int_0^R q_{(r)} \cdot (2\pi r) dr = \frac{2\pi}{\pi R^2} \int_0^R \frac{2\eta P}{\pi R^2} \exp\left(-\frac{2r^2}{R^2}\right) r dr = \frac{0.865\eta P}{\pi R^2} \tag{4.2}$$

In the present simulation, the heat flux, $\overline{q}_{(r)}$ obtained from Eq. (4.2) is used as a surface load, and the load is imposed on the selected set of element faces of the plate surface. The movement of the laser beam is realized by adopting the local coordinate system to apply heat loads as a step. As shown in Figure 4.5, the local coordinates (for example, LS 25, 27, and 29) are generated along the heating line as defined steps first, then at each step the center of the laser beam is located at the origin of the local coordinate and the heat load is applied on the elements placed inside the laser beam (illustrated line circle). In order to ensure convergence, the heat loads are imposed by small increments using *DO loop command.

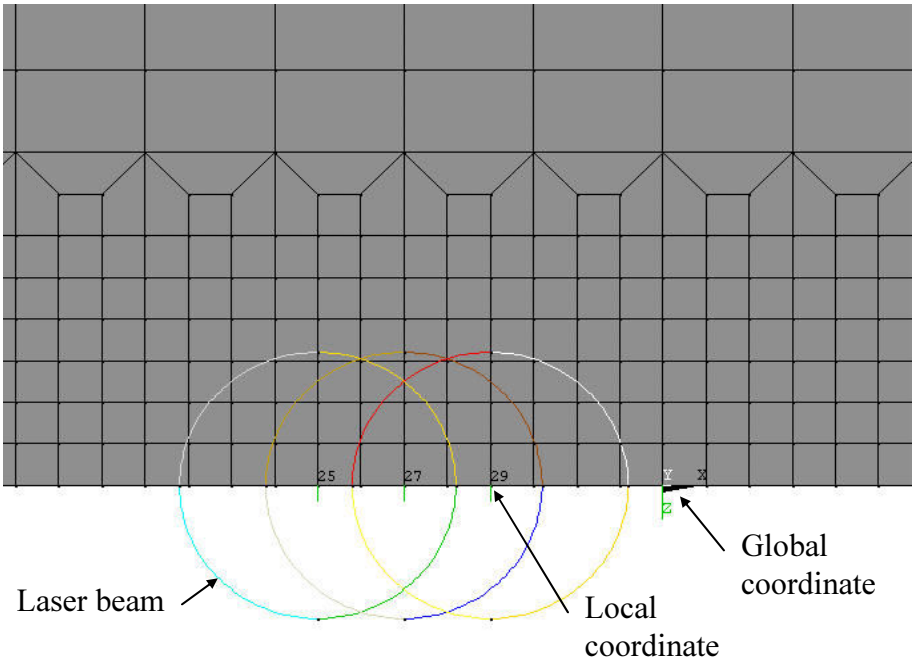

Figure 4.5 Local coordinates and laser beams related to the coordinates.

The heating time, t_s, at each step is described as follows:

$$t_s = \frac{l_p}{v_b} \cdot \frac{1}{n_e} \tag{4.3}$$

where:

l_p = length of plate

v_s = speed of laser beam

n_e = number of elements along the heating line

4.3.6 Boundary conditions

The boundary conditions used include:

- Adiabatic condition is considered on the laser path due to symmetry.
- Heat losses from the plate surfaces to the surroundings take place by means of natural convection and radiation effects.

For the radiant heat loss, q_r,

$$q_r = \sigma \varepsilon_r \left(T_r^4 - T_\infty^4 \right) \tag{4.4}$$

where:
σ = the Stefan-Boltzmann constant
ε_r = the emissivity of radiating surface
T_r = the absolute temperature of radiating surface
T_∞ = the absolute temperature of surrounding

For the convective heat loss, q_c,

$$q_c = h_f \left(T_s - T_\infty \right) \tag{4.5}$$

where:
h_f = the convection coefficient
T_s = the temperature at the plate surfaces

The emissivity of the radiating surface is kept constant ε_r = 0.4 at any temperatures due to limitation of the software used. The convection coefficients are calculated from empirical correlations, which are temperature-position-dependent [68]. For example, for the top surface of the heated plate,

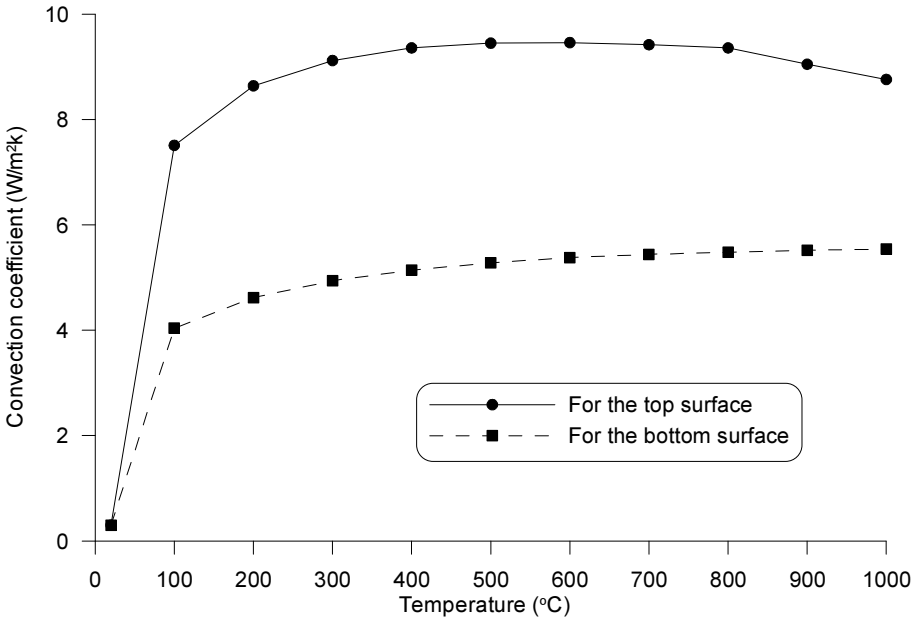

Figure 4.6 Convection coefficients against temperatures.

$$\overline{N}u_L = \frac{\overline{h}L}{k} = 0.15Ra_L^{1/3} \qquad (10^7 \le Ra_L \le 10^{11}) \tag{4.6}$$

where:

$\overline{N}u_L$ = the global Nusselt number

$\overline{h}$ = the global convection coefficient

L = the length of the plate

k = thermal conductivity

Ra_L = the Rayleigh number

The related properties are evaluated at the convection temperature, $T_f \equiv (T_s + T_\infty)/2$. Figure 4.6 shows the convection coefficients dependent on temperatures.

4.4 Deformation Model

Temperature gradients generated through the thickness of the plate cause a differential thermal expansion in the material that is enough to produce large plastic strain to deform the plate. The plate displacements can be calculated by the structural finite element equation (See Eq. 3.48). The deformation model used for the analysis of the structural response of the plate is described in this section.

4.4.1 Assumptions

In developing the numerical deformation model, the following assumptions have been made:

- Deformation occurs symmetrically along the centerline of the plate, so that the simulation is performed with half the plate.
- The plate material is homogeneous.
- Heat generated by plastic deformation is negligible compared with the heat input by laser energy.
- Melting is not involved in the plate during the forming process.
- Phase transformation is not accounted for in the simulation. Thus, both transformation strain and transformation plasticity are ignored.
- The effect of creep is neglected because there is no cyclic thermal load involved.

4.4.2 Elements and meshes

A structural element defined by eight nodes (i.e., SOLID45) is used for three-dimensional modeling of the plate. Each node of the element has three degrees of freedom: translations in the nodal x, y, and z directions. The element supports analysis of plasticity, large deflection, large strain, stress stiffening,

creep and swelling. For the structural analysis, the heat transfer model containing the equivalent thermal element SOLID70 (See Section 4.3.2) can be replaced by this element, and temperatures obtained from the thermal step can be applied as element body loads at the nodes. The geometry, node locations, and the coordinate system of this element is equal to the SOLID70 (See Figure 4.2 a). The following output data are available from the element in a solution: nodal displacements, stresses (principle or equivalent), elastic strains, thermal strains and plastic strains. The identical mesh pattern generated for the thermal analysis (See Figure 4.4 b) is used in the structural analysis. The interpolation function of SOLID45 is given in Appendix B.

4.4.3 Total strain vector

The total strain vector for the general deformation problem is expressed by several strain components [78]:

$$\{\varepsilon\} = \{\varepsilon^{el}\} + \{\varepsilon^{th}\} + \{\varepsilon^{pl}\} + \{\varepsilon^{tr}\} + \{\varepsilon^{tp}\} + \{\varepsilon^{c}\} \tag{4.7}$$

where:

$\{\varepsilon\}$ = total strain vector

$\{\varepsilon^{el}\}$ = elastic strain vector

$\{\varepsilon^{th}\}$ = thermal strain vector

$\{\varepsilon^{pl}\}$ = plastic strain vector

$\{\varepsilon^{tr}\}$ = phase transformation strain vector

$\{\varepsilon^{tp}\}$ = transformation plasticity vector

$\{\varepsilon^{c}\}$ = creep strain vector

In the laser forming problem, the total strain vector is described, according to the assumptions prescribed, as follows:

$$\{\varepsilon\} = \{\varepsilon^{el}\} + \{\varepsilon^{pl}\} + \{\varepsilon^{th}\} \tag{4.8}$$

That is, the current simulation of the forming process accounts for the thermo-elasto-plastic deformation. The elastic and thermal strain models are presented in this section, and the plastic strain model is demonstrated in the subsequent section.

The elastic strain vector is described by the elastic stress-strain relationship, which is defined as:

$$\{\sigma\} = [D]\{\varepsilon^{el}\} \tag{4.9}$$

In another expression,

$$\{\varepsilon^{el}\} = [D]^{-1}\{\sigma\} \tag{4.10}$$

The compliance matrix, $[D]^{-1}$ is:

$$[D]^{-1} = \begin{bmatrix} 1/E & -\nu/E & 0 \\ -\nu/E & 1/E & 0 \\ 0 & 0 & G \end{bmatrix} \tag{4.11}$$

where:

$\{\sigma\}$ = stress vector

$[D]$ = elastic stiffness matrix

E = Young's modulus (input)

ν = Poisson's ratio (input)

G = shear modulus = $\dfrac{E}{2(1+\nu)}$

Both Young's modulus and Poisson's ratio used for the elasticity model are presented in Figure 4.7. The data are available from [65].

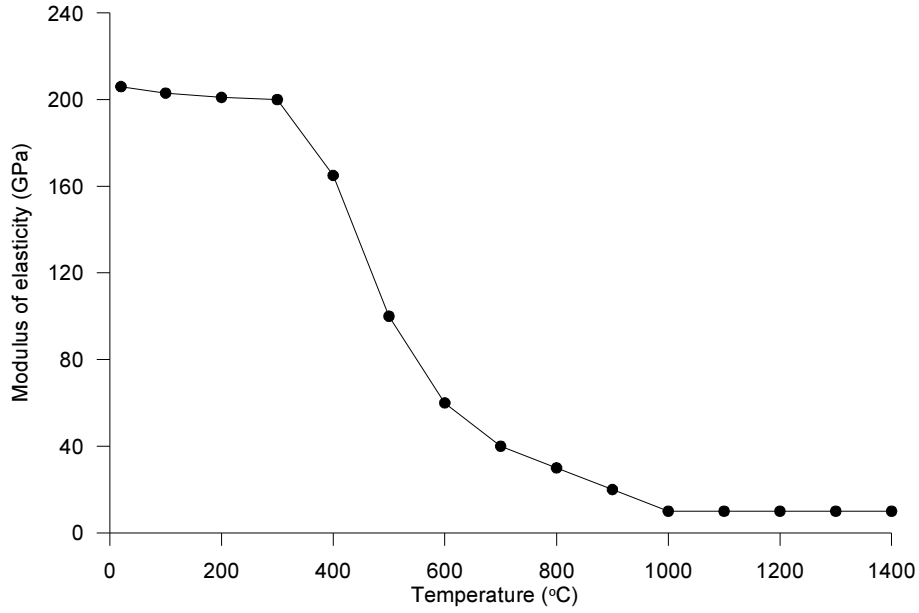

(a)

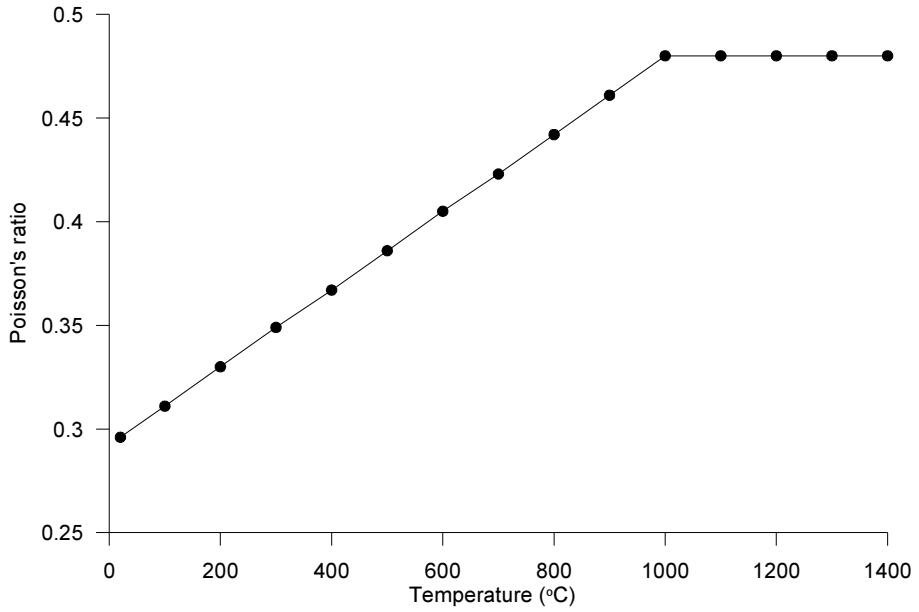

(b)

Figure 4.7 Mechanical properties of carbon-manganese steel DIN 1.0584 (D36): (a) Modulus of elasticity; and (b) Poisson's ratio.

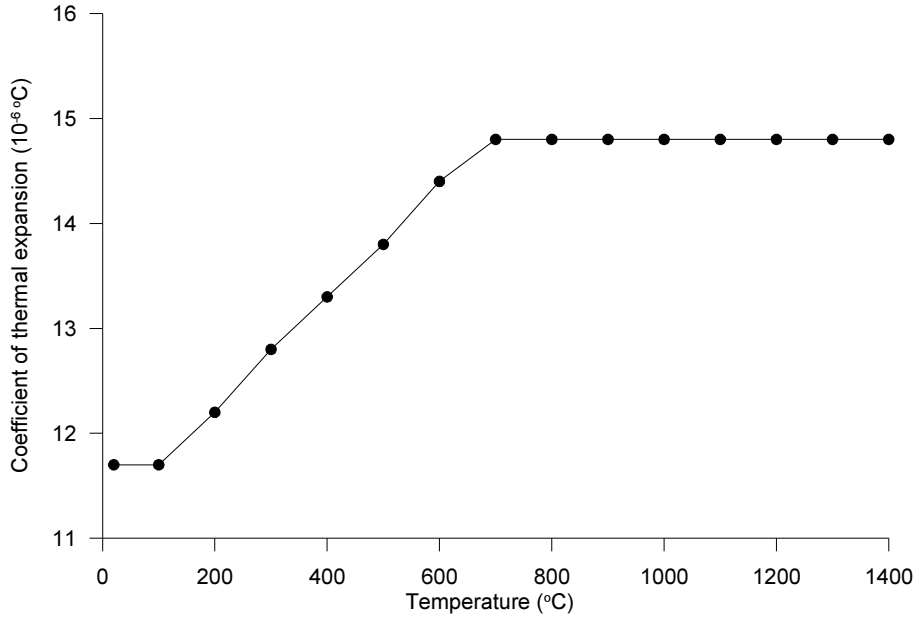

Figure 4.8 Coefficient of thermal expansion of carbon-manganese steel DIN 1.0584 (D36).

The thermal strain vector is expressed in the following form:

$$\left\{\varepsilon^{th}\right\} = \Delta T \left\lfloor \alpha^{se}(T) \right\rfloor^{T} \tag{4.12}$$

where:

$\left\lfloor \alpha^{se}(T) \right\rfloor$ = temperature-dependent secant coefficient of thermal expansion (input)

$\Delta T = T - T_{ref}$ (input)

T = current temperature at the point in question

T_{ref} = reference (strain-free) temperature

For the modeling of the thermal strain vector, the temperature-dependent coefficients of thermal expansion (Figure 4.8) obtained from [65] are input,

and the results of the temperature gradients from the heat load steps of the thermal analysis are imported.

4.4.4 Plasticity model

Plasticity means deformation that is not recovered when loads are removed. Plastic behavior is involved in the laser forming process, and begins when induced stresses (by thermal expansion) exceed the yield point of the material. Plasticity is characterized by the nonlinear relationship between stress and strain, that is, the stress is a nonlinear function of the strain. Their relationship is also path dependent. That is, the stress depends on the strain history as well as the strain itself. The plasticity model defined for the present simulation is described using the three essential ingredients of plastic analysis – *a yield criterion*, *a flow rule*, and *a hardening rule* [70, 74].

The yield criterion is used to predict initial yield. In this laser forming problem, the material is under combined stresses during the plastic deformation. The stress state is represented as a function of the individual components $F(\{\sigma\})$ (called a yield function). The material therefore starts developing plastic strains when

$$F(\{\sigma\}) = \sigma_y \tag{4.13}$$

where:

σ_y = material yield stress

In the present simulation, the yield criterion is assumed to follow the von Mises yield criterion, which is expressed:

$$J_2 = \frac{1}{6}\left[(\sigma_1 - \sigma_2)^2 + (\sigma_2 - \sigma_3)^2 + (\sigma_3 - \sigma_1)^2\right] = k^2 \tag{4.14}$$

where:

σ_1, σ_1, σ_1 = principal stresses
k = a material property

k is determined through a uniaxial tension experiment:

$$\frac{1}{3}\sigma_y^2 = k^2 \tag{4.15}$$

Eq. (4.14) indicates that when $J_2 > k^2$, the stress state is elastic, and when $J_2 = k^2$, plastic strains begin.

The flow rule relates the state of stress to the corresponding increments of plastic strain when an increment of plastic flow takes place. That is, the direction of plastic strain is expressed by the rule that is stated as:

$$\left\{d\varepsilon^{pl}\right\} = \left\{\frac{\partial Q}{\partial \sigma}\right\} d\lambda \tag{4.16}$$

where:
$d\lambda$ = plastic multiplier (which determines the amount of plastic straining)
Q = function of stress called a plastic potential (which determines the direction of plastic straining)

When Q is equal to the yield function F, the flow rule is called the Prandtl-Reuss associative flow rule, which indicates the plastic strains occur in a direction normal to the yield surface as shown in Figure 4.9 (a). $\mathbf{n}_1$ and $\mathbf{n}_2$ are unit vectors in the directions of σ_1 and σ_2, respectively. The associated flow rule is commonly suited for ductile metals, and non-associated rule is used for soil and granular materials.

The hardening rule describes how the yield criterion (yield surface) is modified as the strains develop beyond initial yield. Normally two hardening rules are used for this – isotropic hardening and kinematic hardening. As

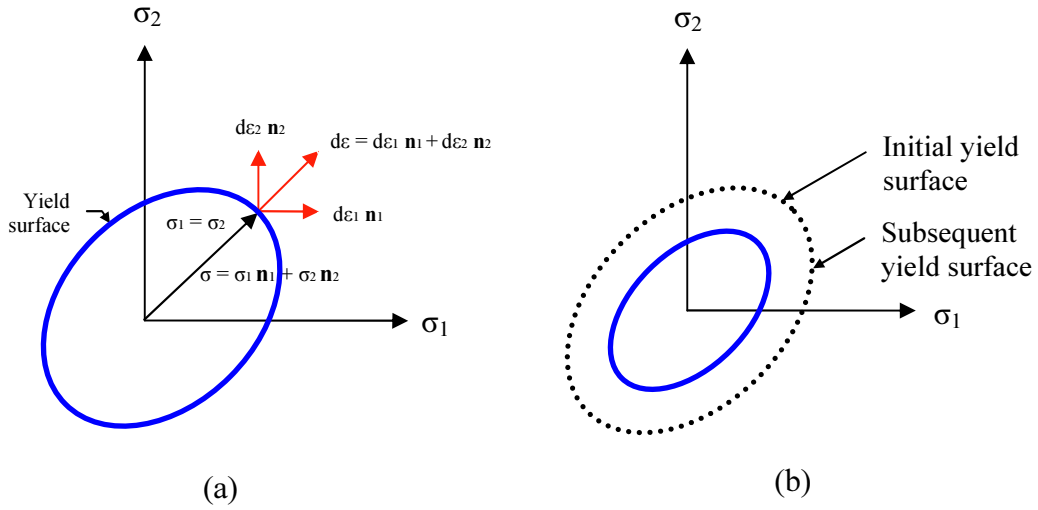

Figure 4.9 Graphical illustrations of: (a) the associative flow rule; and (b) the isotropic hardening rule.

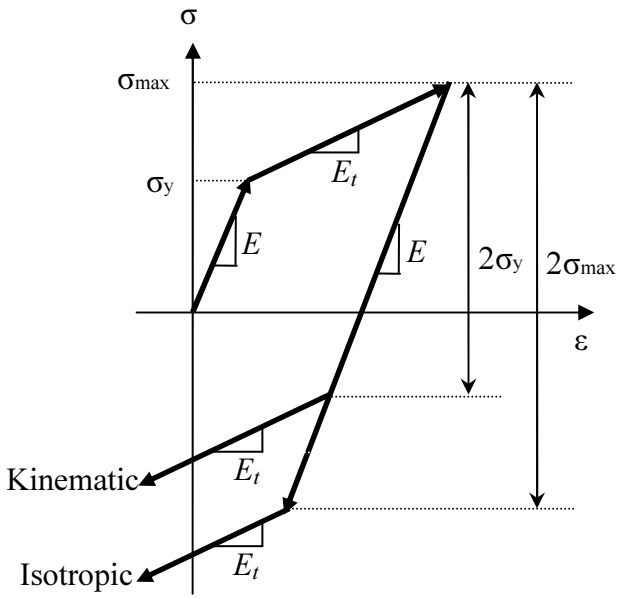

Figure 4.10 Isotropic and kinematic hardening rules.

shown in Figure 4.10, according to the isotropic hardening rule, the elastic range is expanded from the initial value $2\sigma_y$ to the value $2\sigma_{max}$ after reaching σ_{max}. Hence, the experimentally observed Bauschinger effect is not considered in this rule. In the kinematic hardening rule, the Bauschinger effect is taken into account by preserving an elastic range of $2\sigma_y$, but the possibility that the elastic range may increase is ignored. In this study, the isotropic hardening rule is employed due to the suitability of large strain analysis.

In order to calculate the plastic strains by the isotropic hardening rule, the yield function of Eq. (4.13) can be written in the following form because the yield surface remains centered about its initial centerline and expands in size as the plastic strains progress in the isotropic hardening rule (Figure 4.9 b):

$$F\left(\{\sigma\}, W_p\right) = 0 \tag{4.17}$$

where:

$W_p = \int \{\sigma\}^T \{d\varepsilon^p\}$ (= growth of the yield surface)

The plastic multiplier, dλ in Eq. (4.16) is expressed:

$$d\lambda = \frac{\left\{\frac{\partial F}{\partial \sigma}\right\}^T [E]}{\left\{\frac{\partial F}{\partial \sigma}\right\}^T [E]\left\{\frac{\partial Q}{\partial \sigma}\right\} - C\left\{\frac{\partial F}{\partial W_p}\right\}^T [\sigma]^T \left\{\frac{\partial Q}{\partial \sigma}\right\}} \{d\varepsilon\} \tag{4.18}$$

where:

[E] = the elastic material property matrix

Therefore, the incremental plastic strains can be obtained with substitution of Eqs. (4.17) and (4.18) into Eqs. (4.16). It can be seen from the result that the size of the plastic strain is related to the total increment in strain, the current stress state, and the potential yield surface. In the practical plastic analysis, the

loads are applied as a series of small incremental load steps to enable the plasticity model to follow the load-response path as closely as possible.

The ANSYS software provides a multi-linear isotropic hardening model (called MISO) which incorporates the von Mises yield criteria, the associative flow rule, and the isotropic hardening rule. In the model, the stress-strain behavior is expressed by multi-linear curves. Figure 4.11 presents the yield stresses for proof stress $e_p = 0$ of carbon-manganese steel DIN 1.0584 (D36) at different temperatures [65]. The data not available for some high temperatures were linearly extrapolated. The stress-strain behavior of the material after yielding is approximated to tensile strength by means of multi-linear curves as shown in Figure 4.12.

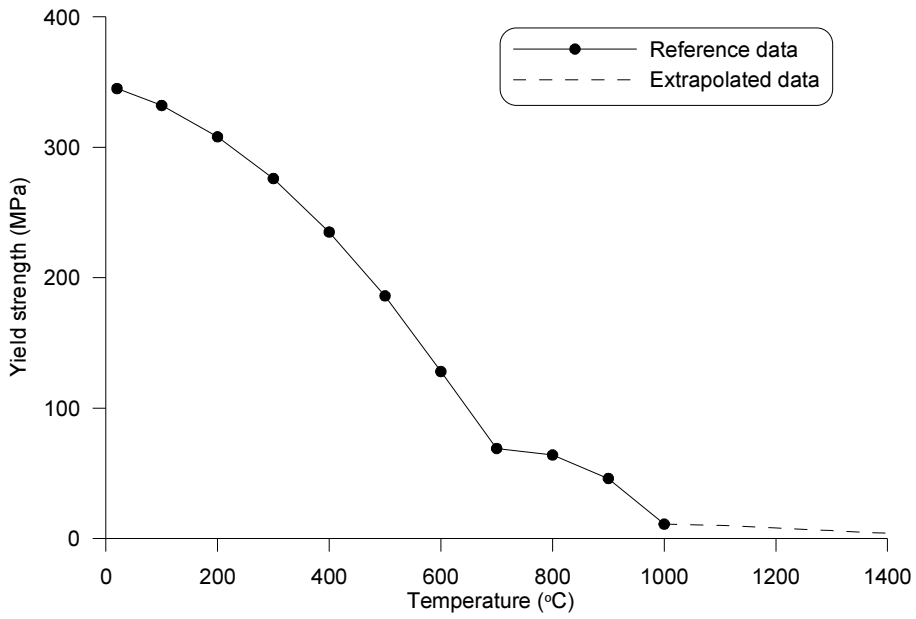

Figure 4.11 Yield strength ($e_p = 0$) of carbon-manganese steel DIN 1.0584 (D36).

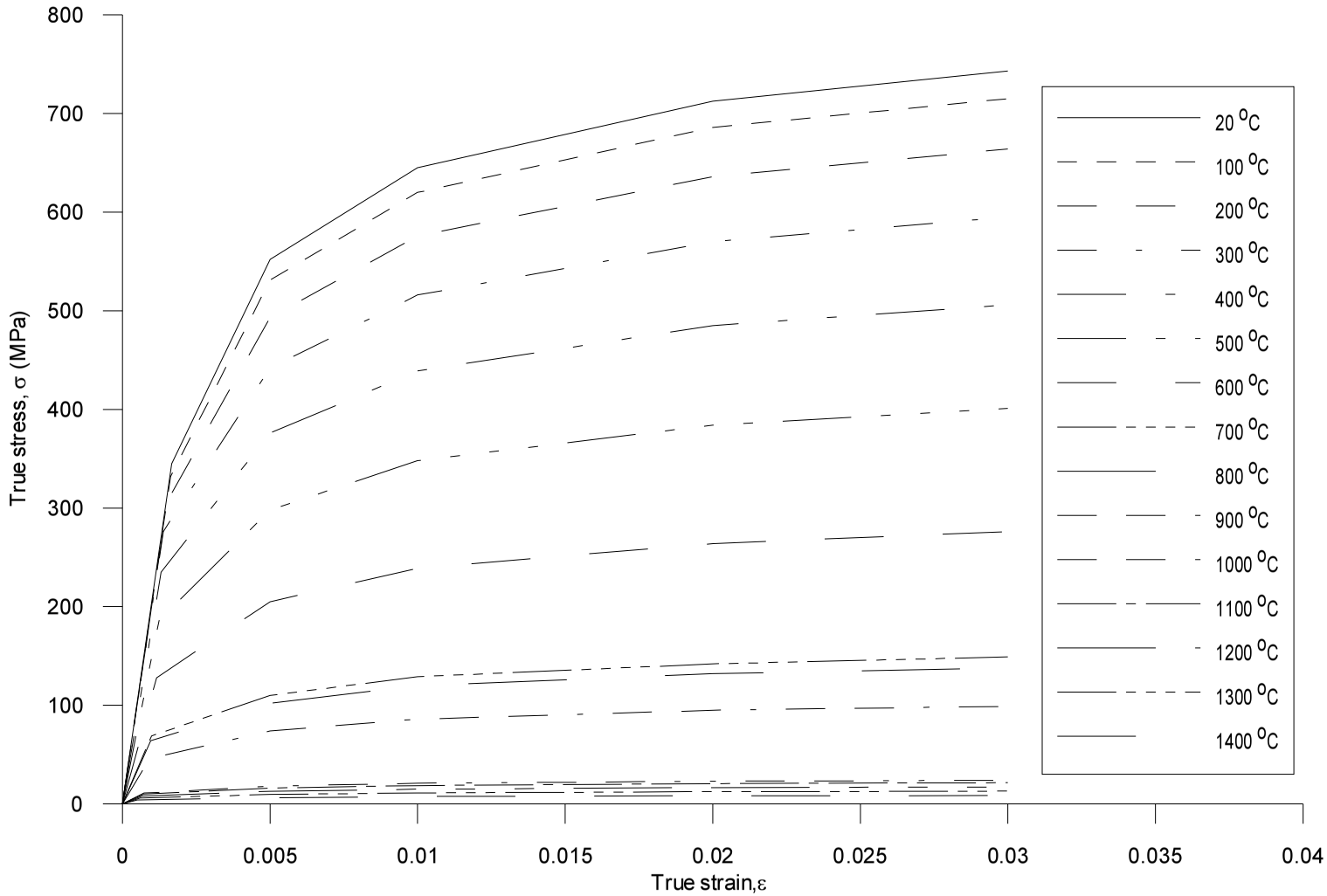

Figure 4.12 Multi-linear stress - strain model of carbon-manganese steel DIN 1.0584 D36.

4.4.5 Geometric nonlinearity

Geometric nonlinearity takes place in the problem in which deformation is large enough that the equilibrium equation (i.e., Chapter 3, Eq. 3.49) must be written with respect to the deformed structural geometry. The deformation resulting from the laser forming is associated with the large strain. The tangent stiffness matrix [*K*] therefore becomes a function of the displacements {u} (See Eq. 3.48), thus the changing geometry should not be neglected. In the present simulation, the large defection effect is included, which is simply done using NLGEOM command.

4.4.6 Boundary conditions

The following boundary conditions are made for the structural simulation:

- Two end-points at the bottom of the symmetric plane are fixed to remove the rigid body motion during the process; and
- There is no displacement across the symmetric plane for all other points on the symmetric plane.

The simulation was conducted using the thermal-stress coupled field method. Especially, since there is not a high degree of nonlinear interaction for the coupling situation, the indirect coupling analysis was used where temperature distributions are first calculated in a nonlinear transient thermal analysis step, then the temperatures are imported and applied as body loads for the subsequent stress analysis.

4.5 Simulation Results

A series of three simulations have been conducted with different forming conditions, as shown in Table 4.3, using the finite element model developed. The absorption coefficient used is 0.75 which value can be obtained using graphite coating in experiment [41]. The first two simulations adopting single heating process were carried out with the conditions equal to published experimental conditions [63] in such a way that the results of the numerical simulation can be evaluated compared with the experimental. A multiple heating process for the last simulation was developed on the base of the single heating to use it for the process optimization in Chapter 7. The numerical model for each forming process was parametrically built using a scripting language, APDL (ANSYS Parametric Design Language) [77]. The computer program listings used for the FE-simulations are given in Appendix C.

Table 4.3 Simulation conditions of the straight-line laser forming.

Case	Laser power (W)	Scanning speed (mm/s)	Beam Diameter (mm)	Number of irradiation	Plate thickness (mm)
1	1500	5	16	1	6
2	3000	10	16	1	4
3	1500	5	16	3	6

4.5.1 Simulation results – Case 1

Simulation of case 1 was run with the following laser parameters: a laser power of 1500 watts; a feed rate of 5 mm/s; and a beam diameter of 16 mm. The plate thickness used was 6 mm. The time taken to heat the plate from point 1 to point 2 was 32 seconds (See Figure 4.1). The plate was cooled down for 168 seconds after heating. Simulation results from thermal and structural analysis steps are

presented here. The temperature response of the plate is described with the following information observed from the thermal analysis step:

- Temperature distributions on and inside the plate at selected times
- Temperature distributions in the direction perpendicular to heating line
- Temperature histories at the central top and bottom points of the plate

In order to demonstrate the material response to temperature profiles in the plate, the following data were obtained from the structural analysis step:

- Stress / plastic strain distributions on and inside the plate at selected times
- Stress / plastic strain histories at the central top and bottom points of the plate
- Residual stresses / residual plastic strains through the plate thickness
- Degree of thickening at the centerline of the plate
- Bend angle histories
- Final deformation

Note that the images depicted in the results are the ones fully expanded across the symmetric plane from the half symmetrical model, and magnified by 100 times.

4.5.1.1 Temperature responses

Temperature responses of the plate are presented in Figures 4.13 to 4.15. The two points shown in the figures indicate the extra nodes used to reflect convection effects in the simulation.

Figure 4.13 shows temperature distributions on the surfaces of the sheet metal at isometric view at three selected times: t =16 sec when the laser beam is passing the center of the plate (a), t = 50 sec when the sheet metal is cooling down (b), and t =200 sec when the process is completed (c). It can be seen from the figures that the temperature reaches a maximum of 728 °C during heating (a) and the heat transferred to the material is lost rapidly to the

surrounding material by conduction effect (b). After finishing the operation, the temperature is measured at about 68 °C along the centerline of the plate and its neighboring region (c). This remaining temperature can be neglected in this analysis because the thermal expansion at this temperature is almost equal to that at room temperature (See Figure 4.8).

Figure 4.14 presents temperature distributions produced through the thickness direction when the laser beam is heating at the center of the plate (i.e., at t = 16.0 sec). Figure 4.14 (a) is captured from the left side view on the X-Y plane crossing the center of the plate. It is noted that the maximum temperature occurs in the rear of the center of the beam during heating, and the temperature gradient is steeper in the front of the center of the beam than that in the rear. Figure 4.14 (b) is captured from the front side view on the Y-Z plane. It is found that the steep temperature gradient is produced through the 6 mm plate thickness during heating, indicating that the TGM (See Chapter 2, page 5) is involved in this forming process.

Figure 4.15 illustrates temperature distributions at the top and bottom surfaces in the direction perpendicular to the heating line (i.e., in the Z-direction) at t = 16.0 sec. It is noticed that the high temperature rise by local heating is confined to a relatively narrow band for Z = ±0.02 m (i.e., to the heated zone and its neighboring zone).

Temperature histories of the central top and bottom points are presented in Figure 4.16. As can be seen in the figure, the temperatures at the central top and bottom surfaces of the plate rise rapidly and reach a maximum of nearly 720 °C and 380 °C, respectively, and then subsequently drops smoothly at the same rate when the laser beam moves away from the top point, indicating that the steep temperature gradient collapses rapidly.

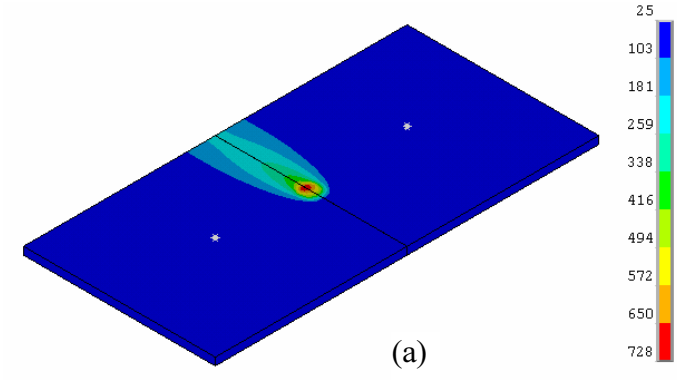

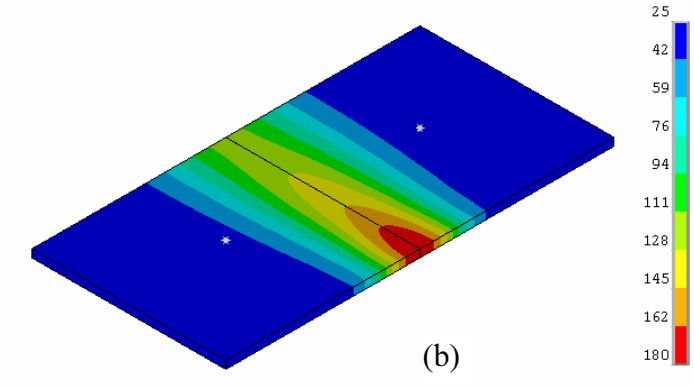

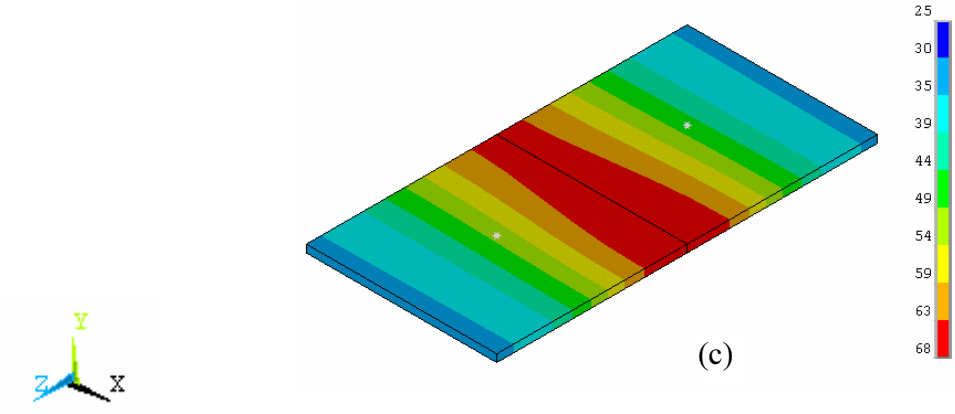

Figure 4.13 Temperature distributions at: (a) 16 sec; (b) 50 sec; and (c) 200 sec. Case 1.

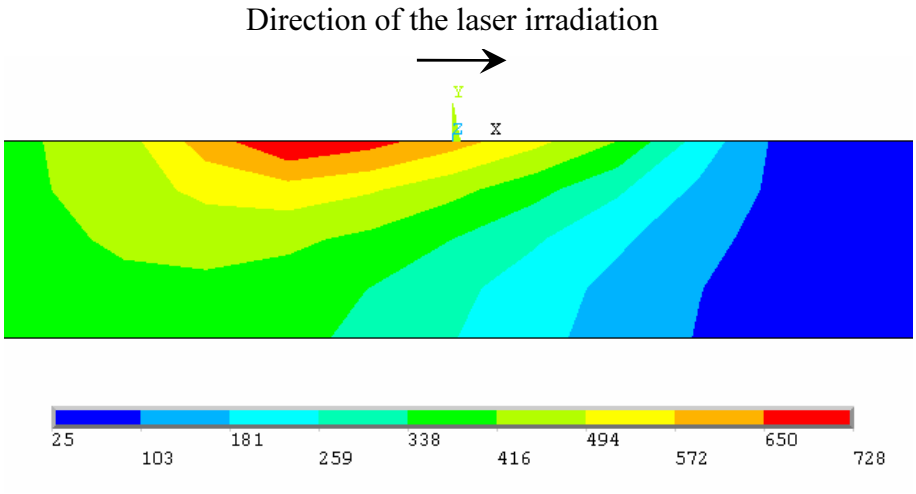

(a)

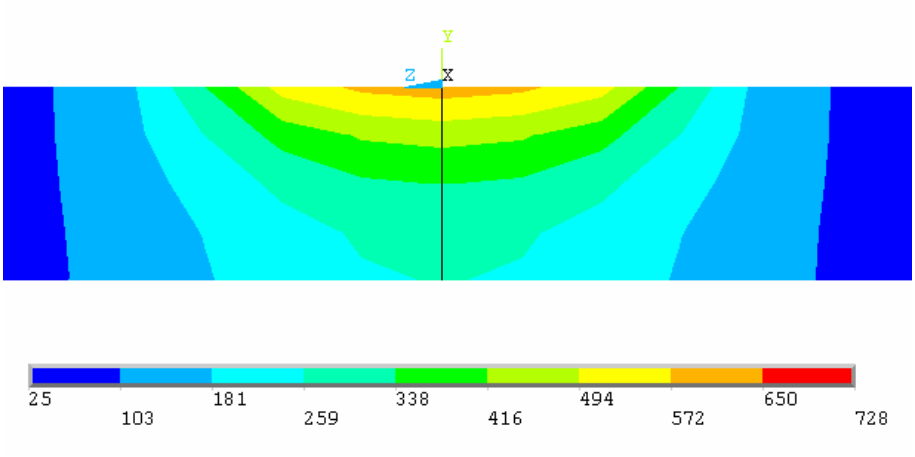

(b)

Figure 4.14 Temperature distributions through the thickness direction at 16 sec: (a) the left side view; and (b) the front side view. Case 1.

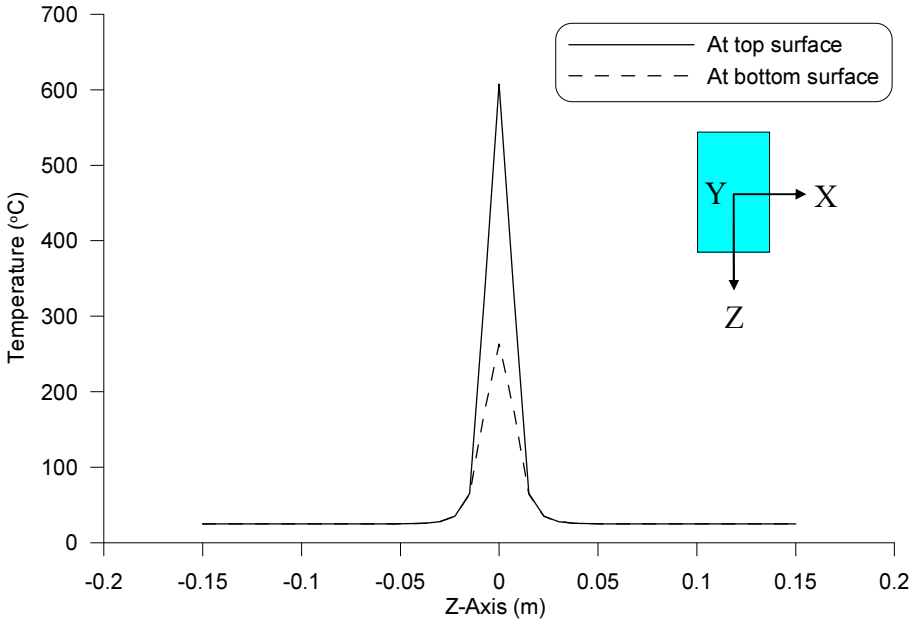

Figure 4.15 Temperature distributions in the Z-direction at 16 sec. Case 1.

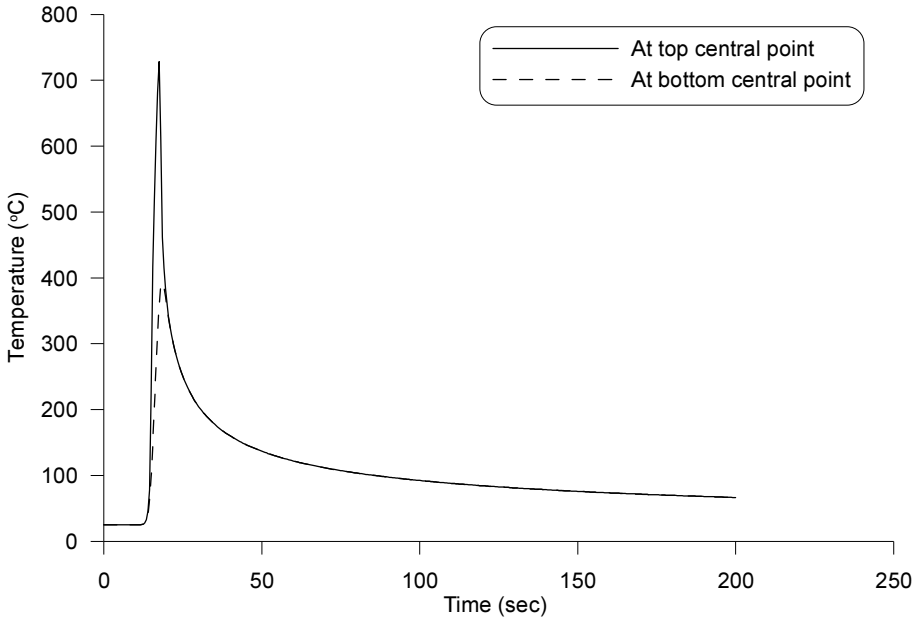

Figure 4.16 Temperature histories at the center of the plate. Case 1.

4.5.1.2 Stress responses

Stress responses of the plate are presented in Figures 4.17 to 4.20. Note that stresses are only investigated with respect to Z-component, σ_z because it is the stress component causing angular change in the process. The positive stress values representing the red region indicate the tensile stresses, and the negative stress values representing the blue region indicate the compressive stresses. The un-deformed plate (i.e., not colored) represents the original specimen before processing.

Figure 4.17 shows the stress distributions on the plate surfaces at three different stages of the process – when the heating is at the early stage (t = 2 sec) (a), when the laser beam is passing the center of the plate (t =16 sec) (b), and when the operation is finished (t = 200 sec) (c). It is noticed from Figure 4.17 (a) that when the heating begins, high compressive stresses of a maximum of 310 MPa arise in the heated surface and its neighboring zone due to thermal expansion by high temperatures, so that the counter-bending (See Chapter 1, Section 1.2.2) is involved at this time. Tensile stresses of a maximum of 120 Mp are produced in the region in front of the laser beam to counteract the thermal expansion constraining material in the surrounding. During the cool-down phase of the heated zone, as shown in Figure 4.17 (b), the compressive stresses change to tensile stresses (a maximum of 270 MPa) due to the contraction of the heated zone. After the operation, the tensile stresses remain at the surface along the centerline of the plate, maintaining the bent shape as shown in Figure 4.17 (c).

Stress distributions through the thickness direction at t = 16 sec when the laser beam is heating at the center of the plate are depicted in Figure 4.18. The figure is captured from the left side view on the X-Y plane crossing the center of the plate (a), and from the front side view on the Y-Z plane (b). It can be seen that the stress distributions correspond to the temperature distributions (Figure 4.14) in that the maximum stress is produced in the rear of the center of the beam, and the stress gradient is steeper in the front of the center of the

beam than that in the rear (Figure 4.18 a). The top surface is deflected into a convex shape when the plate is cooling down. Figure 4.18 (b) shows the thermal expansion of the material in the heated zone that induced high compressive stresses in the area.

Figure 4.19 shows stress histories at two points – one is the top central point of the plate and the other is the bottom central point. It is observed from the figure that when the laser beam approaches the top point (at t = 13.5 sec), the two points undergo the tensile stresses to a maximum of 184 MPa at the top and 167 MPa at the bottom. These stress responses are attributed to the restriction of the surrounding material to the thermal expansion. When the laser beam is placed on the top point, the tensile stresses rapidly change to the compressive stresses due to thermal expansion, and at t = 15.5 sec the compressive stress reaches a maximum of 337 MPa at the top. A maximum compressive stress of 234 MPa at the bottom point occurs at a little bit delayed time (t = 17.5 sec) due to the time taken by heat transfer through the plate thickness. When the laser beam moves away from the top point, the compressive stress at the top point rapidly decreases due to the rapid cool-down in the region, and changes to the tensile stress of 37 MPa at t = 18.5 sec due to the contraction of the material. This tensile stress is maximized to 69 MPa at t = 19.5 sec. On the contrary, during this period of time, the compressive stresses are involved at the bottom point to a maximum of 213 MPa. This stress state is the cause of the bending of the plate towards the laser beam. The compressive stress at the bottom point relatively smoothly decreases due to less cooling effect.

Residual stresses through the plate thickness at the center of the plate are presented in Figure 4.20. It is found that tensile stresses of 124 MPa and 92 MPa remains at the top and bottom points, respectively, and compressive stress of 74 MPa remains at the middle point.

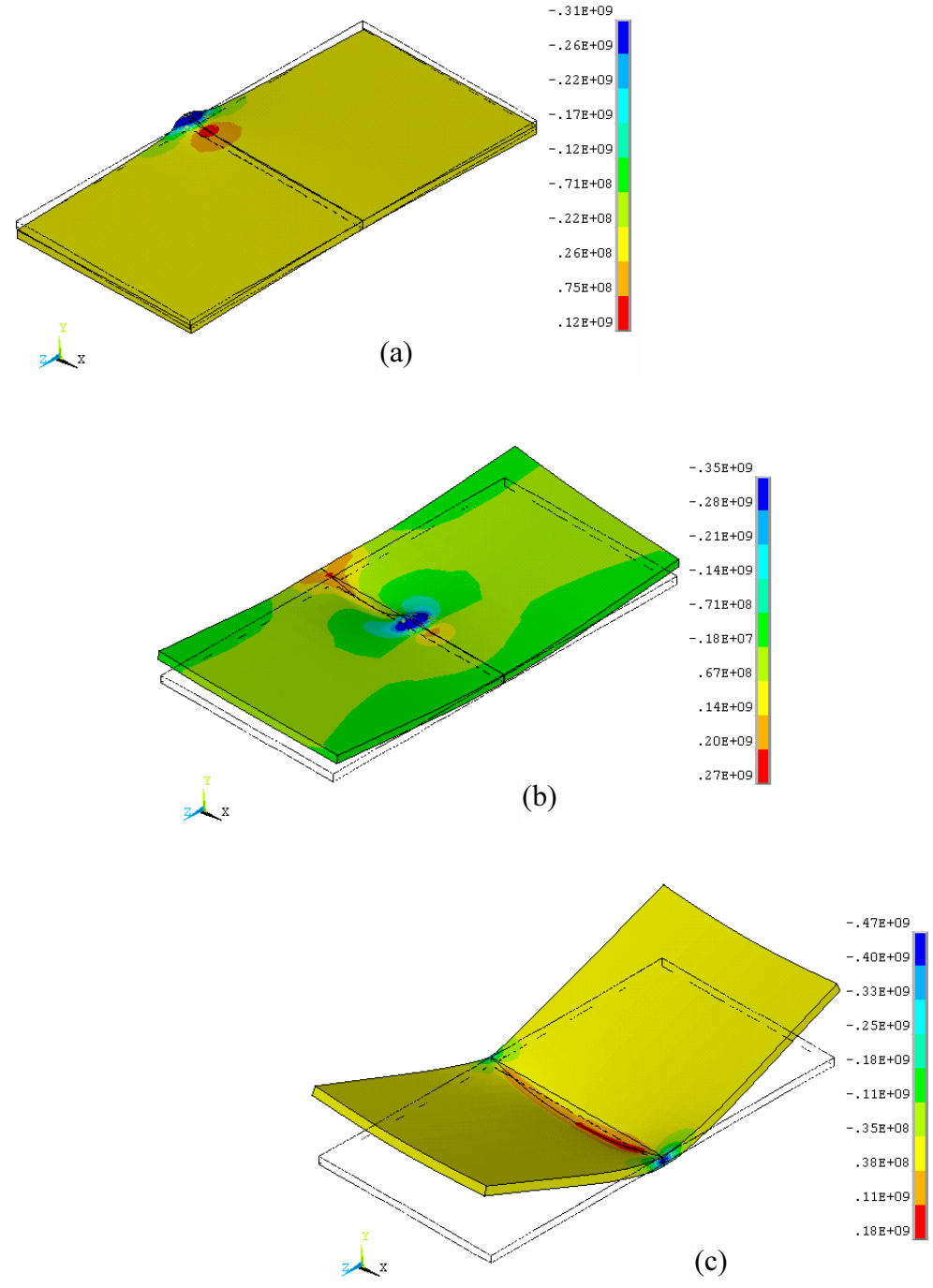

Figure 4.17 Plate stress distributions, σ_z, at: (a) 2 sec; (b) 16 sec; and (c) 200 sec. Deformations are magnified X100 for clarity. Case 1.

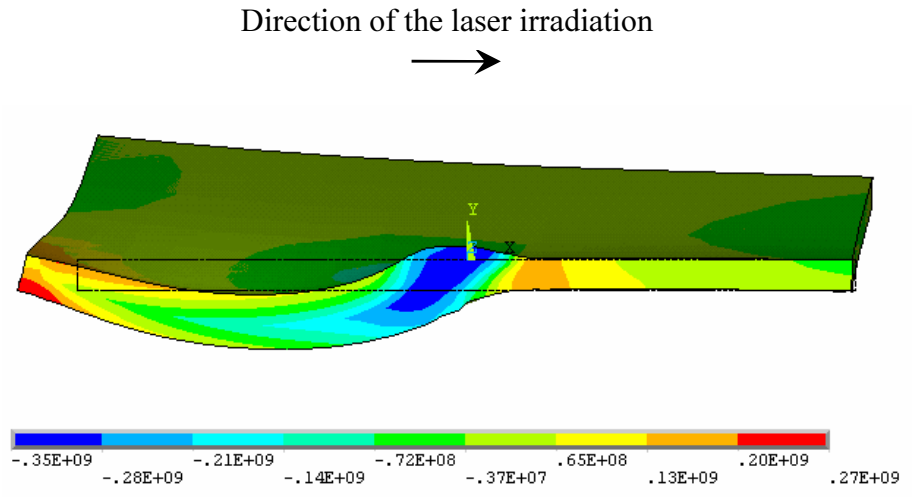

(a)

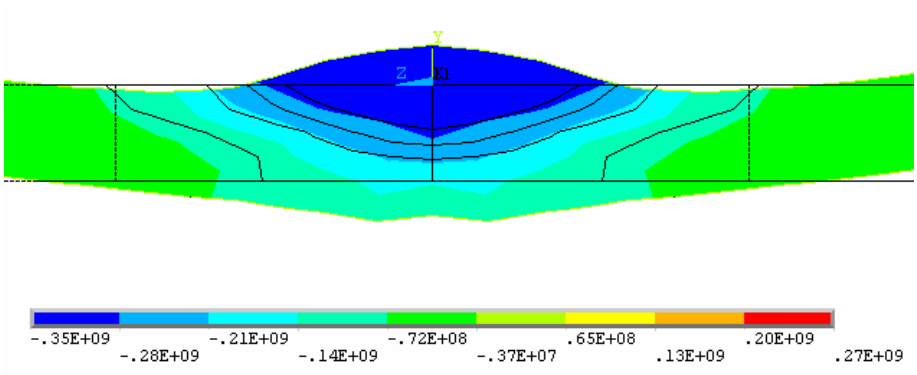

(b)

Figure 4.18 Plate stress distributions, σ_z, at 16 sec: (a) the left side view; and (b) the front side view. Deformations are magnified X100 for clarity. Case 1.

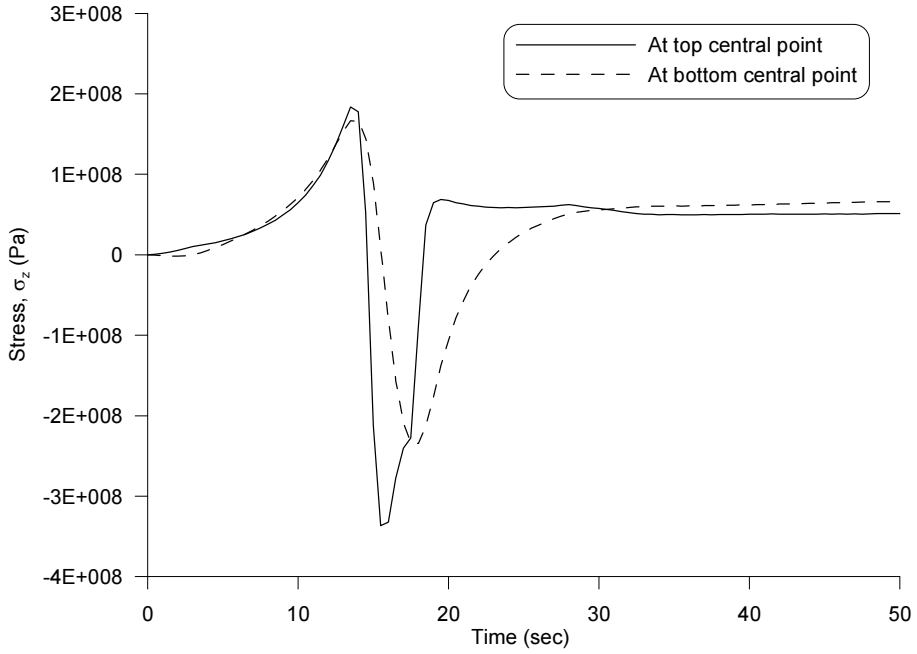

Figure 4.19 Plate stress histories, σ_z. Case 1.

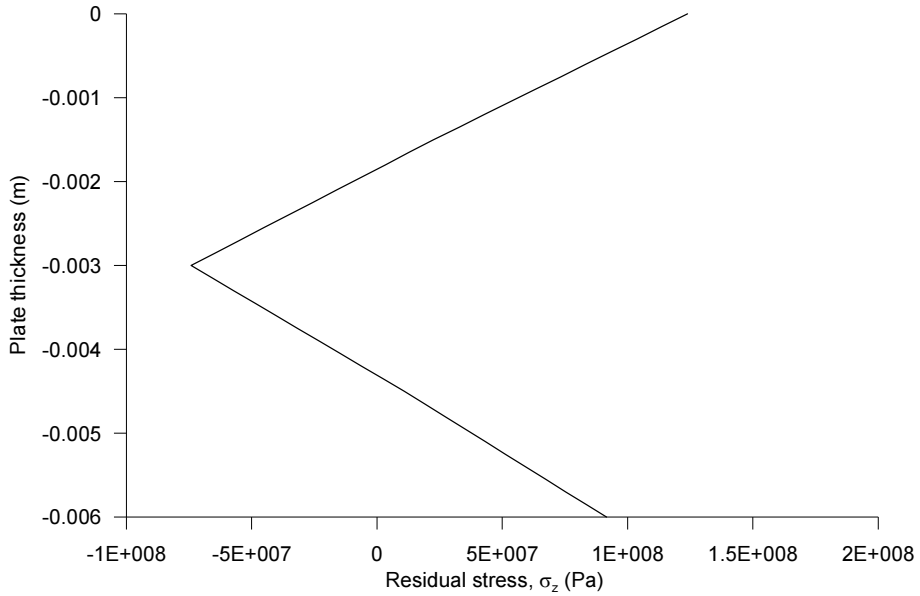

Figure 4.20 Residual stress distributions through the plate thickness. Case 1.

4.5.1.3 Plastic strain responses

Plastic strain responses of the plate are presented in Figures 4.21 to 4.24. Plastic strains shown in the figures are Z-component, ε_z. Positive values of the strains represent tensile strains, and negative values compressive strains. The plates not colored are the original work-piece.

Figure 4.21 shows the plastic strain distributions on the plate surfaces at selected times: t = 2.0 sec when the heating is at the beginning stage (a), t = 16.0 sec when the laser beam is passing the center of the plate (b), and t = 200 sec when the process is finished. The figures show the occurrence of local compressive strains along the heated region during the cool-down phase. The region near the end of the plate remains under tensile strains due to less cooling effect. The peak compressive and tensile strains are equal at approximately 0.004.

Figure 4.22 shows the plastic strain distributions through the plate thickness direction at t = 16.0 sec that are captured on the X-Y plane (a) and on the Y-Z plane (b). It can be seen from Figure 4.22 (a) that as soon as the laser beam passed away, the top (heated) surface experiences the a maximum compressive strains due to contraction and the bottom surface undergoes the tensile strains due to expansion. From Figure 4.22 (b), the plate strains are shown with the plate thickening produced by local heating.

Figure 4.23 shows the plastic strain histories at the central points of the plate. At t = 14.5 sec when the laser beam reaches near the center, tensile strain arises slightly at the top point due to thermal expansion, and the strain changes instantly to compressive strain and has a maximum value of 0.004 at t = 17.0 sec which is maintained until the end of the process. Due to the time taken for heat transfer through the plate thickness, tensile strain at the bottom point initiates at a little bit delayed time (t = 15.0 sec) and is maximized to approximately 0.0004 at t = 17.0 sec after which the tensile stress remains unchanged into compressive stress due to lower cooling effect. Figure 4.24 presents the residual strains along the thickness at the plate center.

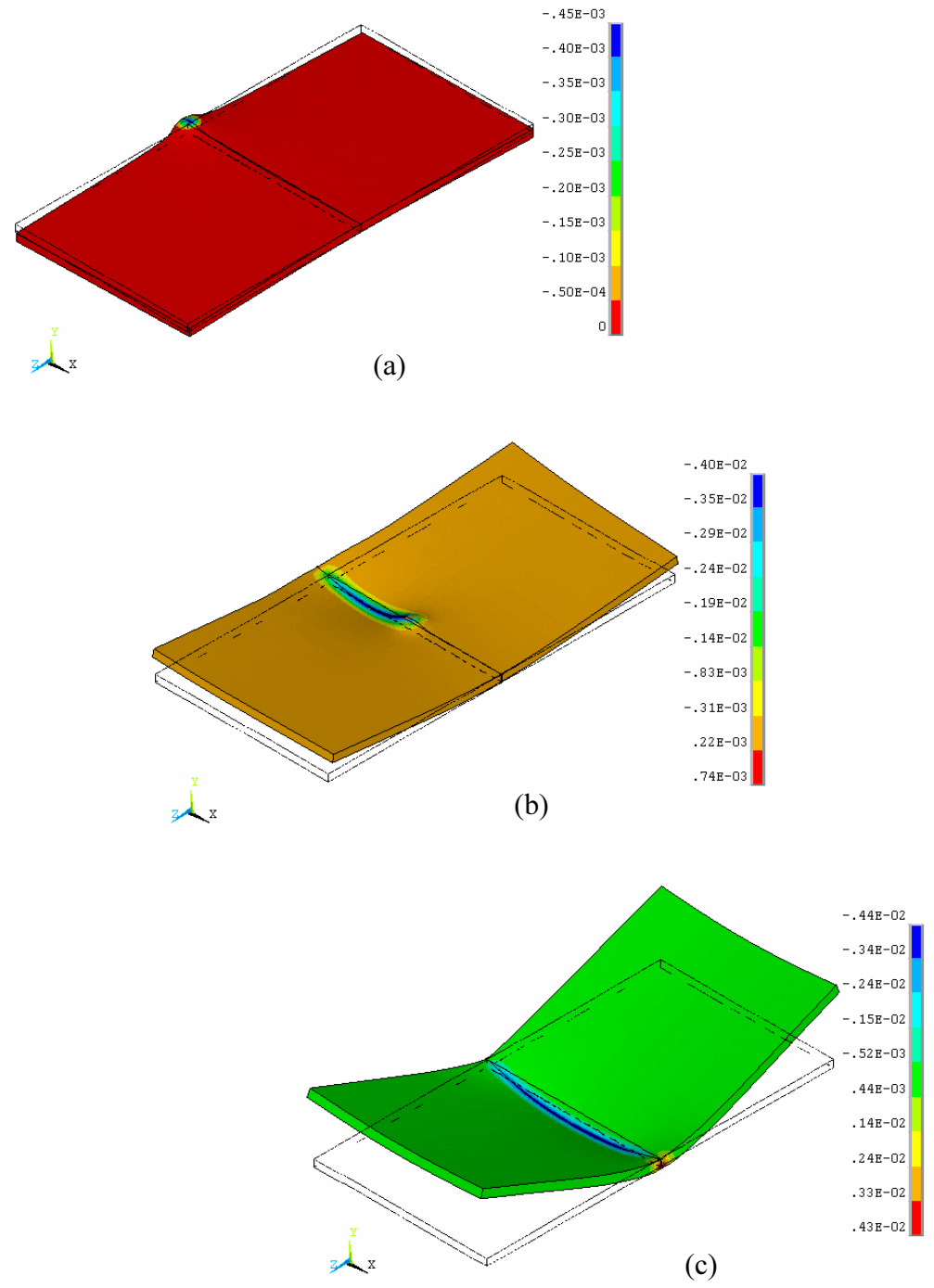

Figure 4.21 Distributions of plastic strain, ε_z at: (a) 2 sec; (b) 16 sec; and (c) 200 sec. Deformations are magnified X100 for clarity. Case 1.

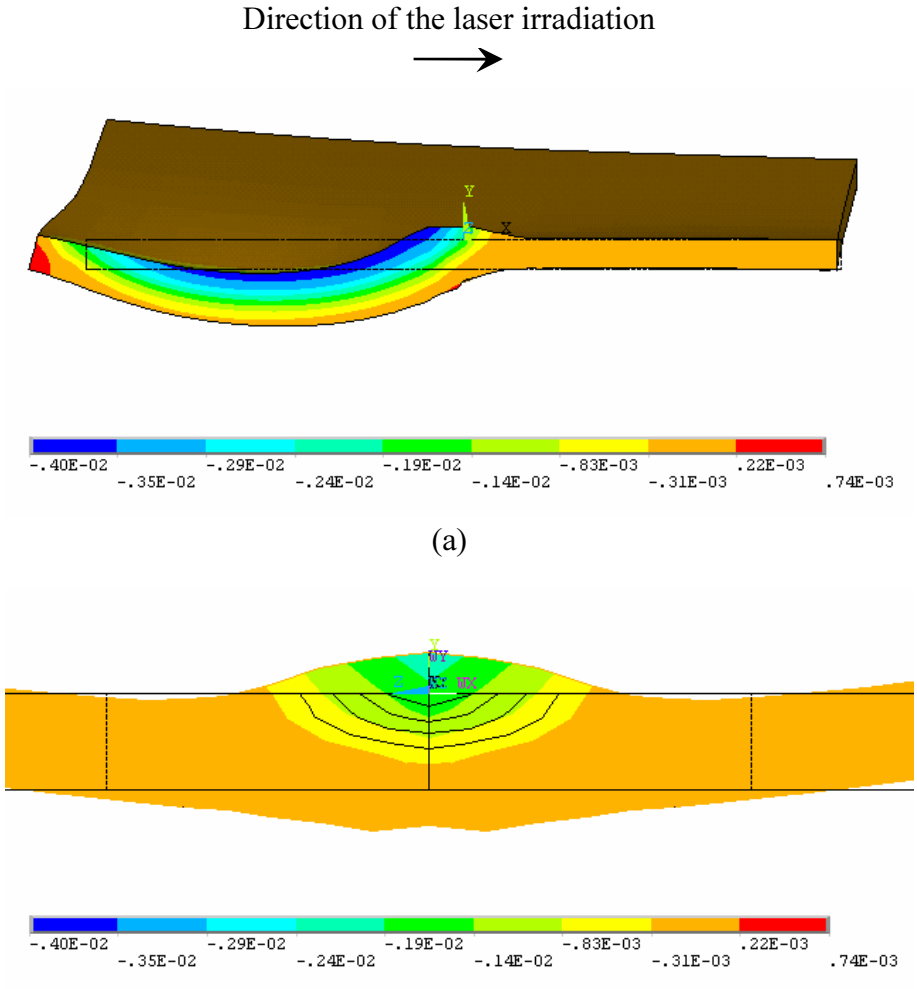

Figure 4.22 Plastic strain, ε_z, distributions at 16 sec: (a) left side view; and (b) front side view. Deformations are magnified X100 for clarity. Case 1.

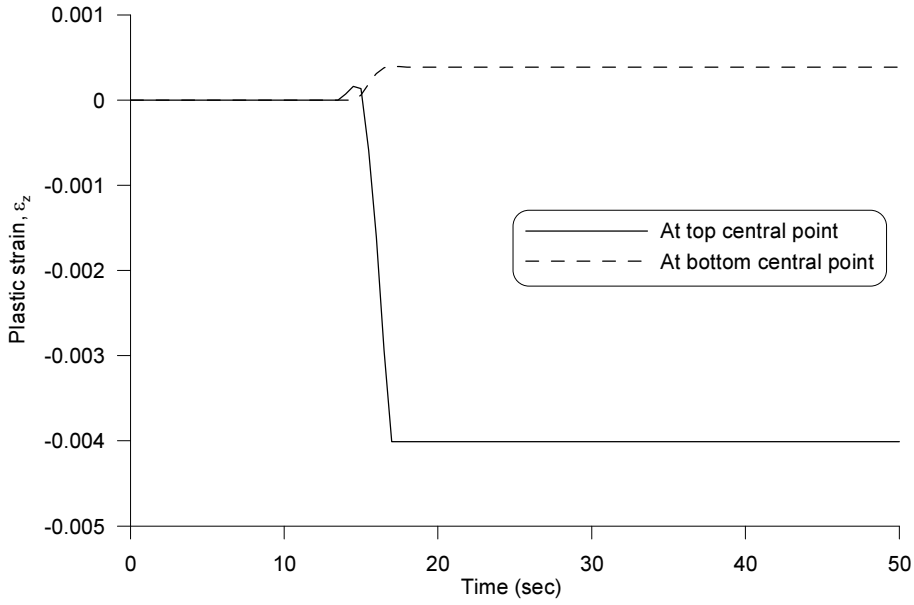

Figure 4.23 Plastic strain histories, ε_z. Case 1.

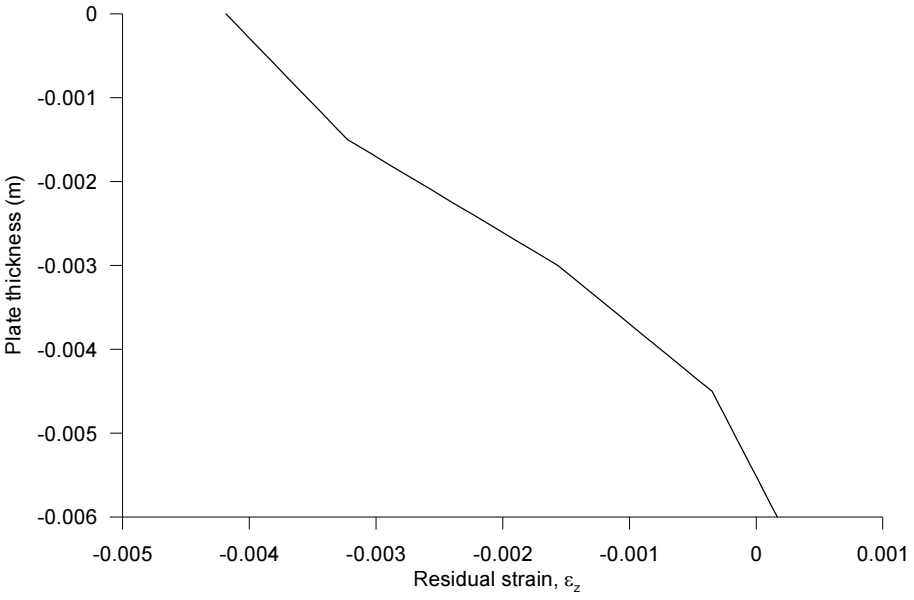

Figure 4.24 Residual plastic strain distributions through the plate thickness. Case 1.

4.5.1.4 Displacement responses

Displacement responses of the plate are illustrated in Figures 4.25 to 4.27. Changes in displacement in the Y-direction along the X-axis are shown in Figure 4.25. In the simulation, a bow-like deformation was produced along the plate centerline. A plate thickening of 2.6 x 10^{-5} *m* occurred near the center of the plate, and there was no distinctive thickening at the regions near the ends of the plate. Some uneven changes near the plate center are attributed to restriction by surrounding material to thermal expansion.

Figure 4.26 presents the bend angle history. The angle is the one measured against line $\overline{OA}$ (See Figure 4.1), which is calculated from the measurements of the displacements of points A and O in the Y- and Z-directions:

$$\alpha = 2\tan^{-1}\left(\frac{y_A - y_O}{z_A - z_O}\right)$$

where:

α = bend angle

y_A and y_O = displacements in the Y-direction at points A and O, respectively.

z_A and z_O = displacements in the Z-direction at points A and O, respectively.

A small counter-bending occurred until t = 7.0 sec, and a permanent bend angle of 0.47° was obtained at t = 33.0 sec. Final deformation achieved from the process is presented in Figure 4.27.

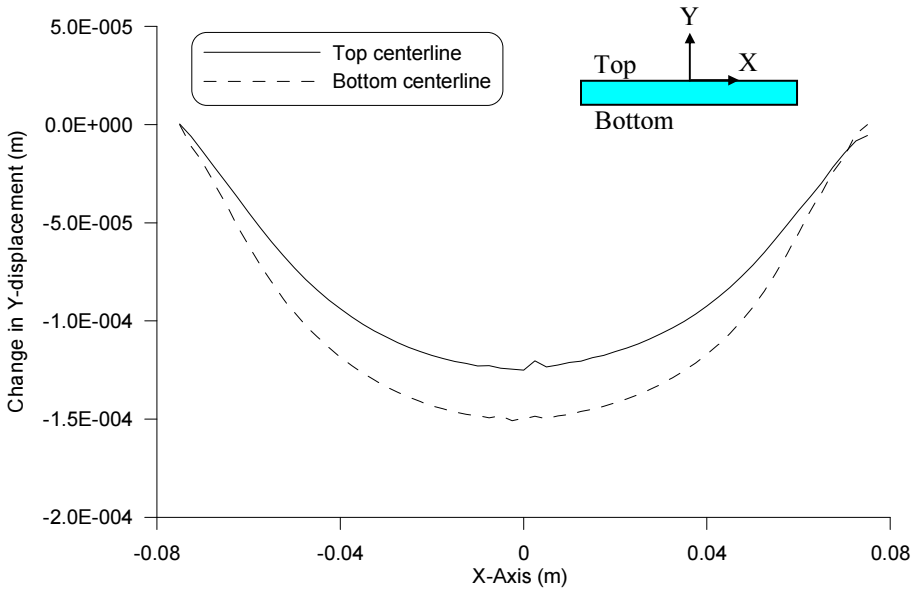

Figure 4.25 Changes in Y-displacements at top and bottom centerlines. Case 1.

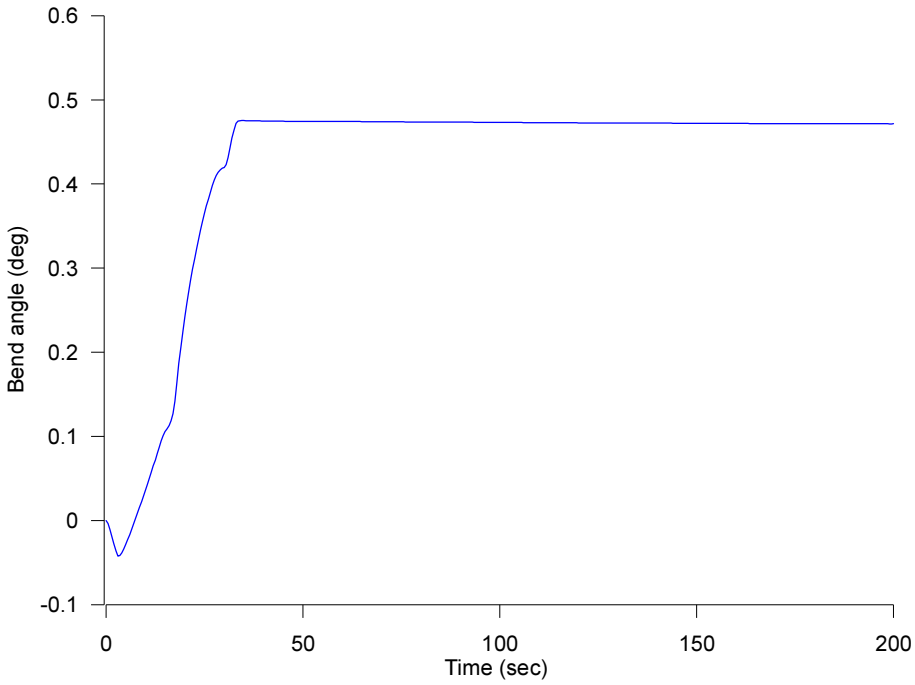

Figure 4.26 Bend angle history. Case 1.

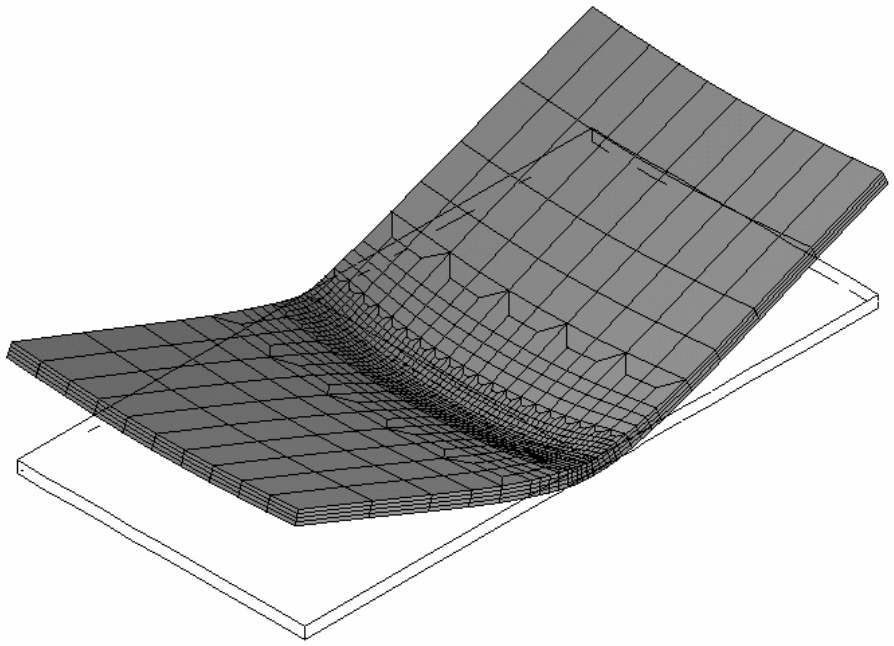

Figure 4.27 Final deformations. Deformations are magnified X100 for clarity. Case 1.

4.5.2 Simulation results – Case 2

In simulation of Case 2, the plate was subjected to a higher laser power of 3000 watts and a faster feed rate of 10 mm/s than Case 1. The beam diameter was kept constant with 16 mm. The plate thickness changed to 4 mm from 6 mm. The time taken to heat the plate was 16 seconds in this test. After heating, the plate was cooled down for 84 seconds.

Results of the simulation are presented in Figures 4.28 to 4.33. As can be seen in the figures, temperature, stress, plastic strain and displacement distributions have the same pattern as that of Case 1 results. A maximum plate temperature of 844 °C arose during the process (Figure 4.28). When the laser beam is passing the plate center (at t = 9.25 sec), a high tensile stress of 63 MPa was induced at the top surface and a maximum compressive stress of 232 MPa at the bottom of the plate to generate a angular change (Figure 4.29). A compressive plastic strain of 0.0087 and a tensile plastic strain of 0.00014 remain at the top and bottom central points, respectively (Figure 4.30). The plate was thickened by approximately 3.7 x 10^{-5} m along the band for $x = \pm$ 0.04 m (Figure 4.31). A final bend angle of 1.32° was achieved at t = 20 sec (Figure 4.32). Figure 4.33 presents the deformations at selected times: t = 8 sec (a), t = 50 sec, and t = 100 sec when the process was completed.

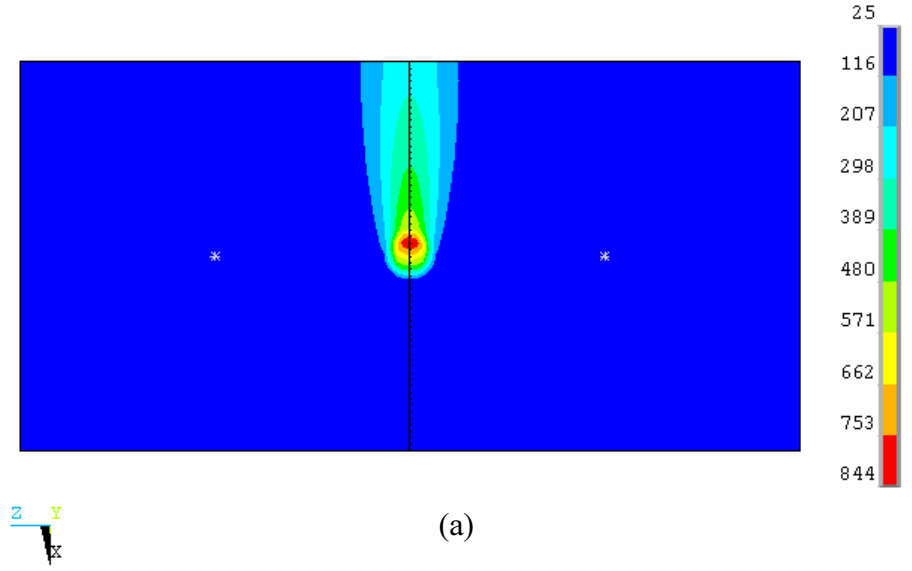

(a)

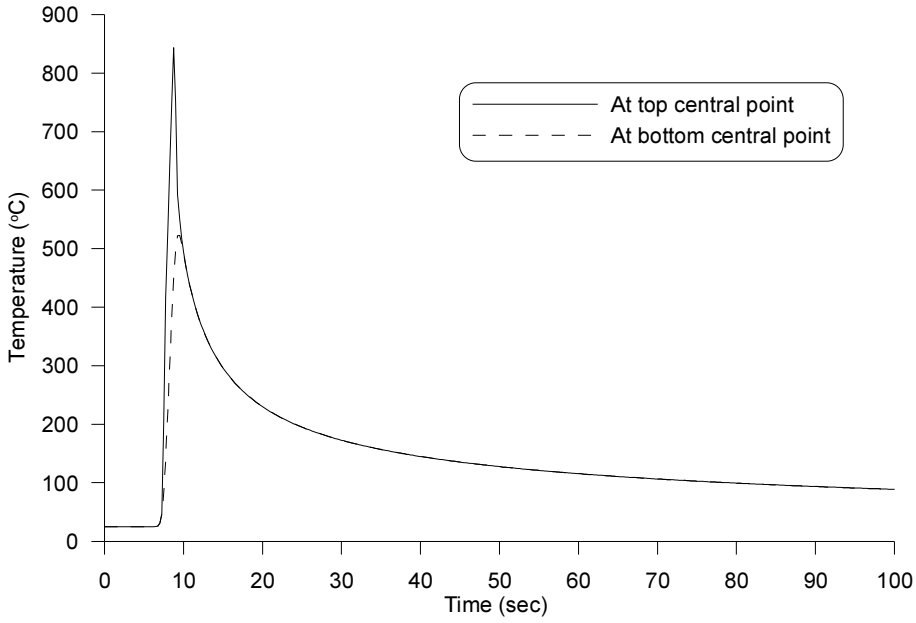

(b)

Figure 4.28 Temperature results: (a) temperature distributions at 8 sec; (b) temperature histories at the center of the plate. Case 2.

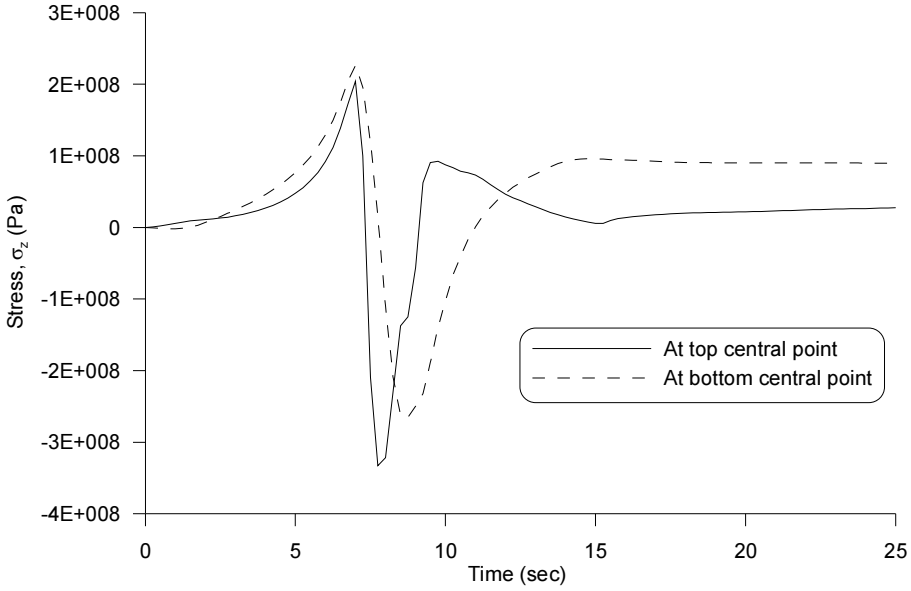

Figure 4.29 Plate stress histories, σ_z at the center of the plate. Case 2.

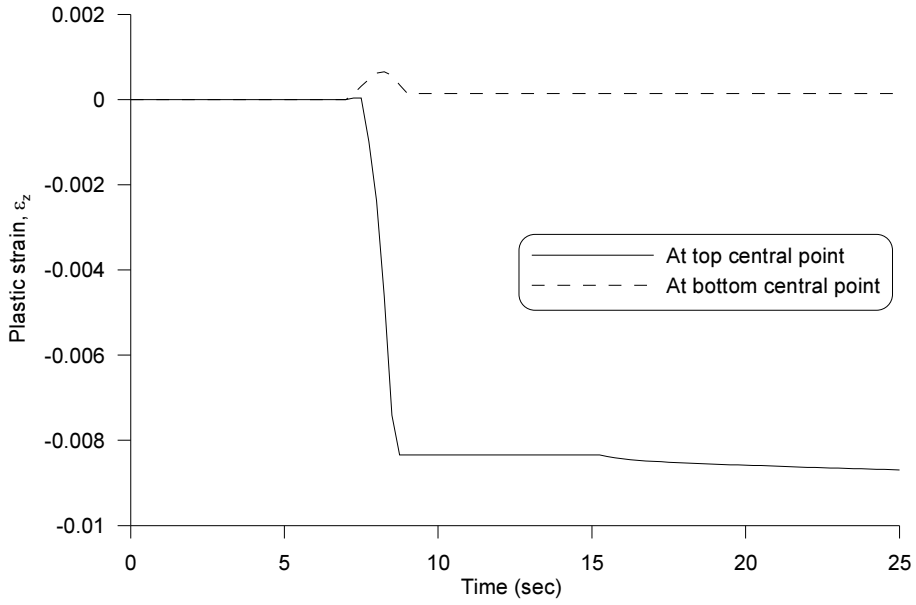

Figure 4.30 Plastic strain, ε_z histories at the center of the plate. Case 2.

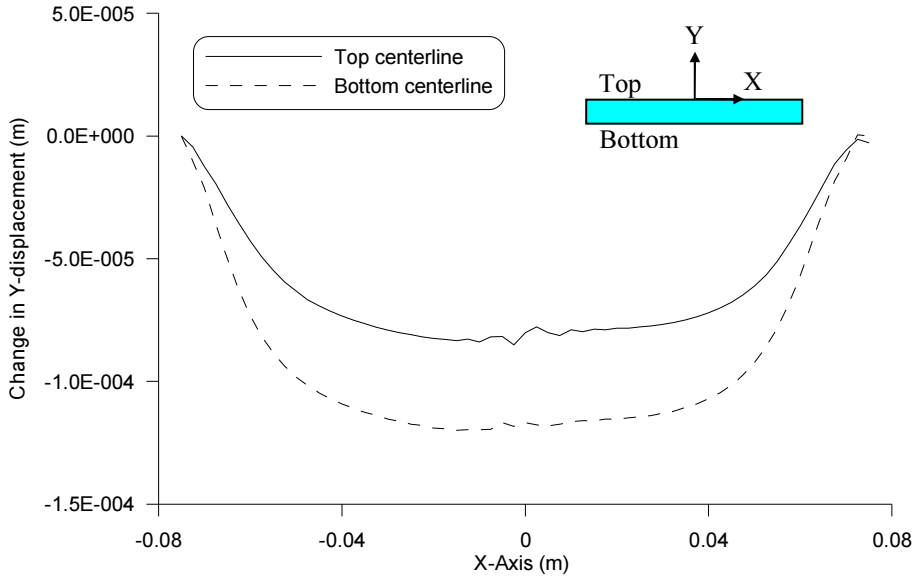

Figure 4.31 Changes in Y-displacements at the top and bottom centerlines. Case 2.

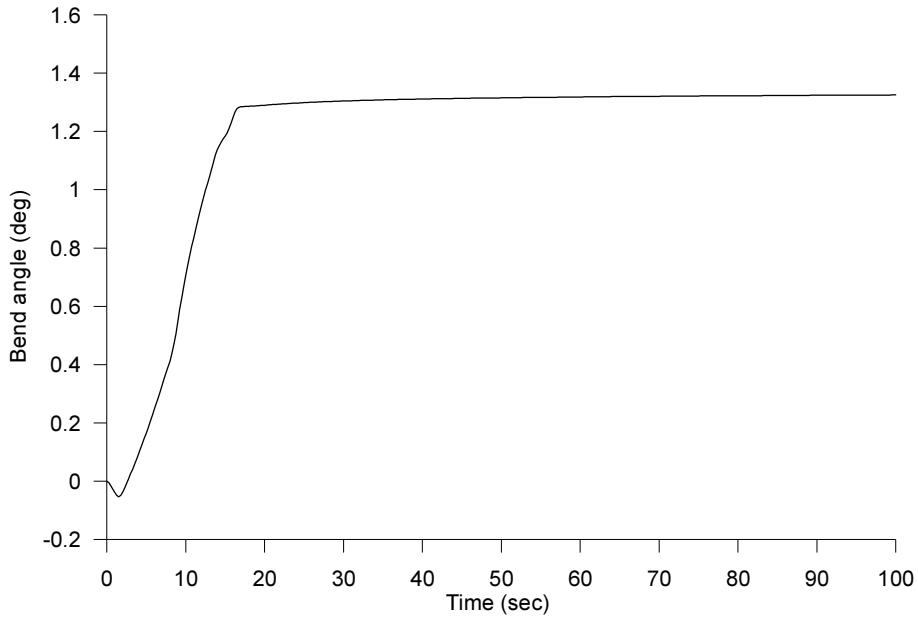

Figure 4.32 Bend angle history. Case 2.

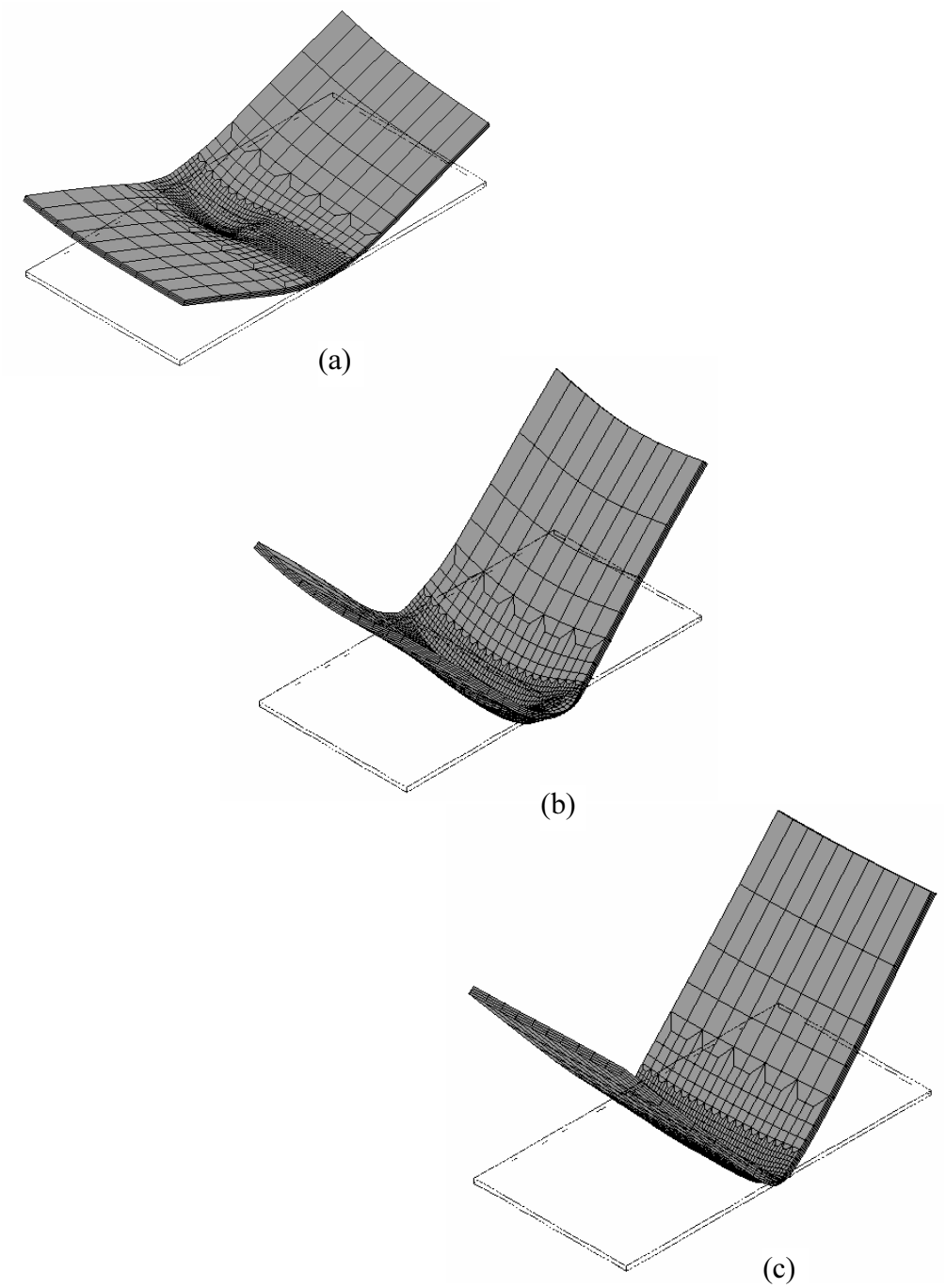

Figure 4.33 Deformations at: (a) 8 sec; (b) 50 sec; and (c) 100 sec. Deformations are magnified X100 for clarity. Case 2.

4.5.3 Comparison of bend angles with published results

The bend angle responses obtained from Cases 1 and 2 are compared with published experimental and numerical data for validation of the current finite element simulation method.

The results from investigations on the laser forming of metallic plates by Kyrsanidi et al. [63] are used for this comparison. They conducted an experimental study on one-edge-clamped plates irradiated by a CO_2 laser with a maximum laser power of 3 kW for evaluating both the influence of the variation of each laser parameter on the forming process and the capability of the algorithm the laser forming simulation they proposed. The material used in the experiment was the ship-building steel 1.0584 (D36). The dimensions of the plates were 300 x 150 mm with a thickness of 4 and 6 mm. For the measurement of the distortion of the plates during the laser forming process, a linear variable displacement transducer was used and the displacement of the plate was monitored. A series of experiments were carried out with a variety of values of the laser parameters such as laser power, scanning speed and beam diameter. Figure 4.34 shows part of the characteristic experimental results of the angular distortion obtained during the laser forming process and the computed results.

The bend angle histories of Case 1 and Case 2 shown in Figure 4.26 and Figure 4.32, respectively, are compared with the reference data in Figure 4.34. From the figures, it is found that the bend angles achieved from the current simulations are equal to those from the experimental data: 0.47° for Case 1 and 1.32° for Case 2. It is also noted that material behaviors in the two numerical cases are similar to those from the reference data in that the counter-bending arise in the early stage of the processes, and the times taken to reach the final bend angles are almost equal as 33 sec for Case 1 and 20 sec for Case 2. The comparisons show that the current simulation results are in good correlation with the results from the experimental results.

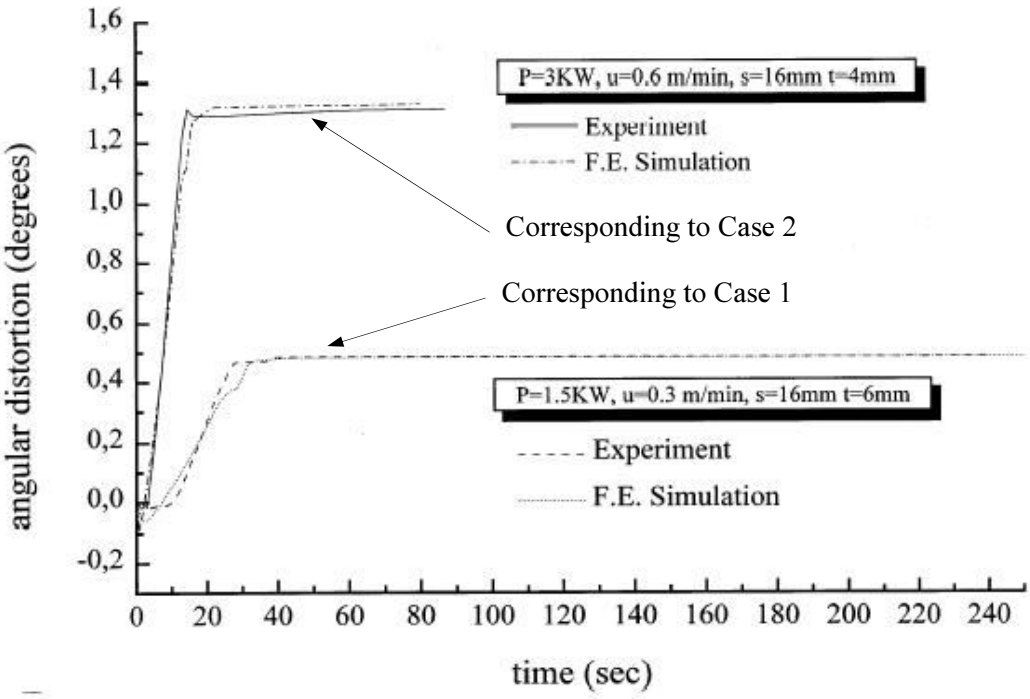

Figure 4.34 Bend angle histories from experiments and simulations. Reproduced from [63].

4.5.4 Simulation results – Case 3

In simulation of Case 3, the plate was subjected to a series of three irradiations with the same laser parameters as Case 1: a laser power of 1500 watts; a feed rate of 5 mm/s; and a beam diameter of 16 mm. The plate thickness was 6 mm. At the first two stages of the operation, heating and cooling times were 32 sec and 93 sec, respectively. At the final stage, the same heating time of 32 sec was applied, but the cooling time changed to 218 sec to promote a complete deformation. The first and last heating started at point 1 and the second at point 2 (See Figure 4.1).

Temperature and displacement results of the test are presented in Figures 4.35 to 4.41. Figure 4.35 shows temperature distributions in the plate at three selected times. The maximum temperatures occurred are 796 °C at stage 2 and 837 °C at stage 3, which are comparable to 728 °C at stage 1 due to incomplete cooling from the previous stage. Figure 4.36 shows temperature histories at the central top and bottom points of the plate. Similar patterns to the results of Case 1 are noticed at each stage, that is, rapid rise during heating and smooth decay during cooling. The plate temperature was 100 °C after completing the operation (at t = 500 sec). Corresponding stress distributions to the temperature distributions are presented in Figure 4.37. The residual stresses at the top and bottom surfaces increased at stages 2 and 3. As shown in Figure 4.38, the compressive plastic strains produced at the top surface were 0.0040 at stage 1, 0.0086 at stage 2, and 0.0134 at the final stage. The relatively small tensile plastic strains arose at the bottom surface, and were kept constant as 3.88×10^{-4} after t = 17.5 sec. The plate thickness increased by a maximum of 6.4×10^{-5} m (1.07 %) near the plate center (Figure 4.39). Bend angle history is presented in Figure 4.40. The bend angle obtained after each stage were 0.48° for stage 1, 0.88° for stage 2, and 1.33° for stage 3. The final V-shaped deformation is presented in Figure 4.41.

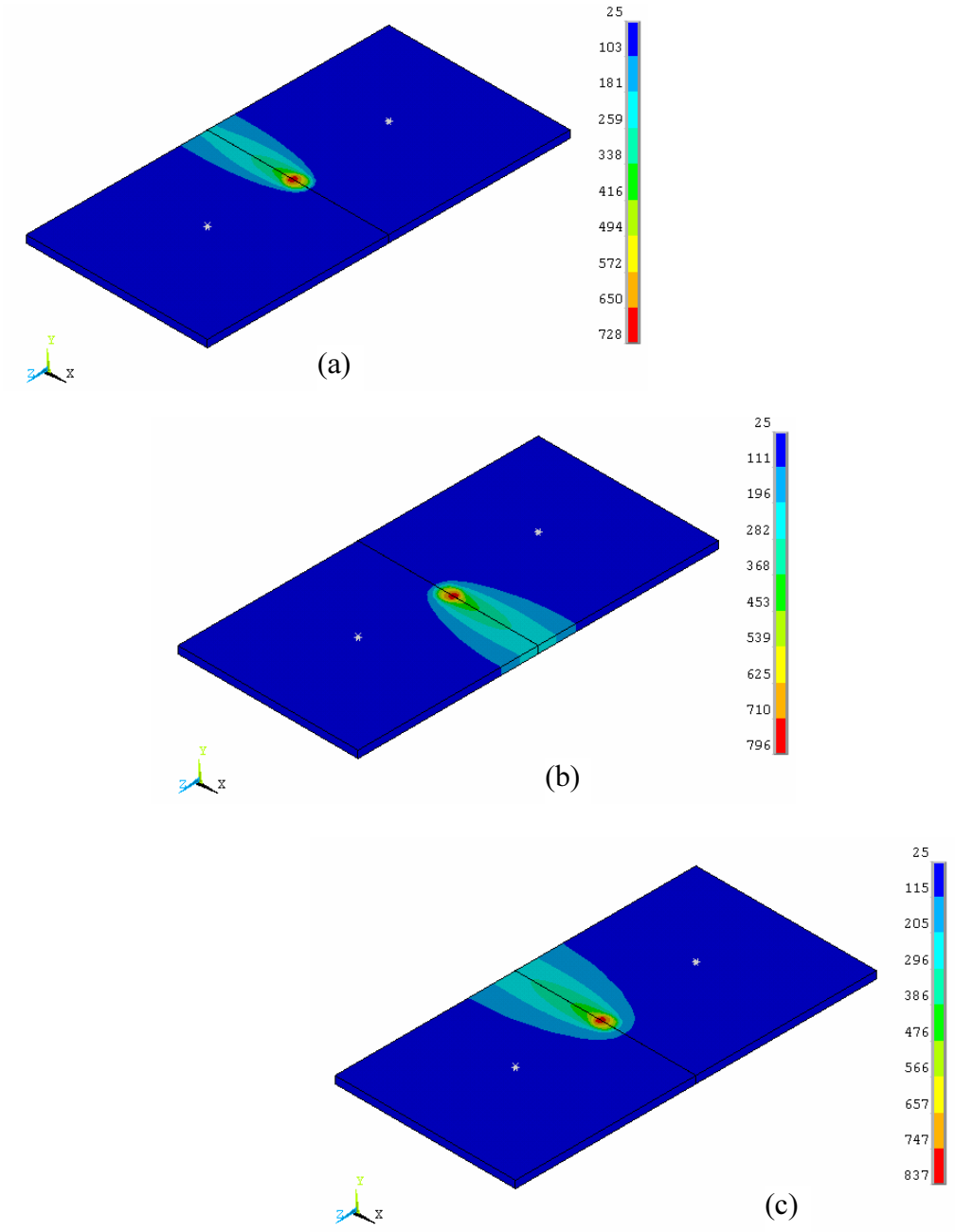

Figure 4.35 Temperature distributions at: (a) 16 sec during stage 1; (b) 141 sec during stage 2; and (c) 266 sec during stage 3. Case 3.

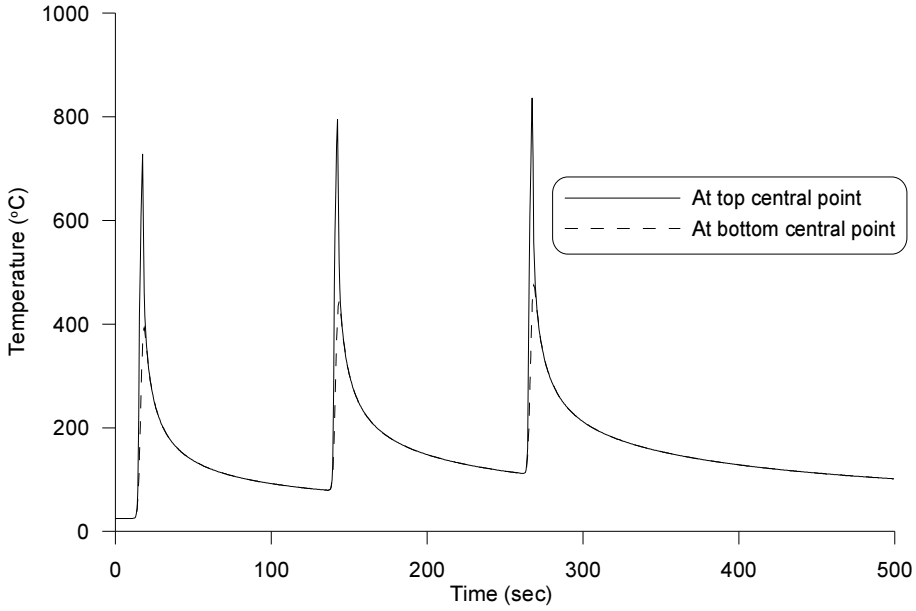

Figure 4.36 Temperature histories at the center of the plate. Case 3.

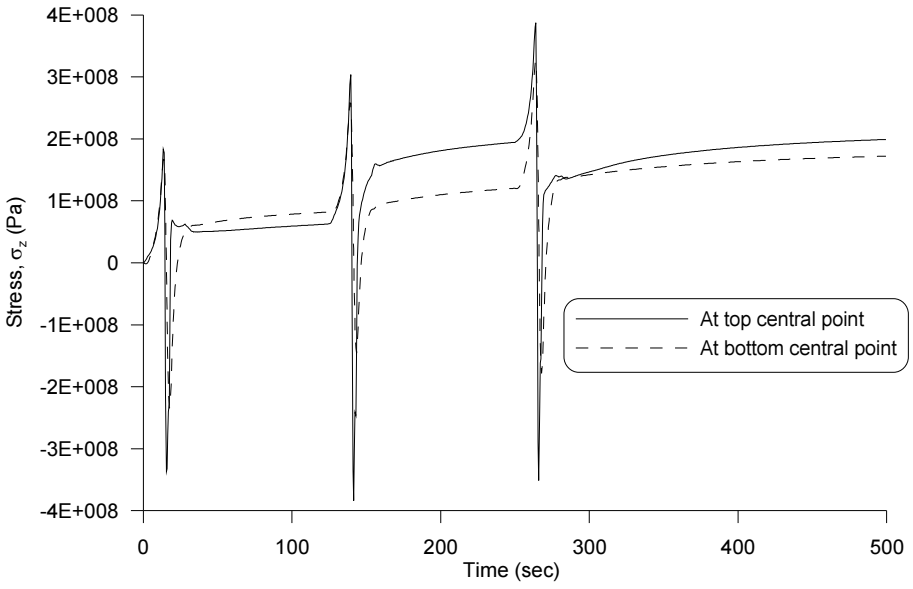

Figure 4.37 Stress, σ_z histories at the center of the plate. Case 3.

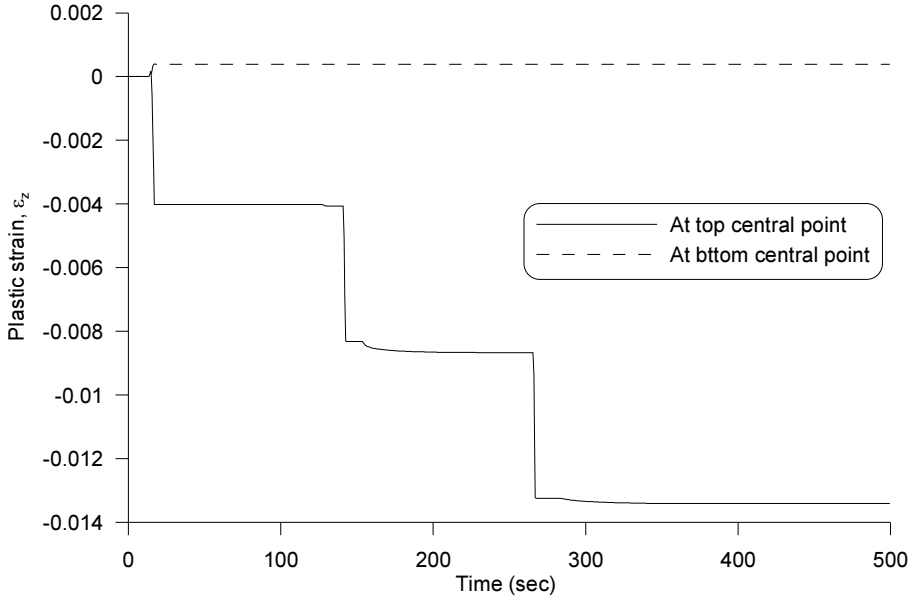

Figure 4.38 Plastic strain, ε_z histories at the center of the plate. Case 3.

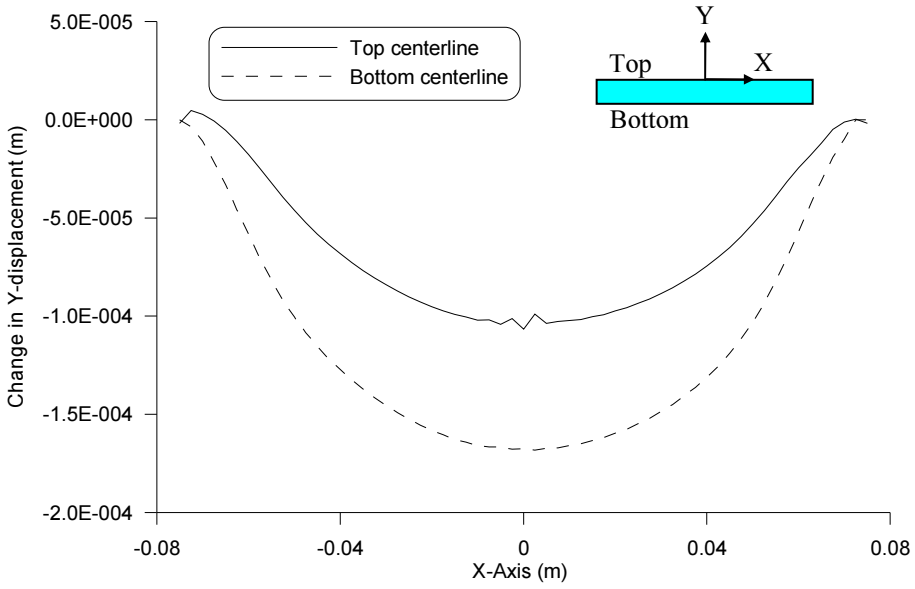

Figure 4.39 Changes in Y-displacements at the top and bottom centerlines. Case 3.

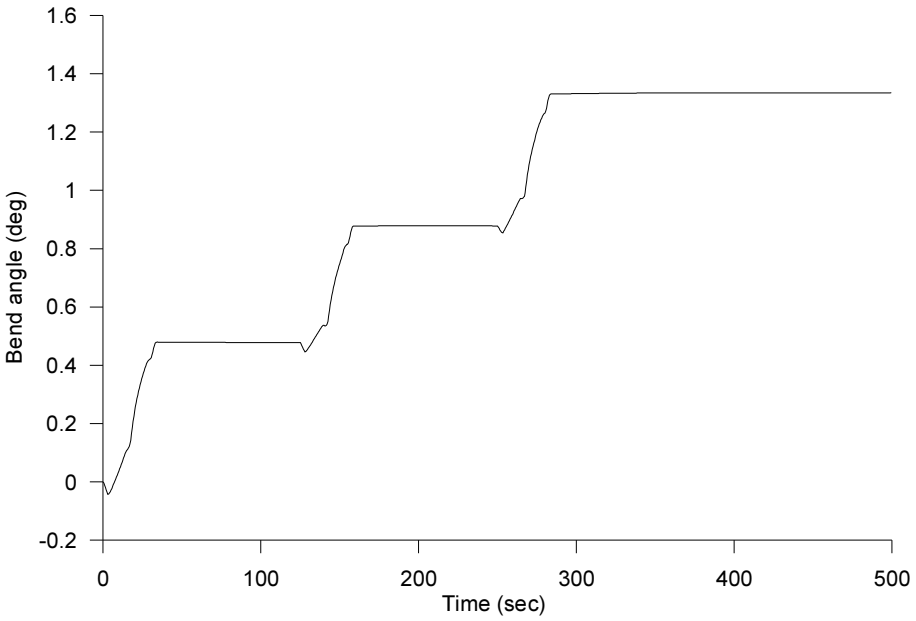

Figure 4.40 Bend angle history. Case 3.

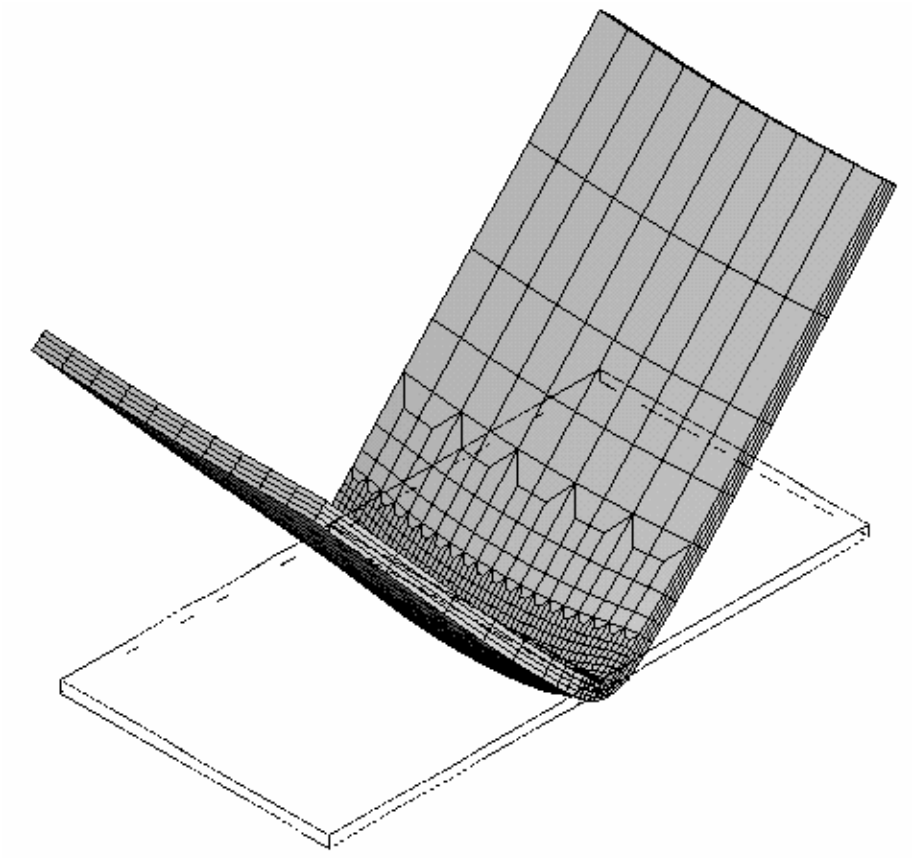

Figure 4.41 Final deformations. Deformations are magnified X100 for clarity. Case 3.

4.6 Summary

This chapter has described the development of the finite element model for the straight-line laser forming process. The numerical simulations investigated the thermal and structural responses of the plate. Two bend angle histories obtained from the simulations are compared to the experimental results reported by Kyrsanidi et al. [63] for validating the capability of the current computational model. The key points of this chapter have included:

- The process adopted for the investigation via the numerical method was the straight-line heating process in which a carbon-manganese steel DIN 1.0584 plate undergoes irradiation over its surface along the centerline of the plate and produces an angular deflection.

- In order to calculate plate temperatures, a nonlinear transient three-dimensional heat transfer finite element model for the process was developed, which accounts for temperature dependent material properties (i.e., thermal conductivity and specific heat). Assumptions included symmetry along the centerline of the plate. A brick element with eight nodes was used. A non-uniform mesh pattern was generated in order to increase simulation accuracy and to reduce computation time. A mean thermal flux density was calculated to impose as the incident surface heat flux. Adiabatic, convection and radiation boundary conditions were applied.

- A rate dependent, three-dimensional deformation model was made to obtain plate displacements, stresses and plastic strains, which considered the elastic, thermal, and plastic strains. The thermal strain model incorporated both the temperature dependent coefficient of thermal expansion and temperature distributions obtained from the thermal analysis. For the plasticity model, the *Von Mises* yield criterion,

the *associative flow rule*, and the *isotropic hardening rule* were employed.

- A series of three simulations were carried out with different process conditions. Results of temperatures, stresses, plastic strains, and displacements were presented and discussed. A bend angle of 0.47° was obtained from Case 1, 1.32° from Case 2, and 1.33° from Case 3.

- For validation of the capability of the proposed finite element simulation method, the bend angle responses obtained from Cases 1 and 2 are compared with published data [63]. It is found that the bend angles achieved from the current simulations are equal to those from the experimental reference data: 0.47° for Case 1 and 1.32° for Case 2. It is also noted that material behaviors in the two numerical cases are similar to those from the reference data in that the counter-bending arise in the early stage of the processes, and the times taken to reach the final bend angles are almost equal as 33 sec for Case 1 and 20 sec for Case 2. The comparisons show that the current simulation results are in good correlation with the results from the experimental results.

Chapter 5

Simulation of Circle-Line Heating

5.1 Introduction

Most of the research on laser forming has concentrated on the straight-line heating process (demonstrated in Chapter 4), the simplest laser forming process by which V-shaped parts are produced. Nevertheless, it is suggested that laser forming is a process capable of producing complex shapes such as sine, dish, saddle, pillow, cone and screw shapes [2, 27]. Magee and Watkins [27] produced a dish-shaped geometry from a flat circular metal sheet applying irradiations along circle lines to the surface of the plate. However, they could not measure the radial waviness of the formed part via experiments. Hennige [26] proposed the quality of spatially curved parts produced by the laser forming process could be identified via finite element simulation.

This chapter contributes to the investigation of the thermal and structural responses of a circular plate during a circle-line laser forming strategy via the three-dimensional finite element simulation. It presents a brief description of the process investigated in this study. The numerical modeling is focused on the mesh generation and the laser beam moving scheme along a circle pattern because the thermal and deformation models defined for the straight-line analysis in Chapter 4 are reused in this simulation. Temperatures and displacements are obtained as simulation results. The emphasis in this chapter is on the characterization of the quality of the deformed geometry through the

investigation of the radial and circumferential waviness. The simulation results are validated with the aid of other verification techniques, rather than a testing program.

5.2 Process Description

Figure 5.1 (a) shows the schematic of the circle-line heating process used for the present simulation. The heating strategy was experimentally investigated by a research group [27] to produce a bowl-shape. However, the quality of the shape obtained could not be fully described due to the difficulty of the measurement of micro-size displacement. In this simulation, a smaller carbon-manganese (DIN 1.0584, D36) circular plate than a mild steel plate used in their experiment is employed. Other process parameters are reduced in a similar rate compared to the experimental data.

The plate undergoes a localized heating by a laser source along a circle line that has a constant distance of 22 mm from the plate center. The incident surface heat flux is conducted through the surrounding material and also transferred to the surroundings by convection and radiation. The dimensions of the plate are 80 mm in diameter. Due to the strong influence of the geometrical induced strain hindrance on the forming result in the circle-line heating process, the degree of the bend angle is degressive compared to the straight-line heating process [26]. Thus, in order to obtain a distinctive forming result in this simulation, the plate with a thickness of 1 mm, instead of 4 or 6 mm used in the straight line irradiation process in Chapter 4, is employed. The plate has a concentric circular hole of 4 mm diameter at its center to hold it by a clamping screw.

The laser parameters used in this analysis are: a laser power of 300 watts; a beam diameter of 12 mm; and a feed rate of 10 mm/s. The absorption coefficient used is 0.75 which value can be obtained using graphite coating in experiment [41]. In order to investigate the effect of the number of heating passes on uniformity of the deformed geometry, a series of four irradiations are

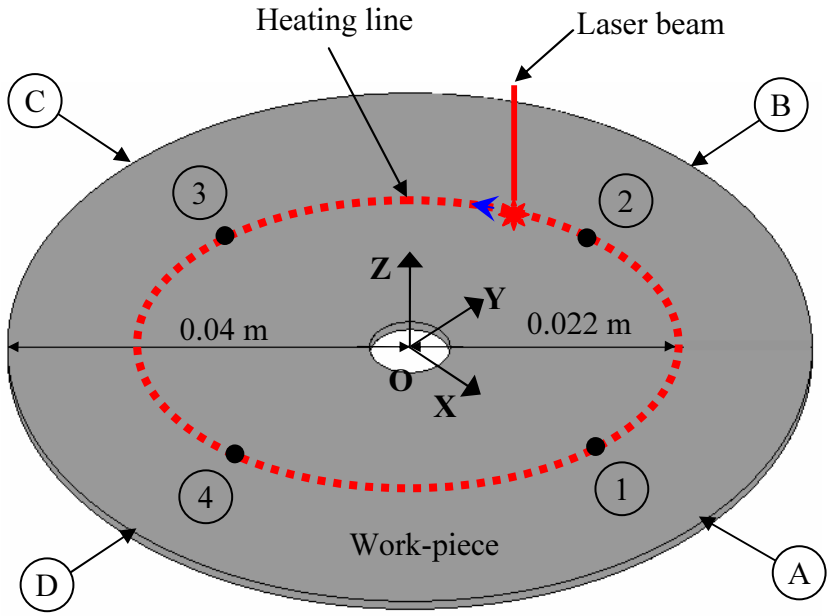

(a)

	Heating phase	Cooling phase
Stage 1	1 → 2 → 3 → 4 → 1 (0) (3.46) (6.91) (10.37) (13.82)	→ E (43.20)
Stage 2	3 → 4 → 1 → 2 → 3 (43.20) (46.65) (50.11) (53.56) (57.02)	→ E (86.40)
Stage 3	2 → 3 → 4 → 1 → 2 (86.40) (89.85) (93.31) (96.76) (100.22)	→ E (129.59)
Stage 4	4 → 1 → 2 → 3 → 4 (129.59) (133.05) (136.50) (139.96) (143.42)	→ E (172.61)

Note: ( ) indicates the times (sec) when the laser beam is passing the points or when the stages are finished.

(b)

Figure 5.1 Schematic diagram of the circle-line heating process (a); and processing stages (b).

applied to the surface of the plate according to the stages shown in Figure 5.1 (b). At stage 1, the laser beam starts at point 1 and rotates anticlockwise along the scanning path. The irradiation ceases when the laser beam returns to the starting point. Thus, it takes 13.82 sec to heat the plate. After heating, the plate experiences a cooling for about 30 sec. The heating starts at point 3 at the next stage, at point 2 at stage 3, and at point 4 at stage 4. The heating and cooling times at each stage are equal to that of stage 1. The total processing time taken is therefore 172.6 sec.

The Z-component of displacement is measured at the top edge of the circular plate in a way to identify circumferential waviness. The magnitudes of the deformation along the four lines (i.e., OA, OB, OC, and OD) are taken for the characterization of radial waviness.

5.3 Finite Element Model

For simulation of the circle-line laser forming process, the heat transfer and structural finite element models are defined using the finite element analysis code ANSYS in the same manner as the models built for the straight-line laser forming in Chapter 4. The ANSYS program listing is given in Appendix C. Due to the circular geometry, a couple of adaptations are made in this modeling as follows:

- The simulation is conducted in a full circular geometry model.
- Uniform three-dimensional meshes are generated in the circular plate with the aid of a particular element called Mesh200.
- The strategy of moving the laser beam in a circular motion is devised.
- A new boundary condition is set up for structural analysis.

In order to build uniform three-dimensional meshes in the circular plate, a quadrilateral “mesh-only” element (i.e., Mesh200) with four nodes is used

which has no degree of freedom and material properties and contributes nothing to the solution. The meshes are generated in the following three steps:

(a) A solid model of rectangular section of the circular plate is produced.

(b) The section area is meshed with the MESH200 element with four nodes.

(c) The volume elements are created with the SOLID70 element by rotating the meshed area.

Upon completing the revolution, the seed meshes have to be deleted to avoid error messages during the simulation. Figure 5.2 displays the mesh pattern created in conjunction with the 3-D thermal element (SOLID70). The meshes consist of a total number of 8400 nodes and 6400 elements (i.e., 80 elements in the circumferential direction, 20 elements in the radial direction, and 4 elements through the plate thickness).

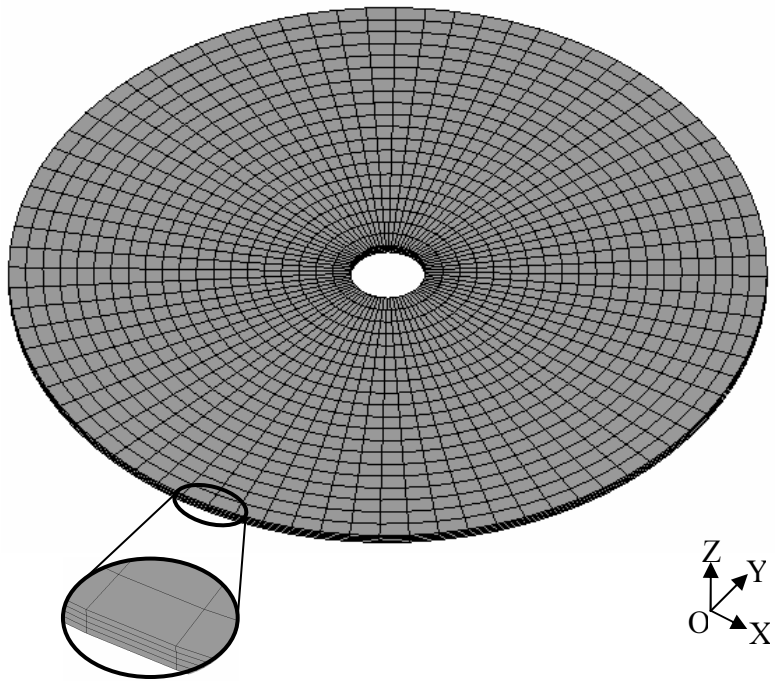

Figure 5.2 Uniform meshes in the circular plate.

The moving effect of the laser beam is accomplished introducing the local coordinates (LC) in a way to designate the heating locations as shown in Figure 5.3. For example, the origin of LC 1 is first generated on point 1, and the heating is conducted for a certain amount of time by the laser beam with the center located on the origin of LC 1. Then, a new local coordinate LC 2 is generated at point 1 to guide the laser beam with origin determined in quadrant I as follows:

$$x' = RS \text{ x } \cos(\theta \text{ x } i) \tag{5.1 a}$$

$$y' = RS \text{ x } \sin(\theta \text{ x } i) \tag{5.1 b}$$

where:

x' = the coordinate on X-axis

y' = the coordinate on Y-axis

RS = the radius of the scanning path

$\theta = (360 / n_s)$ x $(\pi/180)$, n_s is the number of sub-steps of heating.

In order to apply the identical heat density at point 1, the LC 2 should have an orientation angle θ, which can be implemented rotating the LC about Z-axis via *THXY* parameter in LOCAL command. In this simulation, a total number of 80 LCs are created to complete the heating at each stage. i is used to automatically calculate the origins of the LCs, which value may be provided by *Do command according to the defined sub-steps of heating. The rest of the origins of the LCs in quadrants II, III, and IV are calculated in the same manner as in quadrant I.

As a boundary condition for the structural analysis, displacements at the surface of the hole are constrained in the X, Y, and Z-directions in a way to remove the rigid body motion.

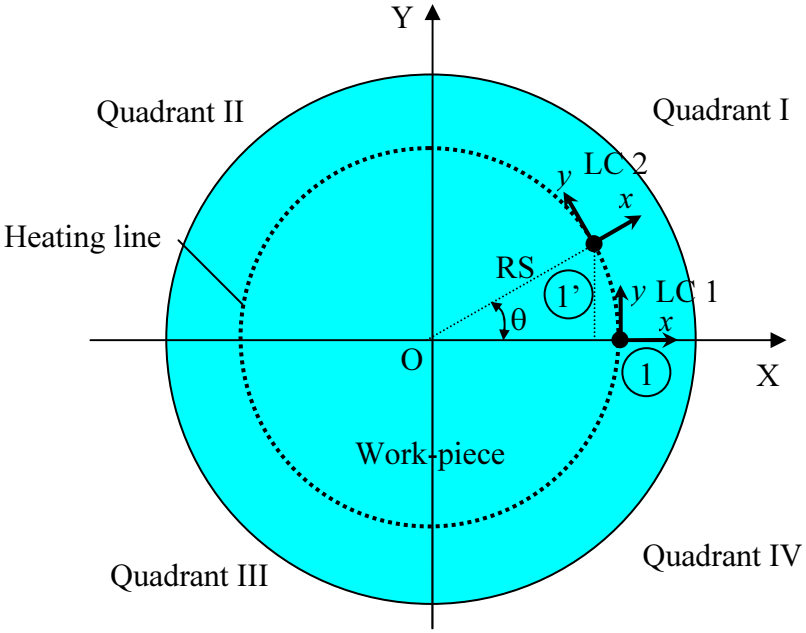

Figure 5.3 Generation of local coordinates.

5.4 Simulation Results

Simulation results of the thermal analysis of the circle-line heating process are presented in Figures 5.4 to 5.8. Temperature distributions on the top surface of the plate produced at stages 1 to 4 are illustrated in Figures 5.4 to 5.7, respectively, at selected times (See Figure 5.1 (b) for each heating position at the selected times). From the figures, it can be seen that the maximum temperatures during the heating phases take place in the rear of the laser beam. It is also noted that the input heat flux is rapidly conducted through the surrounding material. The maximum temperatures reached at each heating stage and the temperature ranges at the end of each stage are listed in Table 5.1.

Table 5.1 Temperatures during heating and after operations.

	Maximum temperature during heating (°C)	Temperature range after operation (°C)
Stage 1	432	124 – 136
Stage 2	527	208 – 219
Stage 3	605	273 – 286
Stage 4	661	326 – 337

As can be seen in Table 5.1, the relatively small temperature differences in the plate at the end of each stage mean we can neglect the temperature effect when the waviness of the deformed part is examined, which may be confirmed with displacement history obtained as a structural result.

Temperature histories at the top and bottom surfaces at point 1 are presented in Figure 5.8. The low maximum temperature differences of about 20 °C were developed through the 1 mm plate thickness at each stage. Thus, the temperatures at the bottom surface are not clearly displayed in the figure. At each stage, temperatures rise instantly when the laser beam approaches to the point, and slowly decay during cool-down phases. The reason for the two rapid temperature rises at stage 1 is that the first one is for the starting irradiation and the second is for the ending irradiation.

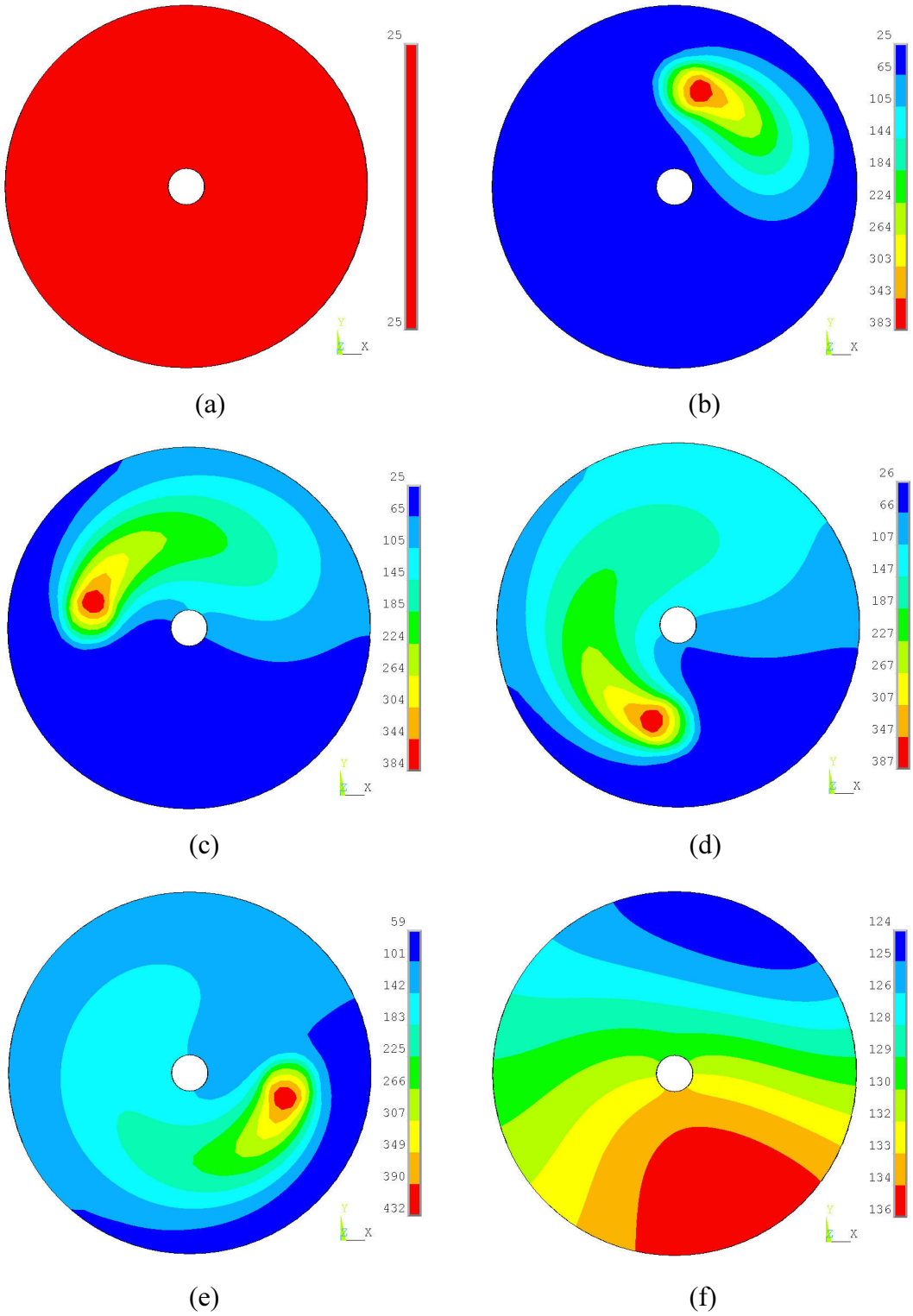

Figure 5.4 Temperature distributions at: (a) 0 sec; (b) 3.46 sec; (c) 6.91 sec; (d) 10.37 sec; (e) 13.82 sec; and (f) 43.20 sec. Stage 1.

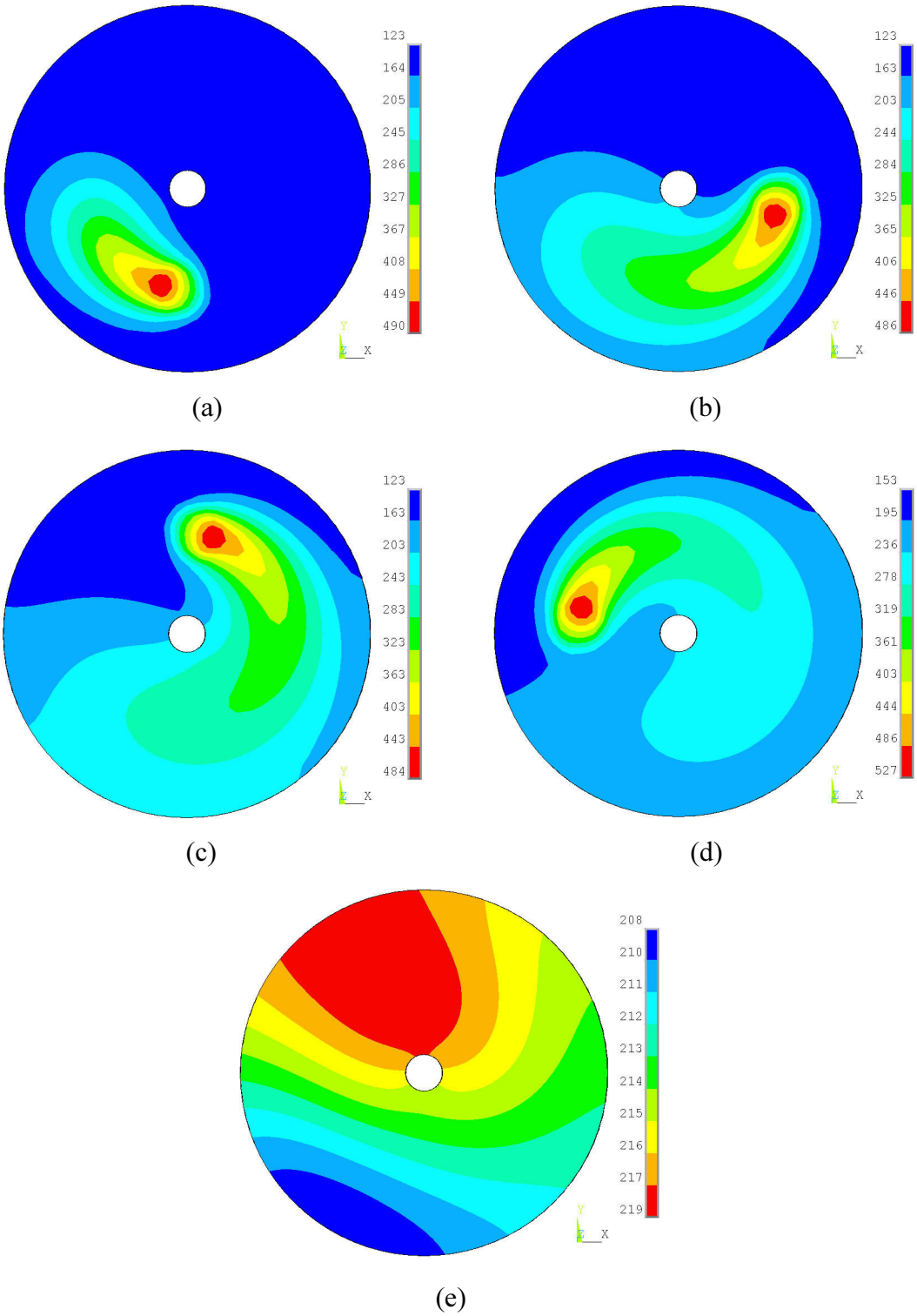

Figure 5.5 Temperature distributions at: (a) 46.65 sec; (b) 50.11 sec; (c) 53.56 sec; (d) 57.02 sec; and (e) 86.40 sec. Stage 2.

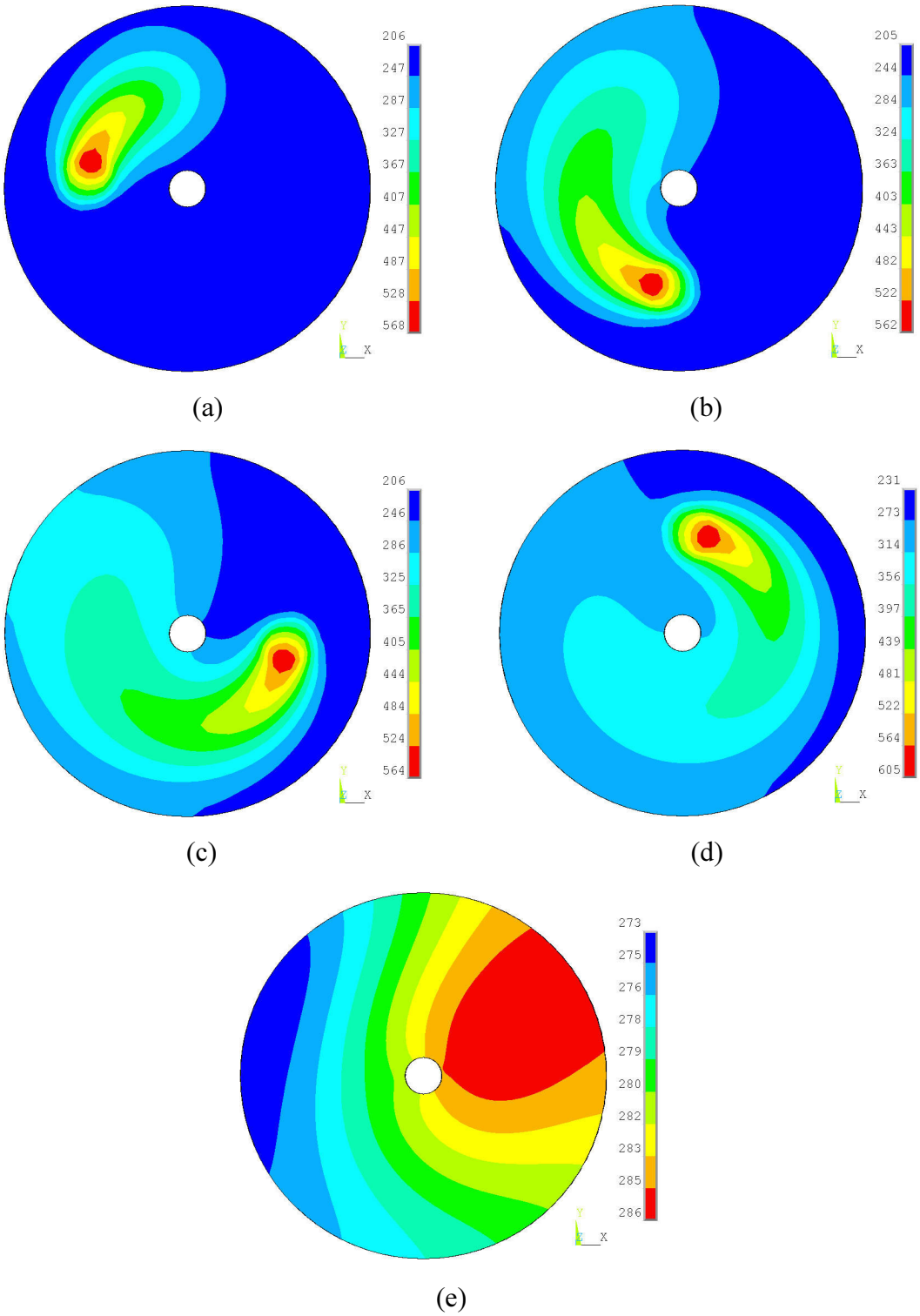

Figure 5.6 Temperature distributions at: (a) 89.85 sec; (b) 93.31 sec; (c) 96.76 sec; (d) 100.22 sec; and (e) 129.59 sec. Stage 3.

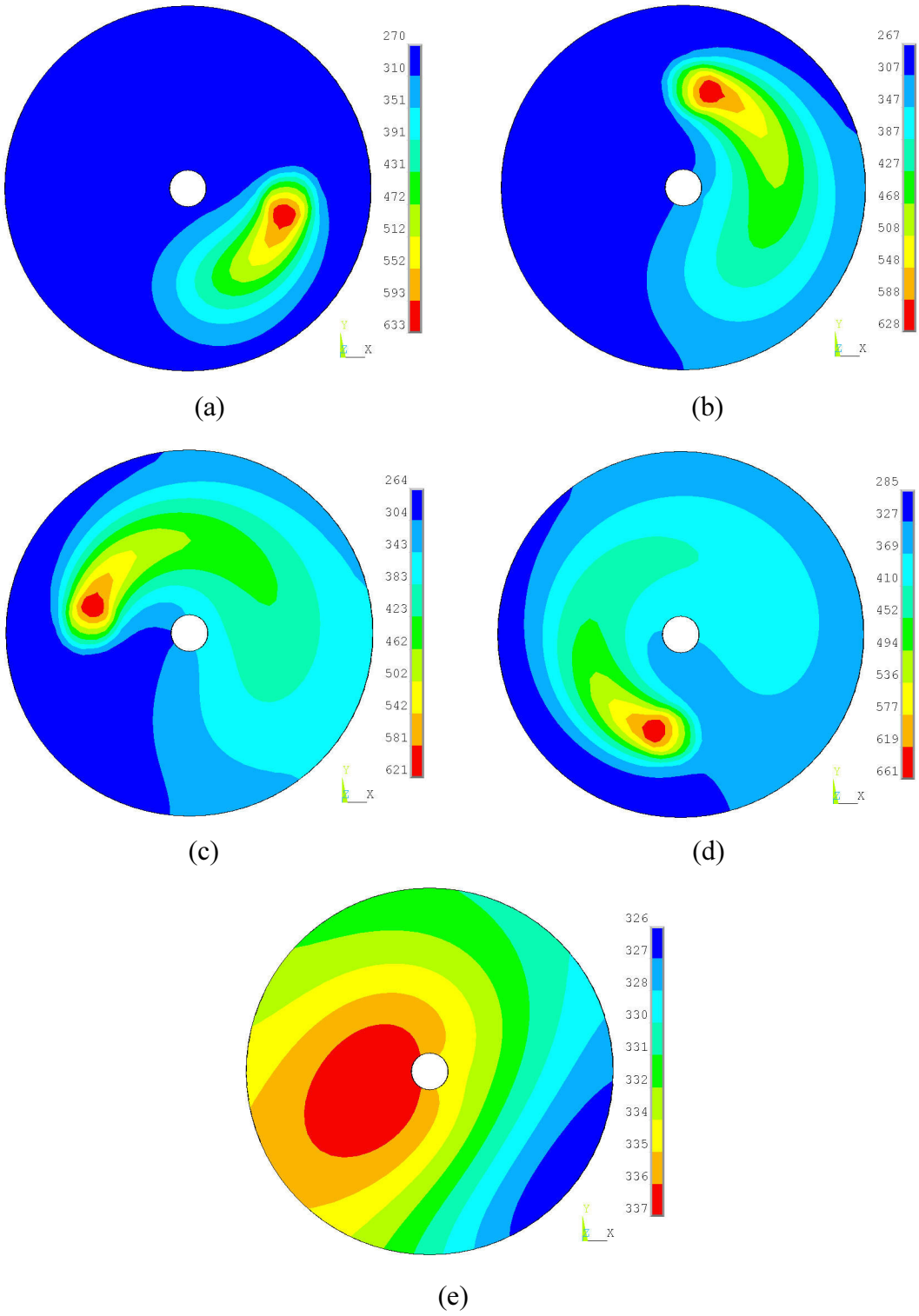

Figure 5.7 Temperature distributions at: (a) 133.05 sec; (b) 136.50 sec; (c) 139.96 sec; (d) 143.42 sec; and (e) 172.61 sec. Stage 4.

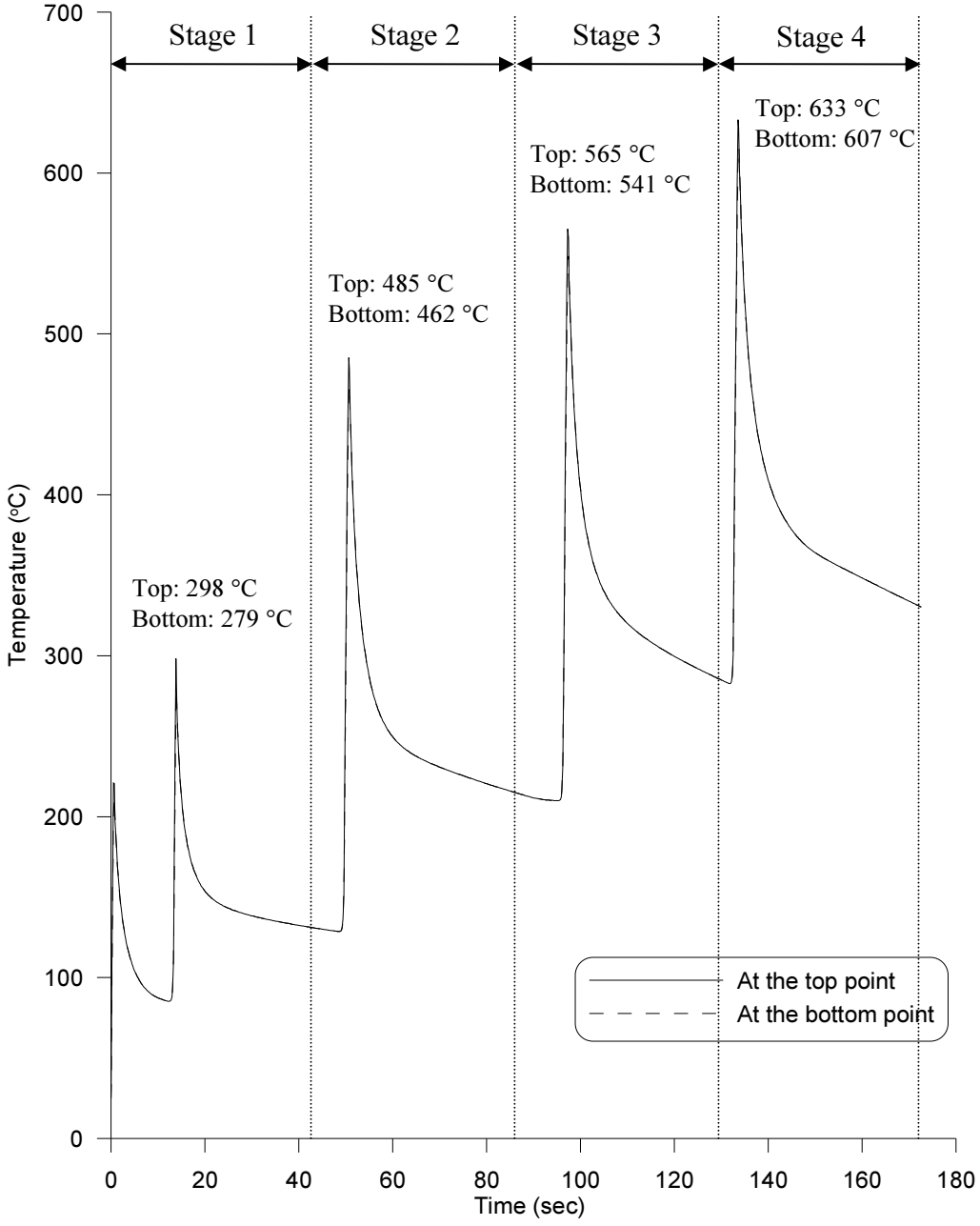

Figure 5.8 Temperature histories at the top (Point 1) and bottom points.

Simulation results of the structural analysis are presented in Figures 5.9 to 5.19. Corresponding deformations of the circular plate to the temperature distributions (Figures 5.4 to 5.7) are shown in Figures 5.9 to 5.12. The bold line circles (not deformed) represent the original work-pieces. As can be seen Figure 5.9, when the plate is initially heated at t = 3.46 sec, the top heated surface expands towards the laser source due to high temperature. Unlike the result from the straight-line heating analysis (See Figure 4.16), a distinctive counter-bending (See Section 1.2.2) can not be found at the early processing stage because the material expansion is fully constrained by surrounding material. When the heated zone is in the cool-down phase at t = 6.91 sec, the circular plate bends towards the laser beam due to contraction at the top surface. Once the distortion develops in the plate, the distinctive thermal expansion generated at the early stage is not produced at the heated regions as can be seen in Figures 5.9 (c) to (e), which is attributed to strict geometrical restriction. Figure 5.9 (f) shows a deformed dish-shaped geometry at the end of stage 1 at t = 43.20. The finial deformations at stages 2, 3, and 4 are illustrated in Figures 5.10 (e), 5.11 (e), and 5.12 (e), respectively. It is noted from the result that the magnitudes of the deformation have increased with the number of the stage, and unsymmetrical geometries were generated.

The Z-components of displacement at points A, B, C, and D are presented with respect to time in Figure 5.13. Unlike the displacement histories from the straight-line heating simulation (Figure 4.25), the deformations first reached peak values at each stage, then collapsed down to certain levels, indicating that much greater thermal strains than plastic strains are involved during heating. The strains against time are presented in Figure 5.14. It is also noticed that the deformations at each stage are almost completed within the given cooling time (i.e., 30 sec), indicating the remaining temperatures in the plate after each stage do not greatly affect change in displacement during the rest of process. The small displacements were achieved in the process as shown in Table 5.2.

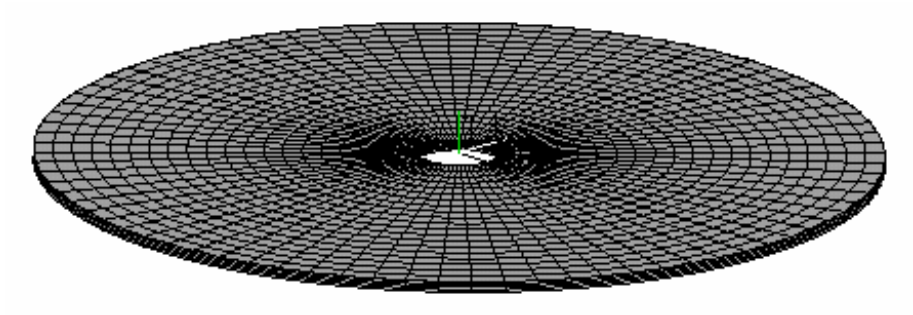

(a)

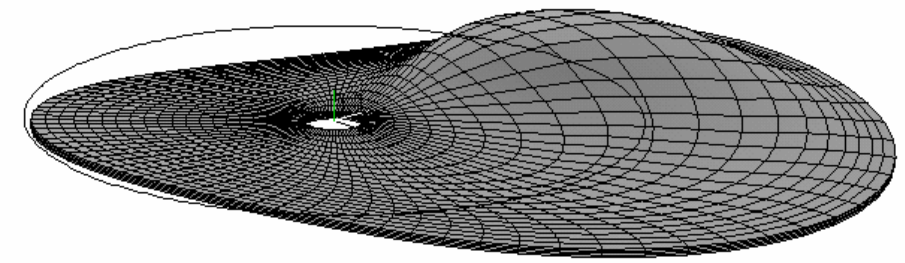

(b)

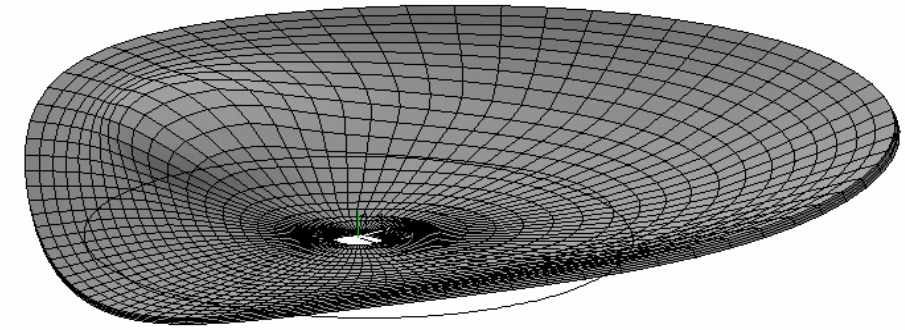

(c)

Figure 5.9 Deformations at: (a) 0 sec; (b) 3.46 sec; (c) 6.91 sec. Deformations are magnified X500 for clarity. Stage 1.

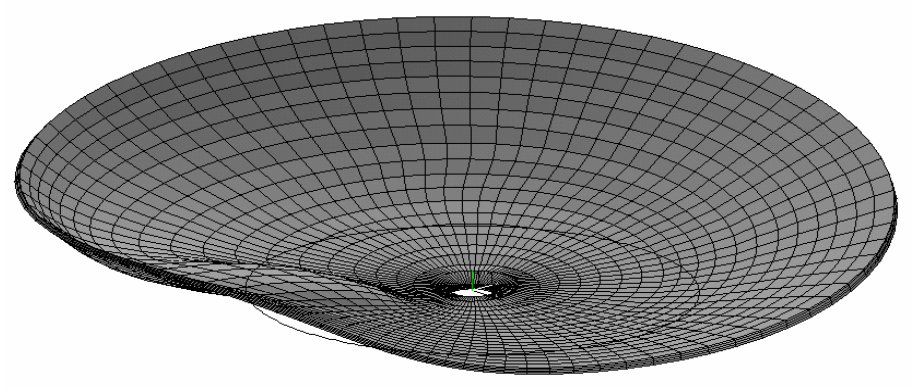

(d)

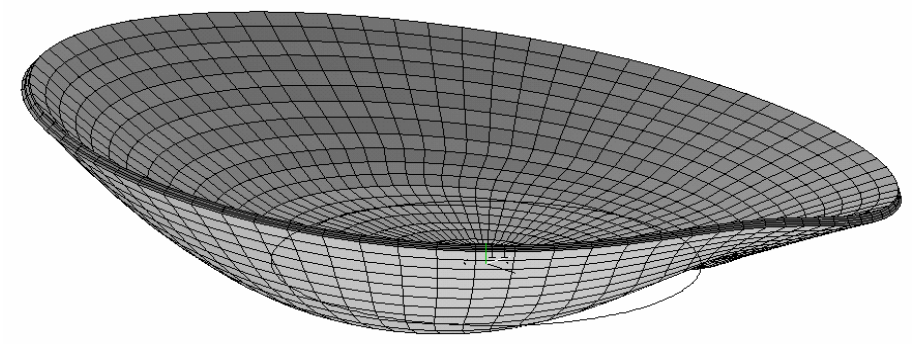

(e)

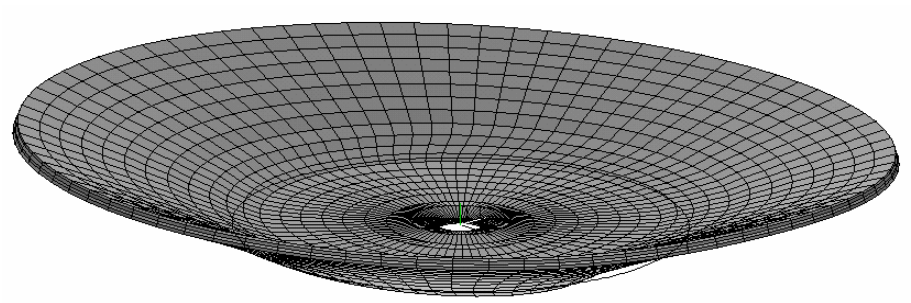

(f)

Figure 5.9 (Continued): (d) 10.37 sec; (e) 13.82 sec; and (f) 43.20 sec.

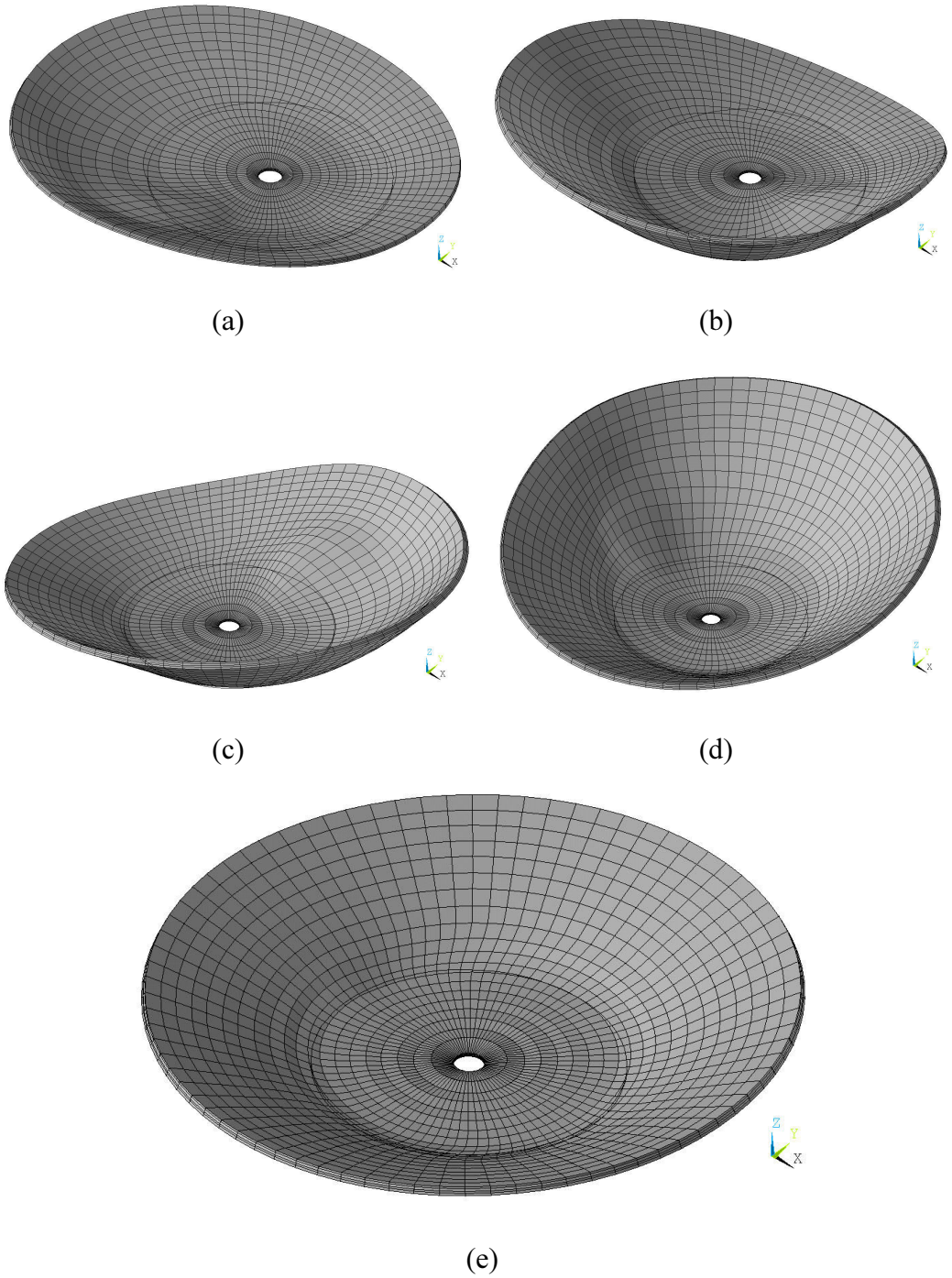

Figure 5.10 Deformations at: (a) 46.65 sec; (b) 50.11 sec; (c) 53.56 sec; (d) 57.02 sec; and (e) 86.40 sec. Deformations are magnified X500 for clarity. Stage 2.

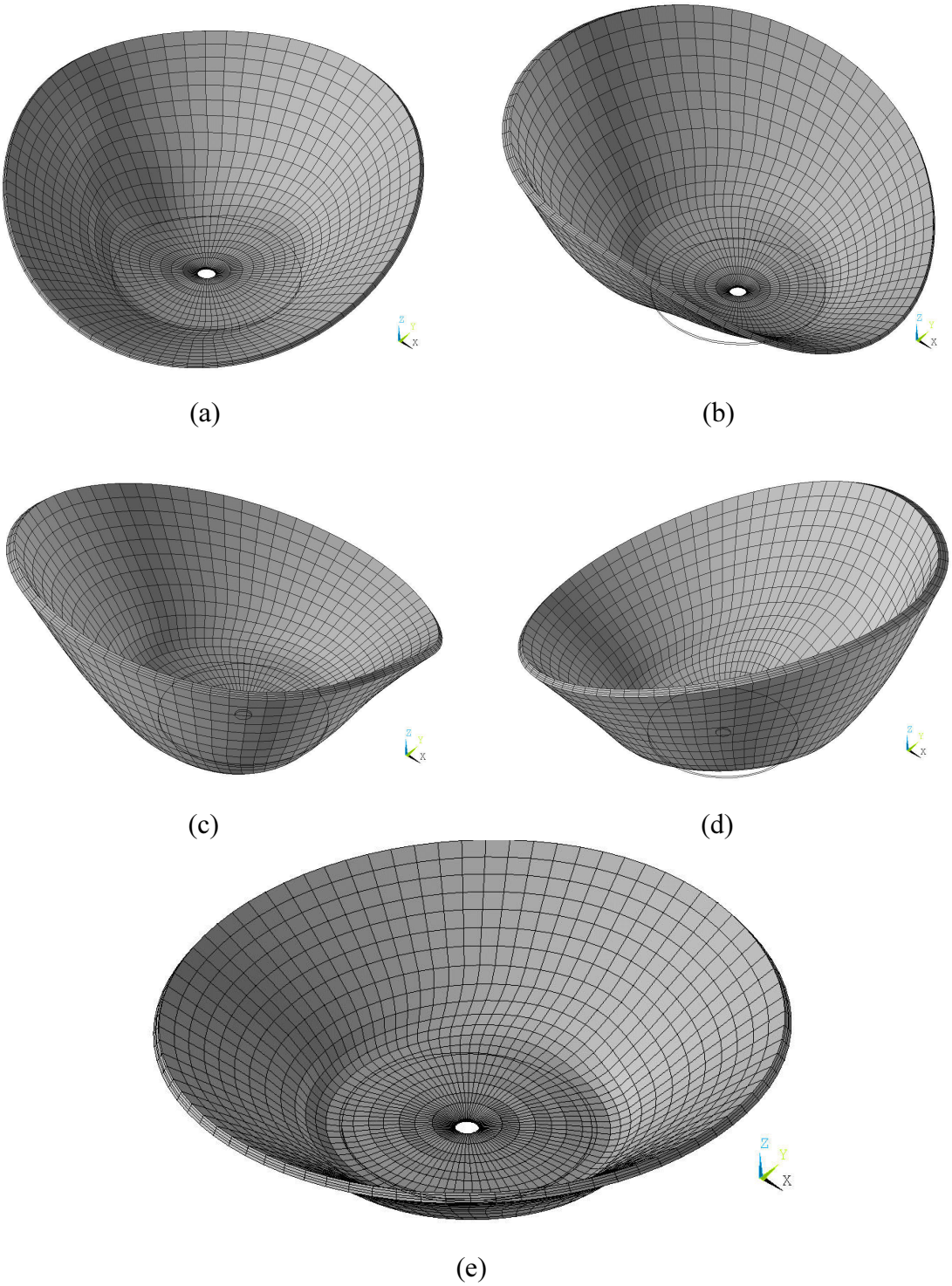

Figure 5.11 Deformations at: (a) 89.85 sec; (b) 93.31 sec; (c) 96.76 sec; (d) 100.22 sec; and (e) 129.59 sec. Deformations are magnified X500 for clarity. Stage 3.

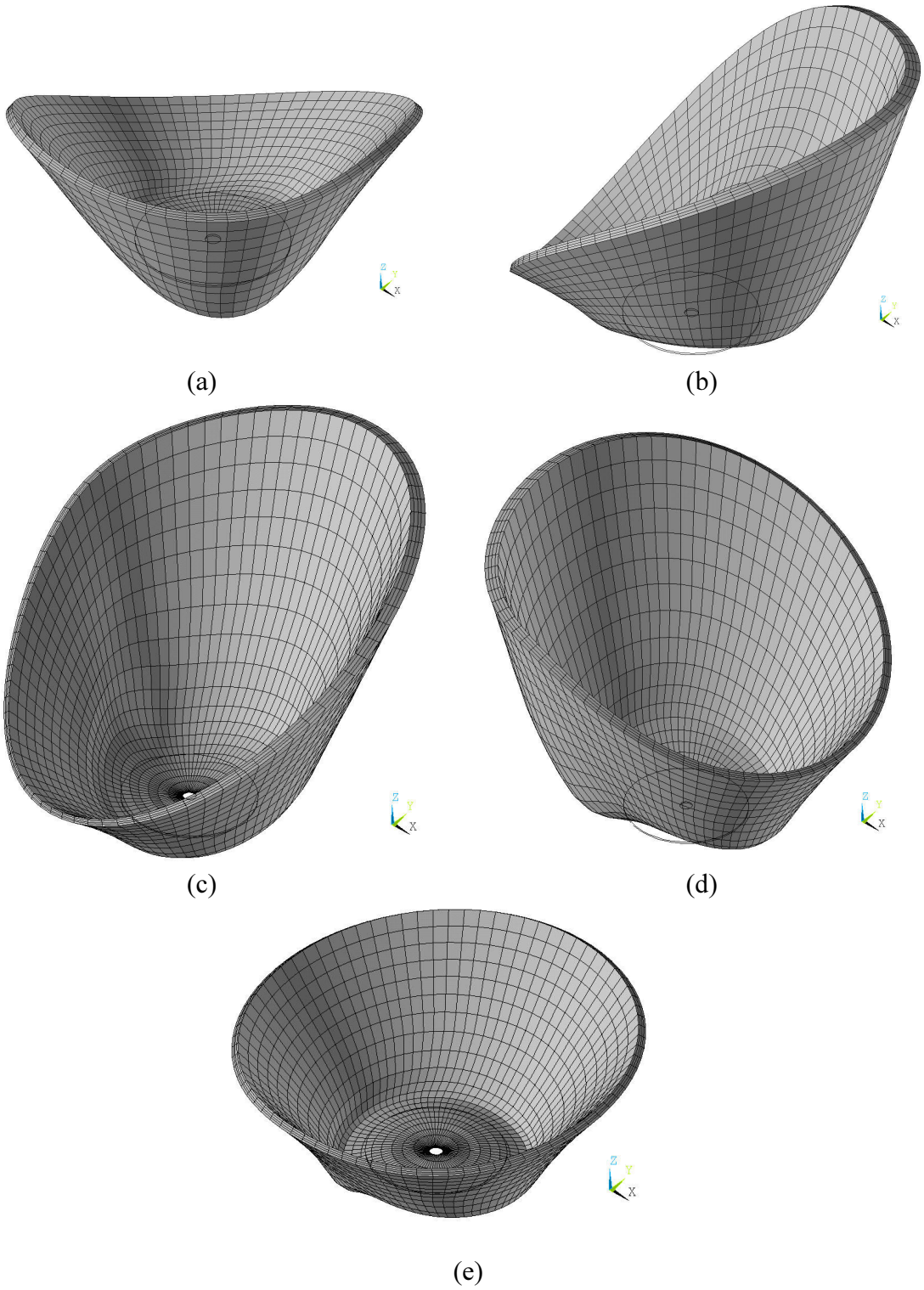

Figure 5.12 Deformations at: (a) 133.05 sec; (b) 136.50 sec; (c) 139.96 sec; (d) 143.42 sec; and (e) 172.61 sec. Deformations are magnified X500 for clarity. Stage 4.

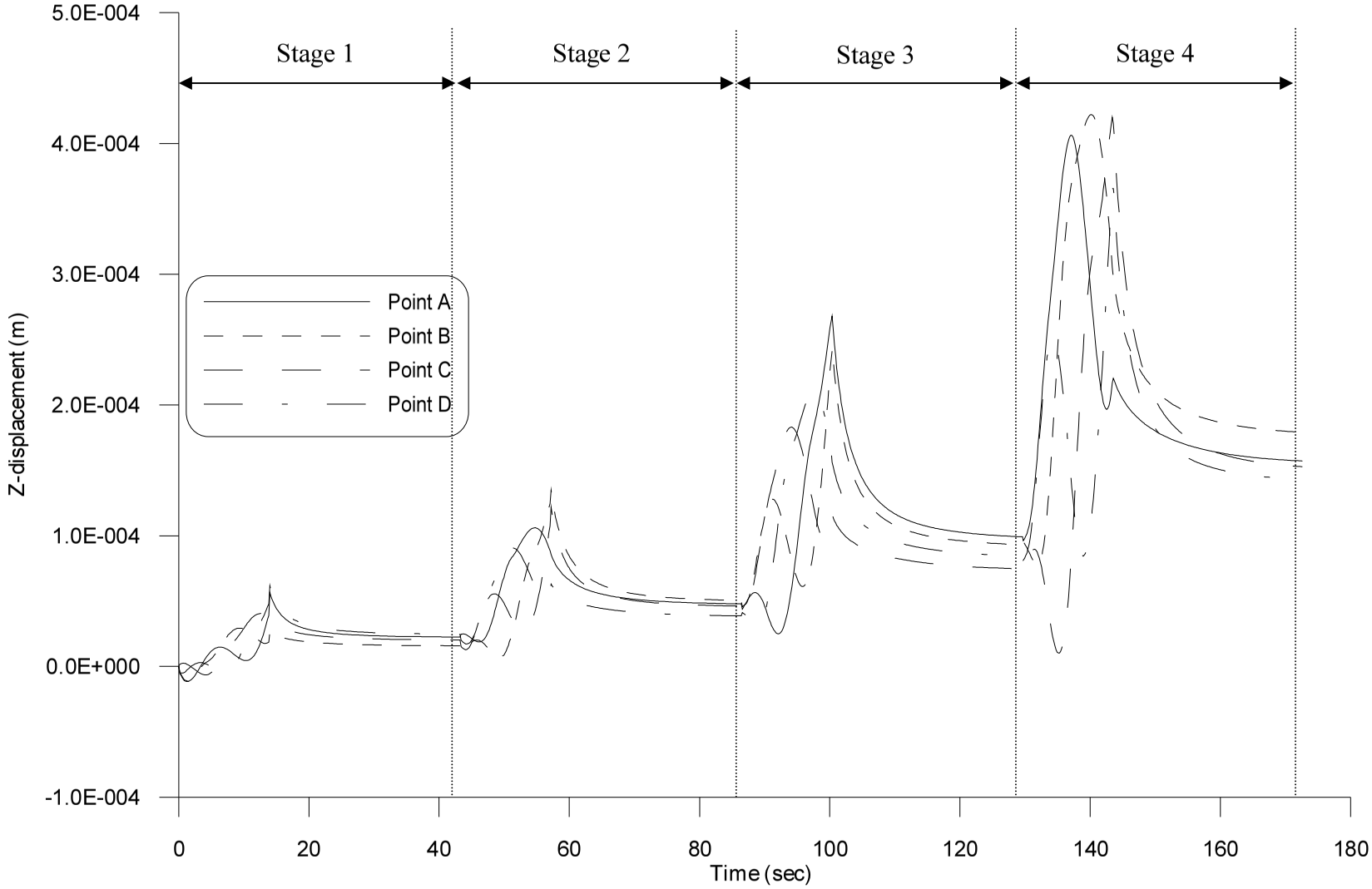

Figure 5.13 Z-displacement histories at points A, B, C, and D.

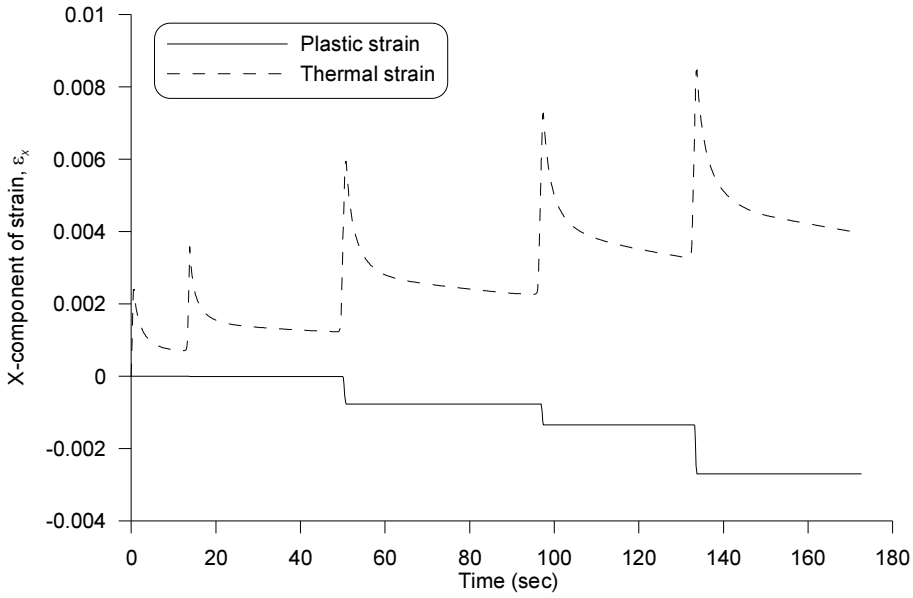

Figure 5.14 Thermal and plastic strains against time.

Table 5.2 Displacements at the end of each stage.

	Displacement in the Z-direction (μm)			
	Point A	Point B	Point C	Point D
Stage 1	22.5	15.8	20.3	24.7
Stage 2	48.0	50.6	46.3	38.8
Stage 3	99.2	93.2	74.8	84.5
Stage 4	157.2	179.1	152.8	142.9

The waviness of the resulting unsymmetrical shape is presented in Figure 5.15 (in the circumferential direction) and Figures 5.16 to 5.19 (in the radial direction). The circumferential waviness is investigated measuring displacements in the Z-direction at the edge of the top surface. It can be seen from Figure 5.16 that with each heating pass, more uneven waviness was developed. That is, the maximum differences of the displacement were 8.9 μm at the end of stage 1, 12.5 μm at the end of stage 2, 25.4 μm at the end of stage 3, and 40.0 μm at the end of the last stage. The locations of the maximum and minimum displacements are related to the starting heating points – the maximum displacements led the starting heating points by 90° and the minimum displacements were lagged by the same size of angle. For example, at stage 1 where the laser beam began heating at point 1 (See Figure 5.1 a), the maximum and minimum displacements occurred at points B and D, respectively.

In order to identify the radial waviness of the dish-shaped geometry, the displacement magnitudes are taken along the lines of OA, OB, OC, and OD at the end of each stage (Figures 5.16 to 5.19). From the figures, it is found that the plate was bent along the circular heating line at the distance of 0.022 m from the center of the plate, and no distortion was generated at the outer regions of the heating line. However, as can be seen in Figure 5.16, uneven distortions were developed at the inner surface of the heating line, which is attributed to the compressive stresses produced in the zone because there is no free space to allow the thermal expansion towards the plate center. The distortions were gradually released, increasing the number of heating passes (Figures 5.17 to 5.18), and almost fully removed at the end of stage 4 forming a convex shape as shown in Figure 5.19.

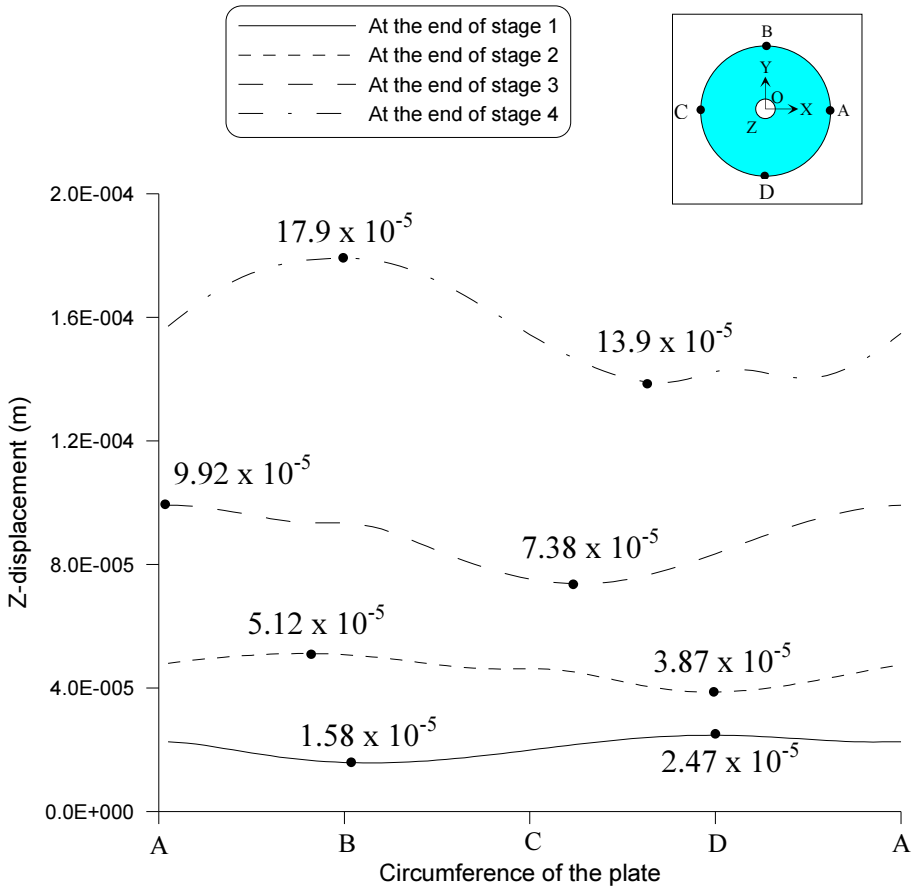

Figure 5.15 Circumferential waviness of the dish-shaped part at the end of each stage.

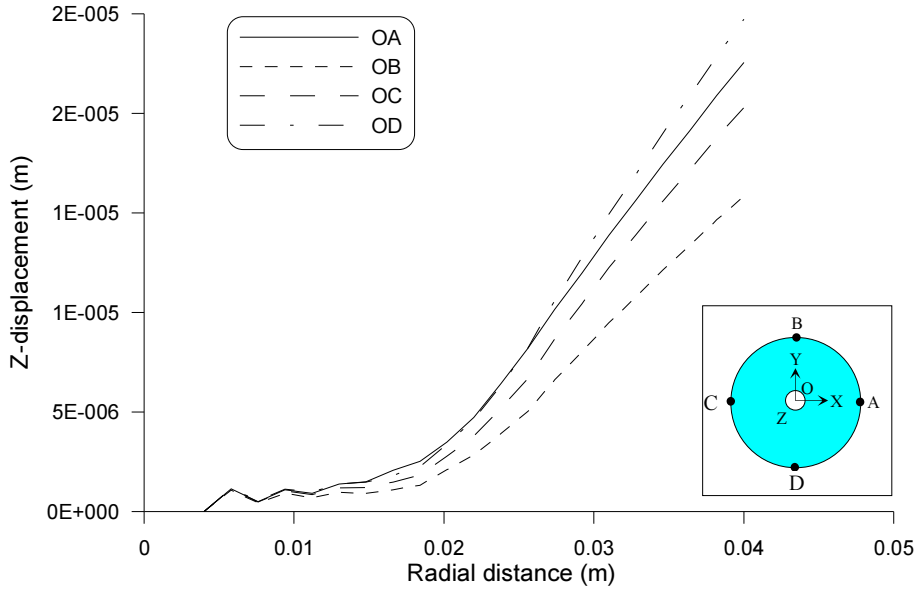

Figure 5.16 Radial waviness of the dish-shaped part at the end of stage 1.

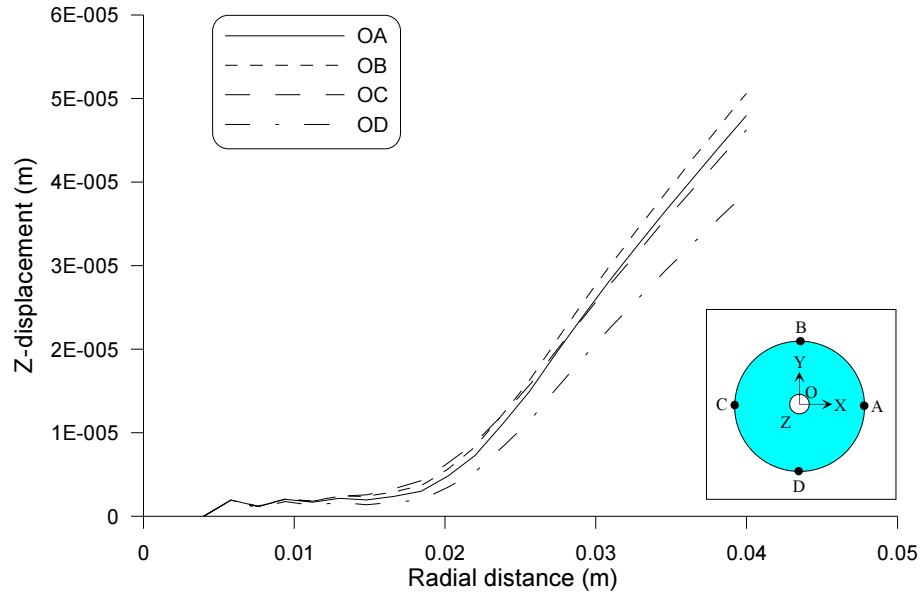

Figure 5.17 Radial waviness of the dish-shaped part at the end of stage 2.

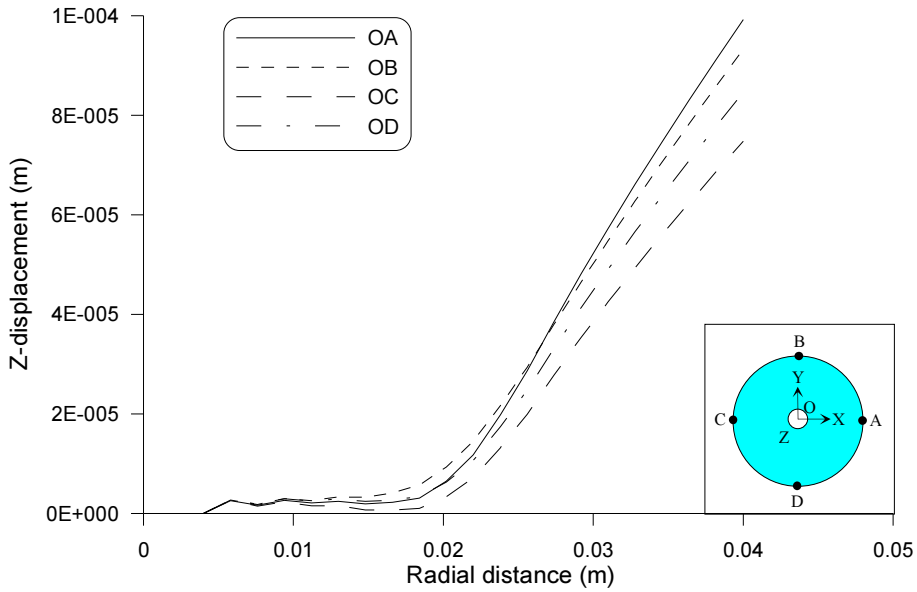

Figure 5.18 Radial waviness of the dish-shaped part at the end of stage 3.

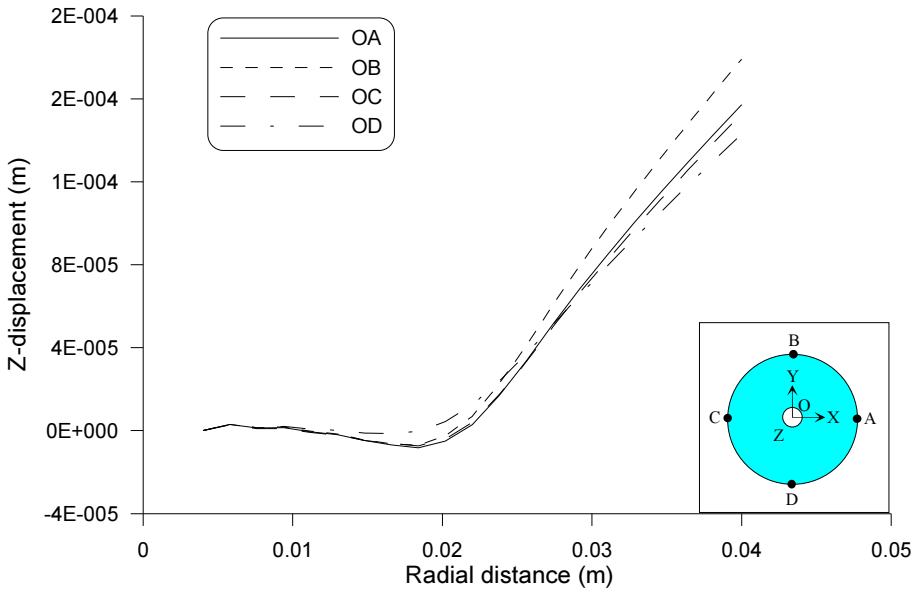

Figure 5.19 Radial waviness of the dish-shaped part at the end of stage 4.

5.5 Model Verification

Although it is recommended that the model developed should be validated showing correlation of the results to reality via a testing program, the verification task is conducted with aid of other techniques due to the limitations of the deployment of a test fixture in this study.

- *Correlation to reference data:*

  The structural response of the material displays correlation to material behavior from an experimental paper by Magee and Watkins [27] in terms of a generation of a dish-shaped geometry with the application of circle-line irradiation pattern. They examined scan patterns with the aim of forming a flat circular plate into a dome shape. The plate samples used were CR4 (Cold rolled) mild steel in a thickness of 2 mm. the diameter of the flat circular plates was 120 mm. A circular hole of 6 mm diameter was laser cut at the center of the plates and used for a clamping screw. The process parameters used in the experiments are: a laser power of 820 Watts, a spot size of 3 mm, and a feed rate of 16.7 mm/s. The scan patterns used in the investigation included star, offset, dividing, and circle line strategies. A coordinate measuring machine was used to measure the height of many points on the samples. Contour plots of the samples were produced. Unfortunately the contour plots could not show the waviness in the radial direction which occurs inherently when the circle line heating pass is adopted. The dividing heating pattern and circle line heating pattern were superior to the others. Irradiation along circular paths generated rounded shapes.

- *Correlation to a similar thermal model validated:*

  The present model has been built on the basis of the similar straight-line laser forming model which was validated through established experimental results (See Chapter 4, Section 4.5.3). The temperature histories from the current simulation show correlation to the results from the heat transfer model used in the straight-line laser forming simulation – the temperature rises instantly during heating and decays slowly during cooling, and the surface heat flux is rapidly transferred to surrounding material by conduction effect. The smooth temperature contour plots indicate that the proper heat flux is imposed on the surface of the material and the heat energy is conducted to surrounding material.

- *Correlation to engineering point of view:*

  The simulation results correlate to engineering judgments. The material is expanded greatly at the initial heating stage (Figure 5.9 b) due to high temperature and loose geometrical restriction, followed by small expansions during the rest of process due to strict geometrical restriction. The deformation magnitudes increase in proportion to the number of heating passes. Unsymmetrical geometries are produced due to unsymmetrical heating application. The bending is caused along the heating line and distortions occurred the inner zone of the heating line due to restriction of the thermal expansion. Compared to the results of the straight-line laser forming, small deformations (a maximum of 179 μm at the end of stage 4) are achieved due to the use of lower laser power (300 Watts) and the stronger geometrical restriction by surrounding material.

5.6 Summary

In the current numerical study a carbon-manganese circular plate is heated at four stages along a circle line by a laser beam to investigate material responses. The plate is supported at its center by a clamping screw. The surface heat fluxes are transferred to surrounding material by conduction and to the surroundings by convection and radiation effects. The thermal and structural models developed for the straight-line heating process in Chapter 4 are adapted for the mesh scheme and structural boundary condition. Uniform meshes are generated via the use of a mesh-only element and revolution method. A moving scheme of the laser beam is described. Simulation results are presented with respect to temperatures and displacements. Material behaviors are illustrated at selected times. Strain histories exhibit the greater thermal strain effect than plastic strain during heating. The quality of the deformed part is identified with both radial and circumferential waviness. An unsymmetrical dish-shaped geometry was induced. The results are validated with the aid of three verification techniques: correlation to reference data, correlation to a validated thermal model, and correlation to engineering point of view. The developed algorithm for the numerical model can contribute to investigating the effects of process parameters by changing the parameters or extending irradiation strategy.

Chapter 6

Simulation of Laser Micro-Adjustment

6.1 Introduction

Due to miniaturization of products, the requirements of precise adjustment of components have increased. Especially the assembly of optical devices (for example, high power diode lasers) requires high accuracy in positioning. However, the adjustment of parts after joining is costly when using mechanical devices because they need to be accessible after joining. As mentioned in Chapter 1 (Section 1.2.4), precise adjustment of components is possible, without mechanical tools, by creating bend angle or changing the length of the parts into a micro size scale by laser micro-adjustment. The objectives of this chapter are to present the capability of the availability of the thermal and structural finite element models, developed in Chapter 4, in the modeling of the laser micro-adjustment process, and investigate the material responses during the operation of the adjustment process via numerical simulation. In order to address the objectives, the simulation of the laser micro-adjustment process is performed using a tube-like structure with three double bridges.

This chapter begins with a brief description of the adjustment process. Then it gives the finite element model, which is basically built on the nonlinear model in Chapter 4. A different element (tetrahedral) is introduced for the mesh of a particular solid geometry with openings. Finally, simulation results of temperatures and displacements are presented and discussed. The structural

behaviors of the material at a heated region are graphically demonstrated. The focus of this chapter is on the characterization of micron size movements induced by laser point heating.

6.2 Process Description

Currently micro cylindrical lenses for beam collimating of diode lasers are adjusted using extensive manipulation equipment to generate the movements of the lenses. This process is expensive and time consuming because the lenses have to be positioned with high accuracy. Olowinsky [15] investigated experimentally the adjustment of the lens using a tube-like actuator that was inserted between the lens and the diode bar. The adjustment was realized in the micron range by irradiating the actuator. However, analysis of the behaviors of the actuator was limited due to the difficulty of the experiment. The laser micro-adjustment process is numerically examined.

The configuration of the structure for the micro-adjustment is illustrated in Figure 6.1 (a). The geometry consists of three double bridges and openings arranged at interval of 120°. The actuator is made from carbon-manganese steel (DIN 1.0584, D36). In order to change its length via the UM mechanism (See Section 2.2.3), the work-piece is first heated at the bridges by a defocused laser beam, then experiences a cooling by conduction, convection and radiation effects. The actuator is fixed at the right end side so that its movement is mainly caused to the left side. The structure has a length of 10 mm, an outer diameter of 10 mm, and a wall thickness of 1 mm. The diameters of the three big and small openings are 5 mm and 0.8 mm, respectively. The laser power used is 100 watts and the beam diameter is 0.4 mm. The absorption coefficient used is 0.75 which value can be obtained using graphite coating in experiment [41].

It has been reported that different and complex deformation can be achieved by heating the points on the bridges in different order [15, 31]. In the current simulation, the adjustment operations are performed at six stages – each

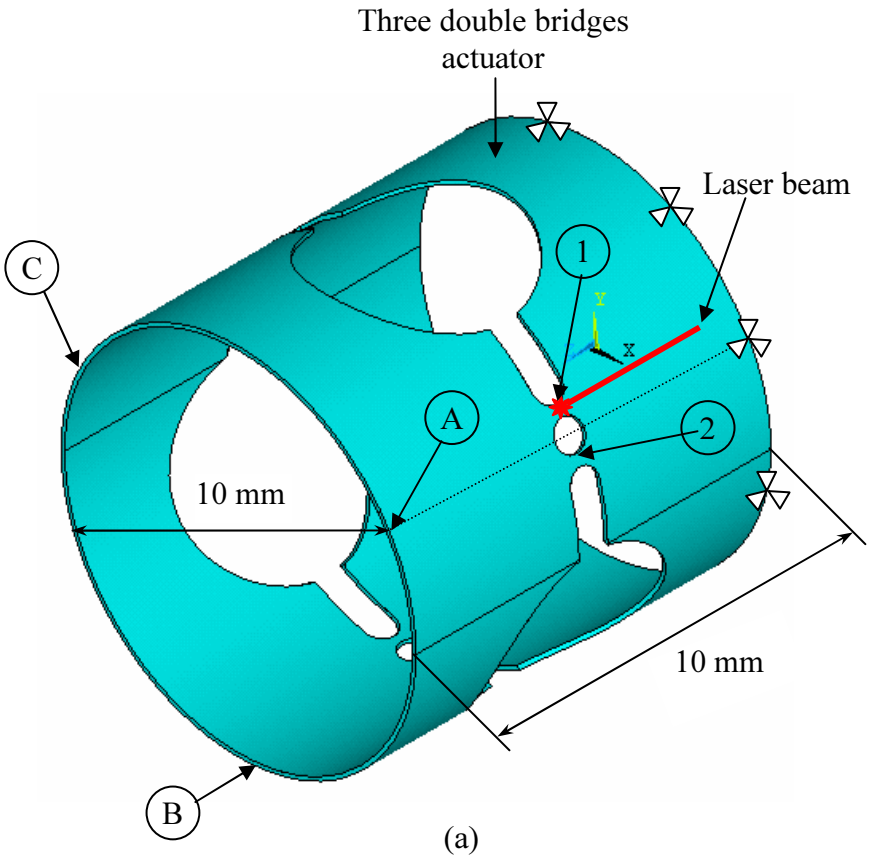

(a)

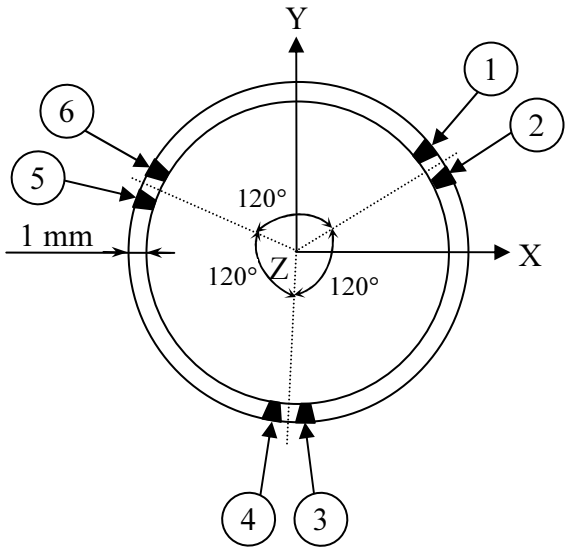

(b)

Figure 6.1 The structure with three double bridges for laser micro-adjustment: (a) geometry and dimensions and (b) heating order.

bridge undergoes heating and cooling in the order of points 1, 2, 3, 4, 5, and 6 as shown in Figure 6.1 (b). At each stage, the heating time taken is 0.005 sec and the cooling time is 0.095 sec. The total processing time is therefore 0.6 sec.

Depending on the significance of a particular application of the deformation, the movements of the structure can be characterized with single or more geometric parameters (for example, displacement or bend angle of a chosen point) [31]. In this study, the Z-component of the laser-induced displacement is identified at the outer edge of the actuator at each stage. In addition, the X- and Y-components of the displacements at point A, B, and C are obtained to investigate the material behavior during the operation.

6.3 Finite Element Model

For the simulation of the adjustment process, thermal and structural finite element models were parametrically built using APDL, a scripting language offered by the code ANSYS [77]. The computer program listing is given in Appendix C. Due to the process similarity to the straight-line heating process in Chapter 4 in terms of heat loading to carbon-manganese steel (DIN 1.0584, D36) by a laser irradiation, most of the models for the present simulation were defined in the same manner as the heat transfer (Section 4.3) and the deformation models (Section 4.4) for the straight-line analysis.

As can be seen in Figure 6.1 (a), the geometry cannot be easily broken into brick elements, thus a three-dimensional tetrahedral solid element (called SOLID87) is adopted for meshing, which has ten nodes and one degree of freedom (i.e., temperature) at each node. This element is applicable to a transient thermal analysis. Convection or heat flux can be applied to the element faces as surface loads. For the structural analysis, the element can be replaced by the equivalent structural element (SOLID92). Figure 6.2 shows the geometry, node locations, and the coordinate system for SOLID87. The circled numbers indicate element faces. The interpolation functions of SOLID87 and SOLID92 are given in Appendix B.

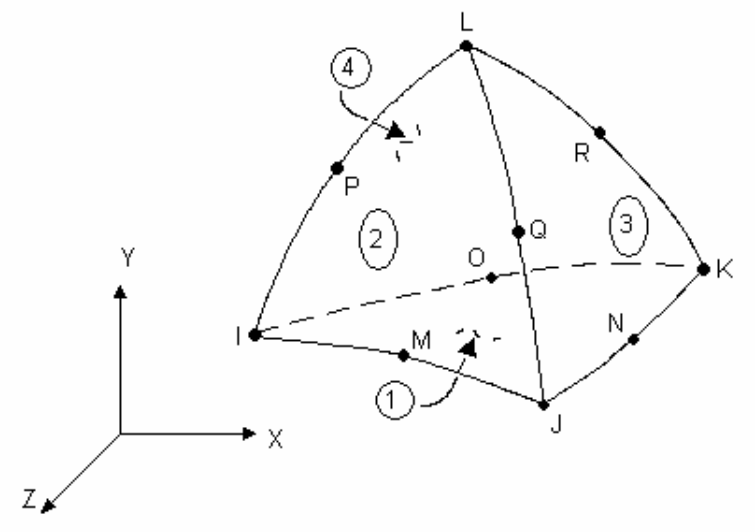

Figure 6.2 3-D 10-node tetrahedral thermal solid (SOLID87) element. Reproduced from [70]

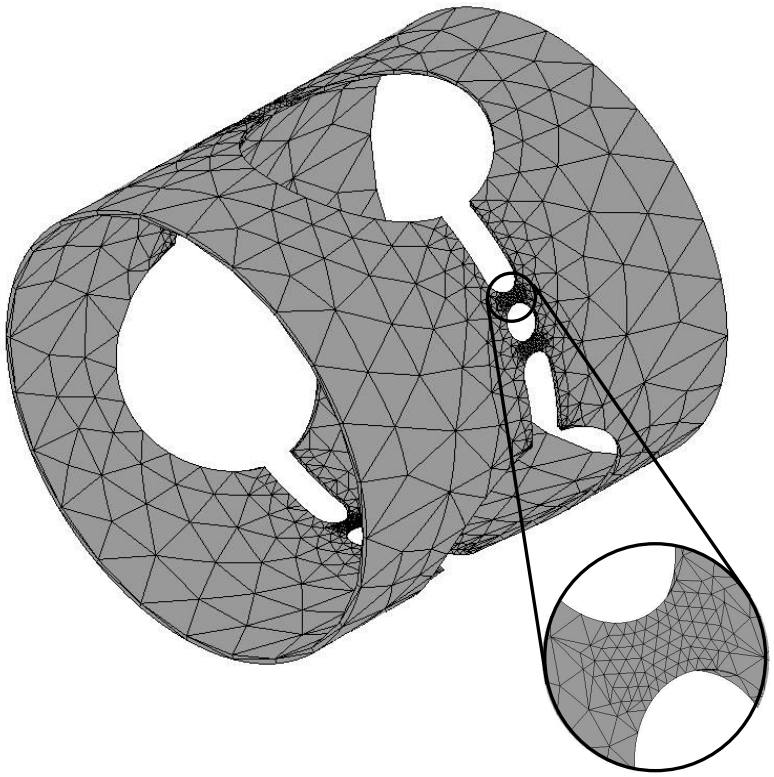

Figure 6.3 Mesh generation.

Meshes are generated in the tube-type structure in two steps: coarse meshes are first made all over the geometry, then the meshes in and near the heating zone are re-meshed to produce fine meshes. With this mesh management, both computational efficiency and solution accuracy can be attained. Figure 6.3 presents the meshes generated. Heat fluxes are applied to the six different regions establishing local coordinates at each position (See Section 5.3 for detailed explanation of the generation of the local coordinates, and Section 4.3.5 in Chapter 4 for selection of element faces inside a laser beam).

6.4 Simulation Results

Simulation results of the thermal analysis are presented in Figures 6.4 to 6.7. Figure 6.4 shows the temperature distributions at selected times: t = 0.001 sec (a), t = 0.003 sec (b), t = 0.005 sec (c) during heating at point 1, t = 0.006 sec (d), t = 0.02 sec (e) during cooling, and t = 0.1 sec (f) at the end of the first stage. From the figure, it is noted that the temperature in the material reached a maximum of 1307 °C at the last heating phase (at t = 0.005 sec) and it cooled down to near room temperature (i.e., 34 °C) very quickly within about 0.1 sec. From the practical point of view, the fast cooling is attributed to heat loss by the conduction effect inside the material. Figure 6.5 shows the temperature distributions during heating at point 2 and cooling. It can be seen that similar temperature profiles to those from stage 1 were produced at stage 2 – the maximum temperature rose to 1333 °C and the heat was rapidly conducted to the surrounding material.

Figure 6.6 shows the temperature histories at the inner and outer surfaces of the center of the heating point at stage 1. It is found that the temperature rapidly increased during heating and slowly decreased during cooling. Unlike the circle-line laser forming in Chapter 5, high temperature difference occurred through the 1 mm thickness steel. That is, the maximum temperatures are 706 °C and 1267 °C at the inner and outer surfaces, respectively. Figure 6.7 shows the temperature histories at points 1, 2, 3, 4, 5, and 6 during the entire process.

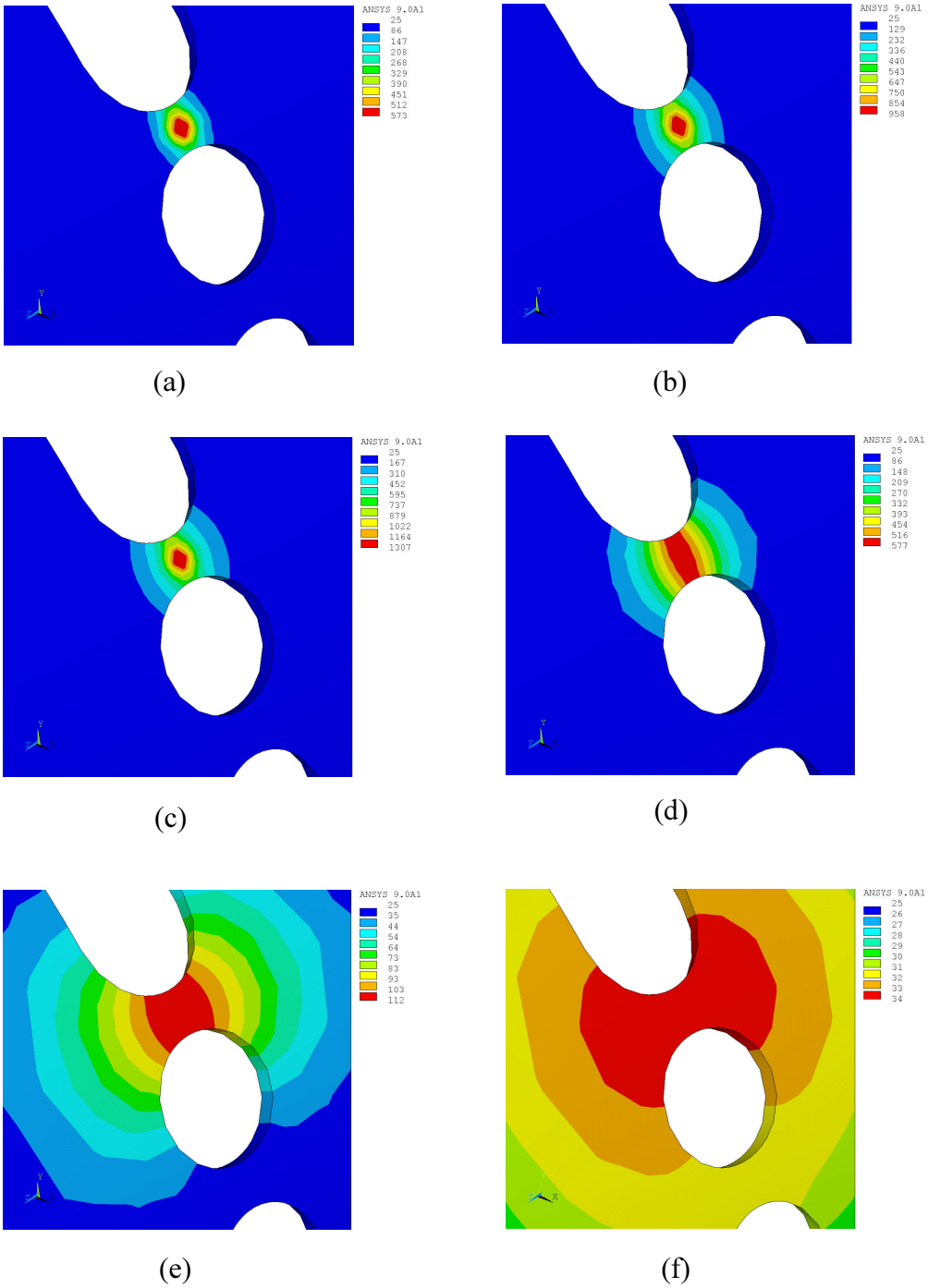

Figure 6.4 Temperature distributions during heating at point 1 and cooling at: (a) 0.001 sec; (b) 0.003 sec; (c) 0.005 sec; (d) 0.006 sec; (e) 0.02 sec and (f) 0.1 sec. Stage 1.

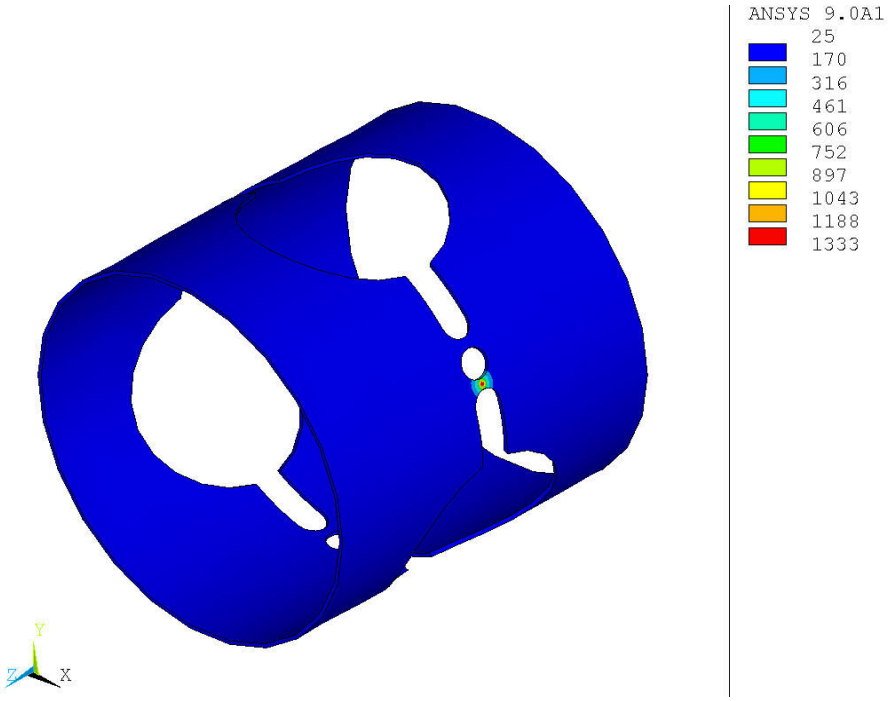

(a)

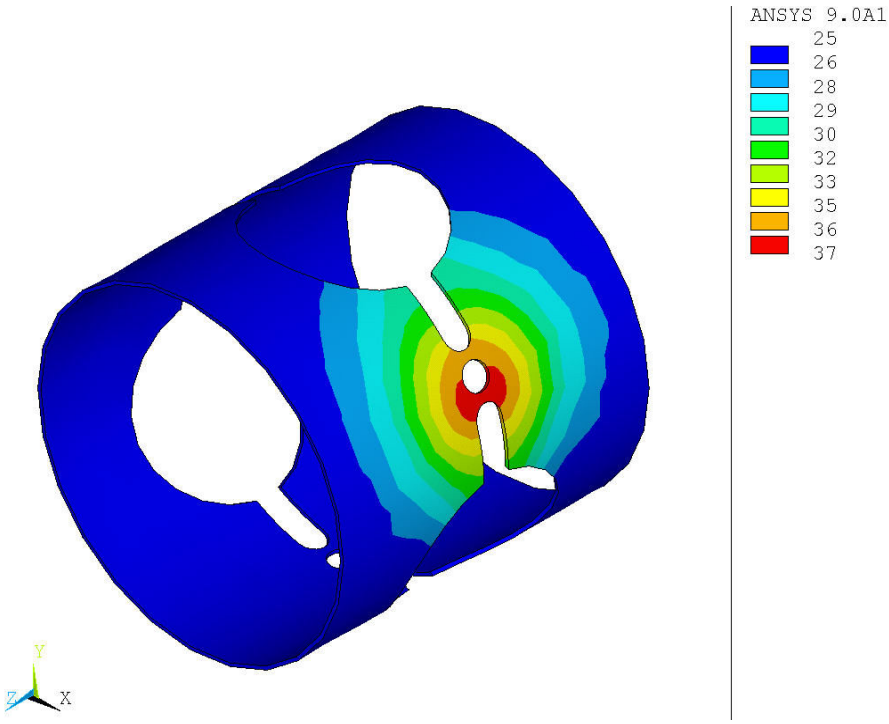

(b)

Figure 6.5 Temperature distributions during heating at point 2 and cooling at: (a) 0.105 sec and (b) 0.2 sec. Stage 2.

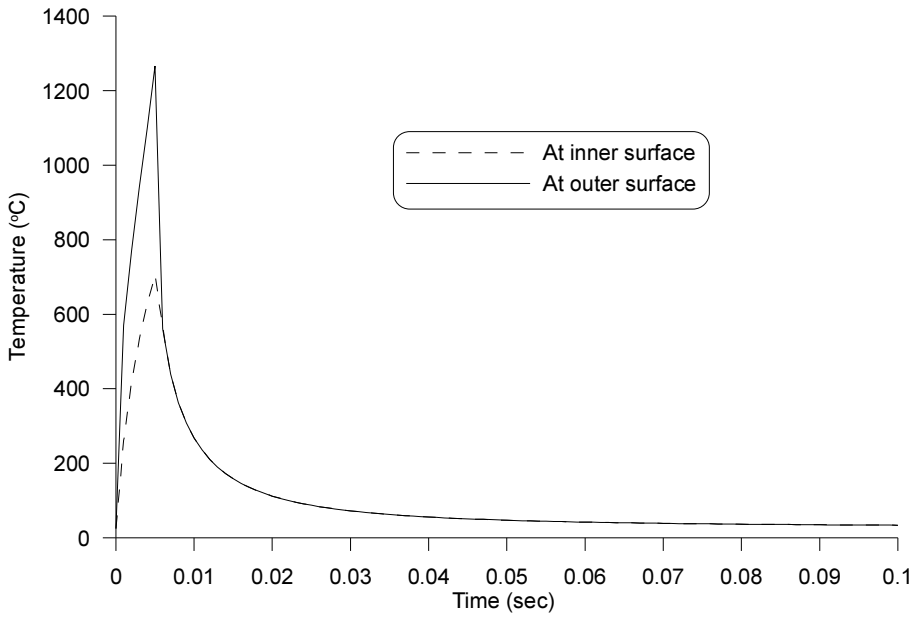

Figure 6.6 Temperature histories at the inner and outer surfaces during heating at point 1 and cooling.

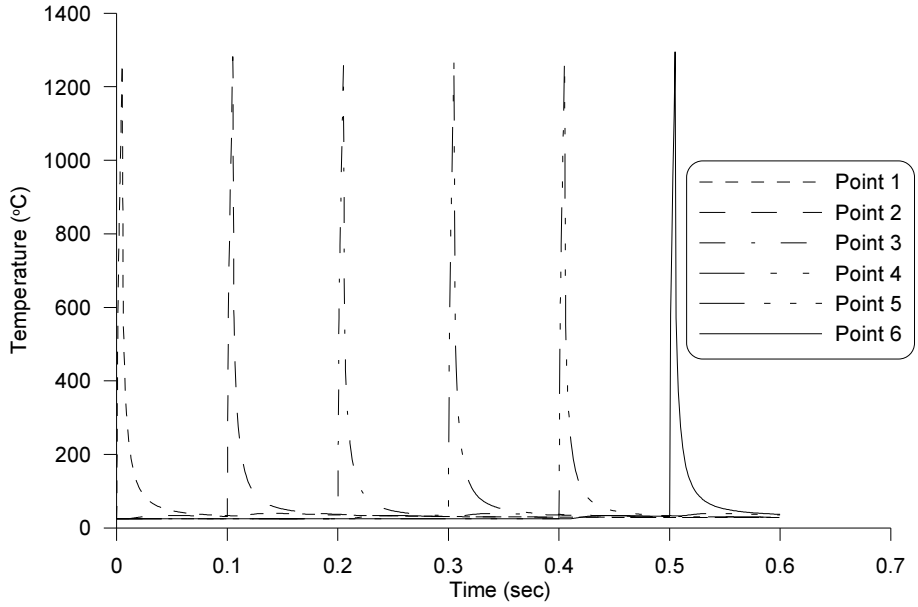

Figure 6.7 Temperature histories at points 1, 2, 3, 4, 5 and 6 during heating and cooling at each point.

The metallurgical effects of the high peak temperatures and thermal cycle on the material used have to be further studied in future. Forming can be achieved at lower temperatures once plastic strain is obtained at the temperatures.

Simulation results of the structural analysis are presented in Figures 6.8 to 6.17. Figure 6.8 shows the material responses, magnified by 100 times, at the bridge at selected times during the operation at point 1: t = 0.001 sec (b) and 0.003 sec (c) during heating, t = 0.006 sec (d), 0.007 sec (e), and 0.02 sec (f) during cooling, and t = 0.1 sec (g) at the end of the stage. During heating, the bridge expands through the thickness direction. It however contracts in the length direction (i.e., Z-direction) of the bridge during cooling, rather than returning to the original position. As the result of this behavior, the bridge thickness increases and the length decreases, indicating that the shortening mechanism (i.e., the UM) is involved in the process.

Figures 6.9 to 6.14 show the three-dimensional deformations, magnified by a factor of 500, at the end of each stage. It can be seen that distortions were developed at each stage due to contractions at heated regions during cooling. The most uniform displacement (shortening) at the edge of the structure was achieved at the end of the last stage.

In order to precisely characterize the material behavior, the movements at points A, B, and C in the X- and Y-directions against time are measured as shown in Figures 6.15 and 6.16. It is noted from Figures 6.15 (a) and 6.16 (a) that the material expanded rapidly during heating and contracted slowly during cooling, and displacements in micron-size were involved during the process. Figures 6.15 (b) and 6.16 (b) present points A, B, and C almost returned to the original locations at the end of the last stage, which is predictable because all bridges contracts at each stage. The deviations in X- and Y-directions after completing the process are listed in Table 6.1. The biggest deviations occurred with 0.946 μm in the X-direction, and 0.641 μm in the Y-direction at point A.

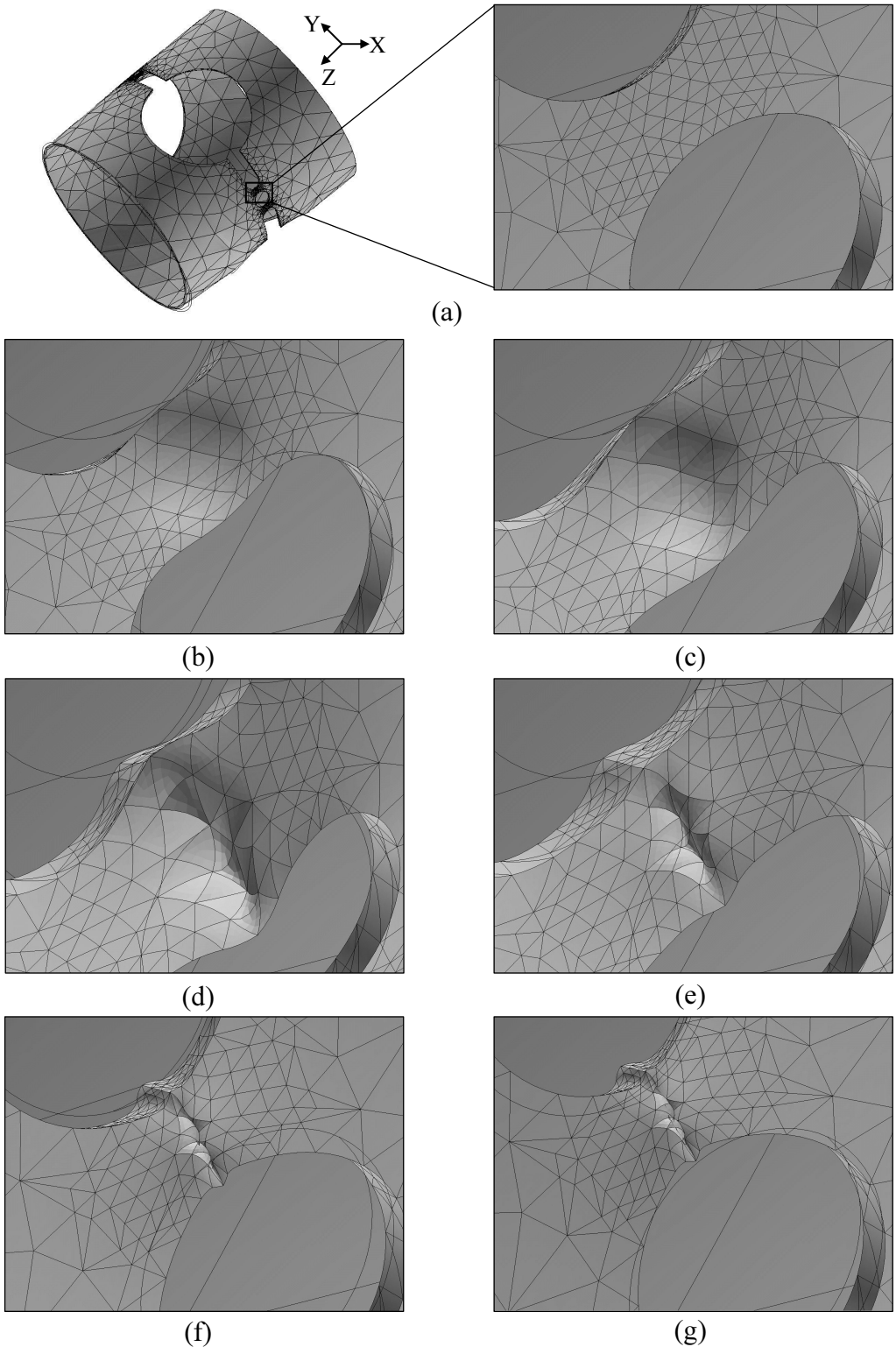

Figure 6.8 Deformations during heating at point 1 and cooling at: (a) 0 sect; (b) 0.001 sec; (c) 0.003 sec; (d) 0.006 sec; (e) 0.007 sec; (f) 0.02 sec; and (g) 0.1 sec. Deformations are magnified X100 for clarity.

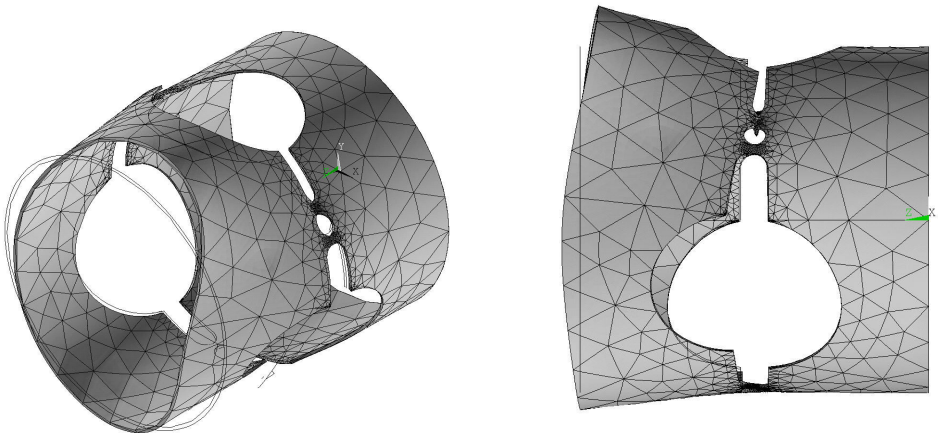

(a) (b)

Figure 6.9 Deformation after heating at point 1 and cooling: (a) isometric view and (b) side view. Deformations are magnified X500 for clarity.

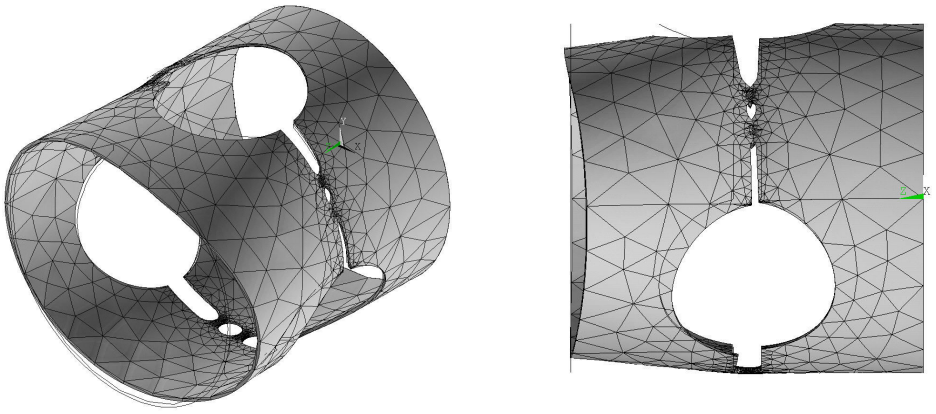

(a) (b)

Figure 6.10 Deformation after heating at point 2 and cooling: (a) isometric view and (b) side view. Deformations are magnified X500 for clarity.

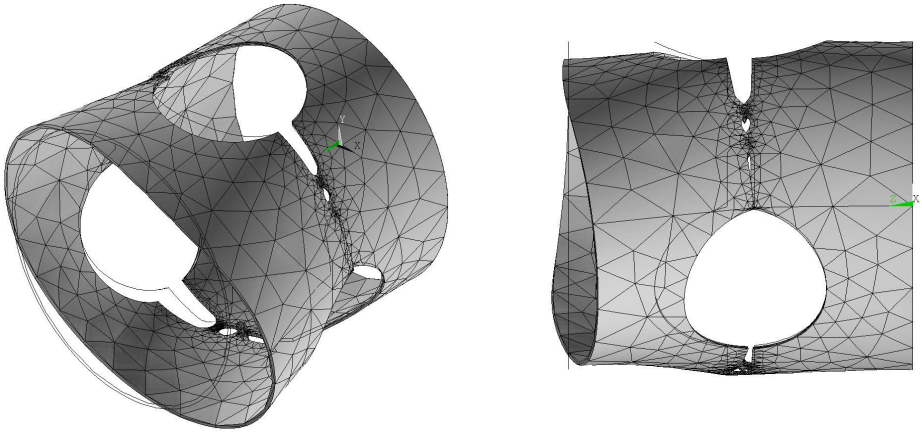

(a) (b)

Figure 6.11 Deformation after heating at point 3 and cooling: (a) isometric view and (b) side view. Deformations are magnified X500 for clarity.

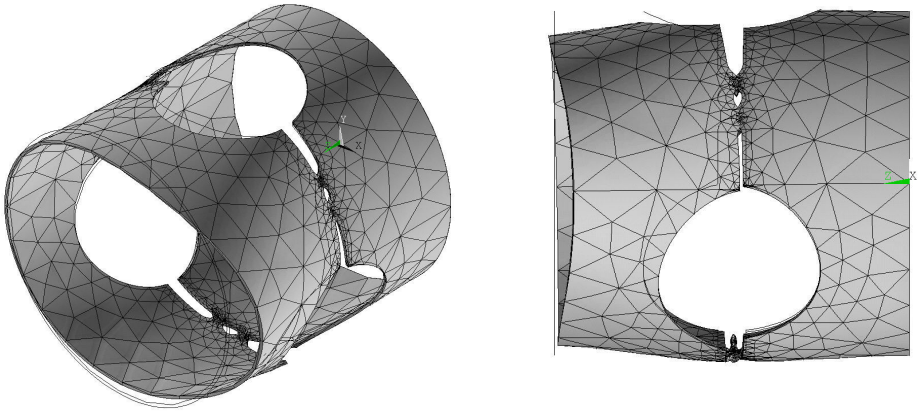

(a) (b)

Figure 6.12 Deformation after heating at point 4 and cooling: (a) isometric view and (b) side view. Deformations are magnified X500 for clarity.

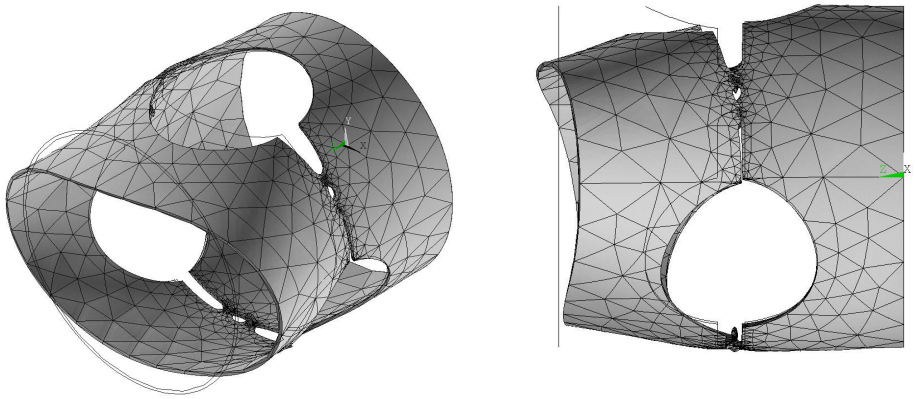

(a) (b)

Figure 6.13 Deformation after heating at point 5 and cooling: (a) isometric view and (b) side view. Deformations are magnified X500 for clarity.

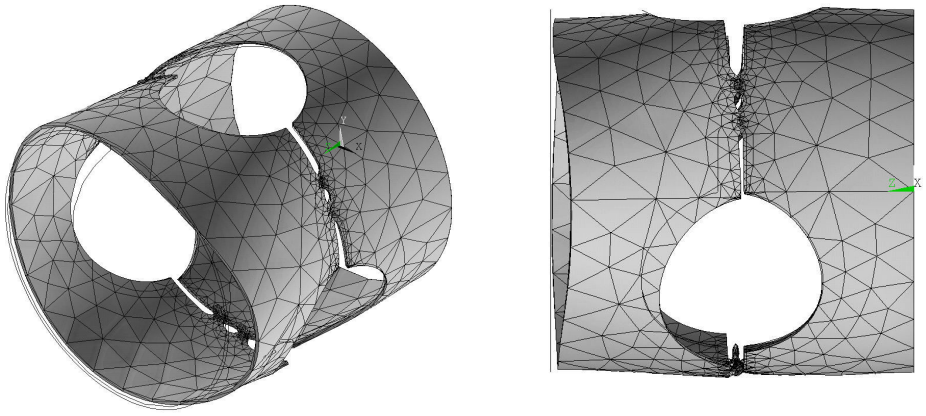

(a) (b)

Figure 6.14 Deformation after heating at point 6 and cooling: (a) isometric view and (b) side view. Deformations are magnified X500 for clarity.

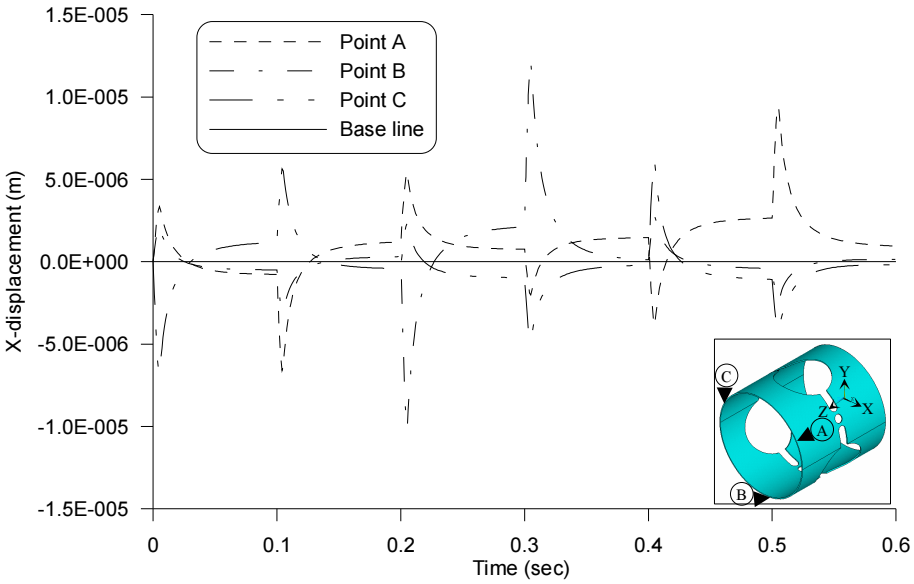

(a)

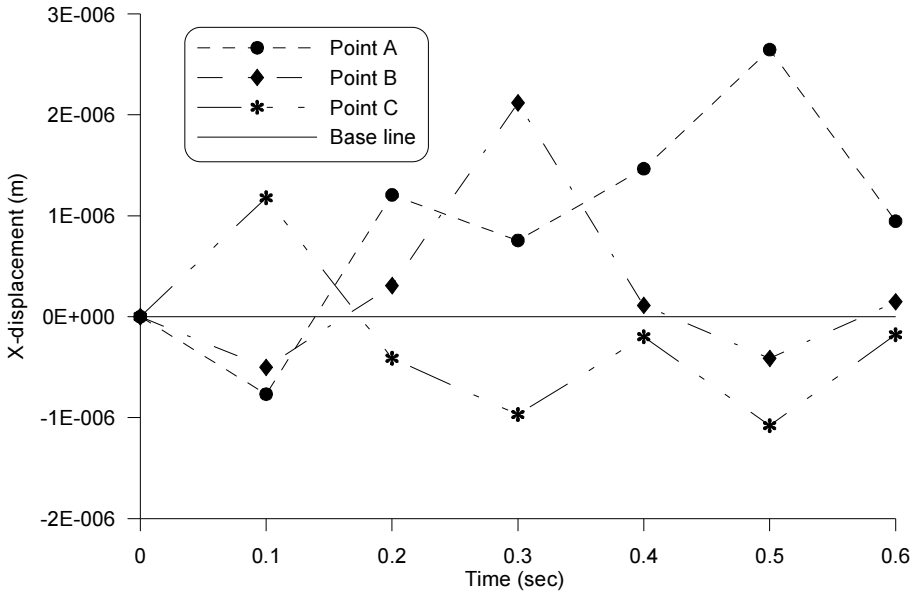

(b)

Figure 6.15 Displacements at points A, B and C in X-direction: (a) against time and (b) at the end of each stage.

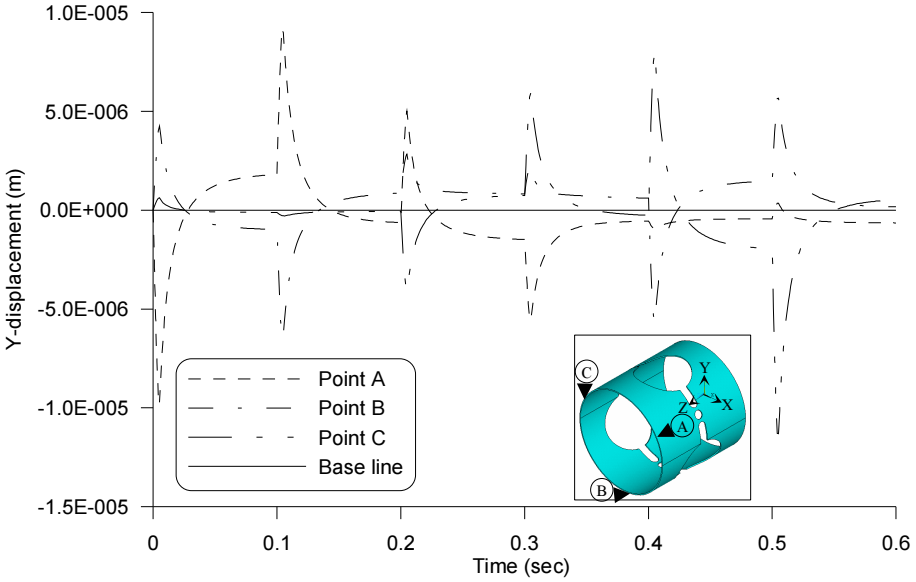

(a)

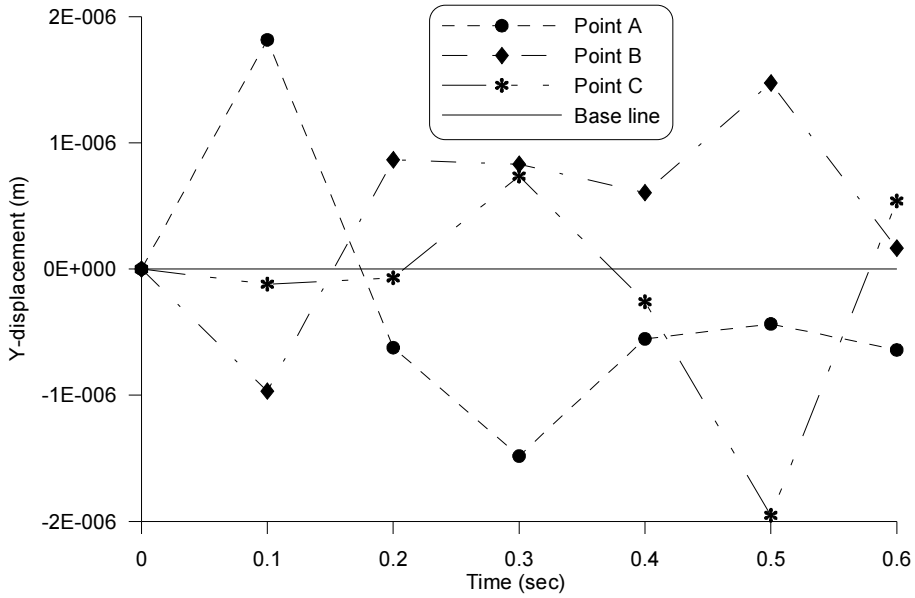

(b)

Figure 6.16 Displacements at points A, B and C in Y-direction: (a) against time and (b) at the end of each stage.

Table 6.1 Deviations in X- and Y-directions at the end of the operation.

	Point A	Point B	Point C
Deviation in X-direction (μm)	0.946	0.147	0.179
Deviation in Y-direction (μm)	0.641	0.166	0.540

Figure 6.17 shows the displacements in the Z-direction at the outer edge of the actuator at each stage. It can be seen that an uneven micron-size shortening was obtained at the end of the operation. The biggest change in length is 1.15 μm at a point in arc AB and the smallest is 0.0586 μm in arc BC.

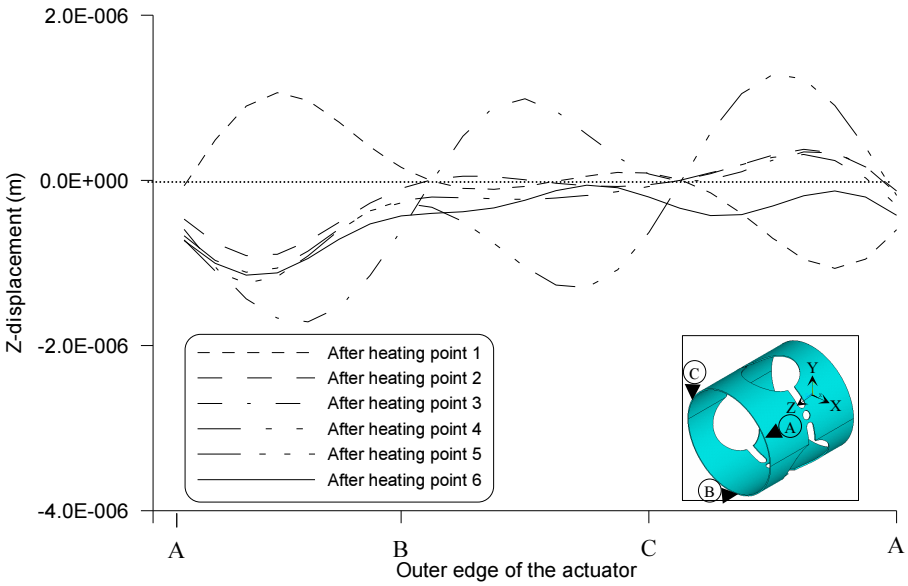

Figure 6.17 Displacement distributions at the outer edge of the structure in the Z-direction at the end of each stage.

6.5 Model Verification

Since a test fixture is not available in this study, other verification techniques, rather than experimental method, are used for validation of the finite element model of the laser micro-adjustment.

Firstly, the displacement histories at points A, B, and C show correlation to those from experimental data by Olowinsky [15] in that the movements of the points almost returns to their original points at the end of the operation.

Secondly, the simulation was performed based on the thermal and structural models validated through the straight-line heating analysis in Chapter 4, which process is basically the same as the adjustment process in terms of the surface heat flux loading and the use of the identical material. The temperature histories and contour plots from the present simulation correlate to those from the straight-line process analysis.

Lastly, the structural behavior of the material shows good agreement to the theoretical description of the UM mechanism. That is, the region expands through the thickness direction during heating, and contracts in the length direction during cooling. Thus, the shortening mechanism is involved in the process.

6.6 Summary

Finite element simulation is carried out for a laser micro-adjustment process where a carbon-manganese tube-like structure consisting of three double bridges is used to be adjusted. A series of six laser point irradiations are applied to the center of the bridges to change the length of the actuator on micron scale. The nonlinear three-dimensional thermal and structural models are built on the basis of the models developed for the straight-line heating process in Chapter 4. An irregular mesh scheme is used introducing a tetrahedral element due to the particular solid geometry with openings.

Simulation results from the thermal and structural analyses are presented in terms of temperatures and displacements. The UM mechanism involved in the process is graphically demonstrated displaying the deformations in a heated bridge at selected times. The shortening in micro-size is identified at the end of the operation. The displacements at points A, B, and C are traced and compared with published displacement histories from a similar laser micro process experiment [15], which show correlation each other in that the movements of the points almost returns to their original points at the end of the operation. The presented finite element model can contribute to find an optimum process parameters (for example, laser power, heating time, and heating order) in order to produce a desired adjustment.

Chapter 7

Process Optimization

7.1 Introduction

As mentioned in Section 1.2.5, laser forming provides many opportunities for manufacturing processes. Some potential applications of laser forming include: Macro-scale laser forming in rapid prototyping and shape correction in the automotive, aerospace and shipbuilding sectors [2, 9, 10, 11, 12]; Precision adjustment of components in micro-scale in the microelectronics industry [13, 14, 15, 16, 17, 18]; Forming in inaccessible areas [5]; and Forming of a wide variety of complex shaped parts [2]. However, research to-date on laser forming has been largely focused, theoretically and experimentally, on the problem of characterization of process parameters on the forming results. Computational simulations of laser forming remain limited only providing the insight into laser forming. Therefore, in order to exploit the benefits of the laser forming process in the manufacturing industry, a method must be developed for determining optimum conditions of the process to satisfy specified design requirements in a given parameter range.

This chapter details the development of an effective method to determine optimum process parameters in laser forming. A design optimization technique is introduced into the finite element analysis of the process. The concept of the design optimization and two optimization techniques are described. The optimum parameter values to produce a predefined bend angle in the straight-

line heating process are determined by two optimization procedures. Optimization results from the two optimization techniques are presented and compared, and a more suitable optimization method for laser forming is chosen. Using the optimization technique selected, the optimum parameters to generate a maximum bend angle are found.

7.2 Design Optimization

In order to underpin the theoretical background of design optimization, the optimization concept and optimization techniques are described in this section.

7.2.1 The concept of design optimization

The fundamental problem of optimization is to arrive at the best possible decision in any given set of circumstances. To address this in an optimization problem, the first step is to choose some quantity, typically a function of several variables, to be minimized, subject possibly to one or more constrains. The next step is to choose an optimization technique (i.e., mathematical method, or algorithm) to solve the optimization problem [79].

A large class of situations involving optimization can be expressed in the following form [80]:

Find a vector of optimization *design variables*, $\mathbf{x} = \lfloor x_1, x_2, x_3, \cdots, x_n \rfloor$

in order to minimize an *objection function*, $f = f(\mathbf{x})$ (7.1a)

subject to

$$g_j(\mathbf{x}) \le g_j^{up} \tag{7.1b}$$

$$h_m^{low} \le h_m(\mathbf{x}) \tag{7.1c}$$

$$w_l^{low} \le w_l(\mathbf{x}) \le w_l^{up} \tag{7.1d}$$

$$\mathbf{x}^{low} \le \mathbf{x} \le \mathbf{x}^{up} \tag{7.1e}$$

where:

$g_j, h_m,$ and w_l = the *state variables* with lower and/or upper bounds, respectively.

$j+m+l$ = the number of state variable constraints.

Eq. (7.1) is called the *general constrained optimization problem*. A feasible design set for the constrained optimization problem is defined only if each state variable limit with a tolerance is satisfied [70]. So if $\mathbf{x}^*$ is a given design set defined as

$$\mathbf{x}^* = \lfloor x_1^*, x_2^*, x_3^*, \cdots, x_n^* \rfloor \tag{7.2}$$

A design set is considered feasible only if

$$g_j(\mathbf{x}^*) \le g_j^{up} + \alpha_i \tag{7.3a}$$

$$h_m^{low} - \beta_i \le h_m(\mathbf{x}^*) \tag{7.3b}$$

$$w_l^{low} - \gamma_i \le w_l(\mathbf{x}^*) \le w_l^{up} + \gamma_i \tag{7.3c}$$

where:

$\alpha_i, \beta_i,$ and γ_i = tolerances.

And

$$\mathbf{x}^{low} \le \mathbf{x}^* \le \mathbf{x}^{up} \tag{7.4}$$

Optimization can be applied to all disciplines, but it is frequently associated with design in engineering. There are various optimization techniques to address the constrained minimization problem stated above.

7.2.2 Optimization techniques

This subsection presents some common algorithms used to solve the constrained optimization problem, Eq.(7.1) – *surface response methodology*, *penalty function technique*, *sequential unconstrained minimization technique*, and *gradient-based technique*.

7.2.2.1 Response Surface Methodology (RSM)

RSM is a method to construct a global approximation of system behaviour. The dependent variables expressed by Eqs. (7.1a to d) are represented as approximated functions via RSM. For example, the objective function (Eq. 7.1a) can be written in a fully quadratic form with cross terms [81]:

$$f \cong \widetilde{f} = a_0 + \sum_i^n a_i x_i + \sum_i^n \sum_j^n a_{ij} x_i x_j \tag{7.5}$$

The coefficients, {a}, in Eq. (7.5) are determined using the method of least squares, which is based on minimizing the following sum of the squared errors (SSE):

$$SSE = \sum_{k=1}^{n_s} \left[\varphi^k (f^k - \widetilde{f}^k)^2 \right] = \sum_{k=1}^{n_s} \left[\varphi^k (f^k - a_0 + \sum_i^n a_i x^k i + \sum_i^n \sum_j^n a_{ij} x^k i x^k j)^2 \right] \tag{7.6}$$

where:

φ^k = the weight coefficient associated with the k^{th} design set.

k = the number of current design set.

n_s = the number of sampling points.

The solution to the unknown coefficient is [70]:

$$\{a\} = \left([d]^T [d]\right)^{-1} [d]^T \{f\} \tag{7.7}$$

where:

$[d]$ = the sampled design matrix expressed as:

$$[d] = \begin{bmatrix} \lfloor 1 \;\; x_{1,1} \;\; x_{2,1} \;\; \dots \;\; x_{n,1} \;\; x_{1,1}^2 \;\; x_{1,1}x_{2,1} \;\; \cdots \;\; x_{1,1}x_{n,1} \;\; x_{2,1}^2 \;\; \cdots \;\; x_{2,1}x_{n,1} \;\; \cdots \;\; x_{n,1}^2 \rfloor \\ \vdots \\ \lfloor 1 \;\; x_{1,n_s} \;\; \cdots \;\; x_{n,n_s} \;\; x_{1,n_s}^2 \;\; x_{1,n_s}x_{2,n_s} \;\; \cdots \;\; x_{1,1}x_{n,n_s} \;\; x_{2,n_s}^2 \;\; \cdots \;\; x_{2,n_s}x_{n,n_s} \;\; \cdots \;\; x_{n,n_s}^2 \rfloor \end{bmatrix} \tag{7.8}$$

A number of simulations have to be performed in order to solve Eq. (7.8). This function approximation process is similarly applied to the state variables, Eqs. (7.1b to d). Thus, the constrained minimization problem, Eq. (7.3) is reformulated with each function approximation of the state variables as:

$$\widetilde{g}_j(\mathbf{x}^*) \le g_j^{up} + \alpha_i \tag{7.9a}$$

$$h_m^{low} - \beta_i \le \widetilde{h}_m(\mathbf{x}^*) \tag{7.9b}$$

$$w_l^{low} - \gamma_i \le \widetilde{w}_l(\mathbf{x}^*) \le w_l^{up} + \gamma_i \tag{7.9c}$$

7.2.2.2 Penalty Function Technique

The basic idea of the penalty method is to transform the constrained problem, Eq. (7.1), into an equivalent unconstrained problem by adding constraints, multiplied by a large penalty term, to the objective function. The additional terms are defined in such a way that if the constraints are satisfied, there is no penalty, but if one or more constraints are violated, a large penalty term is added. Since the objective function is being minimized, the penalty term will indirectly force the constrains to be satisfied [80]. If a penalty function is chosen as $P(\mathbf{X})$, the constrained problem, Eq. (7.1), is converted to an unconstrained problem [79]:

$$F = f(\mathbf{x}) + P(\mathbf{X}) \tag{7.10}$$

Several methods exist for defining the penalty terms: the Exterior Penalty Function (EPF), the Interior Penalty Function (IPF) and Augmented Lagrangian Penalty Function (ALPF). The first two methods have several shortcomings by suffering from numerical difficulties in solving the unconstrained problem [82]. Using the ALPF, Eq. (7.1) is transformed into an unconstrained one [70]:

$$\text{Minimize } F(\mathbf{x}, p_r) = f + f_0 p_r \left(\sum_{i=1}^{n} X(x_i) + \sum_{j=1}^{j} G(g_j) + \sum_{m=1}^{m} H(h_m) + \sum_{l=1}^{l} W(w_l) \right) \tag{7.11}$$

where:

X = the penalty function for the design variable constraints.

G, H, and W = the penalty functions for the state variable constraints.

f_0 = the reference objective function value.

p_r = a response surface parameter.

f_0 is introduced in order to achieve consistent units. From Eq. (7.11), it is noticed that the unconstrained objective function, $F(\mathbf{x}, p_r)$, varies with the design variables and the quantity p_r.

The ALPF used for the design variable constraints is formed, near the upper limit, as:

$$X(x_i) = \begin{Bmatrix} \dfrac{c_1 + c_2}{(x^{up} - x_i)} & if \quad x_i < x^{up} - \varepsilon(x^{up} - x^{low}) \\ \dfrac{c_3 + c_4}{(x_i - x^{up})} & if \quad x_i \geq x^{up} - \varepsilon(x^{up} - x^{low}) \end{Bmatrix} \tag{7.12}$$

where:

$c_1, c_2, c_3,$ and c_4 = constraints that are internally calculated.

ε = very small positive number.

State variable penalties take a similar form.

7.2.2.3 Sequential Unconstrained Minimization Technique (SUMT)

SUMT is one of the techniques to solve the unconstrained optimization problem, Eq. (7.11). The idea behind the approach is to repeatedly call the unconstrained optimization algorithm using the solution of the previous iteration. The unconstrained algorithm itself executes many iterations [82]. In the SUMT, F reaches the minimum unconstrained objective function, $\breve{F}^{(k)}$, at design iteration k to solve Eq. (7.11) at each design iteration [70]; that is,

$$\mathbf{x}^{(k)} \to \breve{\mathbf{x}}^{(k)} \text{ as } F^{(k)} \to \breve{F}^{(k)} \tag{7.13}$$

where:

$\breve{\mathbf{x}}^{(k)}$ = the design variable vector corresponding to $\breve{F}^{(k)}$.

The design variable vector, $\mathbf{x}^{(k+1)}$, to be used in the next iteration (k+1) is determined according to the following equation:

$$\mathbf{x}^{(k+1)} = \mathbf{x}^{(b)} + C(\tilde{\mathbf{x}}^{(k)} - \mathbf{x}^{(b)}) \tag{7.14}$$

where:

$\mathbf{x}^{(b)}$ = the best design set constraints.

C = internally chosen to vary between *0.0* and *1.0*, based on the number of infeasible solutions.

7.2.2.4 Gradient-Based Technique

The *gradient-based technique* is another method to solve the unconstrained minimization problem, Eq. (7.11) using the gradient of the unconstrained objective function. Each search direction is established in each iteration using the steepest descent method and conjugate gradient method [82] by calculating the gradient of the unconstrained objective function. The gradient-based technique is briefly described, based on the ANSYS theory manual [70].

The gradient vector of the constrained objective function is approximately calculated in the following form:

$$\frac{\partial F(\mathbf{x}^{(k)})}{\partial x_i} \approx \frac{F(\mathbf{x}^{(k)} + \Delta x_i \mathbf{e}) - F(\mathbf{x}^{(k)})}{\Delta x_i} \tag{7.15}$$

where:

e = the vector with 1 in its ***ith*** component and *0* for all other components.

$\Delta x_i = \frac{\Delta D}{100}(x_i^{up} - x_i^{low})$ in which ΔD is the forward difference step size.

A search direction, $\mathbf{d}^{(k)}$, for each optimization iteration (k) is established during any iteration to obtain the design parameters for the next iteration (k+1).

$$\mathbf{x}^{(k+1)} = \mathbf{x}^{(k)} + s_k \mathbf{d}^{(k)} \tag{7.16}$$

The line search parameter, s_k, is measured from $\mathbf{x}^{(k)}$ and corresponds to the minimum value of F in the direction $\mathbf{d}^{(k)}$. A combination of a *golden-section algorithm* and *local quadratic fitting technique* (See [79] for details) is used for the solution to s_k. The range of s_k is limited to

$$0 \le s_k \le \frac{S_{\max}}{100} s_k^* \tag{7.17}$$

where:

s_j^* = largest possible step size for the line search of the current iteration (internally computed).

S_{max} = maximum (percent) line search step size.

The key to the solution of the minimization problem of Eq. (7.11) relies on the sequential generation of the search directions. For the initial iteration (k=0), the search direction is assumed to be the negative of the gradient of the unconstrained objective function, and p_r = 1 to search the design parameters in the direction of steepest descent.

$$\mathbf{d}^{(0)} = -\nabla F\left(\mathbf{x}^{(0)}, 1\right) \tag{7.18}$$

For subsequent iterations (k>0), conjugate directions are formed according to the *Polak-Ribiere recursion formula* [83].

$$\mathbf{d}^{(k)} = -\nabla Q(\mathbf{x}^{(k)}, p_r) + r_{k-1}\mathbf{d}^{(k-1)} \tag{7.19}$$

$$r_{k-1} = \frac{\left[\nabla F(\mathbf{x}^{(k)}, q) - \nabla F(\mathbf{x}^{(k-1)}, p_r)\right]^T \nabla F(\mathbf{x}^{(k)}, p_r)}{\left|\nabla F(\mathbf{x}^{(k-1)}, p_r)\right|^2} \tag{7.20}$$

Various steepest descent and conjugate direction searches are performed during each iteration until either convergence is achieved or termination occurs. Hence, each iteration is composed of several sub-iterations that include search direction and gradient computations.

7.2.2.5 Convergence

Minimization is performed on the approximated, penalized function (Eq. 7.11) until convergence is achieved. Convergence is assumed when either the present design set, $\mathbf{x}^{(k)}$, or the previous design set, $\mathbf{x}^{(k\text{-}1)}$, or the best design set, $\mathbf{x}^{(b)}$, is feasible; and one of the following conditions is satisfied [70].

$$\left|f^{(j)} - f^{(j-1)}\right| \le \tau \tag{7.21a}$$

$$\left|f^{(j)} - f^{(b)}\right| \le \tau \tag{7.21b}$$

$$\left|x_i^{(j)} - x_i^{(j-1)}\right| \le \rho_i \tag{7.21c}$$

$$\left|x_i^{(j)} - x_i^{(b)}\right| \le \rho_i \tag{7.21d}$$

where:

τ and ρ_i = objective function and design variable tolerances.

7.3 Optimization for Predefined Bend Angle

Process optimizations were implemented to seek a set of optimum parameter values to generate a specified bend angle. This section begins with a brief description of the optimization problem. Next, a mathematical modeling for the optimization problem is constructed. Then, a description of two numerical techniques to solve the optimization model is presented, which involves the optimization techniques introduced in the previous section. Finally, optimization results are demonstrated and compared, and a better optimization technique for the laser forming process is suggested.

7.3.1 Problem description

As mentioned in Chapter 1, a straight-line heating process in laser forming can be used to produce angular changes from a metal plate. In many practical applications of the process (See Section 7.1), a predefined angular change is required. It is well known that the magnitude of the bend angle is dependent on the process parameters (for example, laser power and feed rate). Therefore, it is available to produce a specified bend angle applying a combination of optimum process parameters.

This study presents optimization procedures to determine the optimum process parameters to generate a bend angle of 3° in a flat plate using a multiple heating process. To do this, the finite element model involving three irradiations developed in Section 4.5.4 is employed, and the optimum parameters are determined by applying design optimization techniques to the numerical model. Optimum values are searched with regard to outstanding input variables such as laser power, feed rate, beam diameter and number of scans. The range of input variables to be searched is listed in Table 7.1. In the following sections, an optimization problem for optimum searching is produced, and two optimization procedures involving the prescribed optimization algorithms are presented.

Table 7.1 The range of input variables to be searched.

Design variable	Range
Laser power, p (W)	1400 – 2000
Feed rate, v (m/sec)	0.001 – 0.008
Beam diameter, d (m)	0.010 – 0.025
Number of passes, n_p	1 – 4

7.3.2 Mathematical modeling

For searching the optimum values of process parameters in the present problem, the objective function is defined as the absolute value of the difference between the numerically calculated angle and the predefined angle of 3° (i.e., $|\alpha - 3.0|$). The maximum plate temperature occurring during the process is set as a constraint because it must remain below its melting point. The input variables such as laser power, feed rate, beam diameter and the number of scans are defined as the design variables. Therefore, the optimization problem can be assembled in the following form:

$$\text{Minimization } f = |\alpha - 3.0| \qquad \mathbf{x} = \lfloor p, v, d, n \rfloor \tag{7.22a}$$

subject to

$$p_{\min} \le p \le p_{\max} \tag{7.22b}$$

$$v_{\min} \le v \le v_{\max} \tag{7.22c}$$

$$d_{\min} \le d \le d_{\max} \tag{7.22d}$$

$$n_{\min} \le n \le n_{\max} \tag{7.22e}$$

$$T_{(0,0,0)} \le 1400 \tag{7.22f}$$

where:

f = the objective function.

α = the calculated angle (degree).

p = the laser power

v = the scanning speed

d = the diameter of the laser beam

n_p = the number of passes

$T_{(0,0,0)}$ = the temperature at the center of the sheet metal.

7.3.3 Numerical techniques used

Two numerical techniques are employed in this section and each technique is applied to solve the optimization problem, Eq. (7.26). One is a *non-gradient method* and the other is the *gradient-based method*. The *non-gradient method* requires only the values of the dependent variables (i.e., objective function and state variables) and not their derivatives. This algorithm is suitable for general engineering problems. On the other hand, the *gradient-based method* uses, as discussed in Section 7.2.2.4, derivatives for the objective function and state variables. This technique is more suitable for problems that require high accuracy. The drawback of this algorithm can be placed on high computation cost. Optimization procedures are performed through the finite element code ANSYS [77]. The computer program listings used for the current simulations are given in Appendix C.

Figure 7.1 shows the procedure of optimum searching involving the *non-gradient method*. It begins with the initial finite element analysis with the following design set: a laser power of 1500 W; a feed rate of 0.005 m/sec; a beam diameter of 0.016 m; and one irradiation. In order to establish both the

objective function approximation ($\widetilde{f}$) and the state variable approximation ($\widetilde{T}$) by means of least squares fitting, a certain number of sampling sets, n_s, are initially generated at random using the random design tool [70] for preliminary trial simulations. If n_s equals or is less than n+2 and the number of defined feasible simulations, random design sets are generated. If n_s is more than n+2 and the number of defined feasible simulations, the approximations are formed. In this study, more than six feasible preliminary simulations are needed for the surface fitting due to the four design variables (i.e., p, v, d and n) associated with the approximations. The constrained minimization problem constructed with the approximated functions is converted to an unconstrained problem, $F(\mathbf{x}, p_r)$. $F(\mathbf{x}, p_r)$ is calculated at each design variable. FE-simulations are iterated with updated design variable until the convergence is achieved. Each iteration is equivalent to one complete analysis loop.

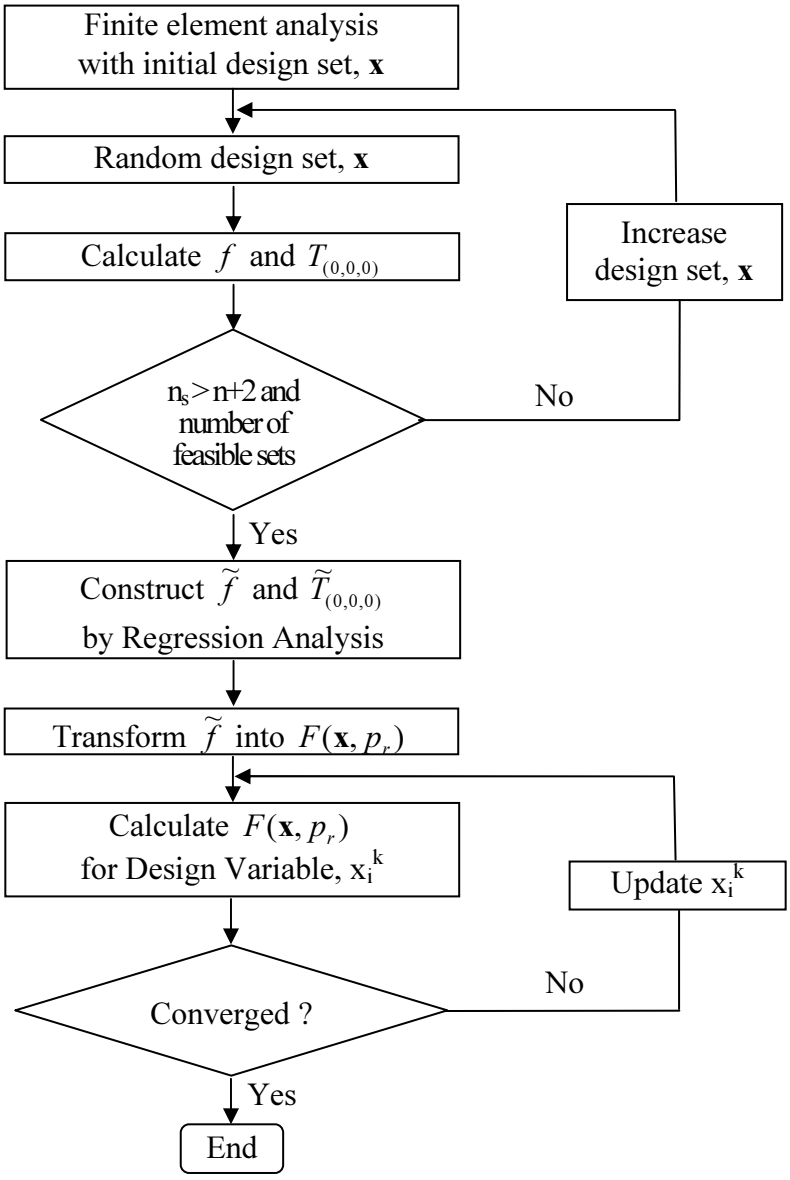

Figure 7.1 Schematic diagram of the optimization procedure involving the *non-gradient method*.

Figure 7.2 shows the schematic diagram of the optimization procedure involving the *gradient-based method*. After the initial finite element analysis, the constrained minimization problem is transformed into an unconstrained problem, $F(\mathbf{x}, p_r)$ on which minimization is performed with simulations. FE-simulations are iterated with design sets updated by the gradient of $F(\mathbf{x}, p_r)$ for each design variable until the design variables are out of the given space. When the best design set chosen after the iterations does not satisfy the defined convergence condition, the design set is updated to repeat this procedure. This means that one optimization iteration will perform several FE-simulations, which is the reason that the *gradient-based method* is more computationally demanding than the *non-gradient method*. If the optimum design set is considered to hit the local minimum, a different design set has to be selected via the *random design tool*, and the whole loop is iterated until the design set hits the global minimum.

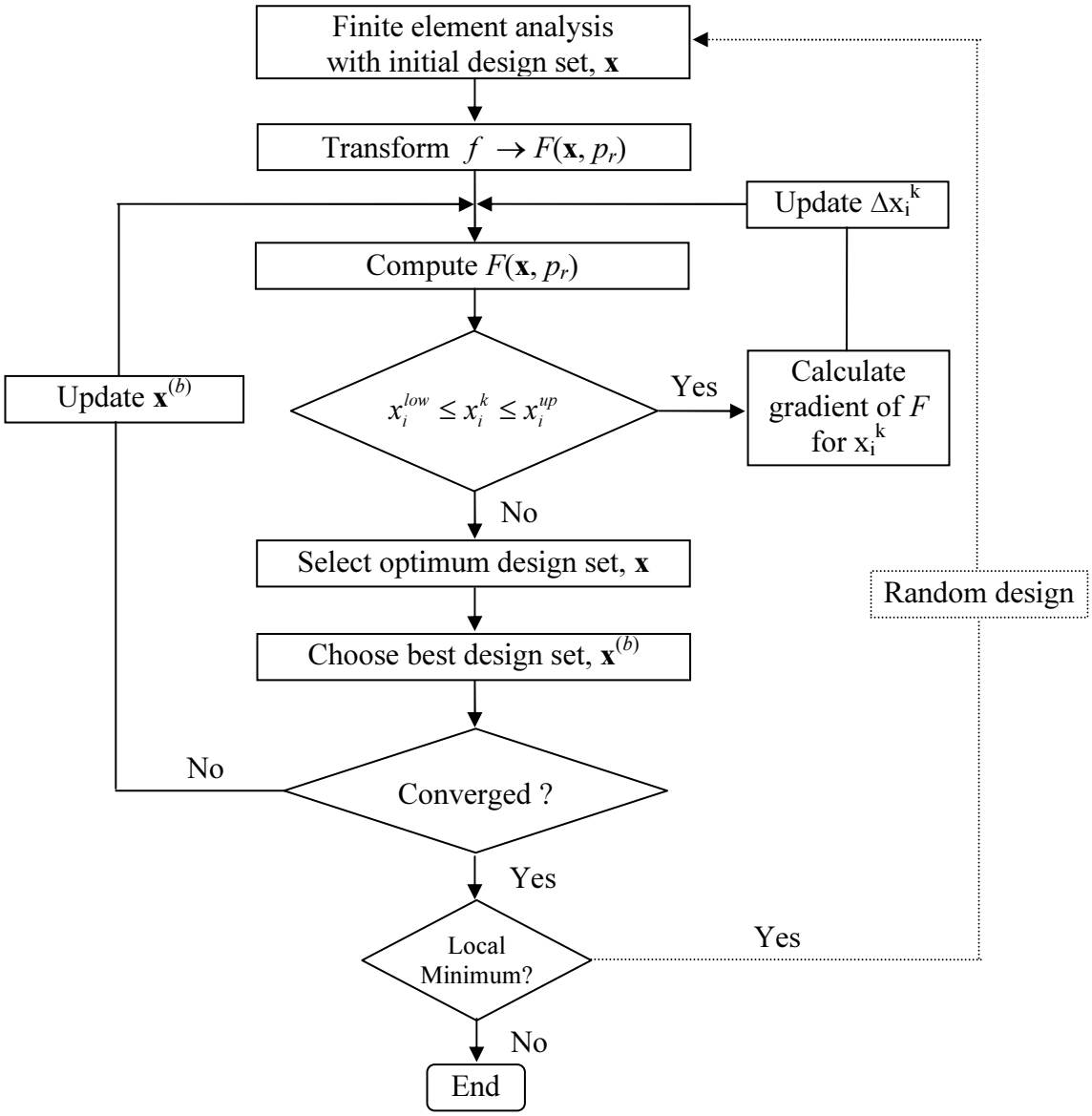

Figure 7.2 Schematic diagram of the optimization procedure involving the *gradient-based method*.

7.3.3 Optimization results

Results obtained by the two optimization procedures are presented and compared in the sub-sections that follow. One of the two optimization techniques, more suitable for the laser forming, is selected to apply it to a new optimization problem in Section 7.4.

7.3.3.1 Results from the non-gradient method

The minimization problem, Eqs. (7.22*a-f*), was solved through the optimization procedure involving the *non-gradient method*. Table 7.2 presents the initial relationship between the independent variables (i.e., laser power, scan speed, beam diameter and the number of scan) and the dependent variables (i.e., bend angle or temperature distribution) generated by the random design tool and FE-simulations to construct the objective function and state variable approximations. In this study, ten feasible sets, rather than six, were obtained in a way to increase the rate of convergence. Infeasible design sets (i.e., sets 5, 9, 12 and 13) due to temperatures exceeding the melting point were removed in the approximation process. A quadratic equation with cross terms was set for a curve fitting of the objective function, and a quadratic fit was set for the state variable. The weight coefficient φ^k in Eq. (7.6) was computed and was based on the objective function values, where the design sets with low objective function values have high weight.

Table 7.2 Initial relationship between independent variables and dependent variables.

Set	Design variables				FE-simulation		
	p	v	d	n	α	$T_{(0,0,0)}$	f
1	1500	0.0050	0.016	1	0.47	728	2.522
2	1908	0.0042	0.016	4	7.83	1134	4.826
3	1723	0.0053	0.023	2	0.46	531	2.542
4	1682	0.0032	0.022	3	2.10	678	0.897
5	1817	0.0015	0.015	2	3.47	*3023	0.467
6	1718	0.0079	0.019	2	0.20	506	2.796
7	1863	0.0049	0.017	4	2.96	803	0.040
8	1902	0.0018	0.021	4	9.20	1235	6.197
9	1755	0.0014	0.016	2	9.20	$*1x10^7$	$1x10^7$
10	1672	0.0069	0.015	3	2.09	835	0.910
11	1865	0.0060	0.011	3	5.06	1213	2.064
12	1630	0.0014	0.010	3	5.06	$*1x10^7$	$1x10^7$
13	1729	0.0013	0.011	3	5.06	$*1x10^7$	$1x10^7$
14	1830	0.0038	0.021	4	3.91	722	0.905

Note: A "*" symbol indicates an infeasible set.

Figure 7.3 presents the variation of the objective function and state variable (i.e., temperature) during the optimization searching process. It is noted from the figure that a total of 22 design sets have been produced for the simulations to find a converged solution in the unconstrained problem. Set 18 is considered to be the optimum process parameter set to produce the predefined bend angle of 3° because it yields the minimum objective function (i.e., 0.037) and satisfies the temperature constraint as 908 °C.

Figure 7.4 shows the variation of the bend angle calculated and the line indicating the target angle of 3° against the design set. It can be seen that the simulation with design set 18 produced a bend angle of 3.04° that is very close to the predefined bend angle.

Figure 7.5 illustrates the variation of the process variables with respect to design set. The optimum values of the process parameters needed to generate the target bend angle of 3° can be found with set 18. The detailed values are listed in Table 7.3. Figure 7.6 shows the bend angle and temperature histories during the laser forming simulation with the optimum processing condition.

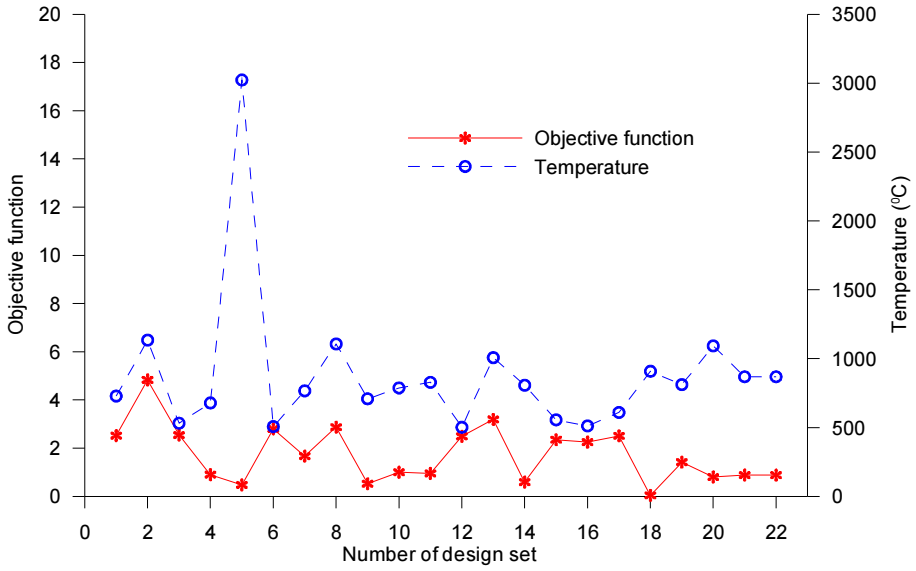

Figure 7.3 Variation of the objective function and temperature during the optimization by the *non-gradient method* to produce a predefined bend angle of 3°.

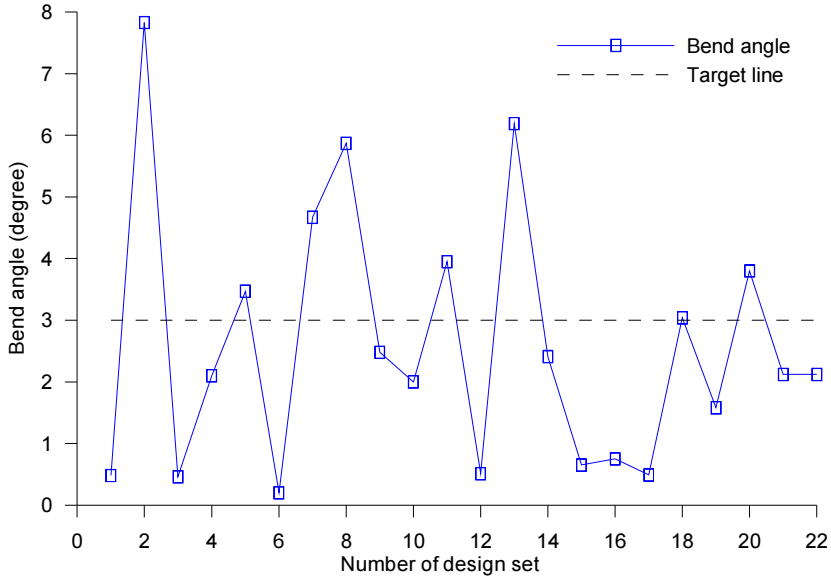

Figure 7.4 Variation of the bend angle during the optimization by the *non-gradient method* to produce a predefined bend angle of 3°.

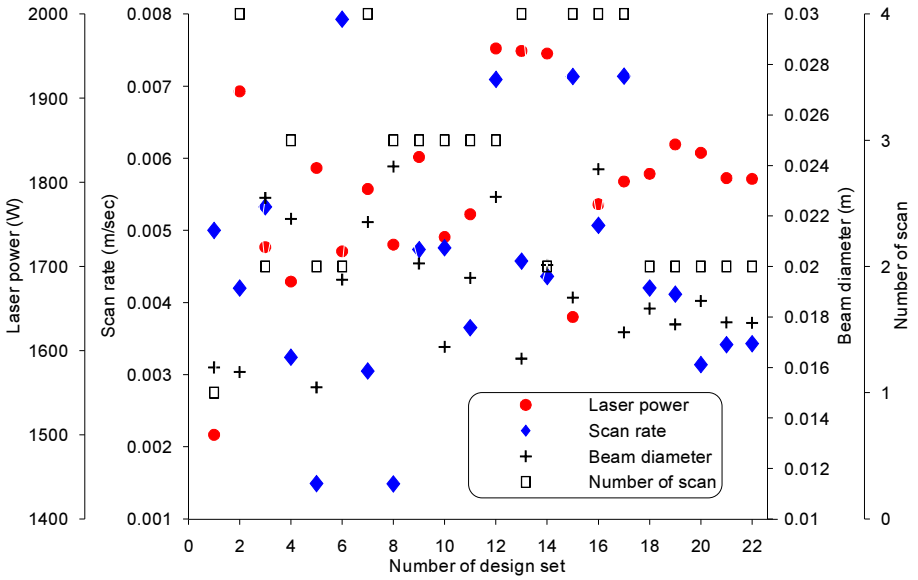

Figure 7.5 Variation of the process variables during the optimization by the *non-gradient method* to produce a predefined bend angle of 3°.

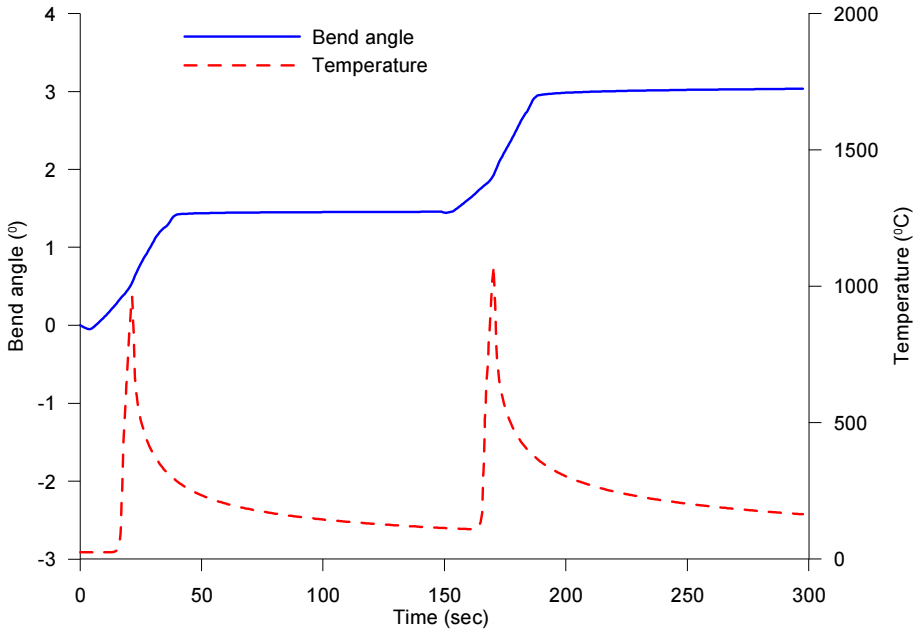

Figure 7.6 The bend angle and temperature histories during the laser forming simulation with the optimum condition from the *non-gradient method*.

Table 7.3 Optimum process parameters obtained by the *non-gradient method* to produce a predefined bend angle of 3°.

Process parameter	Value
Laser power (W)	1810
Scan speed (m/sec)	0.0042
Beam diameter (m)	0.018
Number of passes (n_p)	2

7.3.3.2 Results from the gradient-based method

The minimization problem, Eqs. (7.22*a-f*), was solved using the optimization procedure involving the *gradient-based method* described in Figure 7.2. Figure 7.7 presents the variation of the objective function and temperature against design set during the optimisation processes. The optimisation was converged with design set 3 with which a minimum objective function of 1.6×10^{-4} was achieved and the temperature reached 716 °C. As shown in Figure 7.8, the bend angle of 2.999° was produced with process set 3. Figure 7.9 shows the variation of the process variables against design set. Optimum process parameters to achieve the bend angle of 2.999° are listed in Table 7.4.

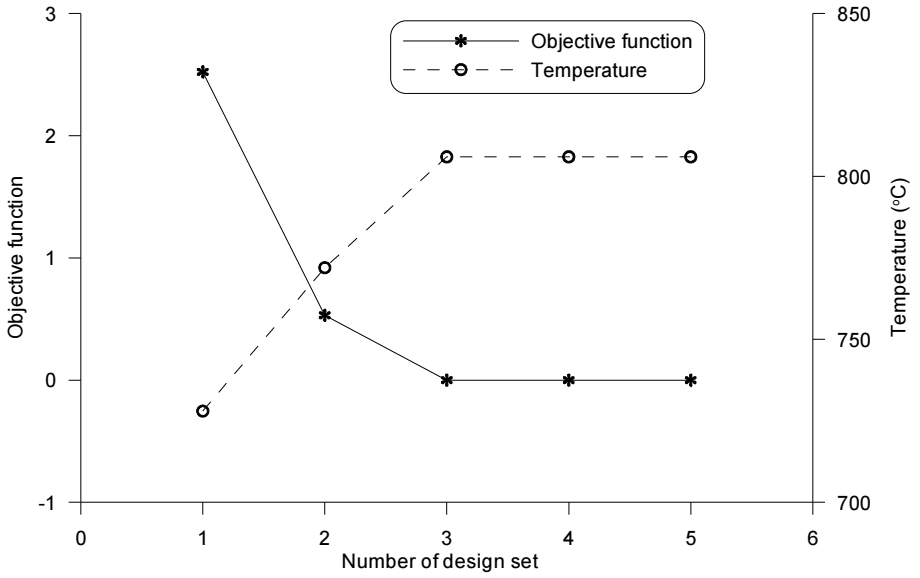

Figure 7.7 Variation of the objective function and temperature during the optimization by the *gradient-based method* to produce a predefined bend angle of 3°.

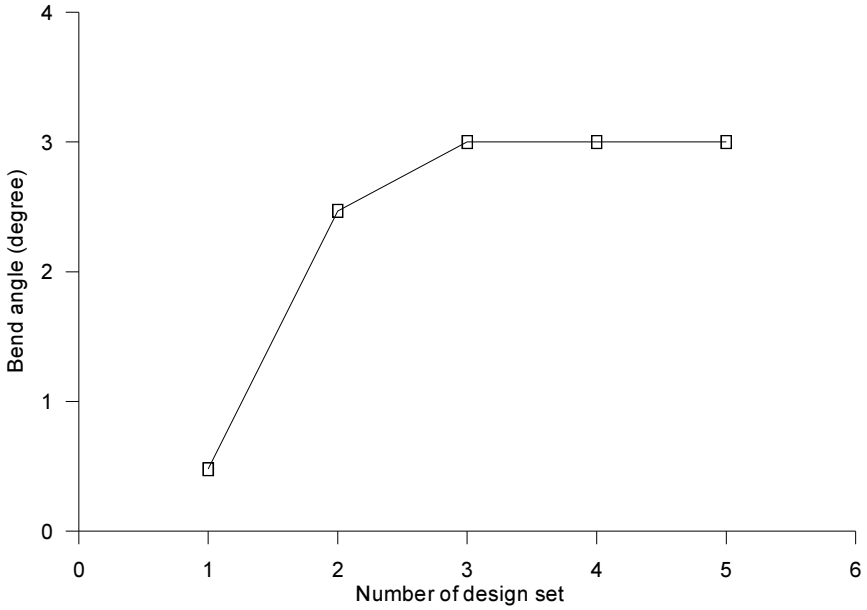

Figure 7.8 Variation of the bend angle during the optimization by the *gradient-based method* to produce a predefined bend angle of 3°.

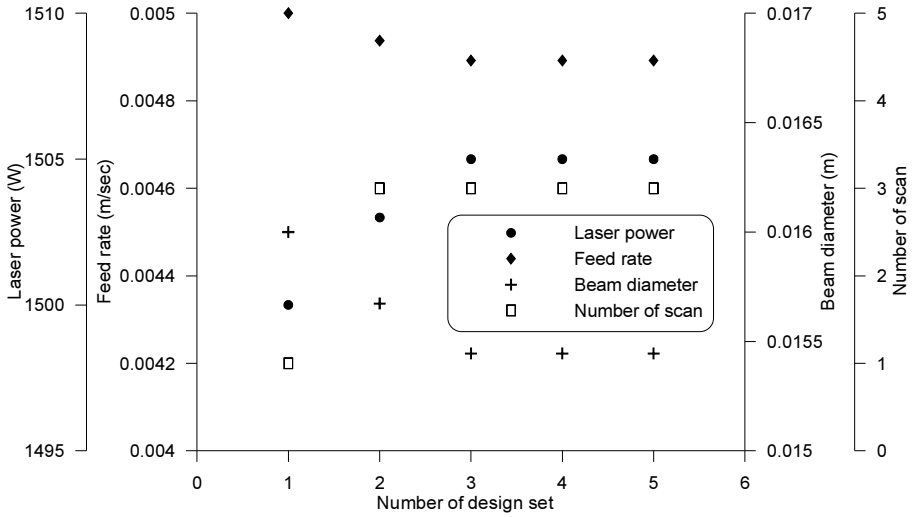

Figure 7.9 Variation of the process variables during the optimization by the *gradient-based method* to produce a predefined bend angle of 3°.

Table 7.4 Optimum process parameters obtained by the *gradient-based method* to produce a predefined bend angle of 3°.

Process parameter	Value
Laser power (W)	1505
Scan speed (m/sec)	0.0049
Beam diameter (m)	0.015
Number of passes (n_p)	3

7.3.3.3 Comparison of the results

Optimization results and simulation times of the *non-gradient method* and the *gradient-based method* to achieve a predefined angle of 3° in a multiple irradiation laser forming are compared to assess suitability as an optimization technique for laser forming. The simulations including the *non-gradient method* and the *gradient-based method* were run on a CYCLONE ASUS system with an AMD Athlon™ 64 processor (3500+, MMX, ~2.2GHz) and a memory of 2048MB RAM. Table 7.5 shows each optimization result and runtime. It is noted from the table that the bend angles obtained from the *non-gradient method* and the *gradient-based method* are very close to the target angle of 3° so there is no accuracy problem in either optimization technique. However, the runtime of the *non-gradient method* (32.68 hours) is much lower than that of the *gradient-based method* (120.26 hours). Therefore, it can be said that the optimization procedure involving the *non-gradient method* is more suitable for the laser forming problem than that involving the *gradient-based method* from the point of view of computing time.

Table 7.5 Comparison of optimization results from the *non-gradient method* and the *gradient-based method*.

Optimization technique / Simulation results		*Non-gradient method*	*Gradient-based method*
Optimization results	Bend angle (°)	2.987	2.999
	Temperature (°C)	908	806
	Laser power (W)	1810	1505
	Feed rate (m/sec)	0.0042	0.0049
	Beam diameter (m)	0.018	0.015
	Number of scan	2	3
Simulation time (Hour)		32.68	120.26

7.4 Optimization for Maximum Bend Angle

In the previous section, it has been demonstrated that a set of optimum process parameters can be found to obtain a desired bend angle via optimization procedures, and the procedure involving the *non-gradient method* is more suitable to seek the optimum condition in the laser forming than the *gradient-based method*.

A new optimization problem is defined in this section as achieving maximum bend angle in one pass in the straight-line laser forming process. It is predicted that the maximum bend angle is produced with the maximum number of irradiations. Thus, a single straight-line irradiation process is considered in this case, and optimum values of laser power, feed rate and beam diameter are sought through the optimization procedure involving the the *non-gradient method*. The range of input variables to be searched is the same as that listed in Table 7.1.

The objective function can be defined as a large positive number subtracted by the expected bend angle because the optimization technique tries to minimize the objective function and the negative values in the objective function may cause numerical problems. The maximum temperature produced in the plate during the process is defined as a constraint again in this case. Therefore, the minimization problem with constraints can be stated as follows:

$$\text{Minimization } f = 100 - \alpha \qquad \mathbf{x} = \lfloor p, v, d \rfloor \tag{7.23a}$$

subject to

$$p^{low} \le p \le p^{up} \tag{7.23b}$$

$$v^{low} \le v \le v^{up} \tag{7.23c}$$

$$d^{low} \le d \le d^{up} \tag{7.23d}$$

$$T_{(0,0,0)} \le 1400 \tag{7.23e}$$

where:

f = the objective function.

α = the calculated angle (degree).

p = the laser power

v = the scanning speed

d = the diameter of the laser beam

$T_{(0,0,0)}$ = the temperature at the center of the sheet metal.

The minimization problem, Eqs (7.23*a*-*e*), was solved through the procedure shown in Figure 7.1. The optimization results are illustrated in Figures 7.10 to 7.12. Figure 7.10 presents the variation of the objective function and temperature with regard to design set during the optimization. The minimum objective function of 97.656 is found in set 11, but the high temperature rise of 2139 °C does not meet the constraint that the maximum temperature should remain below the melting point of 1400 °C. Thus, the next minimum objective function of 97.784 found in set 13 is selected as the solution of the optimization problem. The bend angle achieved with the optimum condition (i.e., design set 13) is 2.216 degrees as shown in Figure 7.11. It is much greater than the bend angle of 0.47 degrees produced with the initial design set (See Figure 4.25). As shown in Figure 7.12, the values of the optimum parameters are: 1999 watts in the laser power; 0.0036 m/s in the feed rate; and 0.0158 m in the beam diameter.

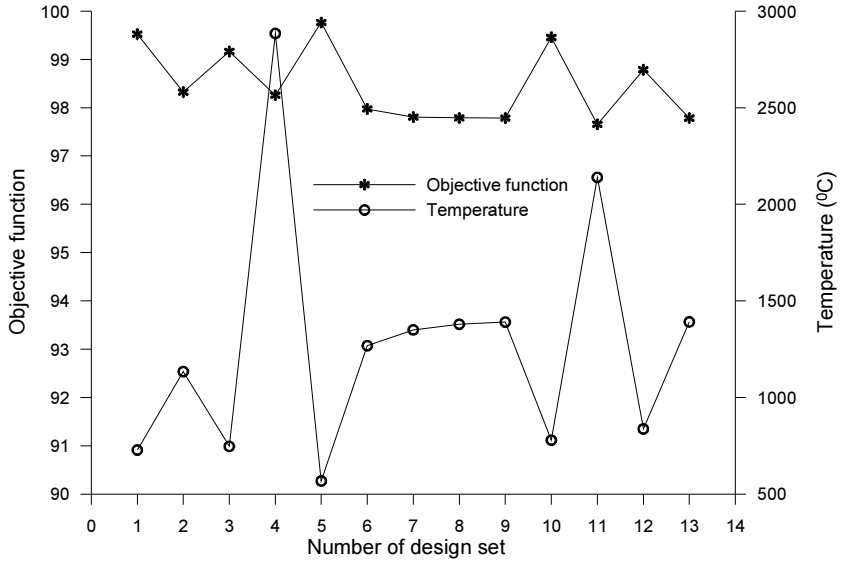

Figure 7.10 Variation of the objective function and temperature during the optimization by the *non-gradient method* to obtain a maximum bend angle.

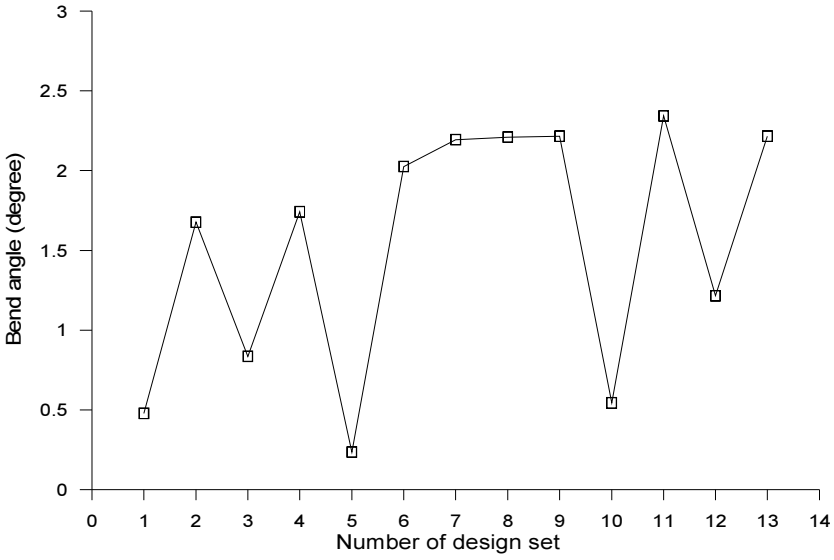

Figure 7.11 Variation of the bend angle during the optimization by the *non-gradient method* to obtain a maximum bend angle.

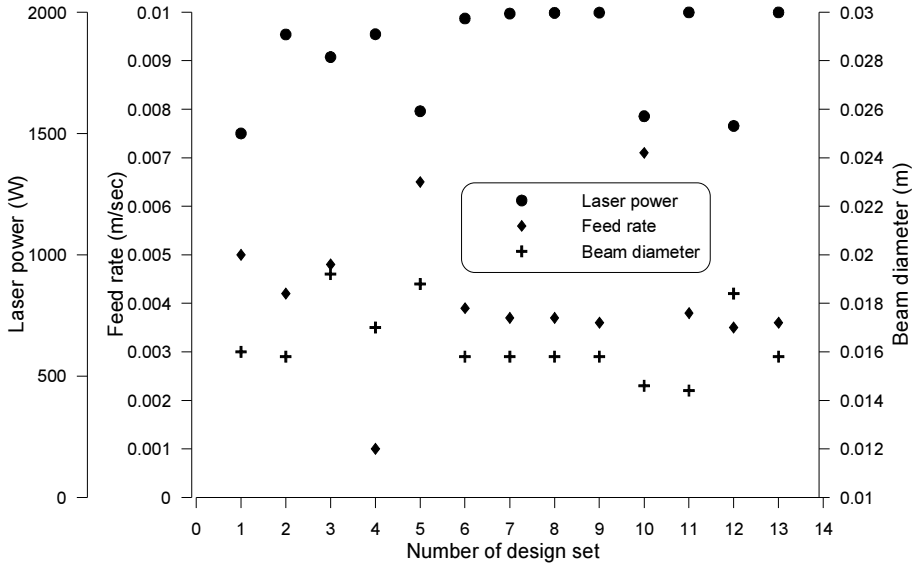

Figure 7.12 Variation of the process variables during the optimization by the *non-gradient method* to obtain a maximum bend angle.

7.5 Summary

This chapter has described the concept of design optimization and optimization techniques. Two kinds of optimum processing searching techniques (i.e., the non-gradient method and the gradient-based method) were applied to an optimization problem to produce a predefined bend angle with multiple passes in laser forming. It was found that the *non-gradient method* is more suitable to seek optimum condition in laser forming. A new optimization problem to produce a maximum bend angle with a single pass in laser forming was solved using the *non-gradient method*. Optimum processing values satisfying the two optimization problems were determined with respect to input variables such as laser power, feed rate, beam diameter and number of passes. The key points of this chapter have included:

- An optimization problem is to find a set of optimum design variables in order to minimize an objective function (typically a function of several design variables), subject to one or more constraints. Some common algorithms used to solve a constrained optimization problem are described, which are *surface response methodology*, *penalty function technique*, *sequential unconstrained minimization technique*, and *gradient-based technique*.

- The scheme of process optimization procedures in laser forming is to introduce the optimization techniques into the finite element analysis of the laser forming process. A dependent variable of the bend angle can be used to construct the objective function, the maximum temperature occurring during the process can be chosen as a constraint, and input variables such as laser power, feed rate, beam diameter and number of passes can be defined as the design variables.

- Two optimization techniques were studied – one is the *non-gradient method* and the other is the *gradient-based method*. The *non-gradient method* requires only the values of the objective function and state variables and not their derivatives. The *gradient-based method* makes use of derivatives for the objective function and the state variables. In order to assess suitability as an optimization technique for laser forming, the two methods were compared by solving an optimization problem to produce a predefined bend angle of 3° with multiple passes in laser forming. It was found that the bend angles obtained from the methods are very close to the target angle: 2.987° from the *non-gradient method* and 2.999° from the *gradient-based method*. However, the runtime of the *non-gradient method* (32.68 hours) is much lower than that of the *gradient-based method* (120.26 hours). Therefore, it is concluded that the optimization procedure involving the non-gradient method is more suitable for the laser forming problem from the point of view of computing time.

- A new optimum process condition was sought by the *non-gradient method* to generate a maximum bend angle in a single pass of laser forming. The maximum bend angle of 2.216° was obtained with a set of optimum process parameters: a laser power of 1999 Watts; a feed rate of 0.0036 m/s; and a beam diameter of 0.0158 m. The maximum bend angle is much greater than the bend angle of 0.47° produced with the initial process parameters.

Chapter 8

Analysis of Process Reliability

8.1 Introduction

In Chapter 7, a predefined bend angle of 3° was obtained via the FE-simulation of the straight-line laser forming process with a set of optimum process parameters. However, under real life conditions the bend angles produced are subject to uncertainties of input (process) variables. For example, the laser power and feed rate could be slightly variable during the forming process, and the material properties and geometric dimensions of the plate used are variable within engineering tolerances. It is therefore required to examine how much the resulting angular changes are affected by the uncertainties of the independent variables in a way to evaluate the robustness of the process.

This chapter aims to apply a well-known reliability analysis to laser forming to assess the reliability of the laser forming process by evaluating the uncertainties of independent variables. The basic concept of the uncertainty analysis in laser forming is to link the finite element analysis of the laser forming process into the standard reliability analyses. Statistical analysis techniques used are described. The procedure of the analysis is presented. An example of the assessment is demonstrated using the straight-line heating process optimized to produce a bend angle of 3° in the previous chapter.

8.2 Analysis Techniques Used

The most common and traditional reliability analysis method for physical and mathematical problems is the Monte Carlo method. This method is performed through statistical sampling experiments on a computer. In this study, two kinds of the Monte Carlo simulations are applied to uncertainty analysis in laser forming – one is the one based on an approximate mathematical model representing the relationship between input variables and output variables, the other is the one generated on a large number of FE-simulations of the laser forming process.

In order to underpin the theoretical background of the two Monte Carlo simulations, the concepts of the techniques adopted in the simulations are described in this section, which involves the response surface methodology, a sampling technique of central composite design, and a statistical distribution. This section begins with a brief description of the Monte Carlo method.

8.2.1 Monte Carlo method [84]

The Monte Carlo method is the process of approximating expected values by sample means. Thus it is an attempt to do computations by a large number of sampled data. The method is stated as follows. Let F be a distribution function on some probability space, Ω, and let g be any real-valued function on the same space. Then the expected value of g with respect to F is

$$E(g,F) = \int_{\Omega} g(x)dF(x) \tag{8.1}$$

If the expectation of g exists, then with probability 1 the mean of g for a large number of samples, M, from F, namely,

$$\mu(g,F,M) = \left(\sum_{i=1}^{M} g(z_i) \right) / M \tag{8.2}$$

tends to E(g, F) as $M \to \infty$, where z_i are independently distributed according to F.

As a computational technique, the Monte Carlo method is simply the attempt to compute Eq. (8.1) approximately, as the mean of $\{g(z_i)\}$, where $\{z_i\}$ is a sequence of pseudorandom numbers generated from the distribution F (See Chambers [84] for details).

As a sampling technique, the Latin Hypercube sampling (LHS) is used [70]. The sampling technique divides the domain of each random input variable into intervals of equal probability. A sample location can be selected randomly within the interval.

8.2.2 Response surface methodology (RSM)

RSM is a method to construct a global approximation of system behavior based on the fundamental assumption that the influence of input variables on output variables can be approximated by a mathematical function, typically a quadratic polynomial. The progress of forming the approximated relationship between the two variables is demonstrated.

Consider that an output parameter f depends on a set of uncertain input variables $\mathbf{x}$. The functional relationship between f and $\mathbf{x}$ is expressed as:

$$f = f(\mathbf{x}) \tag{8.3}$$

An approximate function, $\widetilde{f}$, of the response function, f, can be obtained from the regression analysis of Eqs. (7.5) to (7.8). For convenience, we rewrite the procedure:

$$f \cong \widetilde{f} = a_0 + \sum_i^n a_i x_i + \sum_i^n \sum_j^n a_{ij} x_i x_j \tag{8.4}$$

The coefficients, {a}, in Eq. (8.4) are determined using the method of least squares, which is based on minimizing the following sum of the squared errors (SSE):

$$SSE = \sum_{k=1}^{n_s} \left[\varphi^k (f^k - \widetilde{f}^k)^2 \right] = \sum_{k=1}^{n_s} \left[\varphi^k (f^k - a_0 + \sum_{i}^{n} a_i x^k i + \sum_{i}^{n} \sum_{j}^{n} a_{ij} x^k i x^k j)^2 \right] \quad (8.5)$$

where:

φ^k = the weight coefficient associated with the k[th] design sampling set.

k = the number of current design sampling set.

n_s = the number of sampling points.

The solution to the unknown coefficient is

$$\{a\} = \left([d]^T [d] \right)^{-1} [d]^T \{f\} \quad (8.6)$$

where:

$[d]$ = the sampled design matrix expressed as:

$$[d] = \begin{bmatrix} \lfloor 1 \; x_{1,1} \; x_{2,1} \ldots x_{n,1} \; x_{1,1}^2 \; x_{1,1}x_{2,1} \cdots x_{1,1}x_{n,1} \; x_{2,1}^2 \cdots x_{2,1}x_{n,1} \cdots x_{n,1}^2 \rfloor \\ \vdots \\ \lfloor 1 \; x_{1,n_s} \cdots x_{n,n_s} \; x_{1,n_s}^2 \; x_{1,n_s}x_{2,n_s} \cdots x_{1,1}x_{n,n_s} \; x_{2,n_s}^2 \cdots x_{2,n_s}x_{n,n_s} \cdots x_{n,n_s}^2 \rfloor \end{bmatrix} \quad (8.7)$$

The significant individual regression terms are iteratively added to the regression model through the *forward-stepwise-regression* [70, 85]. To determine if an additional term T_{p+1} would be a significant improvement of the regression model, a *partial Fisher F-test*, F_{p+1}^*, can be used.

$$F_{p+1}^{*} = \frac{\dfrac{SSE_p - SSE_{p+1}}{v_p - v_{p+1}}}{\dfrac{SSE_{p+1}}{v_{p+1}}} \tag{8.8}$$

where:

p = the number of the existing terms.

$SSE_x = SSE$ with x terms.

v_x = the degrees of freedom (DOF) with x terms ($=n_s - x$).

An additional term T_{p+1} is considered to be a significant improvement for the regression model only if the following condition is satisfied:

$$F_{p+1}^{*} > F^{-1}\left(1-\alpha \middle| 1, n-(p+1)\right) \tag{8.9}$$

where:

$F^{-1}\left(..\middle|v_1, v_2\right)$ = the inverse cumulative distribution function of the Fisher F-distribution with v_1 numerator DOF and v_2 denominator DOF.

The SSE can be used to test validity of the response surface. That is, if the SSE is as close as possible to zero, it indicates that a good fit is achieved.

8.2.3 Central composite design (CCD)

The response surface, Eq. (8.4), is determined by a certain number of trial tests, and the accuracy of the response surface analysis depends on the good predictions of the surface. Thus, when sampling design points for the preliminary tests, it is very important to explore the space of input variables in the most efficient way to make a well-defined regression model with a minimum number of sampling points. It has been known that the CCD is the most popular class of designs used for fitting the response surface [81]. Generally, in the sampling technique, when the number of input variables is k,

the sampling points are composed of a central point, $2k$ axial or star points, and 2^k factorial with n_F points located at the corners of an k-dimensional hypercube where n_F is the number of points used in the fractional portion of the design. These points are located at five different probability levels of the input variables. A defining equation is used to determine the probability levels (See [86] for some examples). Figure 8.1 shows the sampling points for k = 3 factors.

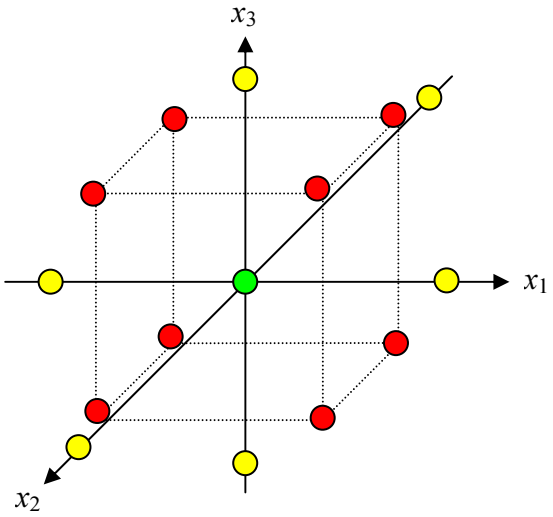

Figure 8.1 Sampling points in the central composite design for k = 3 [85].

8.2.4 Gaussian distribution

A Gaussian distribution of a variable X has two distribution parameters: the mean value, μ and the standard deviation, σ.

The probability density function for a random variable X in a Gaussian distribution is expressed as:

$$f(x) = \frac{1}{\sqrt{2\pi \cdot \sigma^2}} e^{-\frac{1}{2}\left(\frac{x-\mu}{\sigma}\right)^2} \tag{8.10}$$

where:

x = each value which can be taken by the random variable X.

The probability density function of the random variable X represents a measure for the relative frequency at which values of input variables are expected to occur. Figure 8.2 (a) shows the graphical representation of the probability density function of a Gaussian distribution.

The cumulative distribution function of a Gaussian distribution is defined as:

$$F(x) = P\{X \leq x\} \tag{8.11}$$

The cumulative distribution function of the random variable X is the probability that values for the random variable remain below a certain limit x. Figure 8.2 (b) shows graphically the cumulative distribution function of a Gaussian distribution.

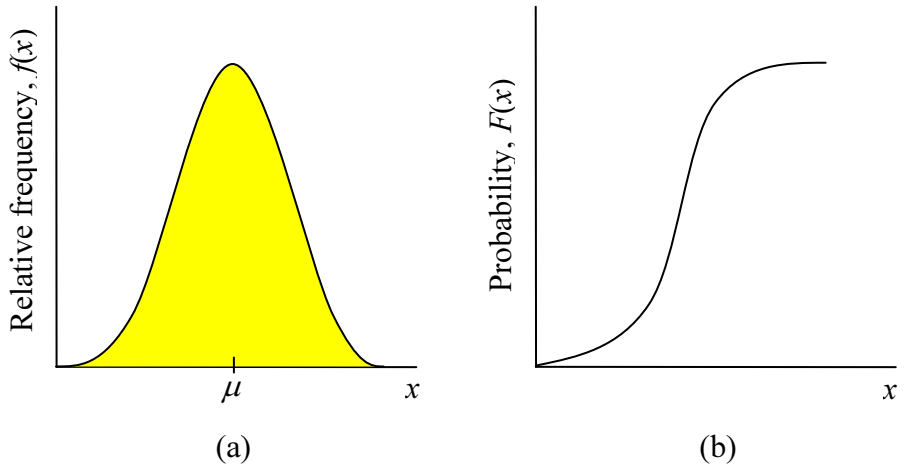

Figure 8.2 Gaussian distribution functions: (a) Probability density function and (b) Cumulative distribution function.

8.3 Analysis of Process Reliability

This section examines the effects of uncertain input variables on the resulting bend angle in a straight-line heating process using the Monte Carlo simulations. Firstly, a laser forming problem to be investigated is briefly described. Next, the reliability analysis procedure is demonstrated. Then, the results of reliability analysis from the Monte Carlo simulations on response surface are described. Finally, results from the Monte Carlo simulations generated on the FE-simulations of the laser forming process are demonstrated, which is compared for validation of the results of the Monte Carlo simulations on response surface.

8.3.1 Problem description

The laser forming process adopted for the reliability analysis is the straight-line heating process with the optimum process parameters to produce a bend angle 3° (See Section 7.3.3.1, Chapter 7). The values of the optimum parameters are rewritten: a laser power of 1810 watts, a feed rate of 0.0042 m/sec, a beam diameter of 0.018 m, and two irradiations. It has been known that the process parameters of laser power p, scan speed v, thermal expansion coefficient β and material thickness t have significant influence on the resulting bend angle α. Thus, uncertainties of those variables are defined as the input variables for the present analysis, and the bend angle is defined as the output variable. It is assumed that the scatter of the input variables can be described with a Gaussian distribution function because it is considered the standard deviations of the variables are very small compared to their mean values. The mean values, μ, and standard deviations, σ, of the variables are listed in Table 8.1. For computer analysis of the process, the parametrically defined finite element model is used as the analysis file.

As simulation results, the distribution of the bend angle is described in terms of the mean value, the standard deviation, and the minimum and maximum values. The relative frequencies at which values of the bend angle are expected to occur, and the probability that the bend angle remains between specified ranges are determined as analysis results.

Table 8.1 Statistical property for input variables for the reliability analysis.

Variable	p (W)	v (m/sec)	t (m)	β (1/°C)
μ	1.81×10^{3}	4.2×10^{-3}	6.0×10^{-3}	1.17×10^{-5}
σ	2.0×10^{-1}	1.0×10^{-5}	1.0×10^{-5}	1.0×10^{-7}

8.3.2 The reliability analysis procedure

As mentioned in the previous section, the Monte Carlo simulations are performed via statistical sampling experiments on a computer. Thus, when the Monte Carlo simulations are carried out based on a large number of FE-simulations of the laser forming process, the Monte Carlo method is very computationally intensive because one sampling experiment represents one simulation loop in the finite element analysis of the laser forming process. Clearly it is needed to limit FE-simulations. Therefore, this chapter has the focus on the Monte Carlo simulations on response surface for the reliability analysis.

The reliability analysis procedure of the Monte Carlo simulations on response surface can be summarized as shown in Figure 8.3. The finite element model is parametrically built to be used as an analysis file. The outputs such as

displacements are calculated with respect to uncertain process parameters by the finite element analysis, and the results are saved in the database to be used for the construction of the response surface. When the number of simulation loops is less than the number of sampling points defined by the CCD, the sampling point is updated for the next simulation. When the number of simulation loops meets the condition defined by the CCD, the response surface is found and it is directly used to assess the input-output relationship. With the regression model formed, thousands of simulations can be carried out within a second, and the simulation results are used for statistical analysis.

The Monte Carlo method based on a large number of FE-simulations always provides correct results if the finite element is correct and a large number of simulation loops are performed [70]. However, it is not feasible to run an infinite number of simulations, thus it is assumed that the limited number of simulations is statistically representative of the results that are evaluated. This assumption can be verified using the confidence limits. For this reason, the Monte Carlo method based on the FE-simulations is carried out, and the results are used for validation of the results from the Monte Carlo simulations on the response surface.

The analyses by the Monte Carlo methods are implemented based on the *ANSYS Probabilistic Design System* (PDS) [77]. The computer program listings used for the simulations are given in Appendix C.

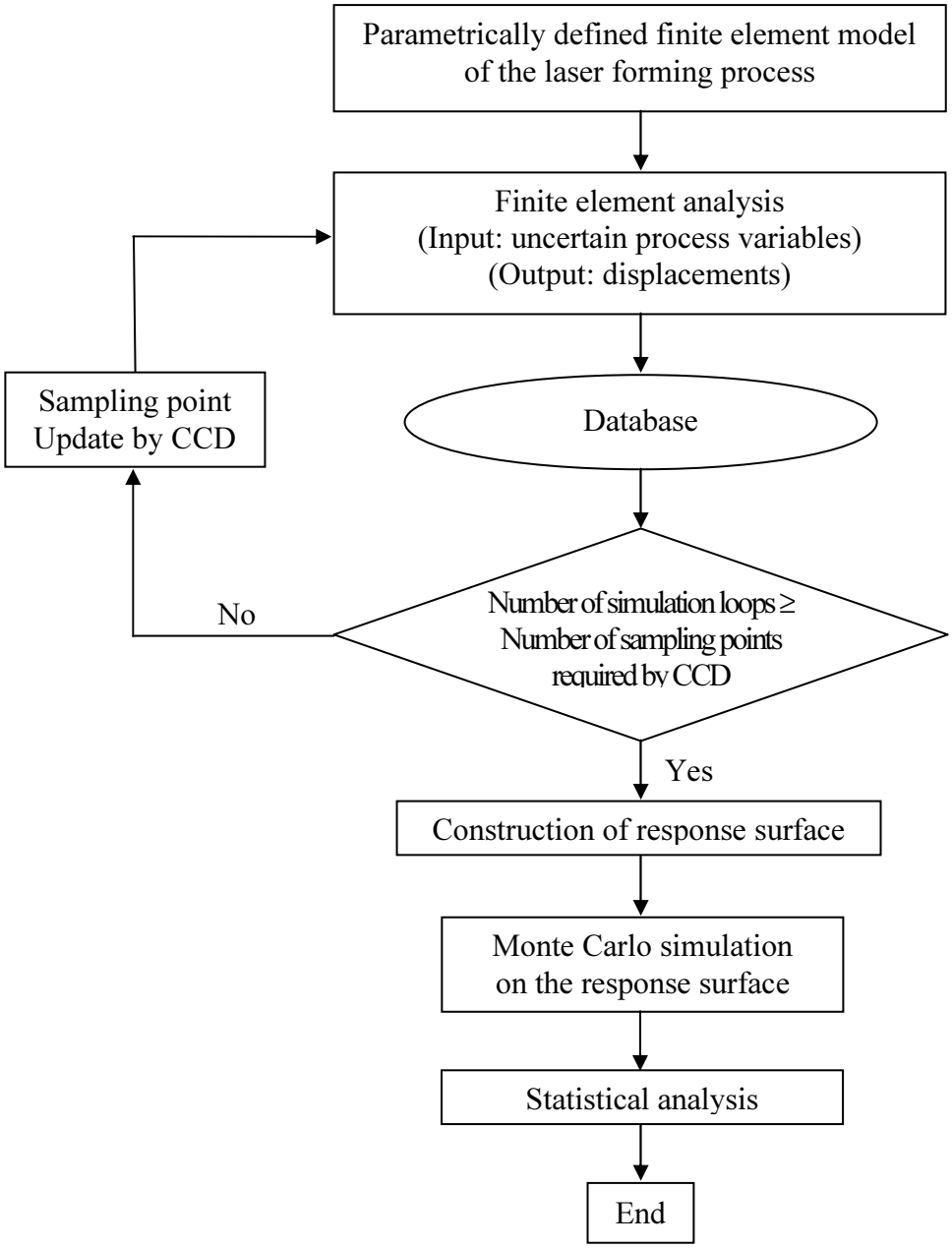

Figure 8.3 Schematic diagram of the reliability analysis procedure by the Monte Carlo simulations on the response surface.

8.3.3 Results from the Monte Carlo simulations on the response surface

Results of the reliability analysis by the Monte Carlo simulations on the response surface are presented in this section. Table 8.2 lists both the 25 design points (i.e., a series of combination of input variables) sampled by the CCD and each corresponding response (i.e., the bend angle) from the FE-simulations. Using these design data, a quadratic approximation model to the bend angle is fitted as shown in Figure 8.4. The output from the ANSYS PDS presents the approximation function in terms of the scaled variables, which can be represented in terms of the actual factors as follows:

$$\begin{aligned}\alpha = & -8.96428 \\ & +3.63457\text{x}10^{3}\ p \\ & -5.63873\text{x}10^{1}\ v \\ & +4.82938\ t \\ & +8.15982\text{x}10^{5}\ \beta \\ & -6.23859\text{x}10^{7}\ v\beta \\ & -6.23859\text{x}10^{9}\ \beta^{2}\end{aligned} \tag{8.12}$$

In order to measure if the response surface gives a good prediction or not, the value of SSE, Eq. (8.5), is calculated and the bend angles from the response surface are compared to the angles from the FE-simulation. As shown in the computer output (Figure 8.5), the SSE-value of 6.7×10^{-8} is as close as to zero, indicating the response surface has the good predictions. The good fitting of the mathematical model is also confirmed by the fact that the residual values between the bend angles from both the response surface and the FE-simulation is very close to zero as shown in Figure 8.6. Figure 8.7 shows two examples of the three-dimensional response surface plots of bend angle against the input variables, laser power and feed rate (a) and laser power and coefficient of

thermal expansion (b). From the figure, it is noted that the process may be more sensitive to coefficient of thermal expansion than laser power, and to laser power than feed rate. The response surface plots of bend angle against other input variables are displayed in Appendix D.

The Monte Carlo simulations based on the response surface, Eq. (8.12), have been conducted with 10,000 sets of testing data (i.e., random input values) within the range of input variables. The random input values are continuously selected from a seed value initialized with the ANSYS system time when the ANSYS session started. Figure 8.8 presents bend angles with respect to sampling points occurring during the Monte Carlo simulations. Variations of input variables occurring during the simulations are given in Appendix D. The relative frequencies of the input variable, laser power, occurring during the simulations are shown in Figure 8.9. It can be seen that, as defined, it represents the Gaussian distribution. The relative frequencies of other process parameters are presented in Appendix D.

As results of the Monte Carlo simulations on the response surface, the relative frequencies at which values of the bend angle are expected to occur are presented in Figure 8.10. It is found from the figure that the distribution of the bend angles is identified with a Gaussian distribution with a mean value of 3.0348° and a standard deviation of 0.0416. The maximum and minimum angles expected to take place are 3.2049° and 2.8818°, respectively.

The cumulative distribution curve of the bend angle is plotted in Figure 8.11. From this figure, it is possible to calculate the probability that the bend angle remains between specialized ranges. For example, it is noticed that there is a 52% probability that the bend angle remains between 2.96° and 3.04°. The probabilities of input variables predicted to occur during the Monte Carlo simulations on the response surface are presented in Appendix D.

Table 8.2 Central composite design and response.

Set	Input variable				Response
	p (W)	v (m/sec)	t (m)	β (1/°C)	α (°)
1	1810.30	0.004200	0.006000	1.170×10^{-5}	3.0350
2	1809.78	0.004200	0.006000	1.170×10^{-5}	3.0331
3	1810.82	0.004200	0.006000	1.170×10^{-5}	3.0368
4	1810.30	0.004174	0.006000	1.170×10^{-5}	3.0551
5	1810.30	0.004226	0.006000	1.170×10^{-5}	3.0147
6	1810.30	0.004200	0.005974	1.170×10^{-5}	3.0348
7	1810.30	0.004200	0.006026	1.170×10^{-5}	3.0350
8	1810.30	0.004200	0.006000	1.144×10^{-5}	2.9295
9	1810.30	0.004200	0.006000	1.196×10^{-5}	3.1396
10	1810.04	0.004187	0.005987	1.157×10^{-5}	2.9914
11	1810.56	0.004187	0.005987	1.157×10^{-5}	2.9933
12	1810.04	0.004213	0.005987	1.157×10^{-5}	2.9710
13	1810.56	0.004213	0.005987	1.157×10^{-5}	2.9728
14	1810.04	0.004187	0.006013	1.157×10^{-5}	2.9916
15	1810.56	0.004187	0.006013	1.157×10^{-5}	2.9935
16	1810.04	0.004213	0.006013	1.157×10^{-5}	2.9711
17	1810.56	0.004213	0.006013	1.157×10^{-5}	2.9730
18	1810.04	0.004187	0.005987	1.183×10^{-5}	3.0964
19	1810.56	0.004107	0.005987	1.183×10^{-5}	3.0982
20	1810.04	0.004213	0.005987	1.183×10^{-5}	3.0763
21	1810.56	0.004213	0.005987	1.183×10^{-5}	3.0782
22	1810.04	0.004187	0.006013	1.183×10^{-5}	3.0965
23	1810.56	0.004187	0.006013	1.183×10^{-5}	3.0984
24	1810.04	0.004213	0.006013	1.183×10^{-5}	3.0764
25	1810.56	0.004213	0.006013	1.183×10^{-5}	3.0783

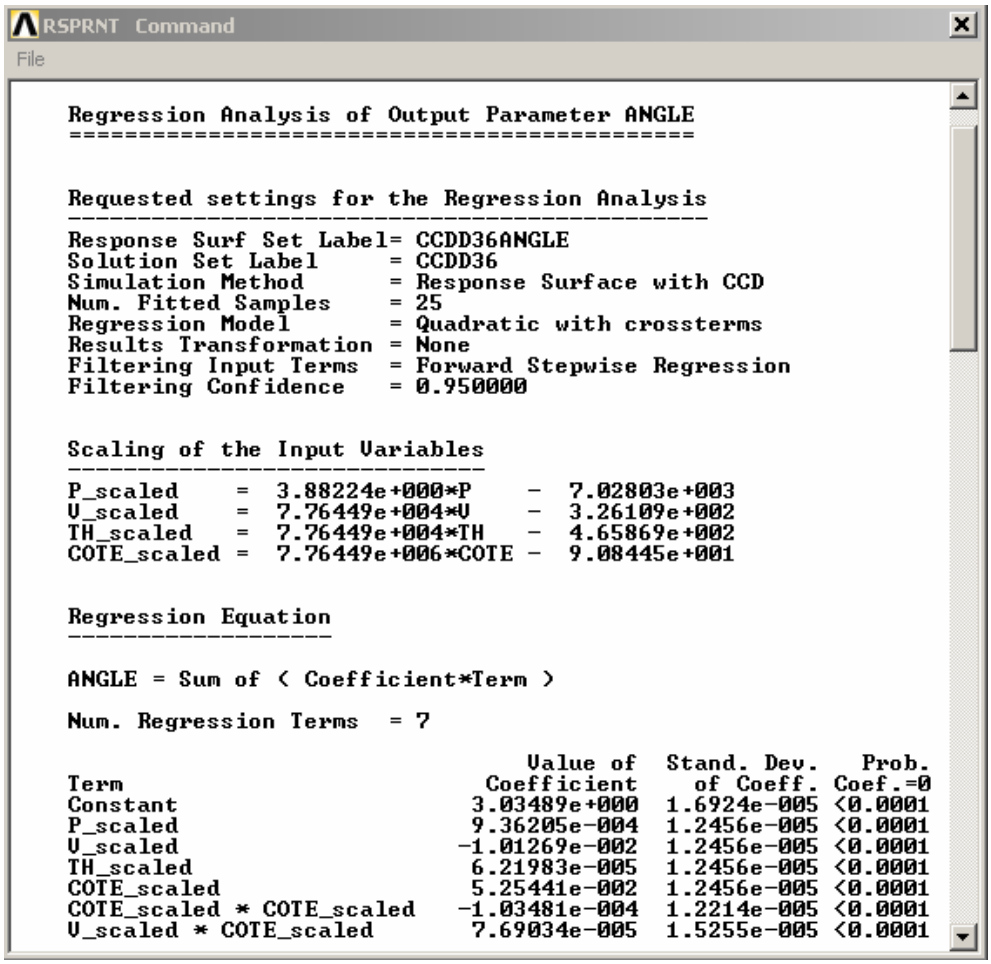

Figure 8.4 Response surface from the central composite design.

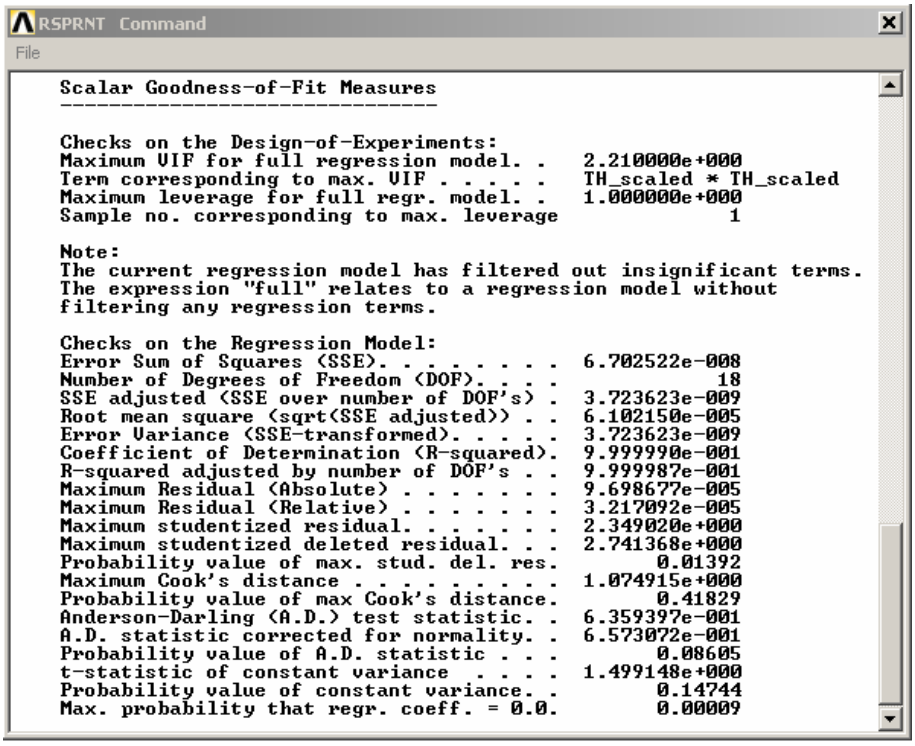

Figure 8.5 Computer output for measuring the quality of response surface fitting.

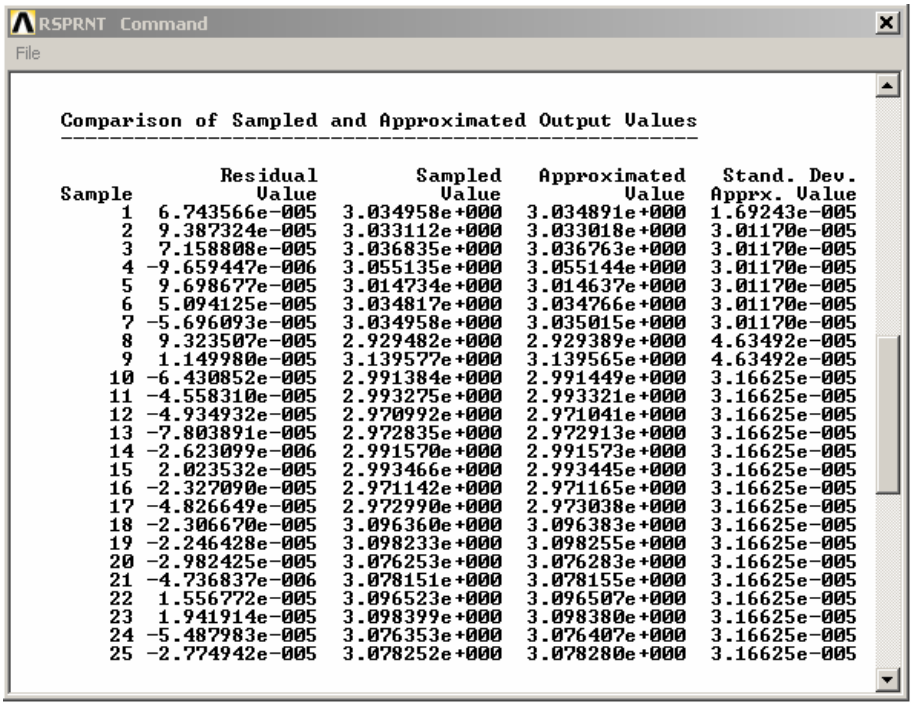

Figure 8.6 Comparison of the bend angles from FE-simulations and response surface model.

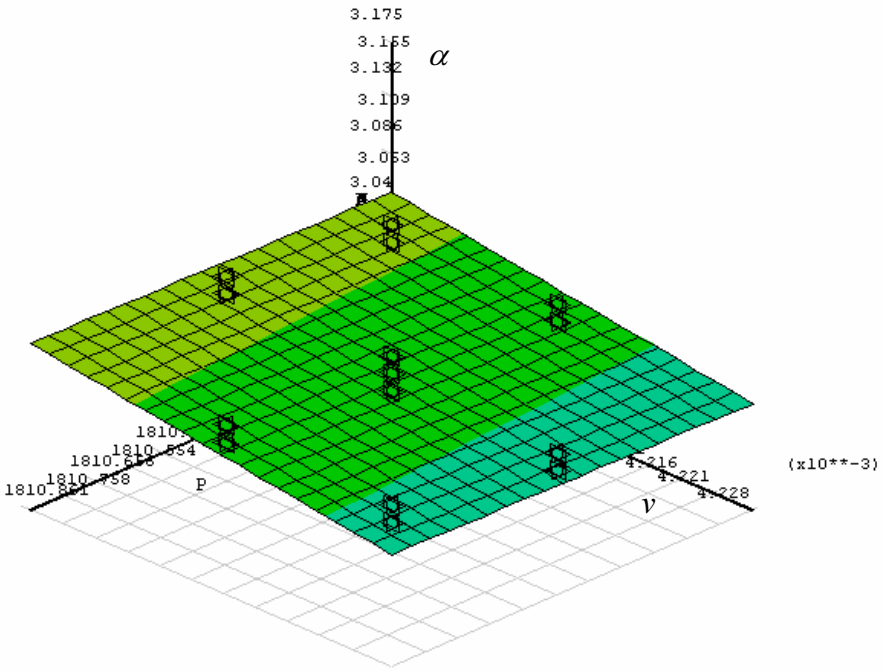

(a)

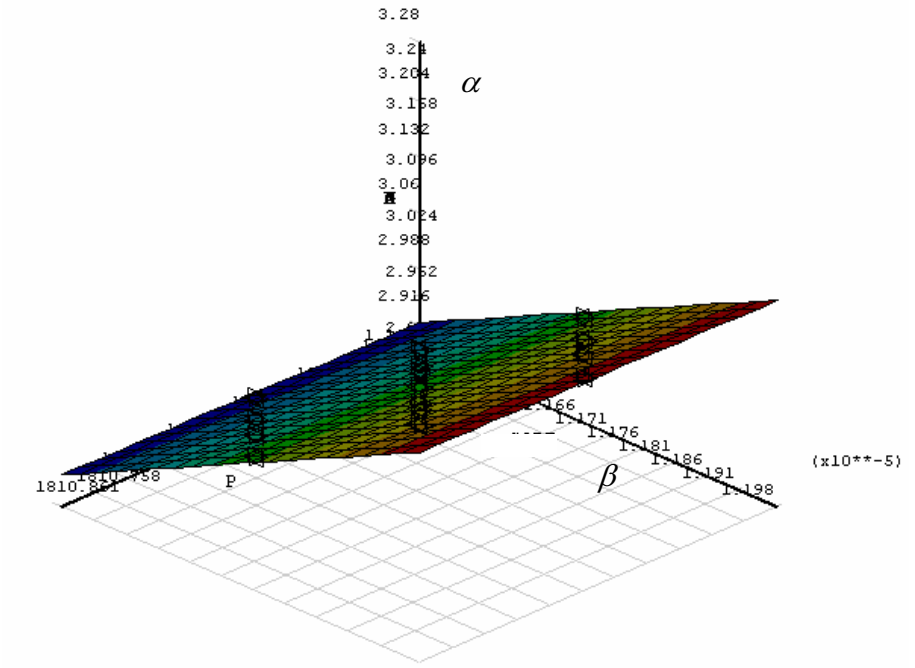

(b)

Figure 8.7 Response surface plots of bend angle: (a) to laser power and feed rate; and (b) to laser power and coefficient of thermal expansion.

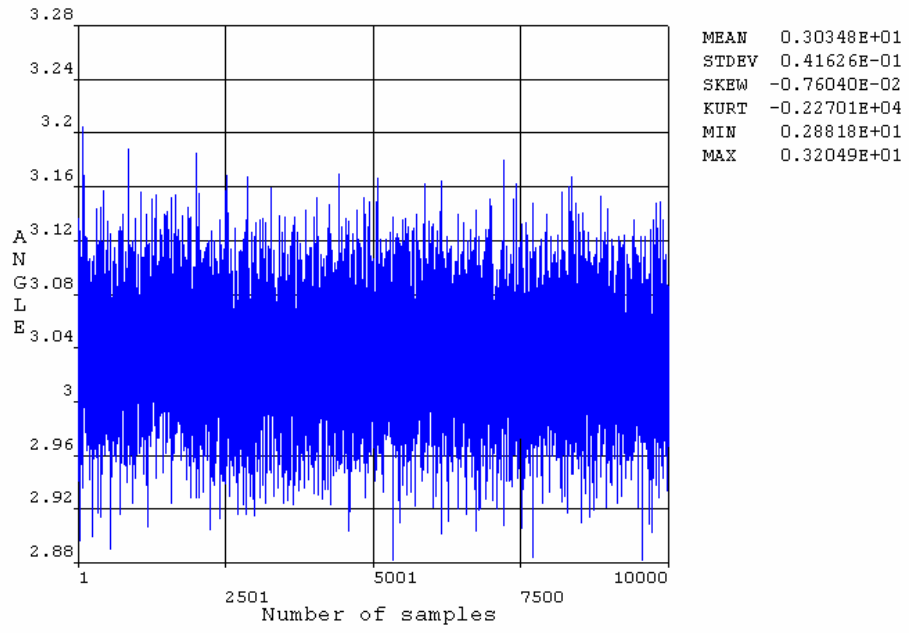

Figure 8.8 Bend angles resulting from the Monte Carlo simulations on response surface.

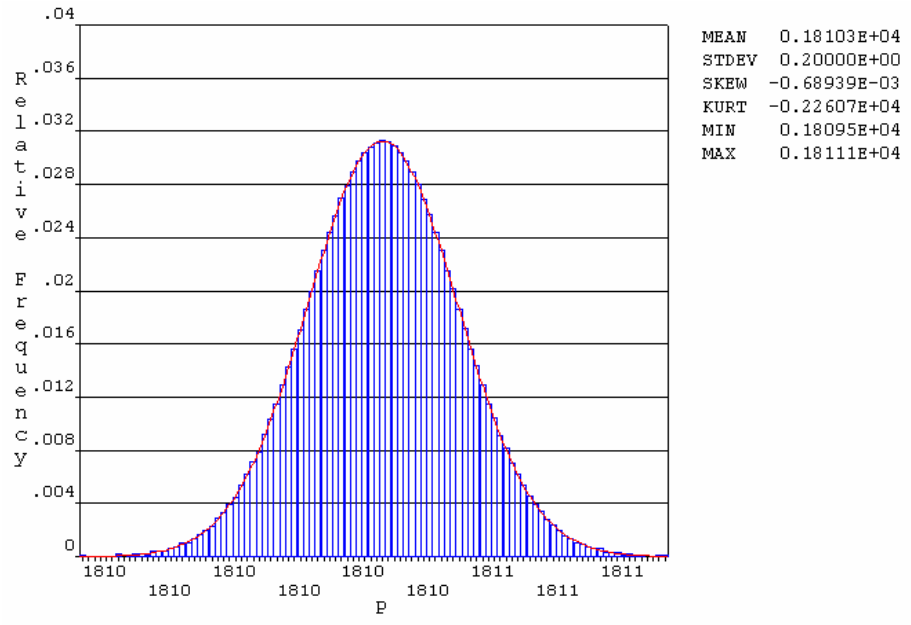

Figure 8.9 Relative frequency of laser power occurring during the Monte Carlo simulations on response surface.

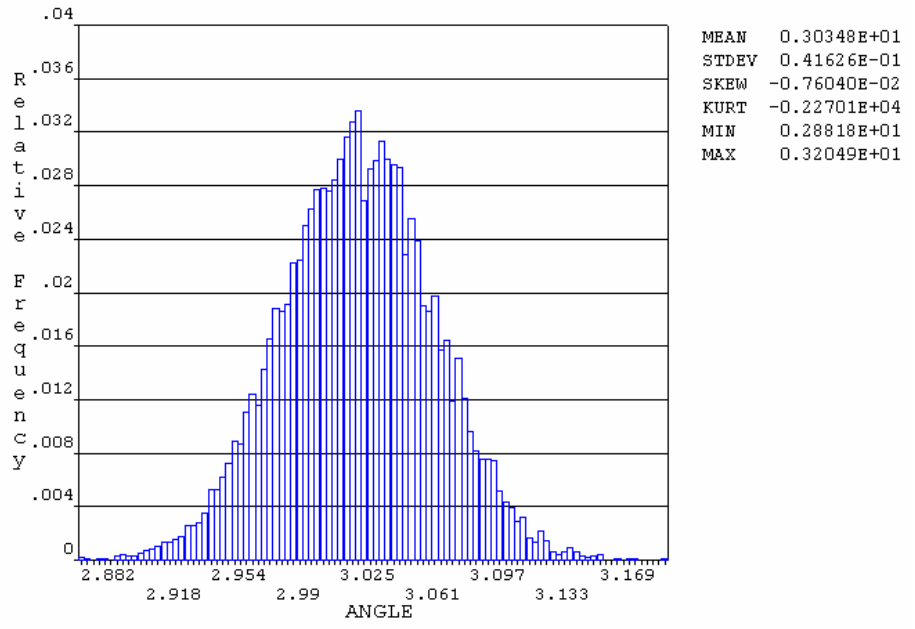

Figure 8.10 Relative frequency of bend angle resulting from the Monte Carlo simulations on response surface.

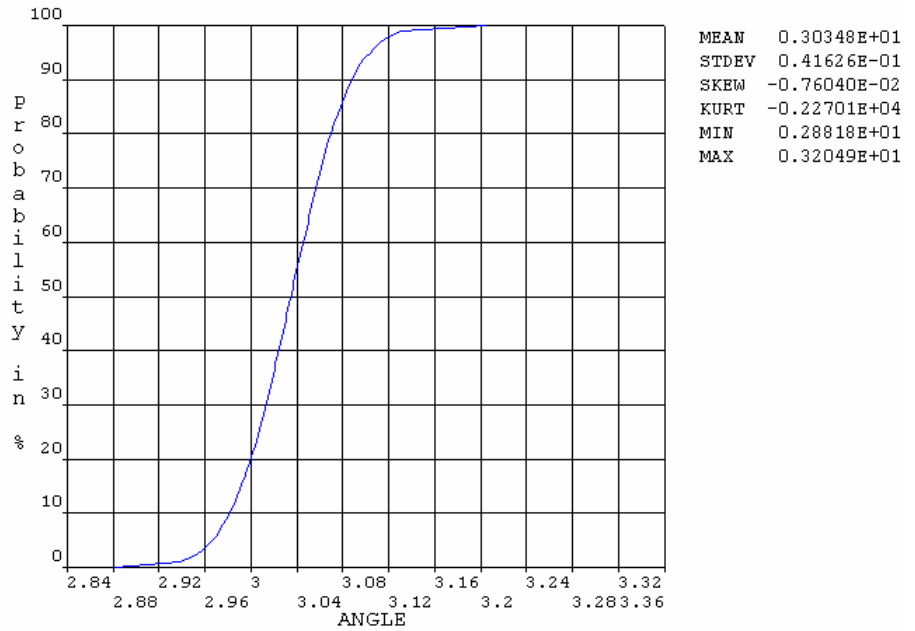

Figure 8.11 Cumulative distribution curve of bend angle resulting from the Monte Carlo simulations on response surface.

8.3.4 Results from the Monte Carlo simulation based on the FE-simulations

Results of the reliability analysis by the Monte Carlo simulation based on the FE-simulations of the laser forming process are presented in this section. For the Monte Carlo simulation, 100 FE-simulations were carried out with the Latin Hypercube sampling technique.

As shown in Figure 8.12, 100 sets of sampling points were created in combination with the uncertain input variables for the Monte Carlo simulations. In order to confirm if the number of simulations is sufficient for the statistical analysis, the mean values of the bend angle are plotted as shown in Figure 8.13. The relatively flat curve of the mean values indicates that the number of simulation is enough to converge the simulation. The histogram bars resembling the Gaussian distribution (Figure 8.14) also indicate that the number of simulations is sufficient.

The relative frequencies at which values of the bend angle are expected to occur are presented in Figure 8.15. It is noted that the distribution of the bend angle has the mean values of 3.0357° and the standard deviation of 0.0463. The expected maximum and minimum bend angles are 3.2367° and 2.9183°, respectively. Figure 8.16 presents the probability that the bend angle remains between special ranges in confidence level of 0.95. From the figure, it is found that there is an about 50% probability that the bend angle remains between 2.96° and 3.04°.

The results of reliability analysis obtained by both the Monte Carlo simulations on the response surface and the Monte Carlo simulations based on the FE-simulations are listed in Table 8.3. As can be seen from the table, there is good agreement between the results from the both methods. The probability is that the bend angle remains between 2.96° and 3.04°.

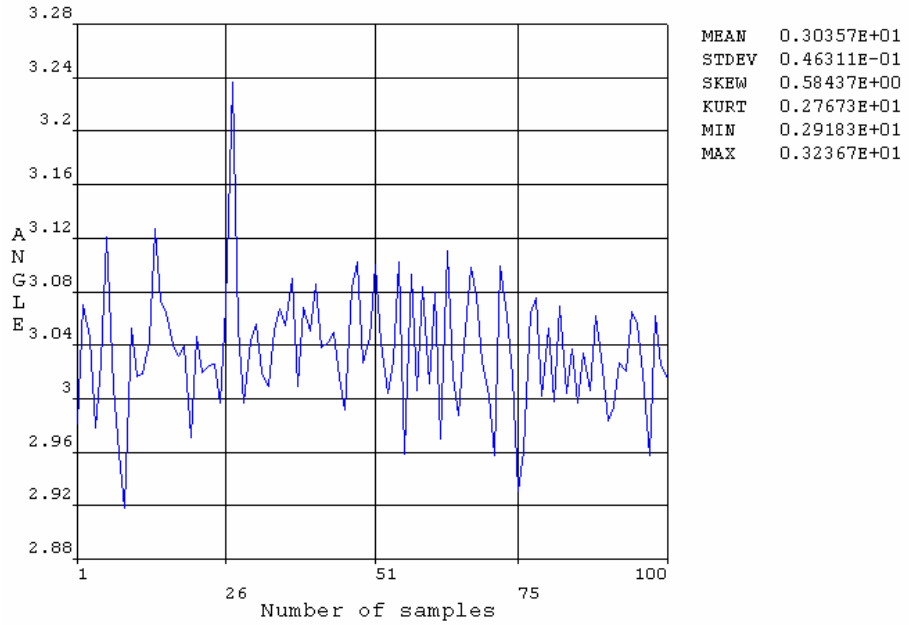

Figure 8.12 Variations of the bend angle regarding the sampling points during the FE-simulations for the Monte Carlo simulation.

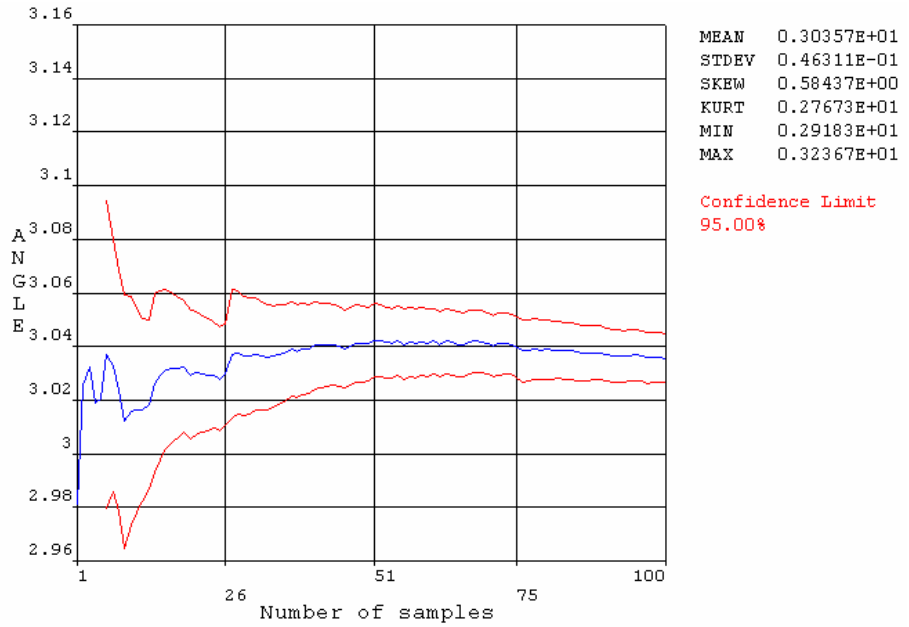

Figure 8.13 Mean value of the bend angle during the FE-simulations for the Monte Carlo simulation.

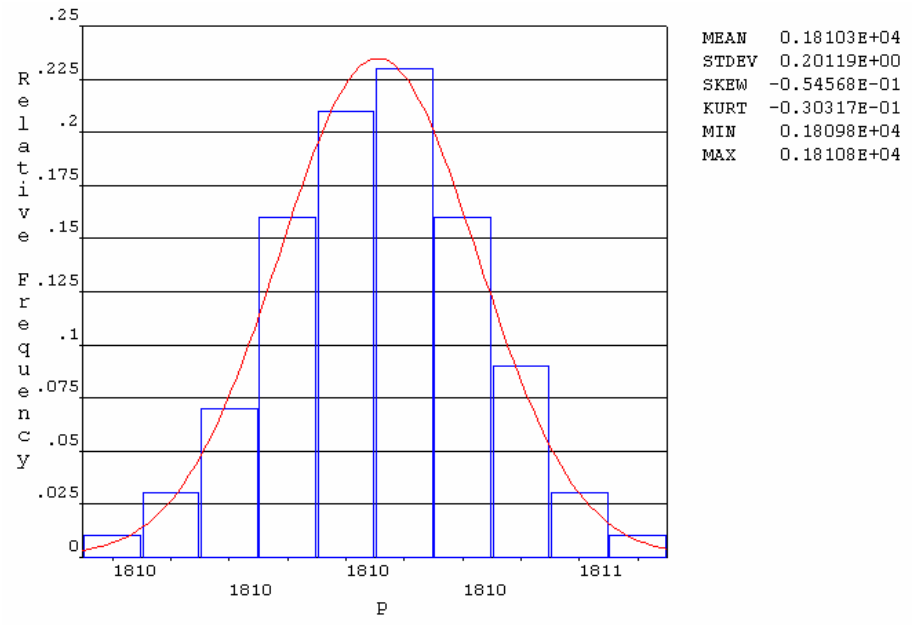

Figure 8.14 Probability density function of the laser power from the Monte Carlo simulation based on the FE-simulations.

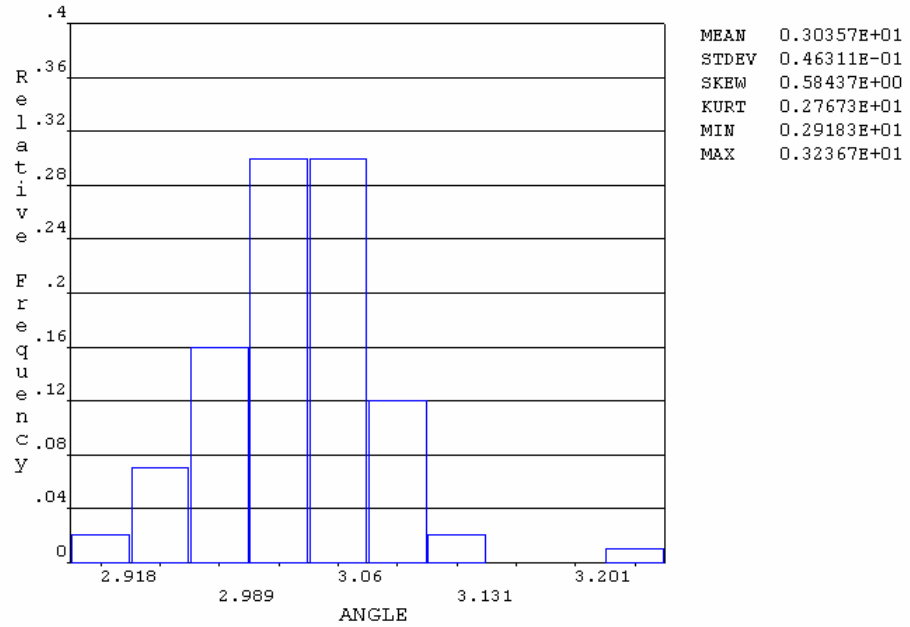

Figure 8.15 Probability density function of the bend angle from the Monte Carlo simulation based on the FE-simulations.

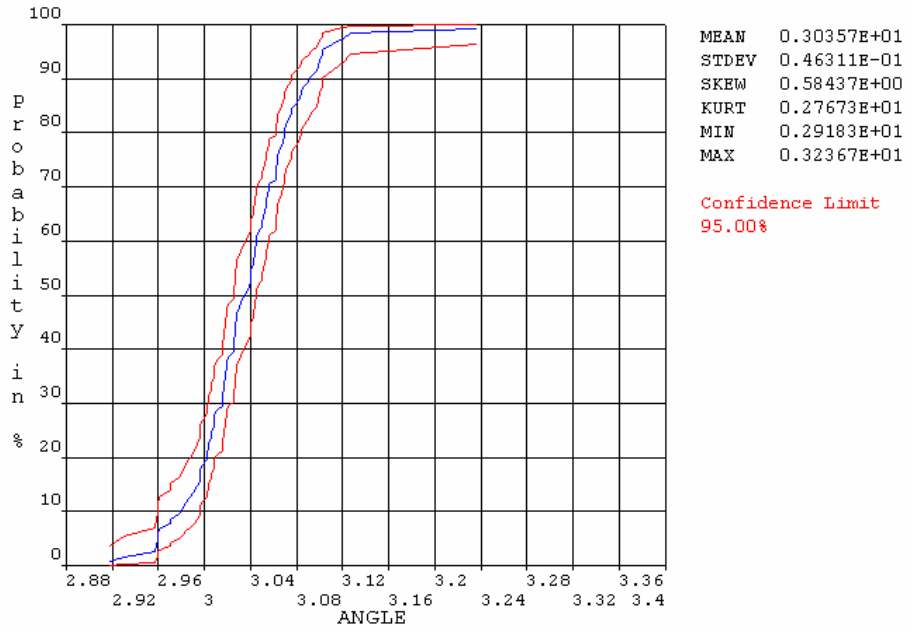

Figure 8.16 Cumulative distribution function of the bend angle from the Monte Carlo simulation based on the FE-simulations.

Table 8.3 Comparison of simulation results from the Monte Carlo simulations on the response surface and the Monte Carlo simulations based on the FE-simulations.

Classification	Distribution of bend angle				Probability (%)
	μ	σ	Min.	Max.	
Monte Carlo simulations on the response surface	3.0348	0.0416	2.8818	3.2049	52
Monte Carlo simulations on the FE-simulations	3.0357	0.0463	2.9183	3.2367	50

8.4 Summary

In this chapter, a well-known reliability analysis method (i.e., the Monte Carlo method) was applied to assess the reliability of the laser forming process. The Monte Carlo simulations were based on the response surface or the FE-simulations of the laser forming process. The procedure of the assessment involved the finite element analysis and the statistical analysis techniques. The reliability analysis was conducted on the straight-line heating process optimized to produce a bend angle of 3° where the bend angle is subject to uncertainties of laser power, feed rate, plate thickness and the coefficient of thermal expansion. It was assumed that the variations of the input variables follow a Gaussian distribution.

For the Monte Carlo simulations on the response surface, an approximation function of the bend angle was determined via simulations with 25 sets of design points from the central composite sampling method. The good prediction of the response surface was confirmed both by calculating the error sum of squares and by comparing the bend angles from the response surface to those from the FE-simulations. The Monte Carlo simulations were performed 10,000 times on the response surface. From the simulation, it was found that the distribution of the bend angle is identified with a Gaussian distribution with a mean value of 3.0348° and a standard deviation of 0.0416. The minimum and maximum angles expected to occur are 3.2049° and 2.8818°, respectively. According to the cumulative distribution function of the bend angle obtained, there is a 52% probability that the bend angle remains between 2.96° and 3.04°.

For validation of the reliability results from the Monte Carlo simulations on the response surface, the Monte Carlo simulations based on 100 FE-simulations of the laser forming process were carried out. The results from the Monte Carlo simulations on the response surface showed good agreement on the results from the Monte Carlo simulations based on the FE-simulations.

Chapter 9

Investigation of Process Sensitivity to Material Properties

9.1 Introduction

As described in Chapter 2, the material properties of the plate used in laser forming have a critical impact on the forming results due to the fact that the process is based on thermal expansion of the material. It has been known that two thermal properties (i.e., the coefficient of thermal expansion and thermal conductivity) play an important role in the process. However, despite their importance, the work to quantitatively characterize the effects of the properties has not been done due to the investigation difficulty through empirical work.

This chapter examines the sensitivities of a straight-line heating process to material properties using a numerical approach. The basic concept of the evaluation is to measure the relationship between input and output variables. The measurements of correlation are based on a statistical analysis of sampled data, for which a large number of numerical simulations are carried out for Monte Carlo simulations. Associations between bend angle and material properties are determined via the Pearson product-moment correlation coefficient that is appropriate for calculation of bivariate correlations in interval/ratio levels of measurement. The material properties of interest involve the coefficient of thermal expansion, thermal conductivity, specific heat, modulus of elasticity, and Poison's ratio.

9.2 Measures of Correlation between Variables

There are a large number of correlation measurements which are capable of calculating associations in different levels of measurement. As listed in Table 9.1, the levels of measurement can be categorized into four [57]. As the measurement moves from the lowest level (i.e., nominal) to the highest level (i.e., ratio), the amount of information increases and the meaningful mathematical operations can be performed.

Table 9.1 Levels of measurement of correlation.

Nominal/categorical measurement	The numbers are employed merely to identify mutually exclusive categories, but cannot be manipulated in a meaningful mathematical manner.
Ordinal/rank-order measurement	The numbers represent rank-orders, and do not give any information regarding the difference between adjacent ranks.
Interval measurement	An interval scale not only considers the relative order of the measures involved but, in addition, is characterized by the fact that throughout the length of the scale, equal differences between measurements correspond to equal differences in the amount of the attribute being measured.
Ratio measurement	This measurement is characterized as in the case with interval scale. However, it is also characterized by the fact that it has a true zero point, which enables it to make meaningful ratio statements with regard to the attribute/variable being measured.

It has been known that the Pearson product-moment correlation coefficient can be used to determine the degree of correlation between two variables in the interval/ratio measurements. The theoretical background of the procedure determining correlation coefficients by the Pearson product-moment correlation coefficient is described on the basis of the works of ANSYS theory manual [70] and Shenkin [87]. This correlation coefficient is based on the degree of linear relationship between two variables, and the static computation is represented by:

$$r = \frac{\sum_{i}^{n}(x_i - \bar{x})(y_i - \bar{y})}{\sqrt{\sum_{i}^{n}(x_i - \bar{x})^2}\sqrt{\sum_{i}^{n}(y_i - \bar{y})^2}} \tag{9.1}$$

where:

r = the correlation coefficient between the variables x and y

n = the number of sampling data

$\bar{x}$ and $\bar{y}$ = the estimates for the mean value of the variables x and y

Because the sample size n is finite, the correlation coefficient usually yields a small, but non-zero value, even if x and y are not associated at all in reality. In this case, the correlation coefficient would be statistically insignificant. Thus, it is needed to find out whether or not a correlation coefficient is significant. The significance of the correlation coefficient can be determined via the null hypothesis testing where the null hypothesis, which is represented by the notation H_0, that the correlation between x and y is not significant at all is made (i.e., H_0: $r = 0$). In this case, the following variable is approximately distributed like the Student's t-distribution with $\nu = n - 2$ degrees of freedom.

$$t = r\sqrt{\frac{n-2}{1-r^2}} \tag{9.2}$$

The cumulative distribution function of the Student's *t*-distribution is:

$$A = \frac{1}{\sqrt{\nu}B\left(\frac{1}{2},\frac{\nu}{2}\right)}\int_{-t}^{t}\left(1+\frac{x^2}{\nu}\right)^{-\frac{\nu+1}{2}}dx \tag{9.3}$$

where:

$B(\ldots)$ = complete Beta function

The larger the correlation coefficient r, the less likely it is that the null hypothesis H_0 is true. Also the larger the correlation coefficient r, the larger is the value of t from Eq. (9.3) and consequently also the probability $A(t/\nu)$ is increased. Therefore, the probability that the null hypothesis H_0 is true can be expressed by $1\text{-}A(t/\nu)$. If $1\text{-}A(t/\nu)$ exceeds a certain significance level, then it can be inferred that the null hypothesis H_0 is true. However, if $1\text{-}A(t/\nu)$ is below the significance level, then it can be inferred that the null hypothesis H_0 is not true and that consequently the correlation coefficient r is significant.

The correlation coefficient r must fall within the range of -1 to +1 (i.e., $-1 \leq r \leq +1$). The absolute value of r indicates the strength of the relationship between the two variables. As the absolute value of r approaches 1, the degree of linear relationship between the variables becomes stronger. The closer the absolute value of r is to 0, the weaker the linear relationship between the two variables. The sign of r indicates the nature or direction of the linear relationship that exists between the two variables. A positive sign indicates a direct linear relationship, whereas a negative sign indicates an inverse linear relationship. A direct linear relationship is one in which an increase in one variable is associated with an increase in the other variables, and a decrease in one variable is associated with a decrease in the other variable. An inverse relationship is one in which an increase in one variable is associated with a decrease in the other variable, and a decrease in one variable is associated with an increase in the other variable.

9.3 Simulation Details

A finite element model developed in Chapter 4 for the straight-line heating process is employed for the investigation of process sensitivities to material properties. In the process, a bend angle of 0.47° was produced with the following initial condition: a laser power of 1500 watts, a feed rate of 0.005 m/sec, a beam diameter of 0.016 m, and one irradiation. The plate dimensions are 0.15 m x 0.3 m x 0.006 m and the material is carbon-manganese steel (DIN 1.0584, D36).

A total of five thermal and mechanical material properties including the coefficient of thermal expansion α, thermal conductivity k, specific heat c_p, modulus of elasticity E, and Poison's ratio ν are defined as input parameters in the numerical model. The input parameters are defined as input variables characterized by the following uniform distribution, described in Appendix E: their mean values are designated to the above initial values, and their lower and upper limits are given as 10% decrease and increase of the mean values, respectively. It is assumed that when the elastic modulus changes, the yield point and the elastic strain change at the same changing rate as the elastic modulus. The distributions of strain-stress curves at plasticity region (See Chapter 4, Figure 4.12) are set at the rate of change in the elastic modulus. The bend angle calculated is defined as output parameter.

For the sensitivity analysis via Monte Carlo simulation, 100 numerical simulation loops are randomly executed using the ANSYS Probabilistic Design System (PDS) [77]. The ANSYS program listing is given in Appendix C. In the FE-simulations, the output parameter is computed as a function of the set of input variables. Latin Hypercube sampling (LHS) method is used for the sampling technique of the input variables (See Section 8.2.1 in Chapter 8). The influences of material properties on bend angle (i.e., the sensitivities) are statistically measured via the Pearson product-moment correlation coefficients.

9.4 Sensitivity Results

Figure 9.1 presents plots of the sample history of each input variable (i.e. β, k, c_p, E and ν) and results of output parameter (i.e., α). From the figure, it can be seen that 100 sets of design points were sampled in combination of the input variables, and the minimum and maximum values of α calculated with the sampled points are 0.2650° and 0.7322° respectively, and the mean value is 0.4901°. The minimum, maximum, and mean values of the input variables sampled are summarized in Table 9.2.

To find whether or not the number of sampling points is sufficient for the statistical analysis, the mean values of α are plotted as shown in Figure 9.2 which confidence limit is 95%. From the figure, the relatively flat curve indicates enough simulations for convergence.

Table 9.2 The mean, minimum and maximum values of input variables.

	Mean	Minimum	Maximum
β (10^{-6}°C)	0.1170×10^{-4}	0.1053×10^{-4}	0.1286×10^{-4}
k (W/m°C)	0.5190×10^{2}	0.4673×10^{2}	0.5703×10^{2}
c_p (J/kg°C)	0.4860×10^{3}	0.4381×10^{3}	0.5339×10^{3}
E (MPa)	0.2060×10^{6}	0.1854×10^{6}	0.2264×10^{6}
ν	0.2960	0.2666	0.3253

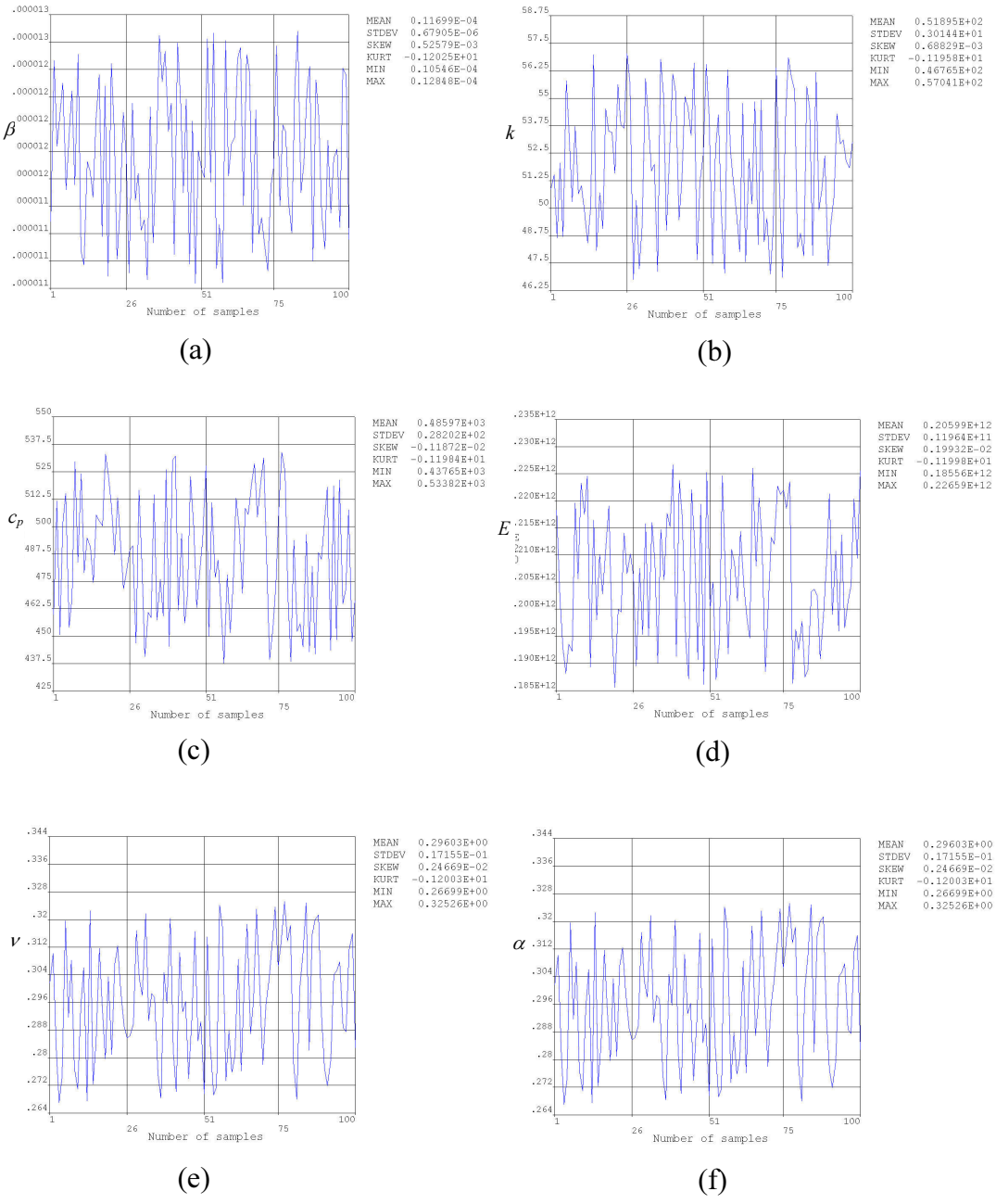

Figure 9.1 Variations of input and output variables: (a) coefficient of thermal expansion, β (10^{-6}°C); (b) thermal conductivity, k (W/m°C); (c) specific heat, c_p (J/kg°C); (d) modulus of elasticity, E (Pa); (e) Poison's ratio, ν; and (f) bend angle, α (°).

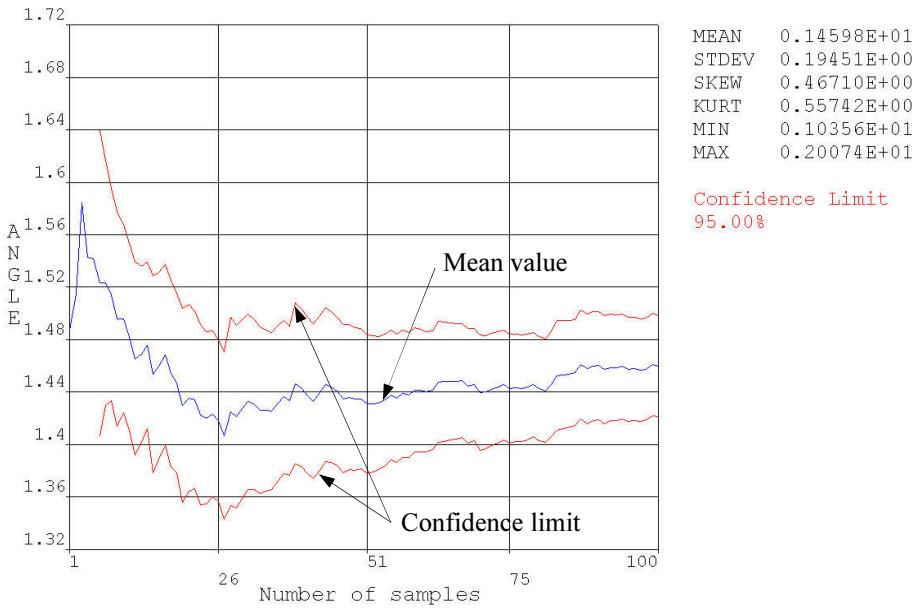

Figure 9.2 Mean value of bend angle.

The evaluation of the statistical sensitivities was based on the Pearson product-moment correlation coefficients between the material properties (input variables) and the bend angle (output variables). Table 9.3 presents the matrix of the correlation coefficients and the probabilities that the correlation coefficients are zero. Probabilities larger than 2.5% indicate that the corresponding correlation coefficient is zero, that is, the correlation is not significant because, in this study, a significant level of 2.5% has been used to indicate insignificant correlation coefficient. From the table, it can be seen that the correlation coefficients of β, k, and c_p are significant to the bend angle α and the correlation coefficients of E and ν is not significant. The only significant correlation coefficients of material properties are plotted in Figure 9.3.

Table 9.3 Matrix of correlation coefficients and probabilities.

	β	k	c_p	E	ν
Coefficient, r	0.574	-0.532	-0.524	(-0.039)	(0.116)
Probability	$4.1\text{x}10^{-10}$	$1.2\text{x}10^{-8}$	$2.2\text{x}10^{-8}$	$7.0\text{x}10^{-1}$	$2.5\text{x}10^{-1}$

Note: The value in bracket indicates that the correlation coefficient is not significant.

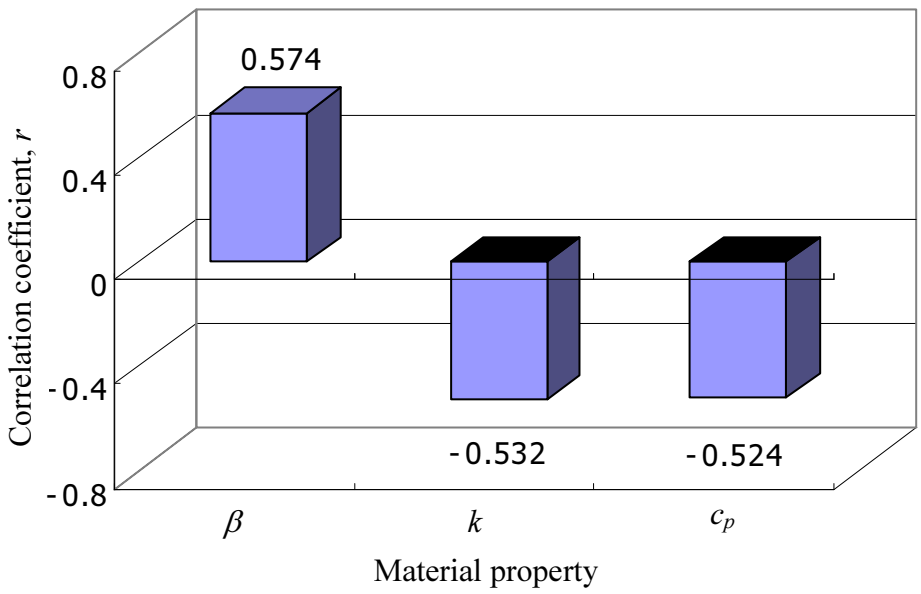

Figure 9.3 Significant correlation coefficients of material properties.

The sensitivities are further discussed with scatter plots which depict the data employed in the correlation analysis in a graphical format.

Figure 9.4 presents the scatter plots including the significant correlation coefficients and the regression lines: (a) of variables α and β; (b) of variables α and k; and (c) of variables α and c_p. From the figure, it can be found that the regression line in Figure 9.4 (a) are positively sloped, and is thus associated with a positive correlation, which reflects fact that a change of the variable β in a specific direction is accompanied by a change in the variable α in the same direction. On the other hand, the regression lines in Figures 9.4 (b) and (c) are positively sloped, and are thus associated with a negative correlation, which reflects fact that a change of the variables k and c_p in a specific direction is accompanied by a change in the variable α in the opposite direction.

The strength of the correlation, which is a function of how close the data points are to the regression line, can be expressed strong, moderate, and weak. To designate the strength of the correlation coefficient, the following guidelines are employed: The correlations for strong, moderate and weak are $|r| \geq 0.7$, $0.3 \leq |r| < 0.7$, $|r| < 0.3$, respectively [87]. As can be seen in Figure 9.4, it is noted that all the thermal material properties of β, k and c_p are moderately correlated to α as $|r| = 0.574$ for β, 0.532 for k, and 0.524 for c_p.

Therefore, it can be concluded that there are a moderate positive correlation between α and β, and moderate negative correlations between α and k, c_p.

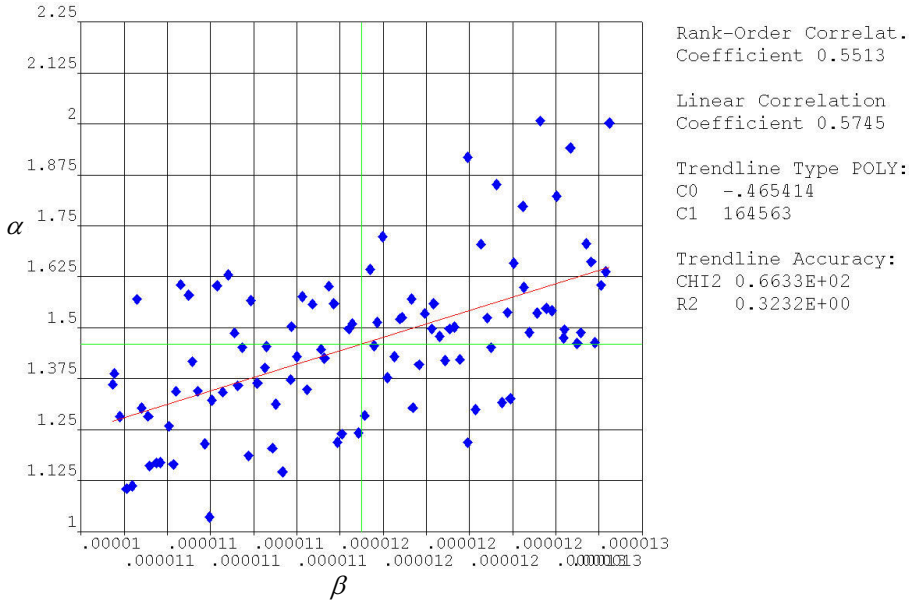

(a)

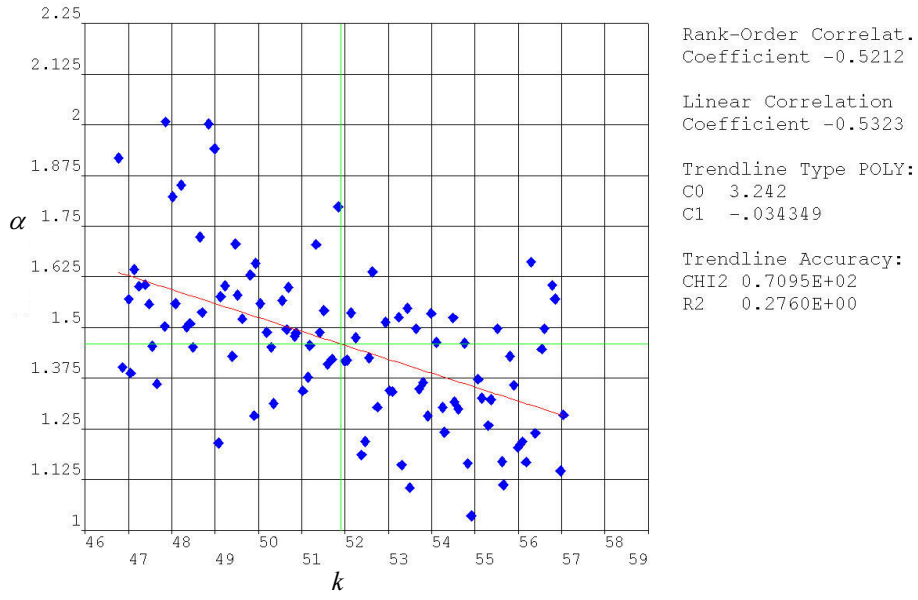

(b)

Figure 9.4 Scatter plots of bend angle: (a) against coefficient of thermal expansion, β (10^{-6}°C); (b) against thermal conductivity, k (W/m°C); and (c) against specific heat capacity, c_p (J/kg°C).

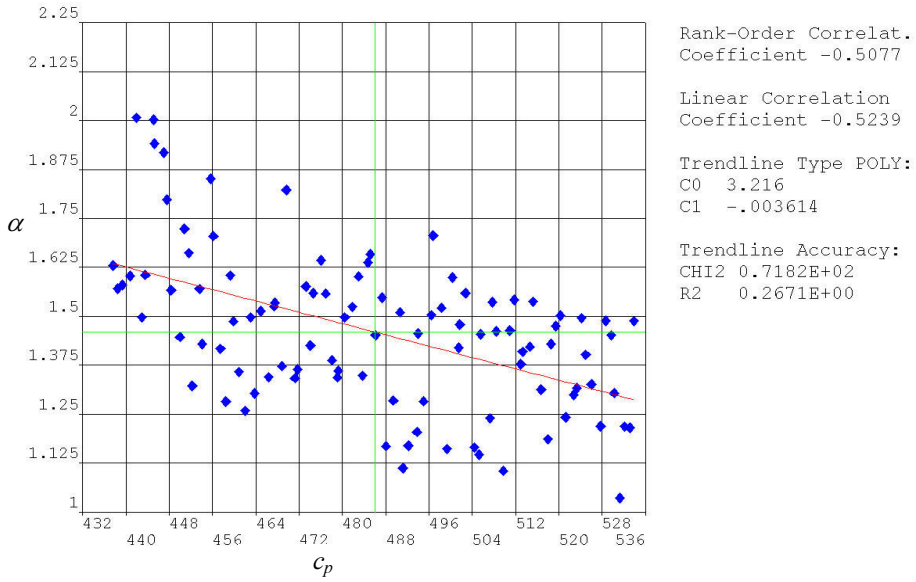

(c)

Figure 9.4 Continued.

9.5 Discussion

The simulation results showed a moderate positive correlation between the bend angle, α, and coefficient of thermal expansion, β. Moderate negative correlations were determined between α and thermal conductivity, k, and specific heat capacity, c_p. Insignificant correlations were found for elastic modulus, E and Poison's ratio, ν. These relationships make sense in point of view of laser bending physics that follows.

As stated in Section 1.2.2 (Chapter 1), the bend angle in laser forming is produced by thermal expansion induced by laser beam heating. The magnitude of the thermal expansion is mainly determined by β and temperature change. Hence, the size of bend angle is positively proportional to β.

In order to increase the bend angle efficiently, high temperature has to be present in the metal sheet during the process because the thermal expansion is converted into more plastic strain than elastic at high temperature (See Figure 1.4). Thus, in addition to β, temperature increase has a critical effect on the magnitude of the bend angle. c_p of a material is defined as heat capacity per unit mass, which is the amount of energy required to raise temperature of one kilogram of the material by one Kelvin. This definition means that when c_p increases, temperature change decreases. Hence, it can be predicted that the size of bend angle is negatively proportional to the property, c_p.

In the current simulations, the TGM forming mechanism (See Section 1.2.2) was involved, and in the mechanism steeper temperature gradient along the plate thickness yields higher bend angle. Therefore, it is predicted the bend angle is negatively correlated to k due to the fact that the magnitude of the temperature gradient decreases as k increases.

In the plate with low E, a small elastic strain is obtained. On the contrary, in the plate with high E, a big elastic strain is achieved, which results in low bend angles compared to that obtained from the plate with low E in the same process condition. This phenomenon was observed by Vollertsen [20]. However, an insignificant correlation between α and E was observed from the simulation results. It can be inferred that the thermal material properties are more important parameters than the mechanical properties in laser forming.

Poisson's ratio is defined as the ratio of the lateral strain to the axial strain in material. This property has little effect on the bend angle in laser forming because the bend angle is produced by three-dimensional thermal expansion.

9.6 Summary

This chapter has statistically examined sensitivities between material properties and bend angle in a straight-line heating process. The material properties involved in the investigation were β, k, c_p, E, and ν. The evaluation was based

on the Pearson product-moment correlation coefficients. Theoretical background of the procedure determining correlation coefficients was presented. To statistically measure the influence of material properties on the bend angle via the Pearson product-moment correlation coefficients, 100 finite element simulations were randomly executed using Monte Carlo simulations, and the bend angles were computed as a function of the material properties. It was assumed that the input variables (i.e., the material properties) were characterized by a uniform distribution.

Correlation coefficients and scatter plots between α and β, k, c_p, E and ν were obtained. It can be summarized that the thermal material properties of β, k and c_p play a more important role than the mechanical properties of E and ν in laser forming. There are a moderate positive correlation between α and β, and moderate negative correlations between α and k, c_p.

Chapter 10

Experiment Protocols

10.1 Introduction

The laser forming simulation and process optimization techniques presented in this thesis represent a promising tool of development of rapid prototyping and flexible fabrication technology. In order to apply the techniques to manufacturing, an experimental verification of numerical results would be required.

However, due to the limitations on experimental capability for this study, other techniques (See Sections 4.5.3, 5.5, 6.5) were employed for validations of the results from the finite element analyses of the three laser forming processes: the straight-line heating process, the circle-line heating process, and the laser micro-adjustment process.

Nevertheless, it is recommended that the verification works should be carried out through testing programs. This chapter therefore presents experiment protocols that are intended for future works. A test fixture and procedure for each of the three processes are described. The simulation conditions and results of the processes presented in Chapters 4 to 7 are summarized to provide test conditions and to ensure comparisons between the simulation results and the test results.

10.2 Straight-Line Heating Process

The schematic view of the test fixture for the straight-line heating process is displayed in Figure 10.1. It includes a test plate clamped to a work bed mounted on a CNC table (3 axis), a laser source, a control unit for the laser and CNC table, and measuring systems for the displacements and temperatures occurring during the process.

For a series of tests as shown in Table 10.1, 300 x 150 mm rectangular ship-building carbon-manganese steel DIN 1.0584 (D36) plates with two different thickness (i.e., t = 4 mm and 6 mm) are required. The samples need to be cut by laser to the correct dimensions in order to reduce any pre-stresses inside the plates that might influence the distortion occurring during the laser forming operation. Prior to forming them, they should be cleaned with a mild acetone solution in order to remove the oil that protects them from oxidation. To obtain an absorption coefficient 0.75 on the plate surface, it has to be coated with graphite [41].

As a laser source, a CO_2 laser with 3000 watts maximum power output operating in continuous wave mode (*cw* mode) is needed. The size of the laser beam on the plate surface can be controlled using a variable laser beam expander. The plate is instrumented with a linear variable displacement transducer (LVDT) and a thermocouple to measure the distortions and temperatures of the plate during the operation, respectively. The LVDT is located in the middle of the bottom surface of the plate edge, and the thermocouple at the central bottom surface of the plate to avoid the interference with the laser irradiation.

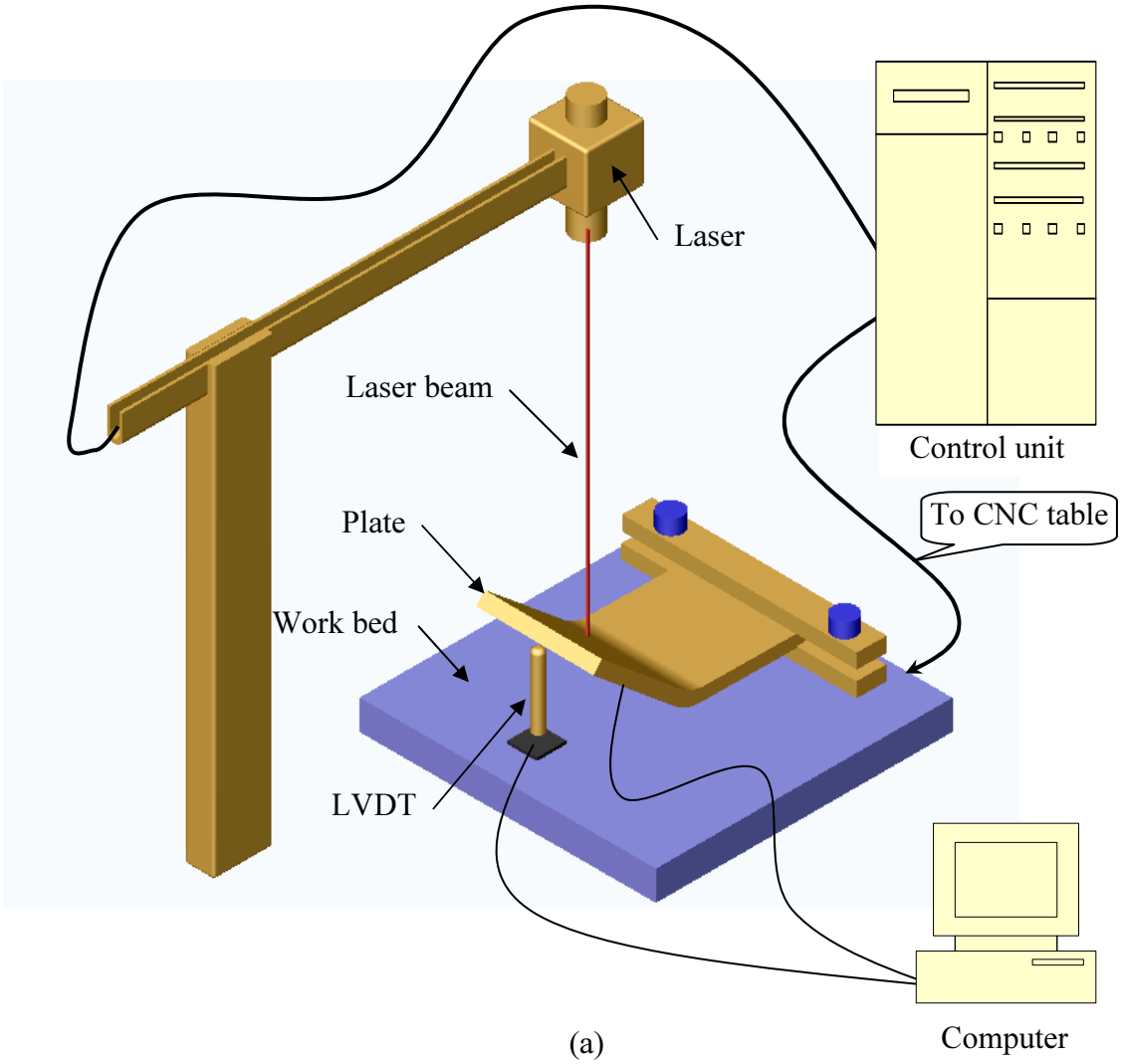

Figure 10.1 (a) Schematic of test fixture for the straight-line heating process and (b) Side view.

Table 10.1 Test conditions and corresponding simulation results for the straight-line heating process.

Case	Process parameters					Simulation results	
	p (W)	v (mm/s)	d (mm)	n	t (mm)	T (°C)	α (°)
1	1500	5	16	1	6	390	0.47
2	3000	10	16	1	4	520	1.32
3	1500	5	16	3	6	530	1.33
4	1810	4.2	18	2	6	716	2.99
5	1999	3.6	15.8	1	6	965	2.22

Values of the process parameters such as the laser power p, the feed rate v, the beam diameter d, the number of scan n, and the irradiation path can be set to the values of each test condition listed in Table 10.1 using the control unit. Control of v, n, and the irradiation path is available via the control of the CNC table. The heating starts outside the plate to impose a uniform heat flux to the plate and, in the processes involving more than one irradiation, the following heating begins in the opposite direction to the previous starting point.

As can be seen in Table 10.1, test cases 1 to 3 are corresponding to the simulation conditions conducted in Chapter 4. Test cases 4 and 5 indicate the optimized process conditions obtained through the SAM (See Section 7.2.2) to produce a predefined bend angle of 3° (See Section 7.3.3) and a maximum bend angle (See Section 7.4), respectively. The table also presents simulation results of the maximum temperature and bend angle for each case. The temperature indicates the one generated at the bottom surface.

10.3 Circle-Line Heating Process

The test fixture for the circle-line heating process is described schematically in Figure 10.2. It consists of a circular test plate clamped to a work bed mounted on a CNC table (3 axis), a laser source, a control unit for the laser and CNC table, and measuring systems for the displacements and temperatures occurring during the process.

For the test, the circular plate is made from the ship-building carbon-manganese steel DIN 1.0584 (D36), which dimension is 80 mm in diameter and 1 mm in thickness. It has a concentric circular hole of 4 mm diameter for a clamping screw. The specimen is necessary to be cut by laser to the correct dimensions in order to reduce any pre-stresses inside the plates that might influence the distortion occurred during the laser forming operation. Prior to forming it, it should be cleaned with a mild acetone solution in order to remove the oil that protects them from oxidation. To obtain an absorption coefficient 0.75 on the plate surface, it has to be coated with graphite [41].

As a laser source, a CO_2 laser with 400 watts maximum power output operating in continuous wave mode (*cw* mode) is required. The size of the laser beam on the plate surface can be controlled using a variable laser beam expander. As shown in Figure 10.2 (c), the plate is instrumented with four linear variable displacement transducers (LVDTs) and a thermocouple to measure the displacements and temperatures of the plate during the operation, respectively. The LVDTs are located in the edge of the plate at interval of right angle, and the thermocouple at the bottom surface of the plate under the irradiation path to avoid the interference with the laser irradiation.

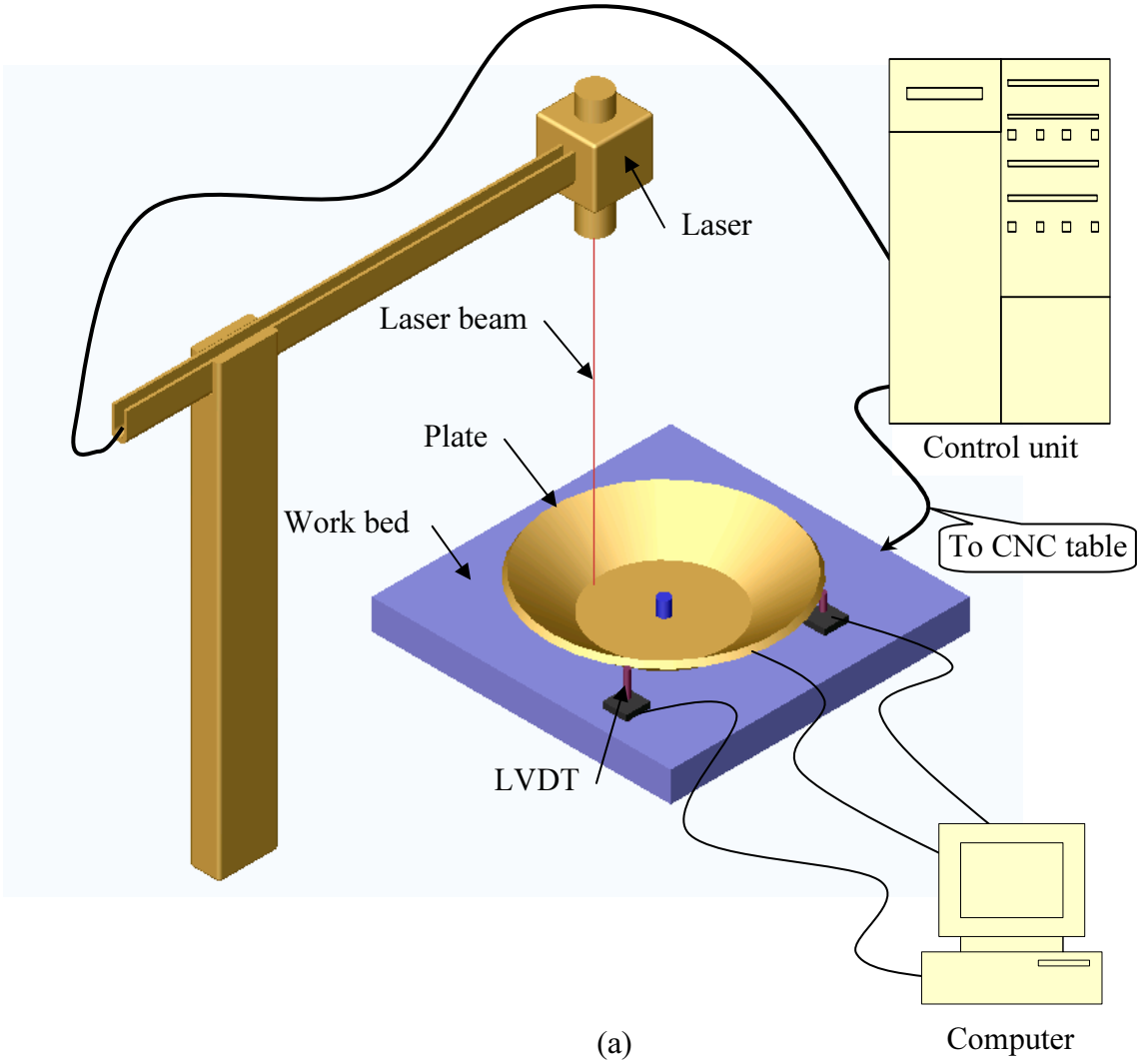

(a)

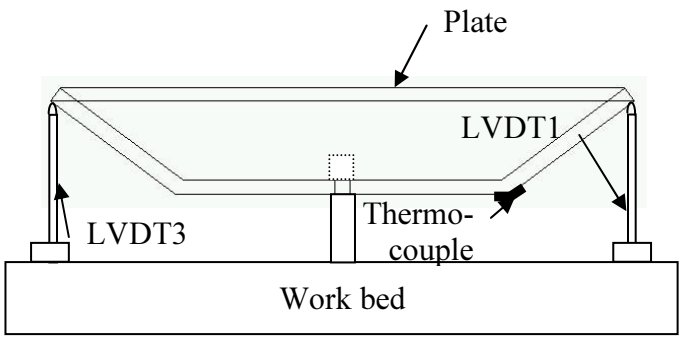

(b)

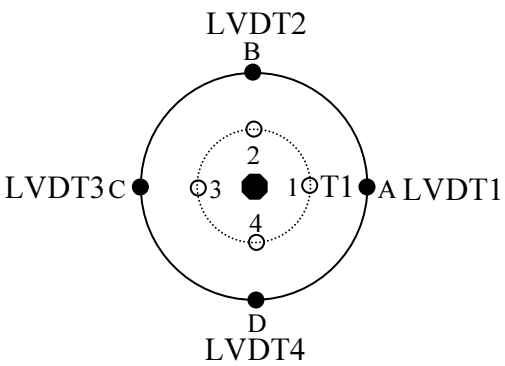

(c)

Figure 10.2 (a) Schematic of test fixture for the circle-line heating process; (b) Side view; and (c) Locations of LVDTs and thermocouple on test plate.

The laser parameters used are a laser power of 300 watts, a beam diameter of 12 mm, and a feed rate of 10 mm/s, which can be set using the control unit. The feed rate and the irradiation path can be controlled via the control of the CNC table. A series of four irradiations are applied to the surface of the plate according to the stages shown in Figure 10.3. At stage 1, the laser beam starts at point 1 and rotates anticlockwise along a circular path with a radius of 22 mm. The heating ceases when the laser beam returns to the starting point, and the plate experiences a cooling period of about 30 sec. The heating starts at point 3 at the next stage, at point 2 at stage 3, and at point 4 at stage 4.

	Heating phase					Cooling phase
Stage 1	① →	② →	③ →	④ →	① →	E
	(0)	(3.46)	(6.91)	(10.37)	(13.82)	(43.20)
Stage 2	③ →	④ →	① →	② →	③ →	E
	(43.20)	(46.65)	(50.11)	(53.56)	(57.02)	(86.40)
Stage 3	② →	③ →	④ →	① →	② →	E
	(86.40)	(89.85)	(93.31)	(96.76)	(100.22)	(129.59)
Stage 4	④ →	① →	② →	③ →	④ →	E
	(129.59)	(133.05)	(136.50)	(139.96)	(143.42)	(172.61)

Note: ( ) indicates the times (sec) when the laser beam is passing the points or when the stages are finished.

Figure 10.3 Processing stage of the circle-line heating process.

The results of temperature and bend angle from the corresponding numerical simulation to the test are presented in Table 10.2. The temperatures indicate the ones generated at the bottom surface.

Table 10.2 Corresponding simulation results to the circle-line heating test.

Classification	Displacement (μm) / Maximum temperature (°C)			
	Point A/ Point 1	Point B/ Point 2	Point C/ Point 3	Point D/ Point 4
Stage 1	22.5 279	15.8 -	20.3 -	24.7 -
Stage 2	48.0 462	50.6 -	46.3 -	38.8 -
Stage 3	99.2 541	93.2 -	74.8 -	84.5 -
Stage 4	157.2 607	179.1 -	152.8 -	142.9 -

10.4 Laser Micro-Adjustment Process

The test fixture for the laser micro-adjustment process is illustrated schematically in Figure 10.4. The fixture is composed of a tube-like structure attached to a rotational module clamped to a work bed mounted on a CNC table (3 axis), a laser source, a control unit for the laser and CNC table, and measuring systems for the displacements and temperatures occurring during the process.

For the test, the tube-like specimen is made from the ship-building carbon-manganese steel DIN 1.0584 (D36), which has a length of 10 mm, an outer diameter of 10 mm, and a wall thickness of 1 mm. The work-piece has two sizes of openings and three double bridges arranged at interval of 120° (See Chapter 6, Figure 6.1 for detailed geometry). The diameters of three big and small openings are 5 mm and 0.8 mm, respectively. The openings must be cut by laser to the correct dimensions in order to reduce any pre-stresses inside the plates that might influence the distortion occurred during the laser forming operation. Prior to forming it, it should be cleaned with a mild acetone solution in order to remove the oil that protects them from oxidation. To obtain an absorption coefficient 0.75 on the plate surface, it has to be coated with graphite [41].

As a laser source, a CO_2 laser with 150 watts maximum power output operating in continuous wave mode (*cw* mode) is required. The size of the laser beam on the plate surface can be controlled using a variable laser beam expander. As shown in Figure 10.4, the work-piece is held in a rotational module, and it is instrumented with a linear variable displacement transducer (LVDT) with a support to measure the displacements and a thermocouple to measure temperatures of the plate during the operation. The locations of the LVDT and thermocouple are shown in Figure 10.4 (b). The LVDT is located at point 1, and the thermocouple at the bottom surface of the actuator under the irradiated point to avoid the interference with the laser irradiation.

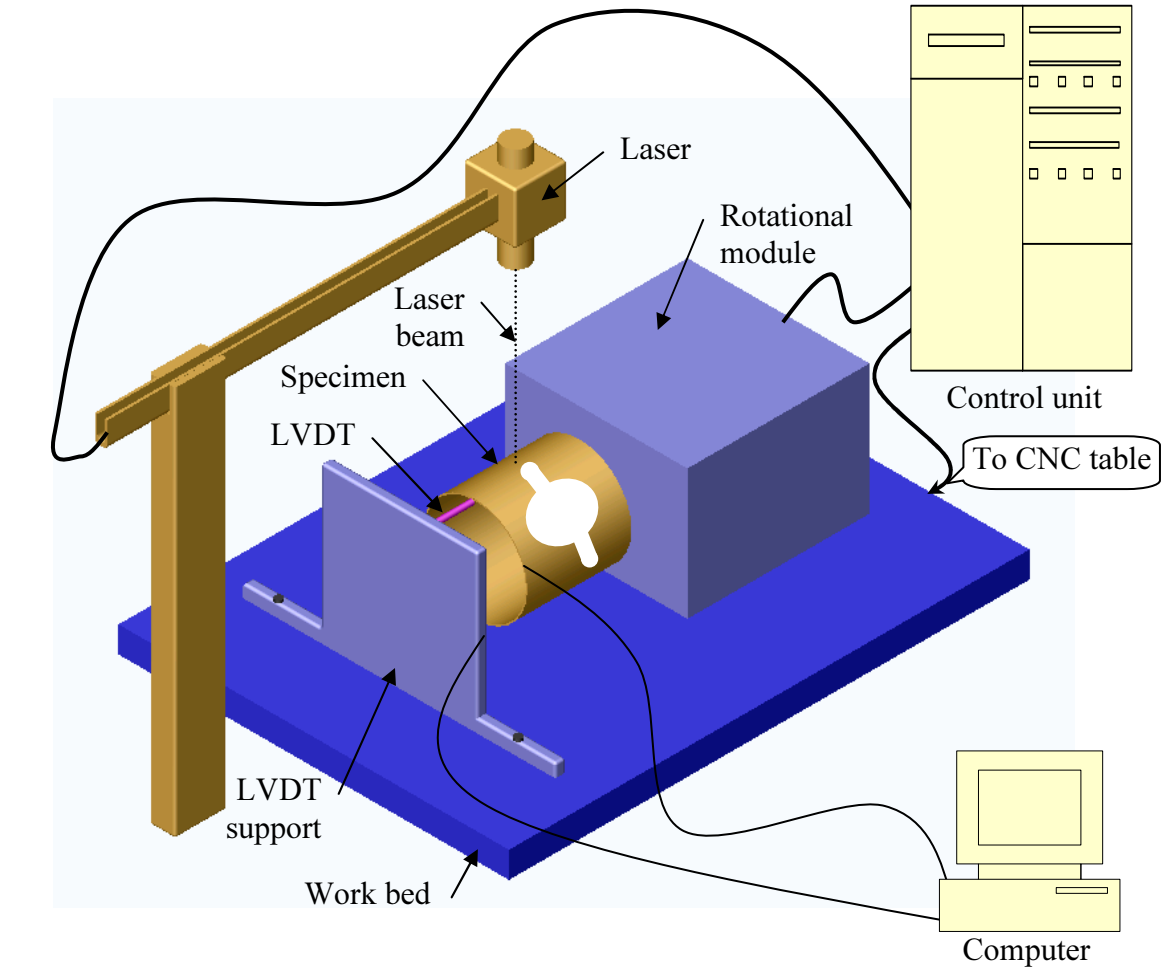

(a)

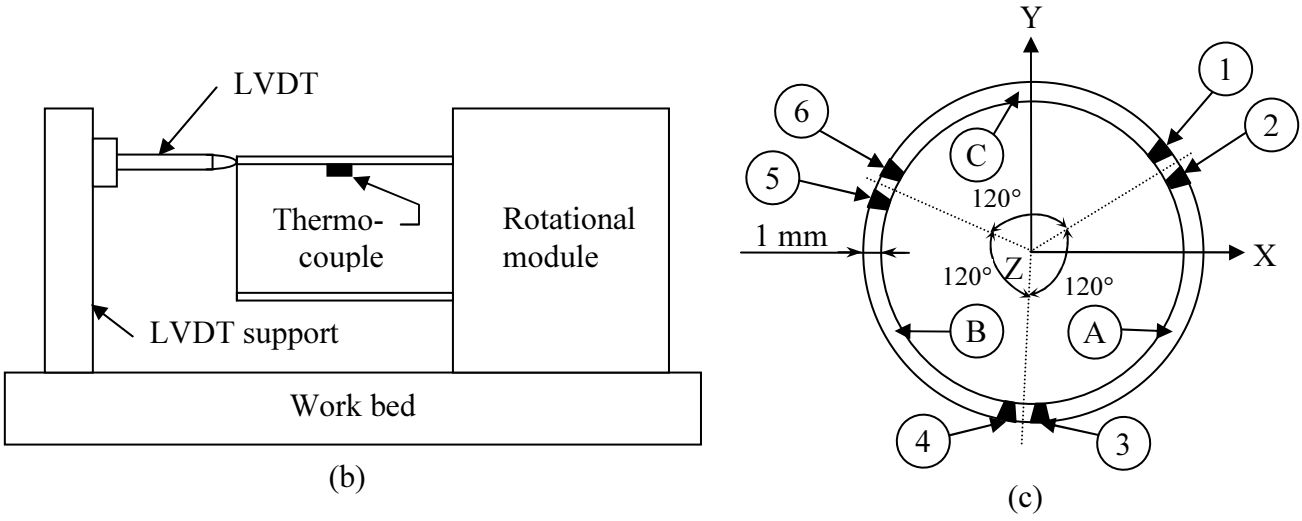

(b) (c)

Figure 10.4 (a) Schematic of test fixture for the laser micro-adjustment process; (b) Side view; and (c) Heating order and locations of displacement measurement.

The laser power applied to the surface of the structure is 100 watts, the beam diameter is 0.4 mm, and the heating time is 0.005 sec. The parameter values as well as the motion of the module can be set using the control unit. A series of six point irradiations are applied to the surface of the actuator in the order shown in Figure 10.4 (c). After heating at each point, the displacements at points A, B, and C are measured rotating the work-piece.

The results of bend angle from the corresponding numerical simulations to the test are presented in Table 10.3 to provide the convenience of comparison between experimental and numerical results. A maximum temperature of 695 °C at the bottom surface was obtained from the simulation.

Table 10.3 Displacement results from simulation corresponding to the laser adjustment test (Unit: μm).

Classification	Point A	Point B	Point C
After heating point 1	1.06	-0.07	-0.70
After heating point 2	-0.89	0.01	0.31
After heating point 3	-1.67	1.00	0.24
After heating point 4	-1.06	-0.23	0.28
After heating point 5	-1.17	-1.05	1.28
After heating point 6	-1.12	-0.24	-0.31

Note: Positive sign indicates expanding of the specimen and negative sign shortening.

10.5 Summary

This chapter has described experiment protocols for three laser forming processes – the straight-line heating process, the circle-line heating process, and the laser micro-adjustment process – which had been simulated in previous chapters. Test fixture and procedure for each process were presented. LVDT and thermocouple were employed to measure displacements and temperatures during the operations, respectively. Simulation conditions and results corresponding to each test case were described.

Chapter 11

Conclusions and Recommendations

This thesis has investigated the laser heating processes of shaping metallic components via the finite element analysis. The investigation has involved the following topics:

- Development of three-dimensional finite element models of the laser forming processes.
- Establishment of an effective method to determine optimum process parameters.
- Assessment of the reliability of the laser forming process.
- Evaluation of the effects of material properties on the forming result.
- Presentation of experiment protocols.

11.1 Conclusions

The main achievements of the work described in this thesis are summarized in separate sub-sections, as follows:

11.1.1 Numerical model and simulation

For the simulations of the laser forming processes, a nonlinear transient three-dimensional heat transfer finite element model and a rate dependent three-dimensional deformation model were developed. The thermal model accounts

for temperature dependent material properties – thermal conductivity and specific heat capacity. The mechanical model involves temperature dependent elastic, thermal, and plastic strains. Using the thermal-stress coupled field method, a large number of computational simulations were carried out for the following processes: straight-line heating, circle-line heating, and laser micro-adjustment. The material used was carbon-manganese steel (DIN 1.0584). The capability of the finite element models was validated comparing the magnitude of the bend angles and material behaviors from the simulations of the straight-line heating processes with published data.

The laser forming mechanism, TGM, was quantitatively identified obtaining temperatures, stresses, plastic strains, and displacements from the single straight-line heating process. A multiple heating process was developed for the simulation of process optimization. An unsymmetrical dish-shaped geometry was produced from the circle-line heating process. The quality of the deformed part was characterized with both radial and circumferential waviness. Micron size movements were induced in a tube-like structure with three double bridges by laser point heating on the bridges. The presented numerical model can contribute to determine optimum process parameters in order to produce a desired adjustment.

11.1.2 Process optimization

A process optimization procedure in laser forming was established by introducing design optimization and optimization techniques into the finite element analysis of the laser forming process. Two optimization techniques (i.e., the non-gradient method and the gradient-based method) were studied by solving an optimization problem to produce a predefined bend angle of 3° with multiple passes in the straight-line heating process. Each optimum process sought by the two methods could satisfy the condition to generate the target angle. However, the optimization procedure involving the non-gradient method was more suitable for the laser forming problem from the point of view of computing time. A new optimum process condition was determined by the

non-gradient method to produce a maximum bend angle in a single pass of laser forming. The maximum bend angle of 2.216° was obtained with a set of optimum process parameters: a laser power of 1999 watts, a feed rate of 0.0036 m/s, and a beam diameter of 0.0158 m.

11.1.3 Process reliability

The reliability of the straight-line heating process provoked by the variations of the process variables was evaluated using the Monte Carlo method. The procedure of the assessment included the finite element analysis and statistical analysis techniques. The reliability analysis was conducted on the process optimized, in Chapter 7, to produce a bend angle of 3°. It was found from the Monte Carlo simulations on the response surface that the minimum and maximum bend angles expected to occur are 2.8818° and 3.2049°, respectively, and there is a 52% probability that the bend angle remains between 2.96° and 3.04°. The results were validated with good agreement on the results by the Monte Carlo simulations based on 100 FE-simulations of the laser forming process.

11.1.4 Property sensitivity

The influence of material properties on the bend angle in a straight-line heating process was examined via the Monte Carlo simulations based on 100 FE-simulations of the process. Sensitivities between bend angle and material properties were statistically measured using the Pearson product-moment correlation coefficients. Moderate positive correlations were determined for the property of coefficient of thermal expansion. Moderate negative correlations were found for the properties of thermal conductivity and specific heat capacity. Insignificant correlations were noticed for the properties of elastic modulus and Poison's ratio. The results correlate to physics of laser bending.

11.1.5 Experiment protocol

Experiment fixtures and procedures for three laser forming processes – the straight-line heating process, the circle-line heating process, and the laser micro-adjustment process – have been presented for future work.

11.2 Recommendations

Important recommendations for future research in improving the laser forming technique arise from the conclusions presented in Section 9.1. The remainder of this chapter summarizes a few potential works.

11.2.1 Experiments

Even though the experiment protocols in this thesis have proposed the uses of LVDTs for measuring displacements and thermocouples for measuring temperatures resulting from laser forming experiments, other measurement tools may be developed or employed to accurately measure three-dimensional shapes and temperatures occurred. Design of experiments has to be established to ensure efficient experiments.

11.2.2 Finite element models

In experiments, the metallic materials experience a slight melting in the position of the laser beam center and phase changes near and under the laser beam paths. However, the numerical models used in this study do not account for the physical phenomena. Considering the material changes in the simulations could result in a gain in accuracy.

11.2.3 Simulation of complex shapes

This thesis has presented the simulation of a complex shape (i.e., dish shape) which was produced by applying four circle-line irradiations with an identical diameter to a circular plate. Multiple circle-line irradiations with different diameters and heating orders can be simulated to investigate an effective

heating strategy and identify the forming quality. Other complex geometrical shapes (for example, saddle, pillow, cone and pipe bending) can by studied by numerical simulations.

11.2.4 Process optimization

Process optimizations have been carried out to generate a desired bend angle or to produce a maximum bend angle in a straight-line heating process. The process variables used in the simulations have been limited to the following input variables: laser power, feed rate, beam diameter and number of passes. The optimization program may be significantly improved by involving laser beam path into the input variables to be optimized to obtain complex geometrical shapes.

11.2.5 Reliability analysis

The variations of the random input variables (i.e., laser speed, feed rate, coefficient of thermal expansion, and plate thickness) used in the reliability evaluation have been assumed to follow a Gaussian distribution in a certain level. It is required to collect the actual scatter of the random variables in each laser forming case and take into account other random input variables (for example, other material and geometry variables) to calculate accurate reliabilities.

11.2.6 Process sensitivity

In addition to the variables of coefficient of thermal expansion, thermal conductivity, specific heat capacity, elastic modulus and Poison's ratio, the sensitivity of bend angle can be evaluated against the following variables: laser power, feed rate and plate geometry to underpin the fundamental understanding of the laser forming process.

11.2.7 Material data at high temperatures

Numerical simulations could be greatly improved if material property data at high temperatures for new materials are developed.

References

[1] Namba, Y., 1985, 'Laser forming in space', In: Proceedings of International Conference on Lasers, Las Vegas, pp. 403-407.

[2] Scully, K., 1987, 'Laser line heating', Journal of Ship Production, 3(4), pp. 237-246.

[3] Altan, T., *Engineering Research Center for Net Shape Manufacturing*, [2004, Dec8], [Online]. Available:http://nsmwww.eng.ohiostate.edu/BendingOverview//html/tooling.html.

[4] Hosford, W. F. and Duncan, J. L. *Sheet Metal Forming: A Review*, [2004, Dec 8], [Online]. Available: www.tms.org/pubs/journals/JOM/9911/Hosford-9911.html.

[5] Frackiewicz, H., 1993, 'Laser metal forming technology', FABTECH INTERNATIONAL, Illinois, pp. 723-747.

[6] Geiger, M., 1994, 'Synergy of laser material processing and metal forming', Annals of the CIRP, 43(2), pp. 563-570.

[7] Walczyk, D. F. and Vittal, S., 2000, 'Bending of titanium sheet using laser forming', Journal of Manufacturing Processes, 2(4), pp. 258-269.

[8] Watkins, K. G., et al., 2001, 'Laser forming of aerospace alloys', In: Aerospace Manufacturing Technology Conference. Seattle, Washington, USA.

[9] Geiger, M., Arnet, H. and Vollertsen, F., 1994, 'Laser forming', In: Proceedings of the LANE, pp. 81-92.

[10] Geiger, M., Vollertsen, F. and Deinzer, G., 1993, 'Flexible straightening of car body shells by laser forming', In: International Congress and Exposition, Detroit, MI, USA: Publ by SAE, Warrendale, PA, USA.

[11] Magee, J., et al., 1998, 'Laser bending of high strength alloys', Journal of Laser Applications, 10(4), pp. 149-155.

[12] Thomson, G. and Pridham, M. S., 1997, 'Controlled laser forming for rapid prototyping', Rapid Prototyping Journal, 3(4), pp. 137-143.

[13] Muller, B., 2001, 'Laser adjustment - models for the design of actuators', LANE, pp. 519-526.

[14] Muller, B., Huber, A. and Geiger, M., 1999, 'Sub-micron accuracy of assembled systems by laser adjustment', In: Advanced Technology of Plasticity, pp. 1037-1042.

[15] Olowinsky, A. and Bosse, L., 2003, 'Laser beam micro forming as a new adjustment technology using dedicated actuator structures', In: Proceedings of SPIE, pp. 285-294.

[16] Otsu, M., Wada, T. and Osakada, K., 2001, 'Micro-bending of thin spring by laser forming and spark forming', CIRP Annals - Manufacturing Technology, 50(1), pp. 141-144.

[17] Hoving, W., 1997, 'Accurate manipulation using laser technology', In: Proceedings of SPIE, 3097, pp. 284-295.

[18] Gartner, E., Fruhauf, J. and Jansch, E., 2001, 'Plastic reshaping of silicon microstructures: process, characterization and application', Mcrosystem technology, 7, pp. 155-160.

[19] *Lasers and laser applications at Liverpool*, [2005, Aug. 30], [Online]. Available: http://www.lasers.org.uk/laserwelding/howalaserworks.htm.

[20] Vollertsen, F., 1998, *Forming and Rapid Prototyping, in Handbook of the EuroLaser Academy*, Schuocker, D. Editor, Chapman & Hall: Vienna, Austria.

[21] Geiger, M. and Meyer-Pittroff, F., 2002, 'Laser beam bending of metallic foils', In: Proceedings of SPIE, 4426, pp. 187-190.

[22] Behler, K., Beyer, E. and Herziger, G., 1988, 'Using the beam polarization to enhance the energy coupling in laser beam welding', Laser Materials Processing, pp. 98-105.

[23] Widlaszewski, J., 2001, 'Thermal deformation of multilevel spatial structures induced by laser pulses', In: Proceedings of the LANE, pp. 569-574.

[24] Magee, J., et al. 1997, 'Laser forming of aerospace alloys', In: ICALEO, pp. 156-165.

[25] Edwardson, S. P., et al., 2001, '3D laser forming of saddle shapes', In: Proceedings of the LANE, pp. 559-568.

[26] Hennige, T., 1997, 'Laser forming of spatially curved parts', In: Proceedings of the LANE, pp. 409-420.

[27] Magee, J., Watkins, K. G. and Hennige. T., 1999, 'Symmetrical laser forming', In: Proceedings of ICALEO, pp. 77-86.

[28] Masubuchi, K., 1992, 'Studies at M. I. T. related to applications of laser technologies to metal fabrication', In: Proceedings of LAMP, Nagaoka, pp. 939-946.

[29] Vollertsen, F. and Rodle, M., 1994, 'Model for the temperature gradient mechanism of laser bending', In: Proceedings of the LANE, pp. 371-378.

[30] Vollertsen, F., 1994, 'Mechanisms and models for laser forming', In: Proceedings of the LANE, pp. 345-359.

[31] Widlaszewski, J., 1997, 'Precise laser bending', In: Proceedings of the LANE, pp. 393-398.

[32] Price, S., [2005, Aug. 30], *CSIRO Manufacturing and infrastructure technology*, [Online]. Available: http://www.cmit.csiro.au/brochures/tech/laserforming/.

[33] Merklein, M. and Geiger, M., 2001, 'A comparative study of two different laser forming mechanisms regarding the mechanical properties of aluminium alloys', In: Proceedings of the LANE, pp. 537-548.

[34] Vollertsen, F., 1994, 'An analytical model for laser bending', Lasers in Engineering, 2, pp. 261-276.

[35] Vollertsen, F., Komel, I. and Kals, R., 1995, 'The laser bending of steel foils for microparts by the buckling mechanism - a model', Modelling Simul. Mater. Sci. Eng., 3, pp. 107-119.

[36] Hao, N. and Li, L., 2003, 'An analytical model for laser tube bending', Applied Surface Science, 208-209(1), pp. 432-436.

[37] Li, W. and Yao, Y. L., 2001, 'Laser bending of tubes: mechanism, analysis, and prediction', Journal of Manufacturing Science and Engineering, Transactions of the ASME, 123, pp. 674-681.

[38] Holzer, S., Arnet, H. and Geiger, M., 1994, 'Physical and numerical modeling of the buckling mechanism' In: Proceedings of the LANE, pp. 379-386.

[39] Hsiao, Y., et al., 1997, 'Finite element modeling of laser forming', In: Proceedings of ICALEO, pp. 31-40.

[40] Yau, C.L., Chan, K. C. and Lee, W. B., 1998, 'Laser bending of leadframe materials', Journal of Materials Processing Technology, 82(1-3), pp. 117-121.

[41] Stern, G., 1990, 'Absorptivity of cw CO2, CO and YAG-laser beams by different metallic alloys', ECLAT'90, pp. 25-35.

[42] Marya, M. and Edwards, G. R., 2000, 'Factors affecting the laser bending of Ti-6Al-2Sn-4Zr-2Mo', Journal of Laser Applications, 12(4), pp. 149-159.

[43] Hu, Z., et al., 2001, 'Computer simulation and experimental investigation of sheet metal bending using laser beam scanning', International Journal of Machine Tools and Manufacture, 41(4), pp. 589-607.

[44] Hu, Z., Kovacevic, R. and Labudovic, M., 2002, 'Experimental and numerical modeling of buckling instability of laser sheet forming', International Journal of Machine Tools and Manufacture, 42(13), pp. 1427-1439.

[45] Shichun, W. and Jinsong, Z., 2001, 'An experimental study of laser bending for sheet metals', Journal of Materials Processing Technology, 110, pp. 160-163.

[46] Sprenger, A., et al., 1994, 'Influence of strain hardening on laser bending', In: Proceedings of the LANE, pp. 361-370.

[47] Otsu, M., Osakada, K. and Fujii, M., 2000, 'Controlled laser forming of sheet metal with shape measurement and using database', In: Proceedings of Metal Forming, pp. 433-438.

[48] Magee, J., Watkins, K. G. and Steen, W. M., 1998, 'Advances in laser forming', Journal of Laser Applications, 10(6), pp. 235-246.

[49] Hanebuth, H. and Hamann, C., 1997, 'Suitability of CuCoBe-alloys for laser beam bending', In: Proceedings of the LANE, pp. 367-374.

[50] Maher, W., et al., 1998, 'Laser forming of titanium and other metals is useable within metallurgical constraints', In: ICALEO, pp. 121-130.

[51] Marya, M. and Edwards, G. R., 2001, 'Study on the laser forming of near-alpha and metastable beta titanium alloy sheets', Journal of Materials Processing Technology, 108(3), pp. 376-383.

[52] Magee, J., et al., 1997, 'Edge effects in laser forming', In: Proceedings of the LANE, pp. 399-408.

[53] Mucha, Z., et al., 1997, 'Laser forming of thick free plates', LANE, pp. 383-392.

[54] Bao, J. and Yao, Y. L., 2001, 'Analysis and prediction of edge effects in laser bending', Journal of Manufacturing Science and Engineering, Transactions of the ASME, 123, pp. 53-61.

[55] Vollertsen, F., Geiger, M. and Li, W. M., 1993, 'FDM-and FEM-simulation of laser forming: a comparative study', In: Proceeding of the Fourth International Conference on Technology of Plasticity, pp. 1793-1798.

[56] Li, W. and Yao, Y. L., 2000, 'Numerical and experimental study of strain rate effects in laser forming', Journal of Manufacturing Science and Engineering, Transactions of the ASME, 122, pp. 445-451.

[57] Li, W. and Yao, Y. L., 2001, 'Numerical and experimental investigation of convex laser forming process', Journal of Manufacturing Processes, 3(2), pp. 73-81.

[58] Cheng, J. and Yao, Y. L., 2002, 'Microstructure integrated modeling of multiscan laser forming', Journal of Manufacturing Science and Engineering, Transactions of the ASME, 124(2), pp. 379-388.

[59] Alberti, N., Fratini, L. and Micari, F., 1994, 'Numerical simulation of the laser bending process by a coupled thermal mechanical analysis', In: Proceedings of the LANE, pp. 327-336.

[60] Chen, G., et al., 1999, 'Experimental and numerical studies on microscale bending of stainless steel with pulsed laser', Journal of Applied Mechanics, Transactions ASME, 66(3), pp. 772-779.

[61] Cosenza, C., et al., 2001, 'Explicit thermo-mechanical analysis of laser forming processes', In: Proceedings of the LANE, pp. 549-558.

[62] Kraus, J., 1997, 'Basic processes in laser bending of extrusions using the upsetting mechanism', In: Proceedings of the LANE, pp. 431-438.

[63] Kyrsanidi, A.K., Kermanidis, T. B. and Pantelakis, S. G., 1999, 'Numerical and experimental investigation of the laser forming process', Journal of Materials Processing Technology, 87(1-3), pp. 281-290.

[64] Tong, K., 1998, 'A numerical study on laser forming of titanium plates', In: Proceedings of ICALEO, pp. 131-140.

[65] Zhang, L. and Michaleris, P., 2004, 'Investigation of Lagrangian and Eulerian finite element methods for modeling the laser forming process', Finite Elements in Analysis and Design, 40(4), pp. 383-405.

[66] Huebner, K. H., et al., 2001, *The finite element method for engineers*, 4th edition, John Wiley & Sons, Inc., New York.

[67] Meinders, T., 1999, *Developments in numerical simulations of the real-life deep drawing process*, Ph.D. Thesis, University of Twente.

[68] Incropera, F. P. and DeWitt, D. P., 2002, *Fundamentals of heat and mass transfer*, 5th Edition, John Wiley & Sons, Inc., New York.

[69] Siegal, R. and Howell, J. R., 1981, *Thermal Radiation heat transfer*, 2nd Edition, Hemisphere Publishing Corporation.

[70] *ANSYS Theory Manual*, 2003, Version 8.0, ANSYS Inc., USA.

[71] Spencer, G. C., 1968, *Introduction to plasticity*, Chapman and Hall.

[72] Chakrabarty, J., 1998, *Theory of plasticity*, 2nd edition, McGraw-Hill.

[73] Huang, Y. and Leu, D., 1995, 'Finite element analysis of contact problems for a sheet metal bending process', Journal of Computers and Structures, 57(1), pp.15-27.

[74] Cook, R. D., Malkus, D. S., Plesha, M. E. and Witt, R. J., 2002, *Concepts and applications of finite element analysis*, 4th Edition, John Wiley & Sons. Inc., New York.

[75] Selvadurai, A. P. S., 2000, *Partial differential equations in mechanics 2*, Springer-Verlag Berlin Heidelberg.

[76] ASM Committee, 1990, *Metals Handbook - Properties and Selection: Irons, Steels, and High-Performance Alloys*, 10th Edition.

[77] *ANSYS software*, 2003, Version 8.0, ANSYS Inc., USA.

[78] Inoue, T. and Arimoto, K., 1997, 'Development and implementation of CAE system "HEARTS" for heat treatment simulation based on metallo-thermo-mechanics', Journal of Materials Engineering and Performance, 6(1).

[79] Walsh, G. R., 1979, *Methods of optimization*, John Wiley & Sons. Ltd., New York.

[80] Asghar Bhatti, 2000, *Practical optimization methods*, Springer-Verlag New York, Inc.

[81] Myers, R. H. and Montgomery, D. C., 2002, *Response Surface Methodology*, 2nd Edition, John Wiley & Sons, Inc., New York.

[82] Venkataraman, P., 2002, *Applied optimization with MATLAB programming*, John Wiley & Sons, New York.

[83] More, J. J. and Wright, S. J., 1993, *Optimization software guide,* SIAM, Philadelphia.

[84] Chambers, J. M., 1977, *Computational methods for data analysis,* Bell Laboratories, Inc. USA.

[85] Neter, J., Kutner, M. H., Nachtsheim, C. J., and Wasserman, W., 1996, *Applied linear statistical models*, 4th Edition, McGraw-Hill.

[86] Montgomery, D. C., 2001, *Design and analysis of experiments*, 5th Edition, John Wiley & Sons, Inc., New York.

[87] Shenkin, D.J., 1997,*Handbook of parametric and nonparametric statistical procedures*, CRC Press Inc., Florida.

[88] Luxon, J. T., Parker, D. E. and Plotkowski, P. D., 1987, *Lasers in manufacturing*, IFS (Publications) Ltd. and Springer-Verlag.

[89] Meijer, J. , 2004, 'Laser beam machining (LBM), state of the art and new opportunities', Journal of Materials Processing Technology, 149, pp. 2-17.

Appendix A

Overview of the Laser

A.1 Laser Light

Light is used for everything from eye surgery to materials processing. An important property of light is that it has no volume, photons have no charge, so when concentrated into a very small space, they do not repulse each other like negative charged electrons do. This is an important property, especially for ultrashort machining. Light moves through space as a wave, but when it encounters matter it behaves like a particle of energy, a photon. The energy of photons is $E = hf$ where h is Planck's constant and f is the wavelength of light. Thus, not all photons have the same amount of energy [88].

The acronym LASER stands for Light Amplification by Stimulated Emission of Radiation. The word radiation refers to 'electromagnetic radiation', of which light is a special case. The key words in the acronym are 'amplification by stimulated emission'. A laser amplifies light and it does this by means of the phenomenon of stimulated emission.

Figure A.1 shows how laser light is created using a ruby laser. Any photon that has been released by an atom using light source should encounter another atom that has another electron in the same excited state, and stimulated emission can occur. The first photon can stimulate or induce atomic emission so that the emitted photon vibrates with the same frequency and direction. It is necessary to have a pair of mirrors at either of the lasing medium to produce

laser light. These mirrors are often known as an optical oscillator due to the process of oscillating photons between the two mirrored surfaces. The mirror positioned at one end of the optical oscillator is half-silvered, therefore it reflects some light and lets some light through. The light that is allowed to pass through is the light that is emitted from the laser. During this process photons are constantly stimulating other electrons to make the downward energy jump, hence causing the emission of more and more photons and an avalanche effect, leading to a large number of photons being emitted of the same wavelength an phase [19].

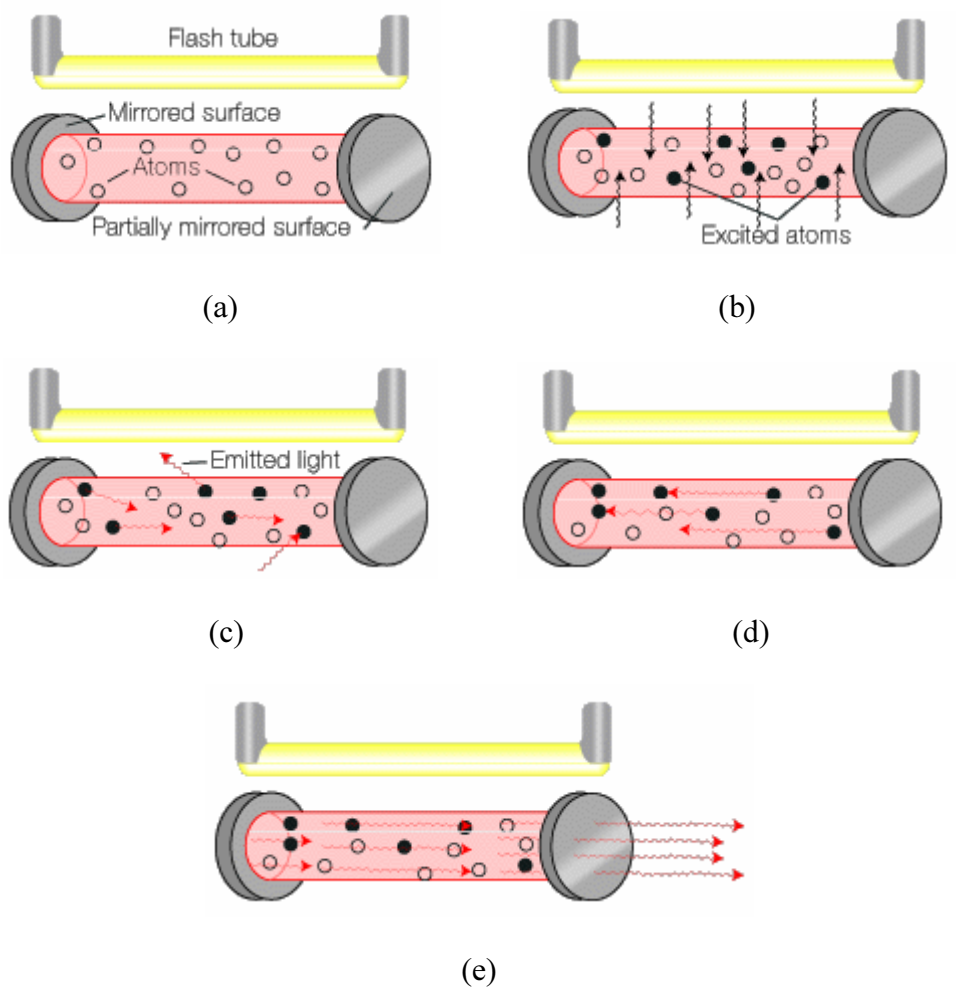

Figure A.1 A graphical illustration how laser light is created: (a) Laser in non-lasing state; (b) The excitation of atoms using light source; (c) Photon emission; (d) The stimulated emission of further photons; and (e) Column of laser light leaving optical oscillator. Reproduced from [19].

A.2 Properties of Laser Light [88]

Due to the release of any photons by an atom, laser light has the unique properties of a wavelength, phase and energy level dependent on the difference between the excited atom and the ground-state energy level. This properties make lasers such useful tools in an incredible variety of industrial applications. The primary properties associated with manufacturing applications are radiance, monochromaticity, coherence and the various forms of output, i.e. continuous pulsed or Q-switched.

The radiance of a source of light is the power emitted per unit area of the source per unit solid angle. Lasers achieve high radiance at relatively low power levels. The amount of power that can be concentrated on a spot by focusing a beam of light is directly proportional to the radiance. In laser work an important concept is the irradiance (frequently called intensity). Irradiance is the power per unit area falling on a surface at a given point. For convenience the units are usually given as watts per square centimeter (W/cm^2).

The term monochromatic literally means single color or single wavelength. However, no light source (or any electromagnetic source for that matter) is perfectly monochromatic. Lasers tend to be relatively monochromatic. One specific wavelength of light is determined by the amount of energy released when the electron drops to a lower-energy orbital. Generally, in processes controlled by thermal effects precise wavelength control is not critical. However, processing of polymeric materials with ultraviolet wavelengths, such as are available from excimer lasers, is entirely different. Thermal effects are negligible, molecular bonds are broken directly by interaction with the ultraviolet light.

Lasers provide a high radiance source of light with a high degree of coherence. Coherence means each photon moves in step with the other (i.e., all photons have wave fronts that move in unison).

The output of industrial lasers may be pulsed or continuous. Materials processing lasers may be either pulsed or continuous whereas lasers used for alignment, measurements and other low power applications usually have a continuous output. Continuous output is referred to as CW (continuous wave) output. Literally, however, it simply means that the power output is constant. Pulsed output may be accomplished by a variety of techniques. By using different pulse generation techniques the pulse duration, pulse energy and reproducibility can be modified over wide ranges. A process referred to as Q-switching is used to increase the peak power. The pulse length is less than a microsecond down to several nanoseconds with peak powers between 10^{6} and 10^{9} W. While Q-switching can be used to generate pulse with high intensities in the ns-range, mode-locking process is used to generate ultrashort laser pulses with pulse duration in the *ps*- to *fs*-range.

A.3 Types of Laser [19]

There are many different types of lasers. The laser medium can be a solid, gas, liquid or semiconductor. Lasers are commonly designated by the type of lasing material employed.

Solid-state lasers have lasing material distributed in a solid matrix (such as the ruby or neodymium:yttrium – aluminum garnet "Yag" lasers). The neodymium – Yag laser emits infrared light at 1,064 nanometers (nm). A nanometers is 1×10^{-9} meters.

Gas lasers (helium and helium-neon, HeNe, are the most common gas lasers) have a primary output of visible red light. CO_2 lasers emit energy in the far-infrared, and are used for cutting hard materials.

Excimer lasers (the name is derived from the terms excited and dimmers) use reactive gases, such as chlorine and fluorine, mixed with inert gases such as argon, krypton or xenon. When electrically stimulated, a pseudo molecule

(dimmer) is produced. When laser, the dimmer produces light in the ultraviolet range.

Dye lasers use complex organic dyes, such as rhodamine 6G, in liquid solution or suspension as lasing media. They are tunable over a broad range of wavelengths.

Semiconductor lasers, sometimes called diode lasers, are not solid-state lasers. Theses electronic devices are generally very small and use low power. They may be built into larger arrays, such as the writing source in some laser printers or CD players.

A.4 Short Pulsed Lasers

An overview of short pulsed lasers in given in Table A.1 [89].

Table A.1 Short pulsed lasers.

Laser	Wavelength (nm)	Pulse length	Frequency (kHz)
TEA CO_2	10600	200 μs	5
Nd:YAG	1060, 532, 355, 266	100 ns, 10 ns	50
Excimer	193 – 351	20 ns	0.1 – 1
Copper vapor	611 – 578	30 ns	4 – 20
Ti Sapphire	775	100 fs	1 – 250

Appendix B

Interpolation Functions

The following pages contain the interpolation functions [70] of the elements (i.e., SOLID70, SURF152, SOLID45, MESH200, SOLID87 and SOLID92) used for the FE-simulations of the laser forming processes.

The interpolation function for the element, SOLID70, is given as follows:

$$\begin{aligned} T = \frac{1}{8}(&T_I(1-\xi)(1-\eta)(1-\zeta) + T_J(1+\xi)(1-\eta)(1-\zeta) \\ &+ T_K(1+\xi)(1+\eta)(1-\zeta) + T_L(1-\xi)(1+\eta)(1-\zeta) \\ &+ T_M(1-\xi)(1-\eta)(1+\zeta) + T_N(1+\xi)(1-\eta)(1+\zeta) \\ &+ T_O(1+\xi)(1+\eta)(1+\zeta) + T_P(1-\xi)(1+\eta)(1+\zeta)) \end{aligned} \tag{B.1}$$

where:

T = temperature

I, J, K, L, M, N, O, P = nodes

ξ, η, ζ = natural coordinates

The interpolation function for the element, SURF152, is given as follows:

$$T = \frac{1}{4}(T_I(1-\xi)(1-\eta) + T_J(1+\xi)(1-\eta) + T_K(1+\xi)(1+\eta) + T_L(1-\xi)(1+\eta)) \tag{B.2}$$

where:

T = temperature

I, J, K, L = nodes

ξ, η = natural coordinates

The interpolation function for the element, SOLID45, is given as follows:

$$\begin{aligned} U = \frac{1}{8}(&U_I(1-\xi)(1-\eta)(1-\zeta) + U_J(1+\xi)(1-\eta)(1-\zeta) \\ &+ U_K(1+\xi)(1+\eta)(1-\zeta) + U_L(1-\xi)(1+\eta)(1-\zeta) \\ &+ U_M(1-\xi)(1-\eta)(1+\zeta) + U_N(1+\xi)(1-\eta)(1+\zeta) \\ &+ U_O(1+\xi)(1+\eta)(1+\zeta) + U_P(1-\xi)(1+\eta)(1+\zeta)) \end{aligned} \tag{B.3}$$

where:

U = displacement

I, J, K, L, M, N, O, P = nodes

ξ, η, ζ = natural coordinates

The interpolation function for the element, SOLID87, is given as follows:

$$\begin{aligned} T = {} & T_I(2L_1-1)L_1 + T_J(2L_2-1)L_2 + T_K(2L_3-1)L_3 \\ & + T_L(2L_4-1)L_4 + 4T_M L_1L_2 + T_N L_2L_3 + T_O L_1L_3 \\ & + T_P L_1L_4 + T_Q L_2L_4 + T_R L_3L_4 \end{aligned} \tag{B.4}$$

where:

T = temperature

I, J, K, L, M, N, O, P, Q, R = nodes

L = natural coordinate

The interpolation function for the element, SOLID92, is given as follows:

$$\begin{aligned} U = {} & U_I(2L_1-1)L_1 + U_J(2L_2-1)L_2 + U_K(2L_3-1)L_3 \\ & + U_L(2L_4-1)L_4 + 4U_M L_1L_2 + U_N L_2L_3 + U_O L_1L_3 \\ & + U_P L_1L_4 + U_Q L_2L_4 + U_R L_3L_4 \end{aligned} \tag{B.5}$$

where:

U = displacement

I, J, K, L, M, N, O, P, Q, R = nodes

L = natural coordinate

Appendix C

ANSYS Computer Program Listings

The following pages contain the ANSYS program listings for the FE-simulations of the straight-line heating process, process optimization, process reliability, and property sensitivity.

```
++++++++++++++++++++++++++++++++++++++++++++++++++++++++++++++++
                    Thermal Analysis of Laser Forming
++++++++++++++++++++++++++++++++++++++++++++++++++++++++++++++++

Definition of Parameters   !!!!
```

```
mptemp,1,20,1500
mpdata,dens,1,1,8018,7416
mptemp

mptemp,1,20,100,200,300,400,500
•
•
•
mpdata,kxx,1,1,51.9,51.1,48.6,44.4,42.7,39.4     (W/mK)
•
•
•
mptemp

mptemp,1,20,100,200,300,400,500
•
•
•
mpdata,c,1,1,486,487,498,515,536,557
•
•
•
mptemp

*DIM,conv_temp,table,11,1
conv_temp(1,1)=20,100,200,300,400,500,600,700,800,900,1000
mptemp,1,27,77,127,177,227,277
•
•
•
mpdata,HF,2,1,2.82,7.51,8.64,9.12,9.36,9.45
•
•
•
mptemp

mshkey,1                ! For mapped meshing.
mshape,0,3D             ! For quadrilateral shape.

Generates Nodes   !!!!
```

```
•
•
•

Generates Elements   !!!!
```

```
nsel,s,loc,y,0
nsel,a,loc,x,-L/2,L/2,L
nsel,a,loc,z,-W/2
sf,all,conv,-2,%conv_temp%
allsel

nsel,s,loc,y,-TH
sf,all,conv,-3,%conv_temp%
allsel

toffst,273
d,nn+1,temp,TEMP_B

solve

TM_INCR=(L/NE_L)/V
*do,ii,1,400,1
TM_STEP=TM_INCR*ii
X_CTR=X1D*(ii-33)
Y_CTR=0
Z_CTR=0

*if,ii,LE,65,then
local,11,0,X_CTR,Y_CTR,Z_CTR
nsel,s,loc,y,-TH,0,TH
nsel,a,loc,x,-L/2,L/2,L
nsel,a,loc,z,-W/2
sfdele,all,all
allsel

*IF,R,EQ,0.005,THEN
nsel,s,loc,x,-X2D,X2D
nsel,r,loc,y,0
nsel,r,loc,z,-(X1D),0
sf,all,hflux,HFLUX
!sflist,all,hflux
allsel

nsel,s,loc,x,-(X1D),X1D
nsel,r,loc,y,0
nsel,r,loc,z,-(X2D),-X1D
sf,all,hflux,HFLUX
!sflist,all,hflux
allsel
```

```
nsel,s,loc,x,-X1D,X1
nsel,r,loc,y,0
nsel,r,loc,z,-X1D,0
nsel,inve
nsel,u,loc,y,-th
nsel,u,loc,z,0
sf,all,conv,-2,%conv_temp%
!sflist,all,conv
allsel

nsel,s,loc,x,-X2D,-X1D
nsel,r,loc,y,0
nsel,r,loc,z,-X2D,-X1D
sf,all,conv,-2,%conv_temp%
!sflist,all,conv
allsel

nsel,s,loc,x,X1D,X2D
nsel,r,loc,y,0
nsel,r,loc,z,-X2D,-X1D
sf,all,conv,-2,%conv_temp%
!sflist,all,conv
allsel

nsel,s,loc,y,-th
sf,all,conv,-3,%conv_temp%
allsel

csys,0

toffst,273
d,nn+1,temp,TEMP_B

time,TM_STEP
autots,on
nsubst,10,100,5
solve
save
•
•
•
save
finish
```

```
++++++++++++++++++++++++++++++++++++++++++++++++++++++++++++++++++++
                    Structural analysis of Laser Forming
++++++++++++++++++++++++++++++++++++++++++++++++++++++++++++++++++++

/PREP7      !!!!
```

```
tb,miso,1,15,12

tbtemp,20
tbpt,,YS20/E20,YS20
•
•
•
tbpt,,0.262,863e6

tbtemp,100
tbpt,,YS100/E100,YS100
•
•
•
tbpt,,0.262,830e6

•
•
•

tbtemp,1400
tbpt,,YS1400/E1400,YS1400
•
•
•
tbpt,,0.262,10e6
finish


/SOLU          !!!!
```

```
nsel,s,loc,z,0
nsel,r,loc,x,-L/2
nsel,r,loc,y,-TH
d,all,uy,0
allsel

nsel,s,loc,z,0
nsel,r,loc,x,L/2
nsel,r,loc,y,-TH
d,all,uy,0
allsel

nsel,s,loc,z,0
nsel,r,loc,x,0
d,all,ux,0
allsel

LDREAD,temp,,,TM_START,,D36_thermal,rth
SOLVE

TM_INCR=(L/NE_L)/V
*do,ii,1,400,1
TM_STEP=TM_INCR*ii
LDREAD,temp,,,TM_STEP,,D36_thermal,rth

time,TM_STEP
nsubst,1
solve
*enddo
save
finish
```

++

Process Optimization

++

~ Thermal analysis ~
objective function =

~ Structural analysis ~
objective function =

```
/OPT
opanl,D36_opt,txt
opvar,maxiob,OBJ,,,0.001
opvar,temp_ctr,SV,0,1400
opvar,uy_edge,SV,0,0.1
opvar,p,DV,1400,2000,0.01
opvar,v,DV,0.001,0.008,0.000001
opvar,r,DV,0.005,0.0125,0.000001
opvar,ns,DV,1,4,0.25

optype,FIRST
opfirst,20,100,0.2

optype,RAND
oprand,20,10
opsel,-1

optype,SUBP
opsubp,30,7
opsel,-1
opeqn,0,0,3,0,0

optype,SWEEP
opsweep,BEST,2

optype,GRAD
opgrad,LAST,0.5

opexe

oplist,all,,1
/axlab,y,miniob
plvaropt,miniob

finish
/exit
```

++

Process Reliability

++

~ Thermal analysis ~

~ Structural analysis ~

```
/PDS
pdanl,D36_opt,txt

pdvar,p,GAUS,1810.3,0.2
pdvar,v,GAUS,0.0042,0.00001
pdvar,th,GAUS,0.006,0.00001
pdvar,COTE,GAUS,11.7E-6,0.0000001

pdvar,angle,resp

PDMETH,RSM,CCD
PDDOEL,p,CCD
PDDOEL,v,CCD
PDDOEL,th,CCD
PDDOEL,COTE,CCD

PDEXE,ccdd36

RSFIT,ccdd36angle,ccdd36,angle
RSPLOT,ccdd36angle,angle,p,v,3D,500

RSSIMS,ccdd36angle,10000

PDMETH,MCS,DIR
PDDMCS,100,NONE,ALL,,,,123457

PDMETH,MCS,LHS
PDLHS,50,1,RAND,NONE,ALL,0.01,0.02,10,CONT

PDEXE,mcsd36

finish
/exit
```

++

Sensitivity Analysis

++

```
COTE=11.7E-6                    ! Coefficient of Thermal Expansion
CODT=51.9                       ! CONDUCTIVITY
SPHT=486                        ! SPECIFIC HEAT
E20=206E9
PSSN=0.296

==================== Thermal Analysis ====================
•
•
•
mptemp,1,20,100,200,300,400,500
•
•
•
mpdata,kxx,1,1,CODT,(51.1/51.9)*CODT,(48.6/51.9)*CODT,(44.4/51.9)*CO
DT,(42.7/51.9)*CODT,(39.4/51.9)*CODT
•
•
•
mptemp

mptemp,1,20,100,200,300,400,500
•
•
•
mpdata,c,1,1,SPHT,(487/486)*SPHT,(498/486)*SPHT,(515/486)*SPHT,(536/
486)*SPHT,(557/486)*SPHT
•
•
•
mptemp

•
•
•
•
•
•

====================== Structural Analysis ====================

•
•
E20=206E9
E100=(203/206)*E20
•
•
•
E1400=(8/206)*E20
```

```
YS20=345E6
•
•
•
YS1400=4E6

•
•
•

mptemp,1,20,100,200,300,400,500
•
•
•
mpdata,nuxy,1,1,PSSN,(0.311/0.296)*PSSN,(0.330/0.296)*PSSN,(0.349/0.296
)*PSSN,(0.367/0.296)*PSSN,(0.386/0.296)*PSSN
•
•
•
mptemp

mptemp,1,20,100,200,300,400,500
•
•
•
mpdata,alpx,1,1,COTE,COTE,(12.2/11.7)*COTE,(12.8/11.7)*COTE,(13.3/11.
7)*COTE,(13.8/11.7)*COTE
•
•
•
mptemp
•
•
•

tb,miso,1,15,8                    ! for Non-linear material property.

tbtemp,20
tbpt,,YS20/E20,YS20
tbpt,,0.005*(206E9/E20),552e6
•
•
•
tbpt,,0.262*(206E9/E20),863e6

tbtemp,100
•
•
•

/PDS
pdanl,D36_SRSM,txt
```

```
pdvar,COTE,UNIF,11.7E-6-0.1*11.7E-6,11.7E-6+0.1*11.7E-6
pdvar,CODT,UNIF,51.9-0.1*51.9,51.9+0.1*51.9
pdvar,SPHT,UNIF,486-0.1*486,486+0.1*486
pdvar,E20,UNIF,206E9-0.1*206E9,206E9+0.1*206E9
!pdvar,PSSN,UNIF,0.296-0.1*0.296,0.296+0.1*0.296

pdvar,angle,resp

PDMETH,RSM,CCD
PDDOEL,COTE,CCD
PDDOEL,CODT,CCD
PDDOEL,SPHT,CCD
PDDOEL,E20,CCD
PDDOEL,PSSN,CCD

PDEXE,ccdd36

RSFIT,ccdd36angle,ccdd36,angle
RSPLOT,ccdd36angle,angle,p,v,3D,500

RSSIMS,ccdd36angle,10000

PDMETH,MCS,DIR
PDDMCS,100,NONE,ALL,,,,123457

PDMETH,MCS,LHS
PDLHS,100,1,RAND,NONE,ALL,0.01,0.02,10,CONT

PDEXE,mcsd36

finish
/exit
```

Appendix D

Further Results of Reliability Analysis

D.1 Response Surface Plots of Bend Angle

This section contains the three-dimensional response surface plots of bend angle against input variables resulting from response surface method with central composite design.

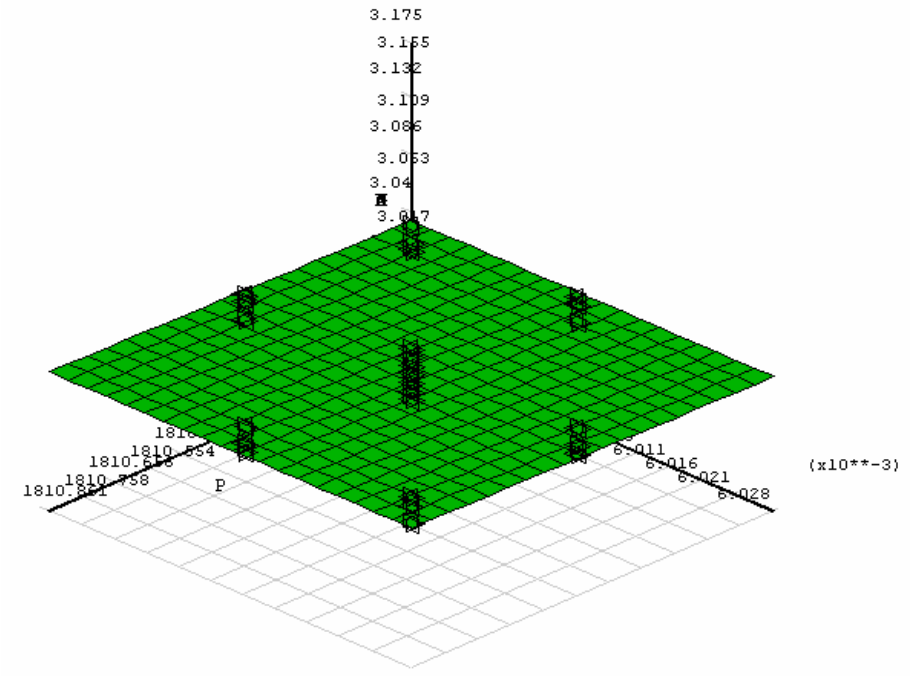

Figure D.1 Response surface plot of bend angle against laser power and plate thickness.

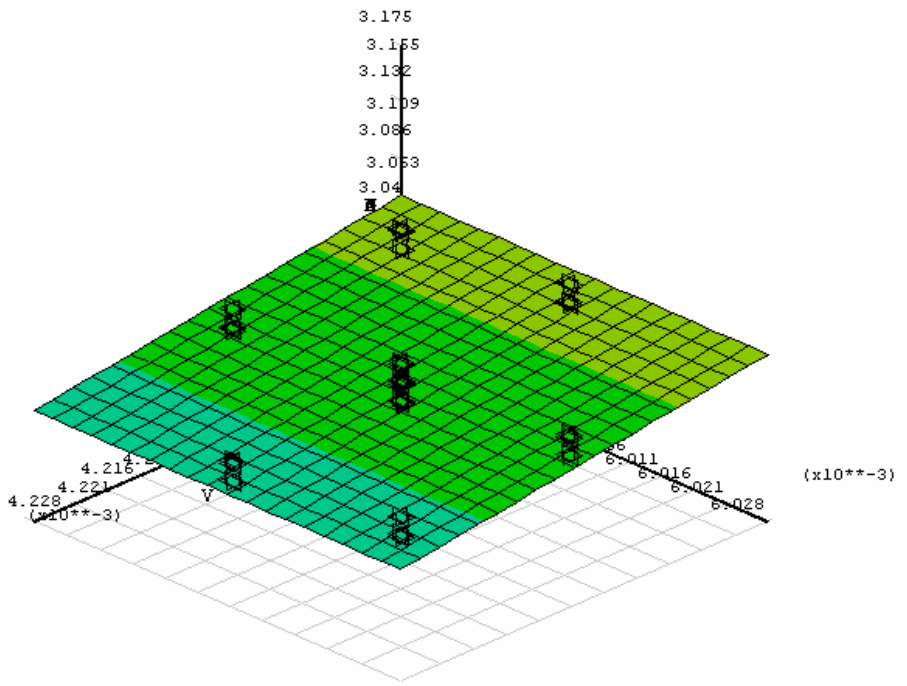

Figure D.2 Response surface plot of bend angle against feed rate and plate thickness.

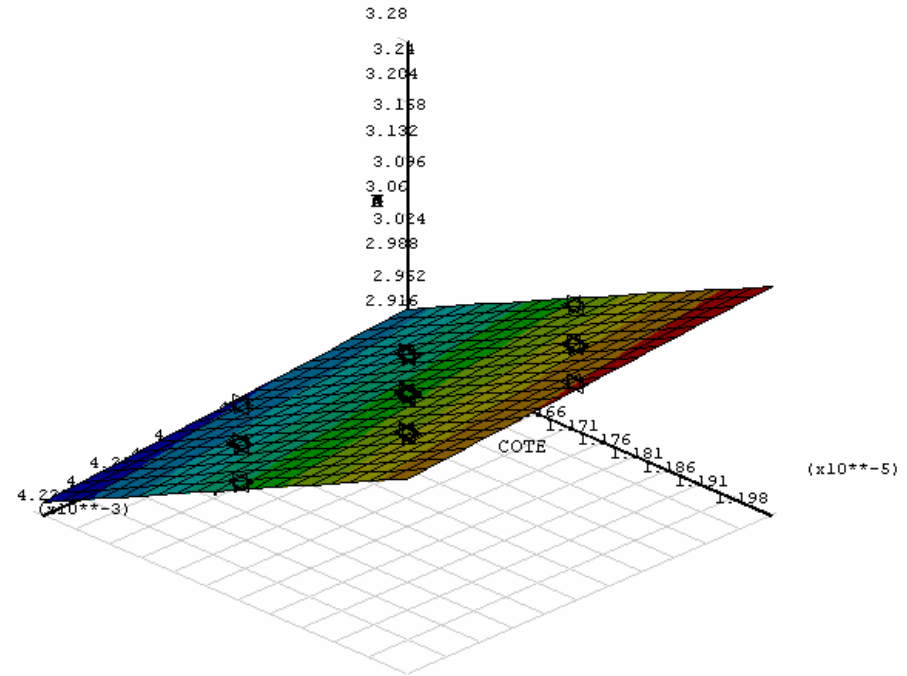

Figure D.3 Response surface plot of bend angle against feed rate and coefficient of thermal expansion.

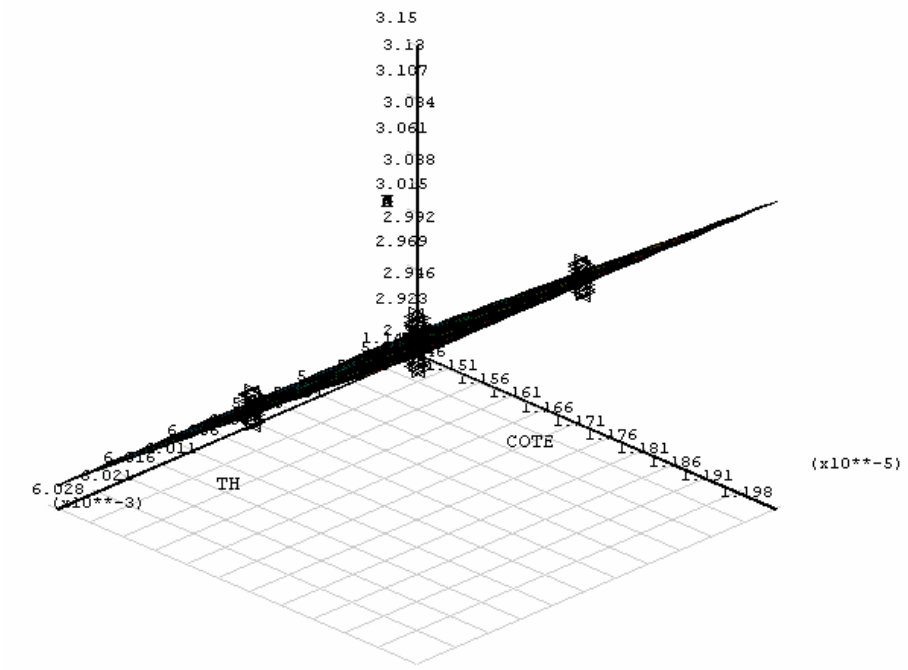

Figure D.4 Response surface plot of bend angle against plate thickness and coefficient of thermal expansion.

D.2 Variation of Input Variables during Monte Carlo Simulations

This section contains variations of input variables (i.e., laser power, feed rate, plate thickness, coefficient of thermal expansion) during the Monte Carlo simulations on response surface.

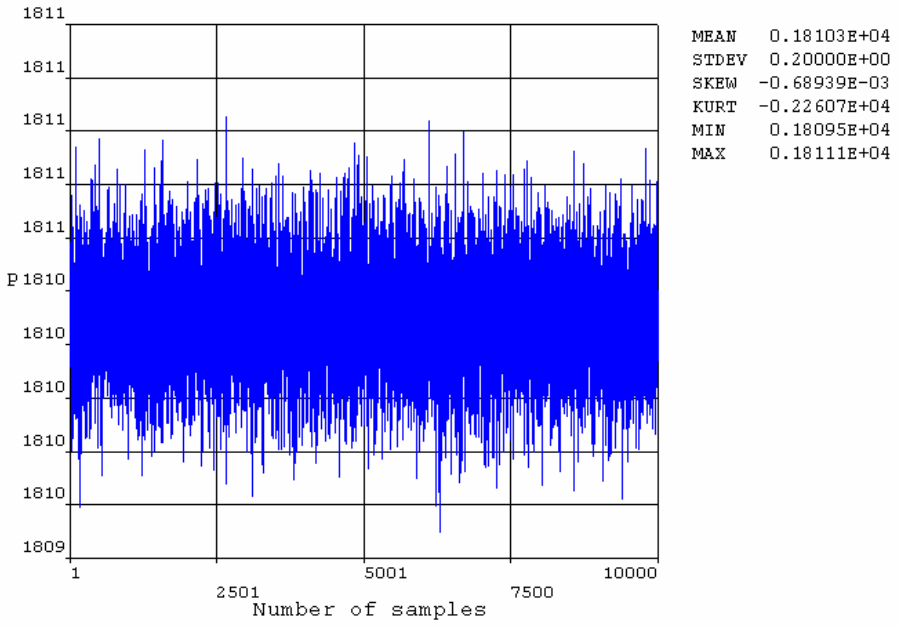

Figure D.5 Variations of laser power during the Monte Carlo simulations on response surface.

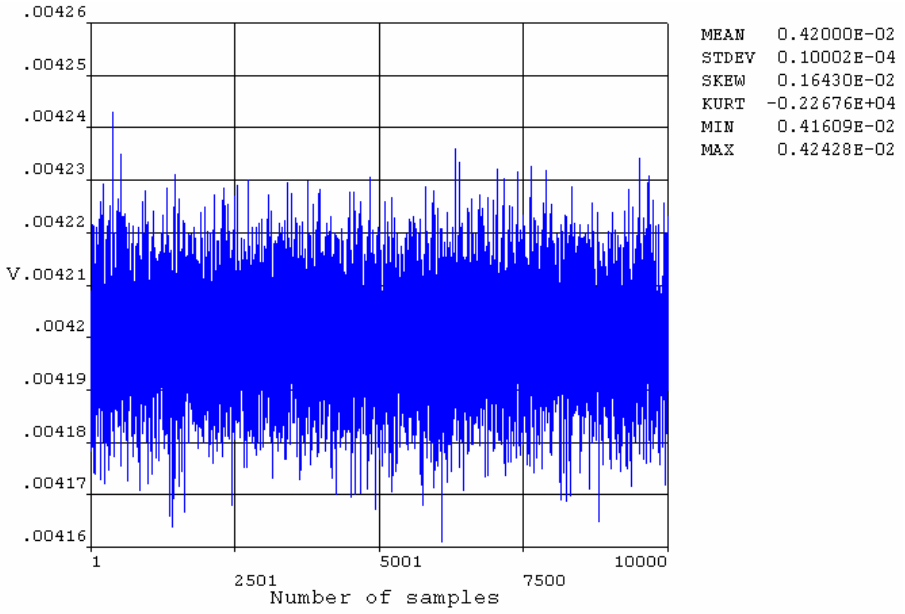

Figure D.6 Variations of feed rate during the Monte Carlo simulations on response surface.

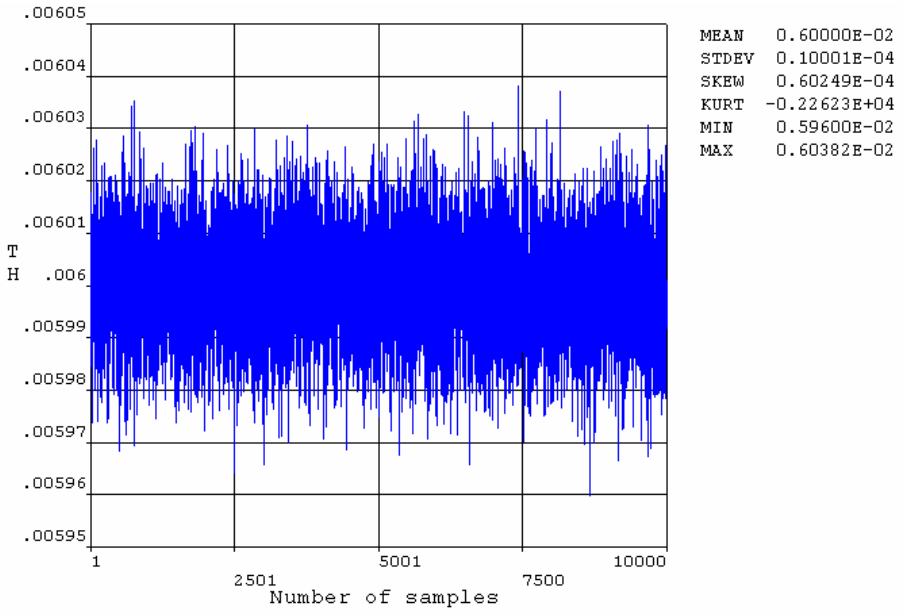

Figure D.7 Variations of plate thickness during the Monte Carlo simulations on response surface.

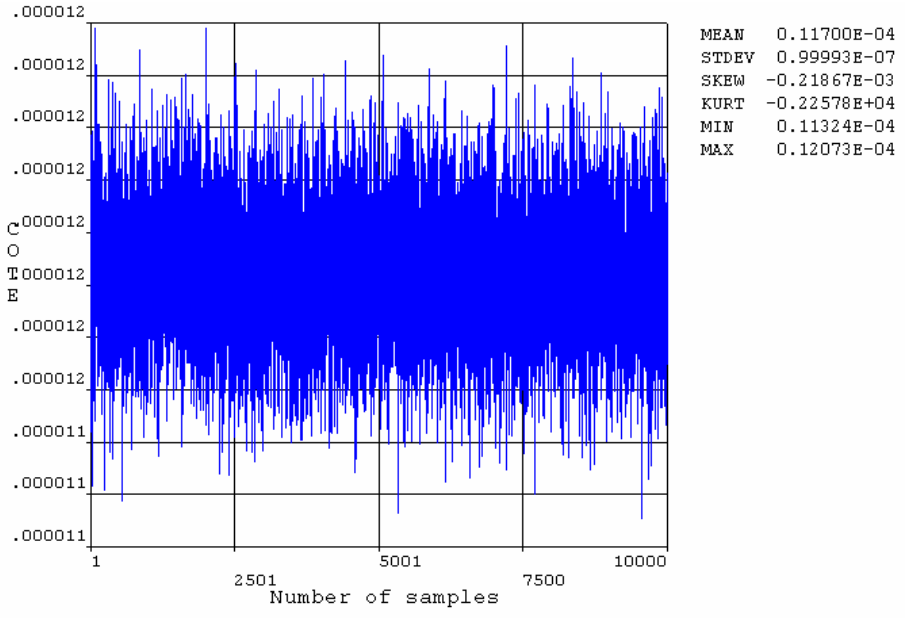

Figure D.8 Variations of coefficient of thermal expansion during the Monte Carlo simulations on response surface.

D.3 Relative Frequency of Input Variables during Monte Carlo Simulations

This section contains relative frequency of input variables (i.e., laser power, feed rate, plate thickness, coefficient of thermal expansion) occurring during the Monte Carlo simulations on response surface.

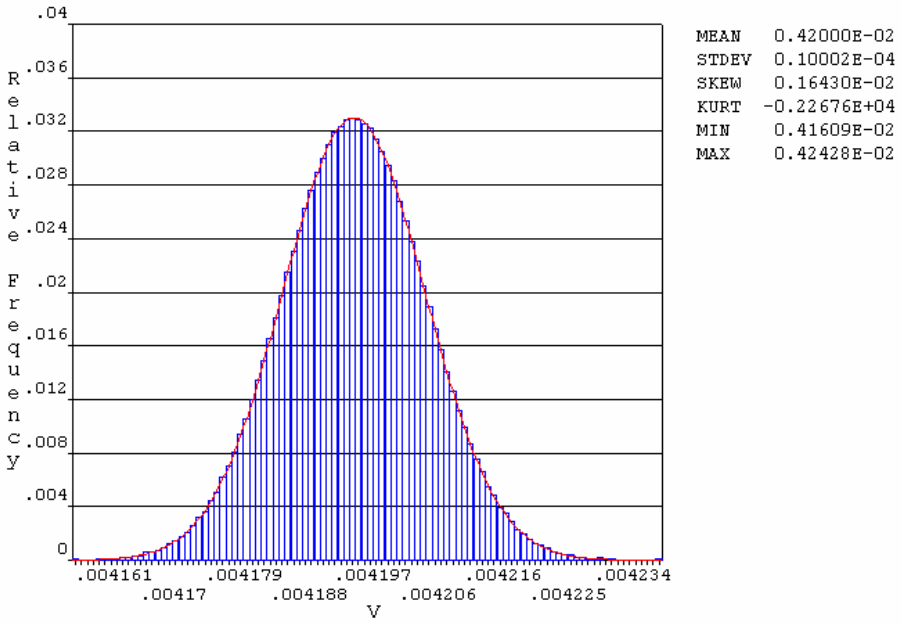

Figure D.9 Relative frequency of feed rate occurring during the Monte Carlo simulations on response surface.

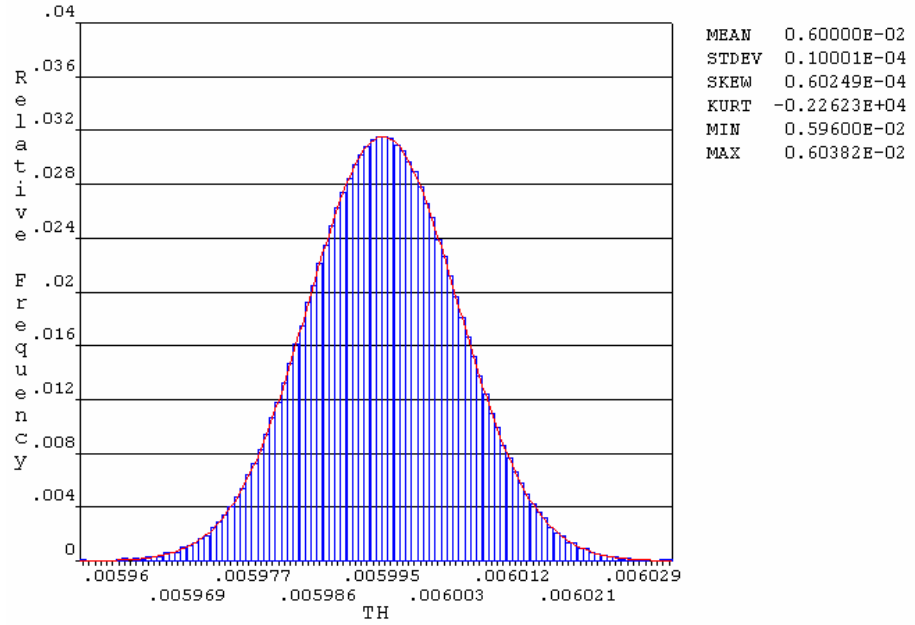

Figure D.10 Relative frequency of plate thickness occurring during the Monte Carlo simulations on response surface.

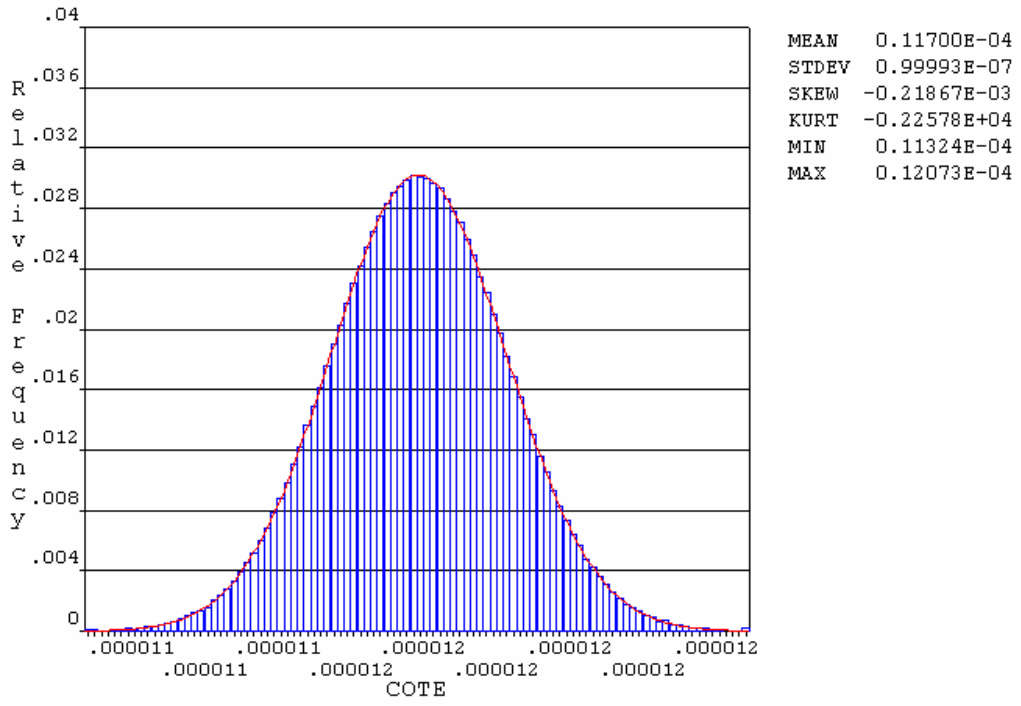

Figure D.11 Relative frequency of coefficient of thermal expansion occurring during the Monte Carlo simulations on response surface.

D.4 Probability of Input Variables occurring during Monte Carlo Simulations

This section contains probabilities of input variables (i.e., laser power, feed rate, plate thickness, coefficient of thermal expansion) occurring during the Monte Carlo simulations on response surface.

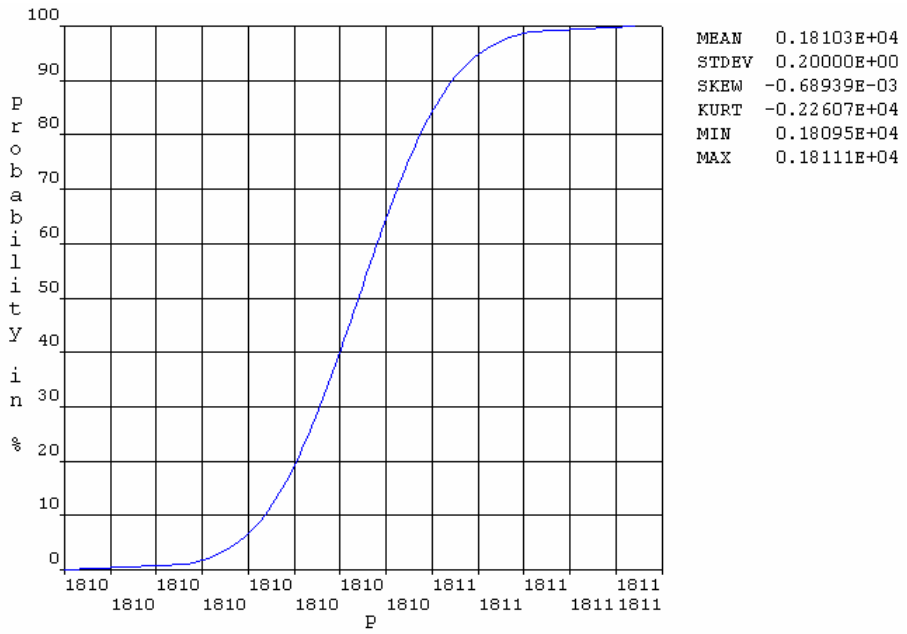

Figure D.12 Cumulative distribution curve of laser power occurring during the Monte Carlo simulations on response surface.

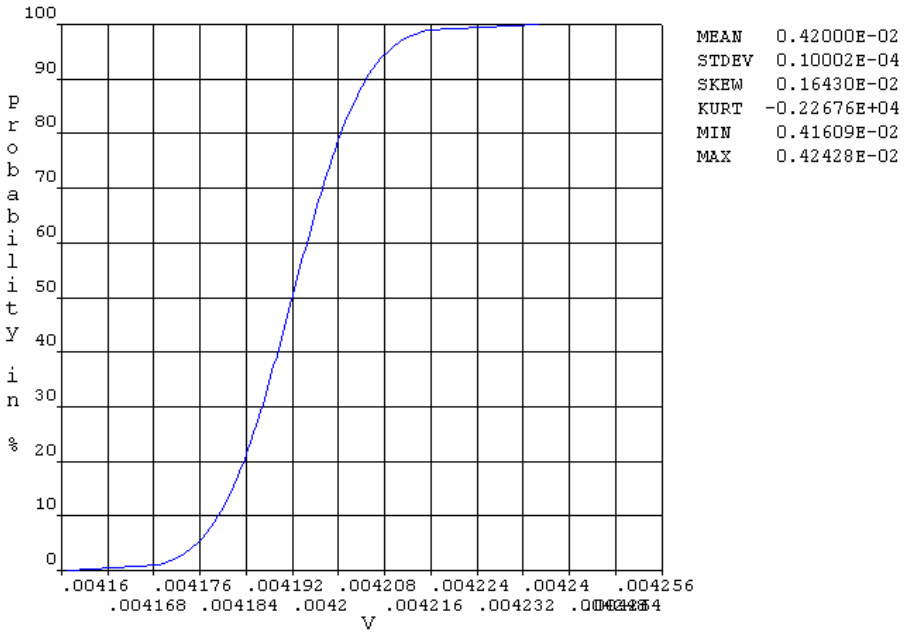

Figure D.13 Cumulative distribution curve of feed rate occurring during the Monte Carlo simulations on response surface.

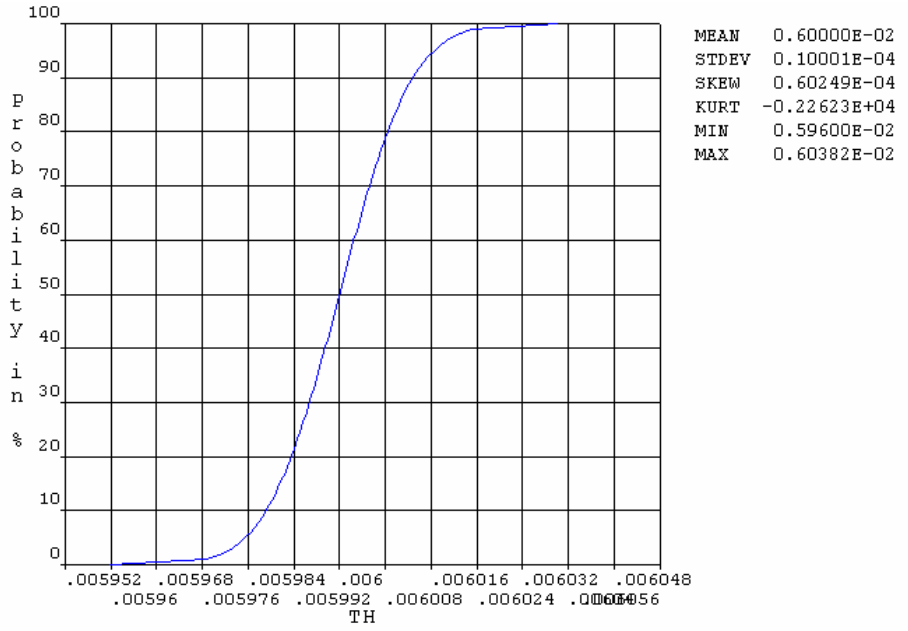

Figure D.14 Cumulative distribution curve of plate thickness occurring during the Monte Carlo simulations on response surface.

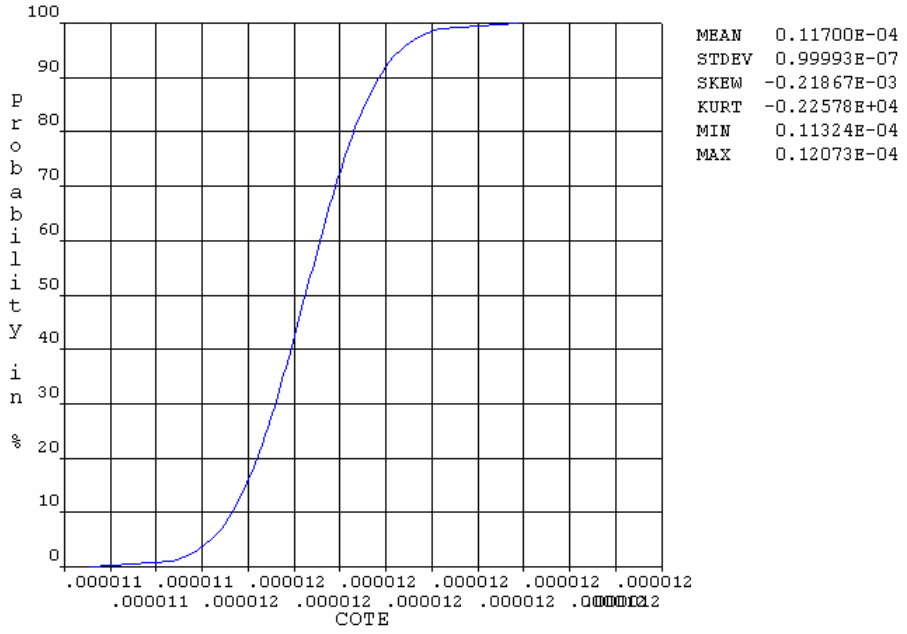

Figure D.15 Cumulative distribution curve of coefficient of thermal expansion occurring during the Monte Carlo simulations on response surface.

Appendix E

Uniform Distribution

A uniform distribution of a random variable X has two distribution parameters, namely the lower limit x_{min} and the upper limit x_{max}. The mean value of a random variable X with a uniform distribution is:

$$\mu = 0.5(x_{min} + x_{max})$$

and the standard deviation is:

$$\sigma = \frac{x_{min} - x_{max}}{\sqrt{12}}$$

The probability density function for a random variable X in a uniform distribution is expressed as:

$$f(x) = \frac{1}{x_{max} - x_{min}}$$

where:

x = each value which can be taken by the random variable X.

The probability density function of the random variable X represents a measure for the relative frequency at which values of input variables are expected to occur. Figure 00 shows the graphical representation of the probability density function of a uniform distribution.

The cumulative distribution function of a uniform distribution is defined as:

$$F(x) = \frac{x - x_{\min}}{x_{\max} - x_{\min}}$$

The cumulative distribution function of the random variable X is the probability that values for the random variable remain below a certain limit x. Figure 00 shows graphically the cumulative distribution function of a uniform distribution.

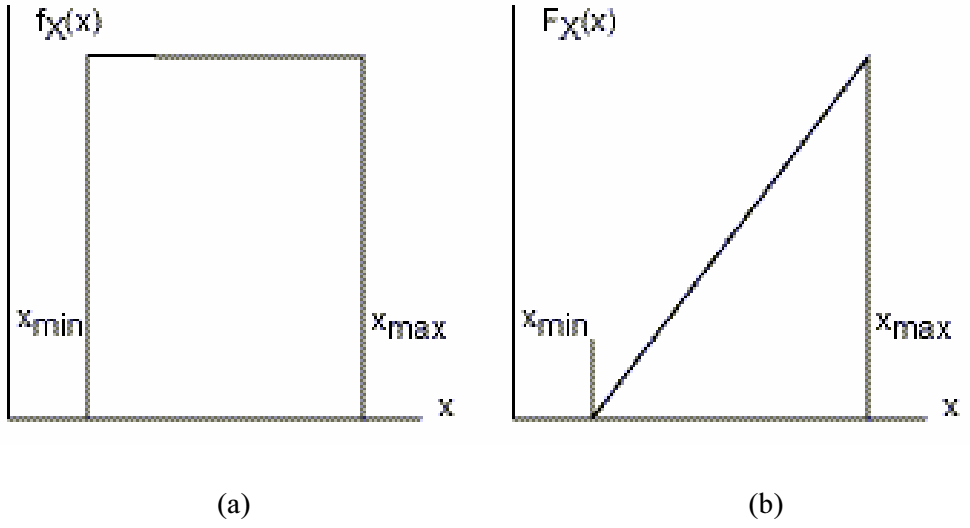

Figure E.1 Uniform distribution functions: (a) Probability density function and (b) Cumulative distribution function. Reproduced from [70].

The inverse cumulative distribution function of a uniform distribution is given by:

$$x = x_{\min} + P(x_{\max} - x_{\min})$$

where:

P = a given probability.